

Nebular Metallicities in Isolated Dwarf Irregular Galaxies

David Conway Nicholls

A thesis submitted for the degree of
Doctor of Philosophy
of the Australian National University



**Australian
National
University**

Research School of Astronomy & Astrophysics

July 2014

Notes on the Digital Copy

This document makes extensive use of the hyperlinking features of L^AT_EX. References to figures, tables, sections, chapters and the literature can be navigated from within the PDF by clicking on the reference. Internet addresses will be displayed in a browser.

Most object names are resolvable in the SIMBAD (<http://simbad.u-strasbg.fr/simbad/>) astronomical database.

The bibliography at the end of this thesis has been hyperlinked to the NASA Astrophysics Data Service (<http://www.adsabs.harvard.edu/>). Further information on each of the cited works is available through the link to ADS.

For Linda...

Disclaimer

I hereby declare that the work in this thesis is that of the candidate alone, except where indicated below or in the text of the thesis. The work was undertaken between January 2009 and February 2014 at the Australian National University, Canberra. It has not been submitted in whole or in part for any other degree at this or any other university.

Chapter 2 is the paper *The Small Isolated Gas-rich Irregular Dwarf (SIGRID) Galaxy Sample: Description and First Results* published in the *Astronomical Journal*, September 2011, volume 142, pp.83 et seq., by David C Nicholls, Michael A Dopita, Helmut Jerjen and Gerhardt R Meurer. The work is entirely that of the candidate.

Chapter 3 is the paper *Resolving the Electron Temperature Discrepancies in H II Regions and Planetary Nebulae: κ -distributed Electrons* published in the *Astrophysical Journal*, June 2012, volume 752, pp.148 et seq., by David C Nicholls, Michael A Dopita, and Ralph S Sutherland. The work is entirely that of the candidate apart from sections 3.6.1, 3.6.2 and 3.8, which were contributed by Michael Dopita.

Chapter 4 is the paper *Measuring nebular temperatures: the effect of new collision strengths with equilibrium and κ -distributed electron energies* published in the *Astrophysical Journal Supplement*, August 2013, volume 207, pp.21 et seq., by David C Nicholls, Michael A Dopita, Ralph S Sutherland, Lisa J Kewley and Ethan Palay. The work is entirely that of the candidate, with the exception of the data in Tables 3.4 and 3.5, computed by Michael Dopita.

Chapter 5 is the paper *Nebular metallicities in two isolated Local Void dwarf galaxies*, published in the *Astrophysical Journal*, January 2014, volume 780, pp. 88 et seq., by David C Nicholls, Helmut Jerjen, Michael A Dopita and Hassan Basurah. The work is entirely that of the candidate.

Chapter 6 is the paper *Metal-poor dwarf galaxies in the SIGRID galaxy sample. I. H II region observations and chemical abundances*, published in the *Astrophysical Journal*, May 2014, volume 786, pp. 155 et seq., by David C Nicholls, Michael A Dopita, Ralph S Sutherland, Helmut Jerjen, Lisa J Kewley, and Hassan Basurah. The work is entirely that of the candidate. Data for two of the objects presented in this paper were obtained by Michael Dopita.

Chapter 7 is the paper *Metal-poor dwarf galaxies in the SIGRID galaxy sample. II. The electron temperature–abundance calibration and the parameters that affect it*, accepted for publication in the *Astrophysical Journal*, July 2014, by David C Nicholls, Michael A Dopita, Ralph S Sutherland, Helmut Jerjen, and Lisa J Kewley. The work is entirely that of the candidate.



David Conway Nicholls

July 2014

Acknowledgments

In an undertaking such as this, it is impossible to single out all those who have contributed to my achieving this goal. Some, however, have been especially important in guiding me, and I wish to thank them explicitly.

First I would like to thank my joint supervisors, Professor Michael Dopita and Dr Helmut Jerjen. I have been exceptionally fortunate to work with and be guided by two such outstanding scientists.

I first met Mike Dopita, when running a government science grants program in the late 1980s. We established a sound working relationship even back then, and Mike was instrumental much later in my applying to study at the RSAA. Mike has been a continuing inspiration and guide in the journey that has led me to complete this thesis. The breadth of Mike's knowledge in the field of nebular physics is astounding. Without him, both his theoretical knowledge and the brilliant WiFeS spectrograph that he designed and brought into being, this work would have been impossible.

My second joint supervisor, Dr Helmut Jerjen, has likewise been profoundly important in guiding me to this goal. Helmut's understanding of the essence of small galaxies is prodigious. His enthusiasm has been both stimulating and infectious. His guidance in attending to the legion of small but essential details of this work has been critically important.

Next I wish to thank Dr. Ralph Sutherland, whose understanding of the intricacies of astrophysical computation is breathtaking. Ralph's encouragement and guidance in the detailed computation of the atomic data needed for the non-equilibrium calculations helped me with one of the major discoveries in this work.

I wish to thank Professor Lisa Kewley for hosting me at the Institute for Astronomy at the University of Hawaii, and for instilling in me the importance of an organised approach to research, a lesson that I have learned well, albeit slowly.

I also wish to thank Dr. Mike Childress for his critically important work in developing a new data reduction pipeline for the WiFeS spectroscopic data.

I am also indebted to my MSc thesis supervisor, Professor Ted Llewellyn, University of Saskatchewan, who taught me long ago how critically important good writing is to communicating science, at every level. It would be remiss of me also not to mention Professor Don Matthewson, with whom I worked as a research assistant in 1968, and from whom I first grasped what scientific research is about, and who also encouraged me to apply to study at RSAA.

Perhaps most important of all, I wish to thank my wife, Linda, for first suggesting in October 2008 that I embark on this wonderful odyssey, and for her patience with my total focus on the work, her continuing encouragement and interest, and for putting up with my endless urges to tell her about the arcane tasks in which I have been involved. Without her support this work would not have been possible.

Finally, I wish to thank my colleagues, students and faculty, at the Research School of Astronomy and Astrophysics, Mt Stromlo, for a wonderfully stimulating environment, and for making me realise that I belong in this august company. The stimulating discussions I

have had with many of the faculty and academic visitors are too numerous to mention. And a special thanks to my talented co-student, Fréd Vogt, whose help, fellowship and sheer *joie de la science* have contributed to making my studies so immensely enjoyable.

There have been so many others who have helped me develop to the point where I was ready for this work. These include my parents, my late first wife, Trish, and my excellent primary school teachers, Iris and Morwood Leyland, St Michael's School, Putney, where I first developed a fascination with science. And also the European Mole, *Talpa europaea*, digging in a garden in Walton-on-Thames long ago on a rare, dark, clear English summer's night, that lured me outside, where I first discovered the glory of the night sky. And the CIA chief of mission in Malaya, in 1959, who showed me the rings of Saturn, the Trapezium and the Orion Nebula, through a 3 inch Edmund Scientific Co. Newtonian telescope. To them, and the legion of others I have not mentioned, I say simply, thank you.

Abstract

The motive for this work was to investigate whether small, isolated gas-rich galaxies show evidence of chemical evolution, by studying their nebular metallicities. I have identified a sample of 83 objects chosen for low luminosity and mass, the presence of active star formation, and isolation from other galaxies and galaxy clusters that might generate tidal effects or enrich the intergalactic medium. From these I have measured the spectra of 35 objects, using the WiFeS IFU spectrograph on the ANU 2.3m telescope at Siding Spring.

In analysing spectra extracted from the WiFeS data cubes, I found that standard ‘strong line’ methods using emission line ratios to measure atomic abundances, gave either erratic or no results. I found that for those galaxies showing the [O III] 4363Å auroral line, the metallicities determined using the standard ‘electron temperature’ method were inconsistent with previous published work. This led me to investigate the conventional assumption that electrons in H II regions are in thermal equilibrium. I show that the non-equilibrium ‘ κ ’ electron energy distribution, found almost universally in solar system plasmas, can explain the long recognised ‘abundance discrepancy’ between recombination line and collisional line abundance calculations in nebular metallicity measurements. This has added an important new dimension to the analysis of nebular spectra.

Using the extensively revised Mappings photoionisation modelling code and new atomic data to analyse the spectra of two exceptionally isolated dwarf galaxies, I find that they exhibit metallicities similar to galaxies in more crowded environments, and appear to have evolved quite normally, through periodic star formation and subsequent enrichment of their interstellar media.

I present a new approach for calculating total oxygen abundance using electron temperatures that appears to give more consistent results than earlier methods. I apply this to my measured spectra, together with the revised Mappings photoionisation modelling code, to explore the physical parameters affecting the measurement of nebular metallicities. In particular, I find strong evidence for several of the observed nebulae being—in part—optically thin. I use the models to show that nebular optical depth affects measured abundances and temperatures, and that electron densities also have an important role. I develop models that give a very good match to the observations.

I conclude that the measurement of abundances and temperatures in H II regions is a more complex question than had generally been assumed, and important physical parameters affecting the measurement processes have in the past not been taken fully into account.

Contents

Notes on the digital copy	0
List of Figures	xi
List of Tables	xv
1 Introduction	1
1.1 H II regions: the birthplace of stars	1
1.2 The origins of the elements	3
1.3 Measuring the physical conditions in H II regions	3
1.4 Metallicity gradients, tidal dwarfs and field dwarfs	4
1.5 Observations, methods and the structure of this thesis	5
2 The Small Isolated Gas Rich Irregular Dwarf (SIGRID) Galaxy Sample	7
2.1 Chapter summary	7
2.2 Introduction	7
2.3 The “SIGRID” sample	9
2.4 Selection criteria	10
2.5 The SIGRID catalog	13
2.6 Sample images	19
2.7 Isolation	26
2.8 Sample completeness	34
2.9 Metallicity	36
2.10 WiFeS and nebular abundance measurements	37
2.11 ‘Sub-dwarf’ galaxies?	38
2.12 ‘Bloaters’	39
2.13 A Blue Compact Dwarf excess?	40
2.14 Conclusion	41

3	Resolving the electron temperature discrepancies	43
3.1	Chapter summary	43
3.2	Introduction	44
3.3	The κ -distribution	45
3.4	What might give rise to κ -distributions in H II regions?	49
3.5	The effect of κ -distributions on collisional excitation in H II regions	50
3.6	The Determination of κ	57
3.7	Conclusion	61
3.8	Evidence for magnetic fields in Milky Way H II regions	62
3.9	The κ -distribution and the temperature fluctuation (“ t^2 ”) method	63
3.10	Collision Excitation Rate ratios	64
4	Measuring nebular temperatures	69
4.1	Chapter summary	69
4.2	Introduction	70
4.3	Rationale for considering non-equilibrium electron energies.	71
4.4	The κ distribution	74
4.5	Collision strength considerations	76
4.6	The Effect of κ on recombination processes	81
4.7	Collisionally Excited Lines	86
4.8	Tools for measuring temperatures	96
4.9	Strong line techniques	105
4.10	Estimating κ	105
4.11	Conclusions	106
4.12	Appendix: Supplementary Data Tables	106
5	Nebular metallicities in two isolated Local Void dwarf galaxies	109
5.1	Chapter summary	109
5.2	Introduction	109
5.3	KK246	110
5.4	HIPASS J1609-04	114
5.5	Observations and Data Reduction	116
5.6	Spectra	120
5.7	Nebular metallicities	122
5.8	Comparison with similar samples	126
5.9	Discussion	130
5.10	Conclusions	131

6	Metal-poor dwarf galaxies: Observations and abundances	133
6.1	Chapter summary	133
6.2	Introduction	134
6.3	Observations	135
6.4	Results	138
6.5	Nebular metallicities	148
6.6	Discussion	161
6.7	Conclusions	163
6.8	Appendix: Emission line flux error estimation	165
7	The electron temperature–abundance calibration and parameters affecting it	169
7.1	Chapter summary	169
7.2	Introduction	170
7.3	Electron temperature and oxygen abundance	172
7.4	The [O III] electron temperature–abundance relation	177
7.5	The effect of optical depth at the Lyman limit	180
7.6	Effect of the UV Spectral Energy Distribution	186
7.7	Pressure effects	188
7.8	Effect of the ionisation parameter, q	192
7.9	The effect of dust	193
7.10	Effect of non-equilibrium κ electron energy distributions	195
7.11	Factors affecting the measurement of electron temperature	197
7.12	Diagnostic grids	198
7.13	Investigating three-dimensional diagnostic graphs	200
7.14	Discussion	201
7.15	Conclusions	203
7.16	Appendix: Revisions to the Mappings photoionisation modelling code	203
8	Conclusions	205
	Bibliography	207
	Appendix A Weather problems encountered	219

List of Figures

1.1	The Rosette Nebula (NGC 2237), a nearly symmetric H II region	2
2.1	DSS2, SINGG and GALEX composite color images of galaxy MCG-01-26-009	12
2.2	The HOPCAT catalog plotting $\log_{10}(m_{HI})$ vs. M_R with SIGRID sample region.	13
2.3	SIGRID galaxies with voids, galaxy clusters and MW dust absorption	18
2.4	Type (i): Centrally condensed H α region(s)	20
2.5	Type (i): Bright H α showing active starburst and outflows	21
2.6	Type (ii): Centrally clumped multiple H α regions	22
2.7	Type (ii): Faint H α compared to R-band	23
2.8	Type (iii): Dispersed H α regions	24
2.9	Type (iv): Separate neighbouring H α regions	25
2.10	Sample bias for the SIGRID objects	34
2.11	SIGRID sample plotted over HIPASS completeness contours	35
2.12	WiFeS datacube image of HIPASS J1609-04 at [O III] 5007Å	38
2.13	Example ‘bloater’: a dIr galaxy with a larger physical extent than expected .	40
3.1	κ - velocity distributions (log scale) for κ from 2 to 50, with Maxwell-Boltzmann distribution.	46
3.2	κ - energy distributions (linear scale) for κ from 2 to 50, with Maxwell-Boltzmann distribution.	47
3.3	κ - energy distributions (log scale) for κ from 2 to 50, with Maxwell-Boltzmann distribution.	48
3.4	$\kappa = 2$ energy distribution with peak-fitted Maxwell-Boltzmann distribution core.	48
3.5	The collisional excitation enhancement ratio over a Maxwell-Boltzmann distribution for different κ -distributions	52

3.6	The lower energy levels and forbidden transitions for the O III ion.	53
3.7	[O III] line flux ratio versus temperature for M-B distributed electrons computed from different methods and by different authors	54
3.8	O III] line flux ratio versus kinetic temperature for the range $\kappa = 2 \rightarrow 100$, compared to the computed Lennon & Burke (1994) equilibrium data	55
3.9	Measured temperatures in H II regions compared with what would be expected if the electrons have a κ -distribution	60
3.10	As figure 9, panel (d), but for planetary nebulae.	61
3.11	Portions of HST images of the η Carina nebula (left) and M17 (right) displaying magnetically-dominated microstructures aligned with the outflow direction	63
4.1	Computed collision strength data for O III from PNPE12	78
4.2	Temperature excesses using older effective collision strength data, compared to the results using effective collision strengths from the latest data	79
4.3	Effect on the excitation rate of truncating the collision strength computations at a range of energies, for a $\kappa=2$ distribution.	81
4.4	κ , best-fit M-B and equal energy M-B distributions	82
4.5	Electron density correction as a function of κ	84
4.6	Error in assuming a fitted M-B distribution instead of a κ distribution, as a function of $\Delta E/k_B T_U$ and κ	85
4.7	Collisional excitation rate for $\kappa=10$ compared to an M-B distribution	87
4.8	Energy level arrangements for temperature-sensitive line ratios	89
4.9	Temperature-sensitive line flux ratio curve for the O III forbidden lines using collision strength data from PNPE12.	93
4.10	Temperature-sensitive line flux ratio curve for the S III forbidden lines using collision strength data from Hudson et al. (2012).	94
4.11	Locus of "apparent" electron temperatures measured using [S III] and [O III] flux ratios, as functions of κ and the kinetic (internal energy) temperature	95
4.12	Errors arising from using old O III atomic data in conventional electron temperature estimates	97
4.13	Effect of density on the flux emission ratios for the p^2 ions, S III, N II, and O III, plotted on a log-log scale	99
4.14	Errors arising in the M-B temperature calculations where no correction is made for density, for O III, S III, and N II, plotted on a linear-log scale.	100
4.15	True kinetic temperature versus electron temperature for [O III] estimated using conventional methods	103
5.1	Left Panel: HST V-band image of KK246. Right Panel: HST (V-I,I) colour magnitude diagram derived from Karachentsev et al. (2006)	112

5.2	KK246 in Visible, H α /R-band, H-band, and GALEX NUV + FUV , all to the same scale	113
5.3	J1609 in UV, Visible, H α /R-band and H-band, all to the same scale	115
5.4	Left Panel: KK246 H α WiFeS IFU image with contours. Right Panel: J1609-04 H α WiFeS IFU image with contours.	117
5.5	Flux-calibrated spectrum of KK246 with principle atomic lines labelled.	120
5.6	Spectra of five individual H II regions in HIPASS J1609-04, and a combined spectrum from regions 2 and 5, with line identification.	121
5.7	Strong line diagnostic grids, showing flux ratios for KK246 and the five regions in J1609-04 (grids computed using data from Dopita et al. 2013).	123
5.8	Strong line diagnostic grids, continued, showing flux ratios for KK246 and the five regions in J1609-04 (grids computed using data from Dopita et al. 2013).	124
5.9	log(N/O) versus oxygen metallicity for the objects observed here and data from van Zee et al. (1998c).	127
5.10	Oxygen abundance versus stellar mass for KK246 (red) and J1609-composite (yellow), plotted with T_e method data for 25 nearby ($D < 5$ Mpc) dwarf irregular galaxies from Lee et al. (2006)	128
5.11	Mass-to-light ratio versus absolute magnitude: $\log_{10}(M_{HI}/L_B)$ versus $M_{B,0}$ for KK246 (red) and J1609-composite (yellow), plotted on data from Figure 2 from Warren et al. (2007)	129
5.12	Metallicity versus $M_{B,0}$ for KK246 (red) and J1609-composite (yellow), plotted on data for Lynx-Cancer Void galaxies from Pustilnik et al. (2011b)	130
6.1	H α slices from WiFeS 35×28 arc sec image cubes.	139
6.2	Spectra for J0005-28, J1152-02, J1225-06s2, J1328+02, J1403-27, and J2039-63A	141
6.3	Spectra for J1609-04(2), J1609-04(5), J2234-04B, J2242-06, J2254-26, and J2349-42	142
6.4	Spectra for J2311-42A and J2311-42B	143
6.5	Close up of the H γ and [O III] 4363 \AA lines for eight of the objects	144
6.6	Spectrum for J1118-17s2 (pipeline "sag" removed).	146
6.7	Section of spectrum for J1118-17s2, showing apparent absence of any [N II] emission lines.	146
6.8	Spectrum of J0005-28, log flux axis. Several Balmer lines are apparent, and the [O III] 4363 \AA line is strong.	147
6.9	Observed flux ratios plotted on the OIII/SII-NII/OII, OIII/OII-NII/H α , OIII/H β -NII/H α and OIII/H β -NII/OII grids	152
6.10	Observed flux ratios plotted on the OIII/SII-NII/SII, OIII/OII-NII/OII, OIII/H β -NII/SII and OIII/OII-NII/SII grids	153
6.11	Log(N/O) versus oxygen abundance, Z	158

6.12	Comparison of diagnostic grids for the ratios $\log(\text{OIII}/\text{H}\beta)$ versus $\log(\text{NII}/\text{OII})$ for electron densities $n_e \sim 5$ and $\sim 50 \text{ cm}^{-3}$ (isobaric case, $\log(P/k) = 5$ and 6) .	160
6.13	T_e versus gas-phase oxygen abundance from Equations 7.2 and 7.5	161
6.14	Left Panel: Oxygen abundance versus neutral hydrogen mass. Right Panel: Oxygen abundance versus absolute B-band magnitude, comparing data from Figure 3 from Pustilnik et al. (2011b) with SIGRID data.	162
6.15	Section of a single WiFeS IFU raw data frame for J0005-28 with cosmic ray artefacts, centred on the $\text{H}\gamma$ line.	166
7.1	Ionic fractions for oxygen species versus radius from Mappings IV	174
7.2	Observed apparent electron temperature versus gas-phase oxygen abundances and Mappings photoionisation model curve for $\log(q)=8.50$	178
7.3	Rosette Nebula (NGC 2237) H II region, in $[\text{O III}]$	181
7.4	Observed apparent electron temperature versus oxygen abundance, with Mappings model curves for the optically thick and $\tau=1$ cases.	182
7.5	normalised fluxes and T_e , versus radius, low metallicity (0.1 solar)	183
7.6	$\log([\text{SII}]/[\text{OIII}_{4959}])$ diagnostic for optical depth, comparing observations with model curves.	184
7.7	$\log([\text{OII}]$	185
7.8	Effect of combining spectra from different optical depths.	186
7.9	Mappings models using different excitation sources.	188
7.10	Mappings models using different electron densities.	190
7.11	As for Figure 7.10, but showing optical thicknesses $\tau = \infty$ and 1	191
7.12	Mappings model curves for the $[\text{O III}]$ electron temperature as a function of oxygen abundance, for a range of values of the ionisation parameter $\log(q)$.	193
7.13	Observed $[\text{O III}]$ electron temperature versus gas-phase oxygen abundances, and Mappings photoionisation model curves with 1 solar depletion dust, and no dust, for a range of $\log(q)$	195
7.14	Mappings models using different κ electron energy distributions.	197
7.15	Observational data plotted on diagnostic grids	199
7.16	SIGRID data plotted on diagnostic grids for $\log(\text{OIII}/\text{H}\beta)$ versus $\log(\text{NII}/\text{H}\alpha)$, overlaid with plots for a range of values of optical thickness and κ , at $\log(q)=8.5$.	200
7.17	Left panel: Three-dimensional rotated projection of $\log(\text{N II}/\text{H}\alpha)$ and $\log(\text{N II}/\text{S II})$ versus $\log(\text{O III}/\text{H}\beta)$ diagnostic grids, showing the optically thick equilibrium diagnostic grids and for four values of the H I optical depth, τ . Right Panel: Similar grids, but with four values of the non-equilibrium parameter κ . . .	201
A.1	Niño3.4 and IOD climate indices for the period 2008-2013, with observing session dates marked as vertical bars.	220

List of Tables

2.1	Small Isolated Gas-Rich Irregular Dwarf Galaxy sample (SIGRID)	14
2.2	Values used for projected cluster exclusion radii and velocity dispersions . .	28
2.3	Comparison of tidal indices	33
3.1	O III Line flux ratios vs kinetic temperature T_U	56
3.2	Collisional Excitation Rate ratios	65
4.1	Collision strength data sources	77
4.2	Recombination rate ratios as a function of κ	86
4.3	Line ratios and M-B temperature fit coefficients from simple collision strength calculations	98
4.4	Line ratios and M-B temperature fit coefficients from MAPPINGS IV	101
4.5	Density parameter d used in equations (4.34) and (4.35)	102
4.6	Linear coefficients for $4\,000\text{ K} < T_U < 25\,000\text{ K}$	104
4.7	Line wavelengths (\AA) (in air) and line strengths and line ratio multipliers for the p^2 and p^4 ions	107
4.8	Line wavelengths (\AA) (in air) and line strengths and line ratio multipliers for the p^3 ions	107
5.1	Compendium of UV, Optical, Near-IR and HI Parameters for KK246	114
5.2	Compendium of UV, Optical, Near-IR and HI Parameters for J1609	116
5.3	Measured line fluxes for the H II regions in KK246 and HIPASS J1609-04, corrected for reddening, in units of $\text{erg s}^{-1}\text{cm}^{-2}\text{\AA}^{-1}$	118
5.4	Uncorrected fluxes ($\text{erg s}^{-1}\text{cm}^{-2}\text{\AA}^{-1}$). For errors see previous table.	119
5.5	Corrected Balmer line ratios and corresponding A_v values	120
5.6	Metallicity and ionisation parameter values	125

5.7	$\log(N/O)$ calculated from $[N_{II}]/[O_{II}]$ flux ratios using equation (7.1), for T_e in units of 10,000K.	127
6.1	Observations of objects from SIGRID sample	137
6.2	Reddening corrected line fluxes normalised to $H\beta=100$, with measured $H\beta$, equivalent widths for $H\alpha$ and $H\beta$, and extinction coefficient, $c(H\beta)$	145
6.3	Metallicity results from Strong Line grids for $\kappa = \infty$	154
6.4	$[O_{III}]$ electron temperatures and gas-phase oxygen abundances	156
6.5	Calculated $[S_{II}]$ line ratios vs gas-phase oxygen abundance ($Z = 12 + \log(O/H)$) for $n_e = 10$ and 100 cm^{-3} and ionization parameter $\log(q) = 7.5$	159
6.6	$\log(N/O)$, $\log(N_{II}/O_{II})$, $[S_{II}]$ line ratios and electron densities	159
7.1	Electron temperatures, gas-phase oxygen abundances, strong line abundances and abundance differences for SIGRID objects	177

CHAPTER 1

Introduction

I may not have gone where I intended to go, but I think I have ended up where I needed to be.

Douglas Adams, *The Long Dark Tea-time of the Soul*

In the early universe, the first stars formed from random turbulence in clouds of pure hydrogen and helium. These stars burned their fuel rapidly, and as super- or hypernovae, expelled their heavier element residues to mix with the primordial interstellar and intergalactic gas (Loewenstein 2001, and references therein). Chemical abundances in gas clouds rose as newly-collapsing galaxies evolved with accompanying generations of star formation. At the same time, as the gas clouds in incipient galaxies were being enriched by early supernovae, they were being diluted with infalling chemically pristine gas, and depleted by starburst-driven galactic-scale outflows (Kobayashi et al. 2007). Thus, the evolution of chemical abundance was complex, and inextricably linked to star formation and galaxy growth.

Potentially, the heavy element abundances in H II regions, and the stellar populations if they can be observed, provide a record of the generations of cosmic star formation, mass accretion, and mass-loss in galaxies. The possibility that small galaxies, distant from the processes of galaxy interaction, accretion and outflows, might retain evidence of primordial conditions, was an initial motivation for this thesis.

1.1. H II regions: the birthplace of stars

When massive stars form in molecular clouds, their extreme ultraviolet (EUV) radiation ionises the gas, and the region around them becomes an H II region, characterised by the emission of radiation from the species in the cloud. In the visible spectrum, this is observable as emission lines from the Balmer sequence of hydrogen, helium, and collisionally excited forbidden emission lines from O⁺⁺, O⁺, N⁺, S⁺ and other minor sources. These emission lines contain information about the physical conditions in the interstellar gas, and a record the history of the star formation history of the galaxy.



Figure 1.1 The Rosette Nebula, NGC 2237, a nearly symmetric H II region, showing the central star cluster and the region evacuated by stellar winds. This three colour image (red=[S II], green= $H\alpha$, blue=[O III] 5007Å) is reproduced with permission from Steven Coates (<http://coatesastrophotography.com>). See Chapter 7.

Our understanding of the spectra of gaseous nebulae (H II regions and planetary nebulae) has evolved much over the past 150 years. In 1864, using what they termed ‘prismatic analysis’, [Huggins & Miller \(1864\)](#) discovered a number of emission lines in nebulae, which they attributed to an unknown element, later named ‘Nebulium’. However, the nature of this element became uncertain as the periodic table was increasingly filled with identified atomic species. The presence of identifiable spectral lines from only the lighter elements in nebulae suggested heavy elements were not present in significant amounts. The true nature of the Nebulium lines was discovered by [Bowen \(1928\)](#), who showed that they arose from forbidden transitions of doubly ionised oxygen and singly ionised oxygen and nitrogen. Bowen also suggested these lines were excited by electron-ion collisions. This idea was taken further by ([Hebb & Menzel 1940](#)), leading to our modern understanding of the physics of H II regions (see, for example, [Peimbert 1967](#); [Stasińska 2002](#); [Dopita & Sutherland 2003](#); [Stasińska 2004](#); [Osterbrock & Ferland 2006](#)). The work presented here draws on our current understanding, based on this long heritage.

1.2. The origins of the elements

In the early to mid 20th Century, much effort was devoted to explaining the origin of elements whose spectral emission lines were observed in nebulae, and in absorption lines in stellar atmospheres. The work of Eddington, Bethe, Fowler, the Burbidges and Hoyle ([Burbidge et al. 1957](#)) was seminal in the development of our understanding of the nuclear synthesis process in stars.

The main elements observed in H II regions are H, He, C, N, O, Ne, S, and Ar. These are produced from hydrogen through a variety of stellar nuclear processes, and on different time scales. O, Ne, S, and Ar are produced rapidly in massive stars via the alpha process and triple alpha process. Helium is produced principally by the CNO cycle in intermediate mass stars, and the proton-proton chain reaction in smaller stars. C and N can be produced by the alpha process, but mostly originate via neutron capture in intermediate mass stars. The alpha process elements, particularly oxygen, are expelled promptly into the interstellar medium—well within the lifetime of the H II region—through core-collapse supernovae. Later, the interstellar medium is enriched with C and N from AGB star winds (although WN stars can enrich the “primary” nitrogen earlier). The prompt production of enormous quantities of oxygen in core-collapse supernova explosions ([Timmes 1991](#)) explains why it is the dominant heavy element present in H II regions, and why the forbidden lines of oxygen are present in virtually all H II region spectra.

This leads us to the realisation that present day interstellar gas is the repository of the stellar evolutionary history of a galaxy. We access this history when new star clusters form to ionise the interstellar medium. The challenge of understanding the processes occurring in H II regions is to develop tools to measure temperatures and abundances from observations of the spectra.

1.3. Measuring the physical conditions in H II regions

There are four approaches that have been used to measure the conditions in H II regions (see the discussions in [Peimbert 1967](#); [Stasińska 2004](#)). The first is the electron temperature or “direct method”, using measurements of the fluxes of collisionally excited [O III] forbidden lines in the optical spectrum. The method requires knowledge of the energy levels and transition probabilities for these lines. The first attempt to use this method appears to have been by [Baker et al. \(1938\)](#). The method is described in detail in [Osterbrock & Ferland \(2006\)](#). However, it measures only a mean of the conditions inside the region and needs to be corrected to allow for different electron temperatures in different zones and for unseen excitation levels ([Stasińska 2002](#)).

The second approach is to measure abundances using recombination lines and the “Balmer jump” ([Peimbert et al. 1993](#)). However, abundances inferred from this approach tend to be consistently higher than those measured using the collisionally excited lines, as noted by [Stasińska \(2004\)](#). This has been termed the “abundance discrepancy”.

The third approach comprises the empirical strong line methods using line ratios of observed nebular species. Because there is no direct measure of the electron energy distribution,

metallicity measurements using these ratios require calibration using the direct method. They suffer from degeneracies between the ionisation parameter and the metallicity. Various approaches have been suggested to resolve these degeneracies using second line ratio combinations (Kewley & Dopita 2002). Several sets of ratios have been used, detailed in Kewley & Ellison (2008).

The fourth approach is photoionisation modelling. This method is the most complex, and involves simulating numerically the processes and interactions that occur in an H II region. The success of this approach is indicated by the remarkably consistent results when a number of different model systems were compared against test objects (Péquignot et al. 2001). The models are continually improving with more efficient computational techniques and revised atomic data. The advantage of the photoionisation model is that one can investigate the effects on the emitted spectrum of changes in physical conditions in a nebula.

To these methods we may now add a fifth, the diagnostic grids developed by Dopita et al. (2013), which avoid the worst of the degeneracies present in the simple strong line methods, and are constructed from photoionisation models such that the ionisation conditions (specifically the ionisation parameter) and the metallicity (i.e., the oxygen abundance) are as far as possible treated as orthogonal and solved for separately. The accuracy of this last method depends on having accurate atomic data (in common with the other methods) and taking into account all the physical processes and their interactions. The latest development, and one of the approaches I have used for the work in this thesis, is the revised Mappings code. It has recently undergone a major overhaul, with new modelling code and the latest atomic data, and is now at version IV.1.4.

1.4. Metallicity gradients, tidal dwarfs and field dwarfs

With the development and refinement of the tools to measure abundances, astronomers have observed H II regions in a wide range of environments. One of the findings has been the metallicity gradient found in spiral galaxies, first identified by Searle (1971). Henry & Worthey (1999) provide a more recent survey of the abundance distributions in spiral and elliptical galaxies. The existence of gradients in isolated spiral galaxies suggests that in outer regions that are less prone to enrichment by frequent local supernovae, the lower metallicity in H II regions is indicative of conditions earlier in the galaxy's history.

The next important finding is that dwarf galaxies, including satellites and tidally disturbed dwarfs, such as the LMC and SMC, have lower metallicities than larger galaxies. This is well illustrated by the data from the Sloan Survey (Tremonti et al. 2004), which demonstrates the “mass–metallicity” relation, a correlation between nebular metallicity and galaxy mass. This exploration has been taken further, to study field dwarf irregular galaxies (e.g., Lee et al. 2003), which continues the mass–metallicity correlation for small galaxies.

Extreme cases of low nebular metallicity have been found in dwarf irregular galaxies such as 1Zw18 and SBS 0335-052W (Thuan et al. 2005; Izotov et al. 2005, 2009). This has led to a debate on how such low metallicity galaxies form. Ricotti & Gnedin (2005) and Ricotti et al. (2008) have suggested, by comparing detailed modelling and observations of Local Group dwarf galaxies that they may form in three ways: as “true fossils” from the ionisation era; by forming most of their stars later, as “survivors” from the re-ionisation era; or as a

combination of the two, as “polluted fossils”. The presence of old stellar populations in isolated dIrr galaxies may provide information on these alternative evolutionary processes. Studying the nebular and stellar make up of the dwarf galaxies in the Local Volume offers the promise of contributing to understanding the evolution of star forming galaxies. It is possible that very isolated dwarf star forming galaxies might harbour information about the enrichment state of the early universe, especially if the star formation episodes are infrequent, and the supernova debris is not well retained, and/or if there is an inflow of pristine primordial gas.

1.5. Observations, methods and the structure of this thesis

The work presented here was aimed at addressing the question of whether isolation is important in the chemical evolution of galaxies. In analysing the observed spectra, I found that I also needed to recalibrate some of the tools used to analyse the physical conditions in H II regions.

I commenced by identifying a sample of 83 small isolated gas-rich irregular dwarf galaxies, the SIGRID sample. It derives its members from the Survey for Ionisation in Neutral Gas Galaxies (SINGG) (Meurer et al. 2006). That in turn was selected from the neutral hydrogen radio signatures from the H I Parkes All-sky Survey (HIPASS) (Meyer et al. 2004), resulting in a sample which as far as possible avoids the bias problems with selecting faint targets optically. Selecting isolated objects for SIGRID required the development of a new isolation index. The sample, the physical parameters, and selection processes are described in Chapter 2, which was published as *The Small Isolated Gas-rich Irregular Dwarf (SIGRID) Galaxy Sample: Description and First Results* in the *Astronomical Journal* (Nicholls et al. 2011).

I observed as many of the SIGRID sample as was possible (35), limited by weather and available telescope time, using the WiFeS integral field spectrograph on the ANU 2.3 metre telescope at Siding Spring. These observations are detailed in Chapters 5 and 6.

When analysing initial spectra, I encountered a problem, that the existing strong line and photoionisation model tools gave discrepant results, or else no results. This led me to consider the possibility that one of the fundamental assumptions about H II regions, that the electron energies are in thermal equilibrium, may be incorrect. I investigated the application of the κ energy distribution in H II regions. This had been measured directly in solar system plasmas (Vasyliunas 1968), and is found throughout the solar system, wherever electron energies are measured. It is best described as a Maxwell-Boltzmann-like distribution, but with a power law tail.

This work provided, unexpectedly, a new explanation for the long-standing problem of the discrepancy between recombination line and collisionally excited line abundance measurements, which had not previously been satisfactorily explained (Stasińska 2004). The work is reported in Chapters 3 and 4, which were previously published in the *Astrophysical Journal* as *Resolving the Electron Temperature Discrepancies in H II Regions and Planetary Nebulae: κ -distributed Electrons and Measuring Nebular Temperatures: The Effect of New Collision Strengths with Equilibrium and κ -distributed Electron Energies* (Nicholls et al. 2012, 2013).

The second of these papers coincided with my work to acquire and prepare latest collision

strength data for incorporation into the Mappings photoionisation code. This was being revised by Dr Ralph Sutherland to accommodate the κ energy distribution, the results of which are described in [Dopita et al. \(2013\)](#).

The first paper reporting the results of applying the new photoionisation modelling code to my observations is presented in Chapter 5. It is reproduced from my paper in the *Astrophysical Journal*, *Nebular Metallicities in Two Isolated Local Void Dwarf Galaxies* ([Nicholls et al. 2014c](#)). It presents data on the temperatures and oxygen abundances in two very isolated dIrr galaxies in the Local Void.

Chapter 6 reports the analysis of spectra from an additional 13 SIGRID objects. I use the direct method, with a new method for obtaining the oxygen abundance, and the new diagnostic grids, to analyse the data. It is reproduced from my paper in *The Astrophysical Journal*, *Metal-poor dwarf galaxies in the SIGRID galaxy sample. I. H II region observations and chemical abundances* ([Nicholls et al. 2014a](#)). In this chapter I use the direct method, with a new method for obtaining the oxygen abundance, and the new diagnostic grids, to analyse the data.

In Chapter 7, I present the follow-up paper to Chapter 6, accepted for publication in *The Astrophysical Journal*, *Metal-poor dwarf galaxies in the SIGRID galaxy sample. II. The electron temperature–abundance calibration and the parameters that affect it* ([Nicholls et al. 2014b](#)). Using the diagnostic grids and the direct method, I explore the parameters effecting the measurement of temperatures and abundances, including optical thickness, the ionisation parameter, pressure, the κ energy distribution, and central stellar excitation sources.

CHAPTER 2

The Small Isolated Gas Rich Irregular Dwarf (SIGRID) Galaxy Sample

Look how the floor of heaven
Is thick inlaid with patens of bright gold.
There's not the smallest orb which thou behold'st
But in his motion like an angel sings...

William Shakespeare, 1564–1616, in *The Merchant of Venice*

This chapter was previously published as 'The Small Isolated Gas Rich Irregular Dwarf (SIGRID) Galaxy Sample: Description and First Results', Nicholls, D. C., Dopita, M. A., Jerjen, H. and Meurer, G. R., 2011, AJ, 142, 83. The work is entirely my own, taking into account suggestions from my co-authors. Minor typographical errors have been corrected, and sections, tables and figures have been renumbered to conform with the layout of the thesis.

2.1. Chapter summary

Using an optically-unbiased selection process based on the HIPASS neutral hydrogen survey, I have selected a sample of 83 spatially isolated, gas-rich dwarf galaxies in the southern hemisphere with cz between 350 and 1650 km s^{-1} , and with R-band luminosities and H I masses less than that of the Small Magellanic Cloud. The sample is an important population of dwarf galaxies in the local Universe, all with ongoing star formation, and most of which have no existing spectroscopic data. The goal is to measure the chemical abundances of these galaxies, using the Integral Field Spectrograph on the ANU 2.3m telescope, the Wide Field Spectrograph (WiFeS). This chapter describes the survey criteria and procedures, lists the survey sample, and reports on initial observations.

2.2. Introduction

The main epoch of galaxy formation, occurring at redshifts $1 \lesssim z \lesssim 4$ (e.g. [Madau et al. 1998](#)) is long past. Large galaxies have evolved far from the pristine state in which they

formed. Mergers, galactic winds, cycles of star birth and death and outflows from active galactic nuclei have not only chemically enriched the interstellar medium of these galaxies, but have also chemically enriched their surrounding inter-galactic space (Kobayashi et al. 2007). Theory predicts that chemical abundances will rise as newly-collapsing galaxies evolve and undergo successive generations of star formation. However, the spread of abundances should narrow with time as the interstellar gas becomes either internally mixed, diluted with infalling chemically pristine gas, or depleted by starburst-driven galactic-scale outflows (De Lucia et al. 2004; Kobayashi et al. 2007). Thus, the chemical abundance in galaxies is inextricably linked to star formation and galaxy growth, providing a record of the generations of cosmic star formation, mass accretion, and mass-loss in galaxies.

In this regard, the gas-rich dwarf galaxies are of particular interest. These galaxies have processed a much smaller fraction of their gas through stars, and so are much less chemically evolved than the more massive disk or elliptical galaxies. Many of them have formed and developed in “quiescent” regions of space, possibly at very early times, away from the centres of dense clusters and the gravitational harassment of massive neighbours, so their star formation and chemical evolution history may well be simpler than for the more massive systems.

A detailed study of the stellar and gas content of these gas-rich dwarf galaxies may therefore be expected to provide answers to the following key questions:

- What is the relationship between mass and chemical abundance for low mass galaxies? The answer could provide sensitive constraints on the mass fraction of the interstellar medium lost to inter-galactic space by galaxy winds. We would like to know whether matter lost from dwarf galaxies can account for the “missing baryon” problem—the discrepancy between the baryonic mass currently contained in visible galaxies, and the baryonic mass inferred from the standard model of cosmology (Bregman 2007).
- What is the total mass of oxygen in each dwarf galaxy? This is determined from the chemical abundance and the total H I mass of these galaxies. Since we know how many stars have formed in the galaxy from I-band photometry, we may obtain tight constraints on the fraction of heavy elements that have been lost to the inter-galactic medium by galactic winds in these systems.
- Is there a chemical abundance floor in the local Universe? Such a floor, predicted to be about 1/100 solar (Kobayashi et al. 2007), would result from pollution of inter-galactic gas by heavy elements ejected in starburst-powered galactic winds, or by black hole jet-powered outflows from massive galaxies.

There is evidence that dwarf galaxies have a wide variety of evolutionary histories (e.g. Grebel (1997); Mateo (1998); Tolstoy et al. (2009)) and that—possibly as a result of this—they display a wide scatter on the mass-metallicity relationship (Tremonti et al. 2004; Lee et al. 2006; Guseva et al. 2009). However, the observed sample of objects in this region of the parameter space is still relatively small.

Although these dwarf systems are dominated by dark matter (Mateo 1998) and they retain much of their original gas content, the inferred chemical yields are much lower than those estimated for more massive galaxies. This suggests that these galaxies may have formed

very early in the history of the Universe and have subsequently had quite severe episodes of mass-loss through galactic winds. The study of small isolated gas-rich dwarf galaxies may provide evidence of the conditions and processes long since erased in larger galaxies and clusters.

Dwarf irregular galaxies (‘dwarf’ defined for the purposes of this study as having a gas+stellar mass less than that of the Small Magellanic Cloud) are numerous throughout the Local Volume but they remain surprisingly poorly studied. Optical catalogs by their nature tend to be incomplete and affected by the Malmquist Bias (Malmquist 1921). Dwarf galaxies can be missed due to their low surface brightness, or mistaken for much more massive and distant objects. The SINGG survey (Meurer et al. 2006) went a long way towards rectifying this situation as it drew its objects from the HIPASS neutral hydrogen survey (Zwaan et al. 2004; Meyer et al. 2004; Koribalski et al. 2004). This provided a complete volume-limited sample for a given H I mass content. Follow-up R-band and H α photometry revealed both the stellar luminosity and the star-formation rate in these galaxies. Much to the surprise of Meurer et al. (2006), evidence for on-going ($\lesssim 10$ Myr) star formation was found in nearly every case. This opens up the possibility of follow-up spectroscopy to establish the chemical abundances in the H II regions of these objects.

Going beyond the SINGG survey, which investigated only $\sim 10\%$ of the HIPASS sources, there are many other small isolated gas-rich dwarf galaxies in the HOPCAT catalogue (Doyle et al. 2005), which could also provide insight into dwarf galaxy evolution. Both the SINGG and HOPCAT galaxies can now be studied very efficiently using integral field units (IFUs). In particular the Wide-Field Spectrograph (WiFeS; Dopita et al. 2007, 2010) at the Australian National University (ANU) 2.3m telescope at Siding Spring Observatory is ideally suited for the study of these galaxies. The WiFeS instrument is a highly efficient double-beam, image-slicing integral-field spectrograph with spectral resolutions $R = 3000$ and 7000 , covering the wavelength range 3500\AA to $\sim 9000\text{\AA}$. It offers a contiguous 25×38 arc sec field-of-view, well matched to the angular size of these objects. Such an instrument obviates the need to obtain optical photometry in either broad or narrow bands, and allows us to extract the complete spectra of each of the individual H II regions present in the galaxy. Motivated by the opportunity to study dwarf galaxy formation and evolution in the Local Volume ($D \lesssim 20$ Mpc), we have identified a volume-limited sample of small, isolated gas-rich dwarfs. In this paper, we describe the characteristics of this sample, and describe initial results.

2.3. The “SIGRID” sample

It is conventional to identify dwarf galaxies using their optical characteristics (such as their morphological appearance or their spectrum). This has been done by surveys such as the Sloan and Byurakan (York et al. 2000; Abazajian et al. 2003; Markarian 1967). Of necessity this introduces an optical Malmquist bias into the sample, whereby fainter galaxies are present in larger numbers close by, while brighter galaxies are more strongly represented at greater distances (Malmquist 1921; Butkevich et al. 2005).

We can avoid the optical bias problem—or at least substantially reduce it—by using the neutral hydrogen 21cm signatures of gas rich dwarf galaxies as a means of identifying

the sample members. It is then necessary to identify optical counterparts of these H I sources—H II regions and stellar populations. In the case of the HIPASS survey this was undertaken through the HOPCAT optical counterparts study which used COSMOS data as its optical source (Doyle et al. 2005). Taking this process further, Meurer et al. (2006) presented a selection of 468 HIPASS objects for follow-up H α and R-band studies, of which to date 362 have been observed. Using H I surveys to identify galaxies was also used as a means of checking sample completeness in the 11HUGS survey (Kennicutt et al. 2008).

Both the SINGG and 11HUGS surveys include objects of a range of masses and luminosities, with and without close neighbours. In this work we target specifically small isolated dwarf galaxies.

Starting with the SINGG and HOPCAT catalogs, based on the HIPASS neutral hydrogen survey, we have identified a sample of 83 small isolated gas-rich dwarf galaxies in the Southern Hemisphere, in the Local Volume, beyond $cz \sim 350 \text{ km s}^{-1}$. We have also drawn on the catalogs by Karachentsev et al. (2008, 2011) for additional targets.

In addition to the SINGG data, the DSS and GALEX surveys have been used to identify objects that show no evidence of organised structure, but do show evidence of current star formation associated with the H I and H II regions¹.

Through this selection process we automatically exclude dwarf objects similar to LGS3 in the Local Group that retain some (“warm phase”) H I but exhibit no current star formation (Young & Lo 1997; Hunter & Elmegreen 2004). Using the reasoning from Young & Lo (1997), this implies the H II regions in our objects arise from “cold phase” gas, with the inference that they represent cold gas inflow regions (whether or not these are a contributing source of star formation). Objects with neutral hydrogen but lacking obvious UV and H α emission are therefore unlikely to have significant O- and B-star populations.

We have also excluded, as far as possible, low surface brightness (LSB) objects whose brighter regions might be mistaken for isolated dwarfs. An example of this is HIPASS J0019-22 (MCG-04-02-003), which from the GALEX images is clearly a faint face-on low surface brightness spiral galaxy, and identified as an LSB galaxy by Warren et al. (2007). Likewise, we have used HIPASS velocity profile widths to exclude larger, side-on objects with substantial rotational velocities. We refer here to our sample as the Small Isolated Gas Rich Irregular Dwarf or “SIGRID” sample.

2.4. Selection criteria

The objects identified in this survey are gas-rich; they show evidence of current star formation; they are less luminous than the SMC; they have lower neutral hydrogen masses than the SMC; they are isolated; they are irregular or centrally condensed, with no spiral structure evident; they are separate from major galaxy clusters; and they are generally located between the Local Group and the Fornax Cluster in distance.

We used the HIPASS (Meyer et al. 2004), HOPCAT (Doyle et al. 2005) and SINGG (Meurer et al. 2006) catalogs and the NED and HyperLEDA databases to select objects having the

¹It is worth noting that these sources trace somewhat different stellar populations: O and B stars in the GALEX UV objects and O stars in the SINGG H II regions.

following characteristics:

- (i) Gas rich with evidence of star formation (ionised hydrogen emission, bright in UV)
- (ii) Low R-band absolute magnitude: $M_R > -16.7$
- (iii) Low neutral hydrogen mass: $\log_{10}(m_{HI}) < 8.7(M_{\odot})$ ²
- (iv) HIPASS H I rotation velocity $w_{50} < 130 \text{ km s}^{-1}$
- (v) Isolation: no immediate nearby neighbours or evidence of tidal effects
- (vi) Located outside regions around nearby galaxy clusters where infall would distort redshift (see Table 2.2)
- (vii) Irregular morphology showing no evidence of spiral structure (GALEX, DSS and SINGG)
- (viii) Distance: redshift recession velocity between 350 and 1650 km s^{-1} and flow corrected recession velocity $< 1650 \text{ km s}^{-1}$
- (ix) Declination: from HIPASS, south of $+2^{\circ}$

Every object was inspected visually, using, where available, the SINGG $H\alpha$ and R-band images; the DSS optical images; and GALEX UV images. Except where already observed in this program, the SIGRID sample only includes objects that show evidence from the SINGG or GALEX imaging of active star formation and young stellar populations. An example is given in Figure 1, which shows the DSS2, GALEX and SINGG composite colour images of galaxy MCG-01-26-009 (HIPASS J1001-06; SIGRID 45). These images demonstrate the optical appearance; the presence of $H\alpha$ emission; and the extended UV from a young stellar population.

There is some uncertainty as to whether this object is tidally influenced by NGC 3115 at an angular separation of 91 arc minutes. There are several published semi-direct distance measurements for the larger object, including globular cluster and planetary nebula luminosity function methods. Taking the average of these measurements gives a distance that is somewhat larger than the flow-corrected redshift distance. However, only the flow-corrected redshift distance is available for SIGRID 45, and while there may be systematic errors in the flow-corrected distances, they are likely to be similar for both. As a result, using the flow-corrected distances in estimating tidal effects is probably the most reliable approach. On this basis, SIGRID 45 is included in the sample.

²Criterion (iii) was based on using the SMC as a yardstick, but it also emerged naturally from the sample selected using the other parameters: in the SINGG data, from which absolute R-band magnitudes could be determined reliably, only 11 objects meeting criterion (ii) had $\log_{10}(m_{HI}/m_{\odot}) > 8.7$. Of these, 8 were low surface brightness galaxies, one was in a congested field, and only two were potential SIGRID candidates, neither with exceptional $\log_{10}(m_{HI})$.

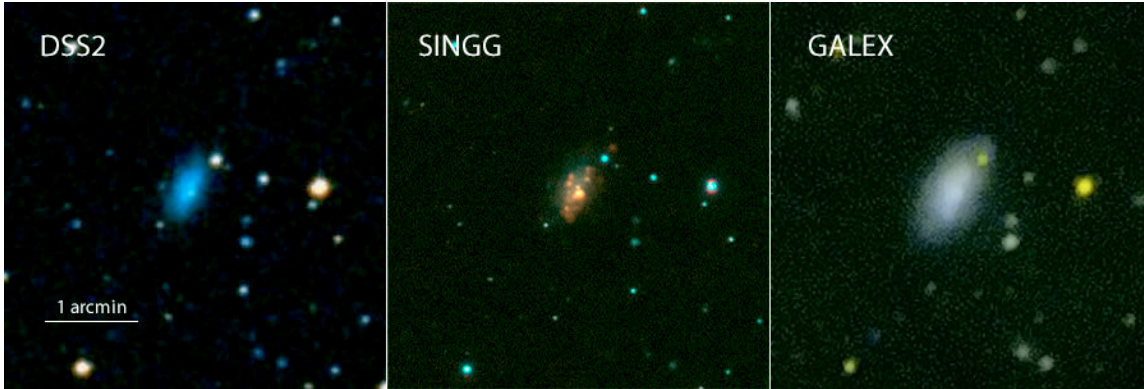


Figure 2.1 DSS2, SINGG and GALEX composite color images of galaxy MCG-01-26-009

The degree of isolation was estimated visually from these sources, and using the NED database. The isolation criterion was further refined the sample using variants of the “main disturber” techniques described by [Warren et al. \(2007\)](#) and Karachentsev’s tidal index ([Karachentsev et al. 2004](#)), as described in §6.3 below.

From the 4500+ HIPASS objects, the 3600+ HOPCAT optical counterparts, the 462 SINGG objects and additional HIPASS identifications by [Karachentsev et al. \(2008\)](#), 83 galaxies have been selected using the above criteria and constitute the SIGRID sample.

Figure 2 shows a plot of the log neutral hydrogen mass, determined from the 21cm integrated intensity from the HIPASS catalog, vs the R-band absolute magnitude, determined from the HOPCAT R-band magnitudes and the HIPASS local heliocentric recession velocities. No attempt has been made in this graph to correct M_R for local flows, as it is primarily intended to illustrate the sample size. The blue rectangle shows the SIGRID sample as a subset of HOPCAT. Note that not all the objects within the rectangle are included in the sample, as some have been excluded because of near neighbours, evidence of structure etc.

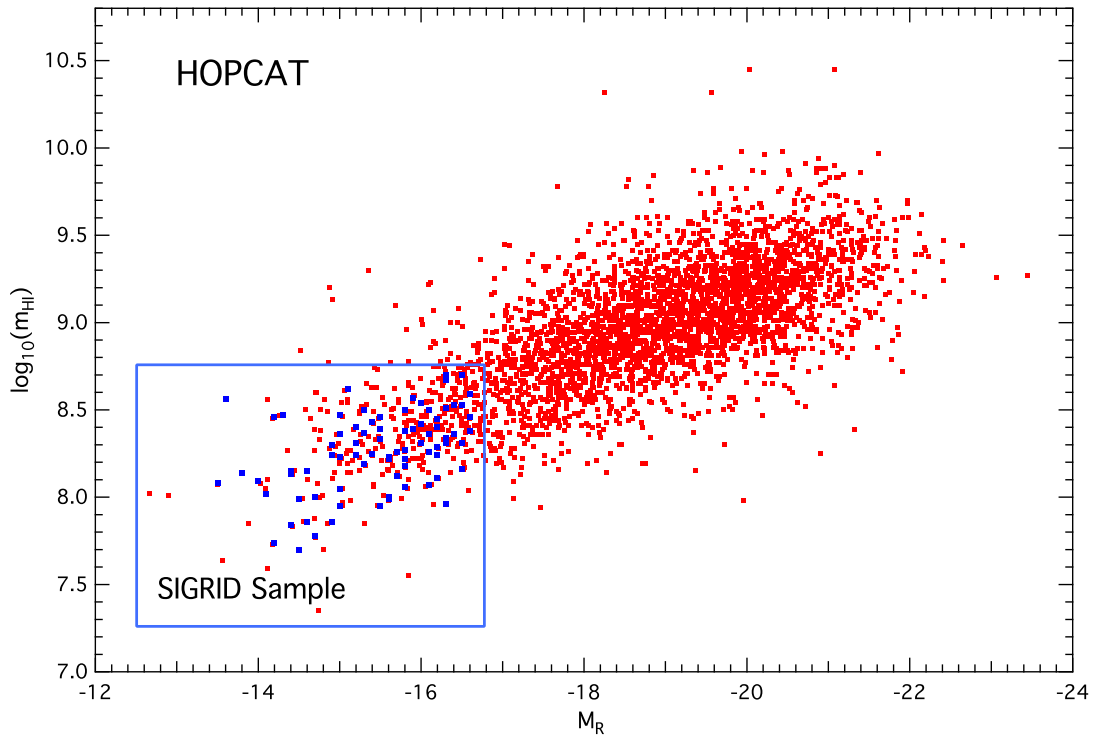


Figure 2.2 The HOPCAT catalog plotting $\log_{10}(m_{\text{HI}})$ vs. M_R showing the SIGRID sample region. Sample galaxies are shown in blue: some potential members have been excluded due to other selection criteria.

2.5. The SIGRID catalog

Table 2.1 shows the full SIGRID sample. Velocity values are flow corrected using the [Mould et al. \(2000\)](#) model, including Virgo, Great Attractor and Shapley Supercluster infall, except where direct distance measurements are available. These are converted to recession velocities taking $H_0 = 73 \text{ km s}^{-1} \text{ Mpc}^{-1}$. Neutral hydrogen masses are taken from the HIPASS catalog. Absolute R-band magnitudes are derived from apparent magnitudes listed in the HOPCAT catalog, except where available from the SINGG catalog (52 of the 83 objects).

Figure 3 shows the SIGRID objects plotted using a Hammer-Aitoff projection with the Local (Tully) Void, local mini-voids ([Tikhonov & Karachentsev 2006](#)) and galaxy clusters (Fornax, Eridanus, Antlia, Hydra, Virgo and Centaurus30). Milky Way high dust absorption regions (gray) are calculated from [Schlegel et al. \(1998\)](#). The Supergalactic Plane is shown in green.

The apparent lack of SIGRID candidates in the region below the Milky Way dust absorption region, between 300° and 240° RA, is most probably due to the Local (Tully) Void ([Tully et al. 2008](#); [Nasonova & Karachentsev 2011](#)). Only four objects in the SIGRID sample (#68, 69, 70, 71) occur within the 50 radius of this void, including the object [KK98]246 (SIGRID 68), currently the most isolated dwarf galaxy known and the only confirmed galaxy located within the void ([Kreckel et al. 2011](#)).³

It is evident in Figure 3 that none of the SIGRID sample are located near the centres of the

³The authors are indebted to the reviewer for pointing out the nature of this object and the importance of its inclusion in the sample.

Table 2.1 Small Isolated Gas-Rich Irregular Dwarf Galaxy sample (SIGRID)

SIGRID ID	HIPASS ID	Optical galaxy ID	RA(J2000) (h m s)	Dec (d m s)	V_{hel} (km s ⁻¹)	D (Mpc)	w_{50} (km s ⁻¹)	$\log(M_{HI})$ $\log(M_{\odot})$	M_B (mag)	Tidal index	Type
1	J0002-52	ESO149-G013 [†]	00 02 46.3	-52 46 18	1500	20.3	111.4	8.45	-16.2	-1.4	i
2	J0005-28	ESO409-IG015	00 05 31.8	-28 05 53	726	10.2	52.8	8.23	-15.3	-2.1	i
3	J0023-27	6dFJ0023042-275537	00 23 04.2	-27 55 37	1539	21.0	121	8.54	-16.0	-0.5	i
4	J0031-22	ESO473-G024 [*]	00 31 22.5	-22 45 57	550	7.3	47.9	8.01	-13.7	-0.9	iii
5	J0043-22	IC1574 ^{*†}	00 43 01.8	-22 13 34	363	4.7 ^{**}	43.9	7.63	-14.7	-1.0	iii
6	J0107+01	UGC006695	01 07 46.4	01 03 49	628	9.2	59.6	7.86	-15.1	-2.8	i
7	J0110-42	ESO243-G050	01 10 48.8	-42 22 31	1472	19.7	60.6	8.18	-15.3	-2.3	i
8	J0206-60	ESO114-G028	02 06 15.8	-60 56 24	1451	18.8	68.8	8.11	-16.1	-1.7	i
9	J0231-54	2dFGRS S857Z501	02 31 55.2	-54 33 06	1394	18.0	85.3	8.39	-15.4	-1.3	i
10	J0253-09	SDSSJ025328.63-085905.5	02 53 28.6	-08 59 06	1423	18.8	87.1	8.24	-15.0	-0.1	i
11	J0255-10	LEDA 3994671	02 55 19.6	-10 49 17	1575	20.7	99.7	8.70	-16.2	-1.1	i
12	J0305-19	UGCA051	03 05 58.7	-19 23 29	1672	22.2	48.8	8.31	-16.3	-0.1	i
13	J0334-51	ESO200-G045 [*]	03 35 02.2	-51 27 13	1030	12.51	47.2	8.05	-14.8	-0.5	iii
14	J0334-61	AM0333-611	03 34 15.3	-61 05 48	1171	14.6	97.9	8.31	-15.0	-1.3	i
15	J0354-44	ESO249-G027	03 54 29.3	-44 45 13	1227	15.63	101.8	8.46	-16.4	-0.4	i
16	J0359-46	AM0358-465	03 59 56.3	-46 47 06	1018	12.32	80.8	8.22	-15.3	-0.3	i
17	J0406-52	NGC1522	04 06 07.9	-52 40 06	907	10.6	102.4	8.40	-15.9	-1.1	i
18	J0408-35	ESO359-G022	04 08 45.6	-35 23 22	1429	18.55	85.3	8.12	-15.6	-0.6	i
19	J0411-35	ESO359-G024 [*]	04 10 57.5	-35 49 52	850	10.26	69.7	8.28	-15.3	-1.4	ii
20	J0427-22	ESO484-G019	04 27 19.9	-22 33 34	1632	21.3	75.3	8.34	-16.2	-1.1	i
21	J0428-46	ESO251-G003	04 28 41.2	-46 19 16	1391	17.8	65	8.23	-15.5	-1.2	i
22	J0434-65	AM0433-654	04 33 54.7	-65 41 52	1239	15.2	38.5	8.00	-15.5	-0.9	i
23	J0439-47	ESO202-IG048 [*]	04 39 49.2	-47 31 41	1368	17.5	57.9	8.53	-16.7	-1.2	ii
24	J0446-35	ESO361-G009	04 46 57.9	-35 54 54	1348	17.3	97.3	8.50	-15.9	-1.2	i
25	J0448-60	ESO119-G005	04 48 17.1	-60 17 38	989	11.6	74	8.24	-15.9	-0.8	i
26	J0448+00	UGC03174	04 48 34.5	+00 14 30	669	9.1	105.6	8.57	-16.1	-0.7	ii
27	J0455-28	APMUKS(B)B045339.97-282253.5 [*]	04 55 39.1	-28 18 11	998	12.6	62.4	8.15	-14.1	-1.3	iii

[†]No GALEX observation

^{*}Observed in the SINGG program

^{**}Distances directly measured values from the literature, as reported in NEID; all others are calculated from redshifts and the flow model.

^aThe 'Type' category classifies the morphology of the H α regions and is described in §5. It is only evaluated for objects with SINGG images, where information on the H α regions is available.

Table 2.1 Small Isolated Gas-Rich Irregular Dwarf Galaxy sample (SIGRID) (continued)

SIGRID ID	HIPASS ID	Optical galaxy ID	RA (h m s)	Dec (d m s)	V_{hel} (km s ⁻¹)	D (Mpc)	w_{50} (km s ⁻¹)	$\log(m_{HI})$ $\log(M_{\odot})$	M_R (mag)	Tidal index	Type
28	J0457-42	ESO252-IG001 [†] *	04 56 58.7	-42 48 14	660	7.1	67.4	8.40	-14.6	-2.0	
29	J0503-32	ESO422-G025	05 03 45.9	-32 19 51	1215	15.5	100.1	8.31	-15.9	-1.1	
30	J0517-32	6dFJ0517216-324535 [*]	05 17 21.6	-32 45 35	796	9.5	65.3	8.00	-14.6	-0.5	ii
31	J0523-34	AM0521-343 [†] *	05 23 23.7	-34 34 29	960	11.9	68.4	8.19	-15.7	-0.4	iii
32	J0527-20	ESO553-G046	05 27 05.7	-20 40 41	541	6.1	62.3	7.70	-14.5	-2.2	
33	J0536-52	ESO204-G022	05 36 26.0	-52 11 03	1292	14.3 ^{**}	85.4	8.59	-16.2	-1.5	
34	J0543-52	ESO159-G025	05 43 06.2	-52 42 02	1101	11.8 ^{**}	97.8	8.53	-16.3	-0.9	
35	J0558-12	LCSBL02890	05 58 02.3	-12 55 47	911	12.0	101.3	8.36	-16.1	-0.5	
36	J0615-57	ESO121-G020	06 15 54.2	-57 43 32	578	6.1 ^{**}	68	8.46	-13.4	-1.9	
37	J0617-17	HIPASS J0617-17 [†]	06 17 53.9	-17 09 04	855	11.0	42.4	8.47	-14.5	-1.6	
38	J0848-26	ESO496-G010	08 49 06.0	-26 19 18	809	9.2	61	7.96	-16.3	-1.2	
39	J0903-23	ESO497-G004	09 03 03.1	-23 48 31	806	9.1	95.2	8.15	-14.8	-0.8	
40	J0927-32	UGCA165	09 27 25.9	-32 00 35	1086	13.6 ^{**}	83.5	8.67	-16.4	0.0	
41	J0931-34	ESO373-G006	09 31 50.0	-34 08 17	1046	12.5	66.1	8.06	-15.9	-0.2	
42	J0935-05	6dFJ0935505-053441 [*]	09 35 50.5	-05 34 41	1499	22.8	49.6	8.36	-16.4	-1.9	iii
43	J0940-03	[RC3]0938.0-0340 [*]	09 40 25.9	-03 53 07	1453	22.4	53.6	8.29	-16.6	-1.5	iii+iv
44	J0944-00b	SDSSJ094446.23-004118.2	09 44 43.7	-00 40 20	1223	18.8	124.8	8.39	-16.3	-1.0	
45	J1001-06	MCG-01-26-009 [*]	10 01 33.6	-06 31 30	748	8.2	38.4	7.78	-14.3	-0.5	ii
46	J1039+01	UGC05797 [*]	10 39 25.2	+01 43 07	711	7.2	47.8	7.95	-15.3	-2.1	iii
47	J1103-34	ESO377-G003	11 03 55.2	-34 21 30	998	11.1	52.6	8.22	-15.5	-1.1	
48	J1107-17	2MASXJ11070378-1736223 [*]	11 07 03.8	-17 36 22	993	11.9	110	8.26	-15.7	-2.0	ii
49	J1111-24	ESO502-G023	11 12 13.8	-24 13 55	1455	19.9	102.5	8.40	-16.5	0.0	
50	J1118-17	HIPASS J1118-17 [*]	11 18 03.1	-17 38 31	1068	13.5	56.6	8.56	-13.5	-2.2	iv
51	J1137-39	ESO320-G014	11 37 53.2	-39 13 13	654	6.0 ^{**}	40.2	7.74	-13.7	-2.4	
52	J1142-19	ESO571-G018	11 42 50.9	-19 04 03	1415	20.0	111.5	8.31	-16.7	-1.7	
53	J1150-12	MCG-02-30-033 [*]	11 50 36.4	-12 28 04	1278	19.0	97.1	8.36	-16.5	-1.0	ii
54	J1223-13	UGCA278 [*]	12 23 10.3	-13 56 45	1163	16.0	83.3	8.27	-16.1	-1.8	iii

[†] No GALEX observation

^{*} Observed in the SINGG program

^{**} Distances directly measured values from the literature, as reported in NED; all others are calculated from redshifts and the flow model.

^{††} The 'Type' category classifies the morphology of the H α regions and is described in §5. It is only evaluated for objects with SINGG images, where information on the H α regions is available.

Table 2.1 Small Isolated Gas-Rich Irregular Dwarf Galaxy sample (SIGRID) (continued)

SIGRID ID	HIPASS ID	Optical galaxy ID	RA (h m s)	Dec (d m s)	V_{hel} (km s ⁻¹)	D (Mpc)	w_{50} (km s ⁻¹)	$\log(M_{HI})$ (M_{\odot})	M_R (mag)	Tidal index	Type
55	J1244-35	ESO381-G018 [†]	12 44 42.4	-35 58 00	625	5.3**	39.8	7.84	-13.4	-1.3	iii
56	J1259-19	SGC1257.3-1909*	12 59 56.3	-19 24 47	826	8.5	47.2	8.14	-13.5	-1.8	iii
57	J1305-40	KK981182	13 05 02.1	-40 04 58	620	5.8**	38	8.08	-12.7	0.0	iii
58	J1308-16	MCG-03-34-002*	13 07 56.6	-16 41 21	959	11.4	56.6	8.07	-16.0	-1.2	I
59	J1309-27	AM1306-265*	13 09 36.6	-27 08 27	684	6.2	58.6	8.19	-14.9	-0.6	iii
60	J1322-28	LEDA 2793496*	13 22 44.3	-28 57 11	990	11.7	102.5	8.25	-15.4	-3.6	iii
61	J1337-28	ESO444-G084*	13 37 20.0	-28 02 42	587	5.1**	58.9	8.62	-14.2	0.0	iii
62	J1349-12	HIPASS J1349-12*	13 49 10.0	-12 45 35	1395	21.3	90.2	8.50	-16.4	-0.3	iii
63	J1350-35	ESO383-G092	13 50 42.0	-35 54 55	1411	17.2	46	8.38	-16.5	-0.4	iii
64	J1355-23	ESO510-G015*	13 55 03.3	-23 12 54	1372	18.5	65.2	8.43	-15.5	-0.9	iii+iv
65	J1403-27	ESO510-IG052*	14 03 34.6	-27 16 47	1326	17.5	119.8	8.72	-16.6	-1.8	I
66	J1443-33	ESO386-G013	14 43 04.3	-33 29 26	1378	17.8	93.1	8.33	-15.5	-1.5	iii
67	J1609-04	MCG-01-41-006*	16 09 36.8	-04 37 13	829	14.8	71.9	8.30	-16.1	-2.9	ii
68	J2003-31	ESO461-G036	20 03 51.0	-31 41 53	428	7.8**	71.6	8.02	-14.1	-	iii
69	J2039-63	LEDA 329372*	20 38 57.2	-63 46 16	1656	22.8	49.2	8.31	-16.5	-1.4	I
70	J2056-16	HIPASS J2056-16** [†]	20 56 51.0	-16 30 37	1453	22.8	66.7	8.38	-16.2	-0.1	iii
71	J2142-06	LEDA 1034072*	21 42 26.9	-06 19 58	1249	19.9	62.7	8.26	-16.5	-2.0	iii
72	J2207-43	ESO288-IG042*	22 07 50.9	-43 16 43	1396	20.0	58.4	8.51	-16.4	-2.5	iii
73	J2234-04	MCG-01-57-015*	22 34 54.7	-04 42 04	889	14.1	92.9	8.50	-16.2	-0.2	iii
74	J2239-04	UGC4433*	22 39 09.0	-04 45 37	831	12.0**	57.5	8.37	-16.0	-1.2	iii
75	J2242-06	LEDA 1028063** [†]	22 42 23.5	-06 50 10	899	14.1	62.6	7.95	-15.6	-0.7	ii
76	J2254-26	MCG-05-54-004*	22 54 45.2	-26 53 25	819	12.1	126.6	8.46	-16.1	-2.1	I
77	J2255-34	ESO406-G022*	22 55 52.6	-34 33 18	1286	18.2	66.8	8.16	-16.6	-0.6	ii
78	J2259-13	LEDA 938611	22 59 46.2	-13 23 22	1219	17.9	54.9	7.99	-15.9	-4.0	iii
79	J2311-42	ESO291-G003	23 11 10.9	-42 50 51	1381	19.1	94	8.19	-16.5	-1.3	iii
80	J2334-45b	ESO291-G031*	23 34 20.8	-45 59 50	1487	20.5	89.7	8.42	-16.0	-0.6	iii
81	J2349-22	LEDA 812517	23 49 51.8	-22 32 56	1020	14.6	69.7	7.99	-14.7	-3.0	iii
82	J2349-37	ESO348-G009*	23 49 23.5	-37 46 19	647	7.7**	84.9	8.47	-15.1	-0.5	iii
83	J2352-52	ESO149-G003*	23 52 02.8	-52 34 40	574	6.2**	47.9	8.13	-14.9	-6.8	ii

[†] No GALEX observation

* Observed in the SINGG program

** Distances directly measured values from the literature, as reported in NIED; all others are calculated from redshifts and the flow model.

^a The 'Type' category classifies the morphology of the H α regions and is described in §5. It is only evaluated for objects with SINGG images, where information on the H α regions is available.

main galaxy clusters. We have specifically excluded any galaxy that could be infalling into the cluster with high peculiar velocity, as discussed in Section 2.7.

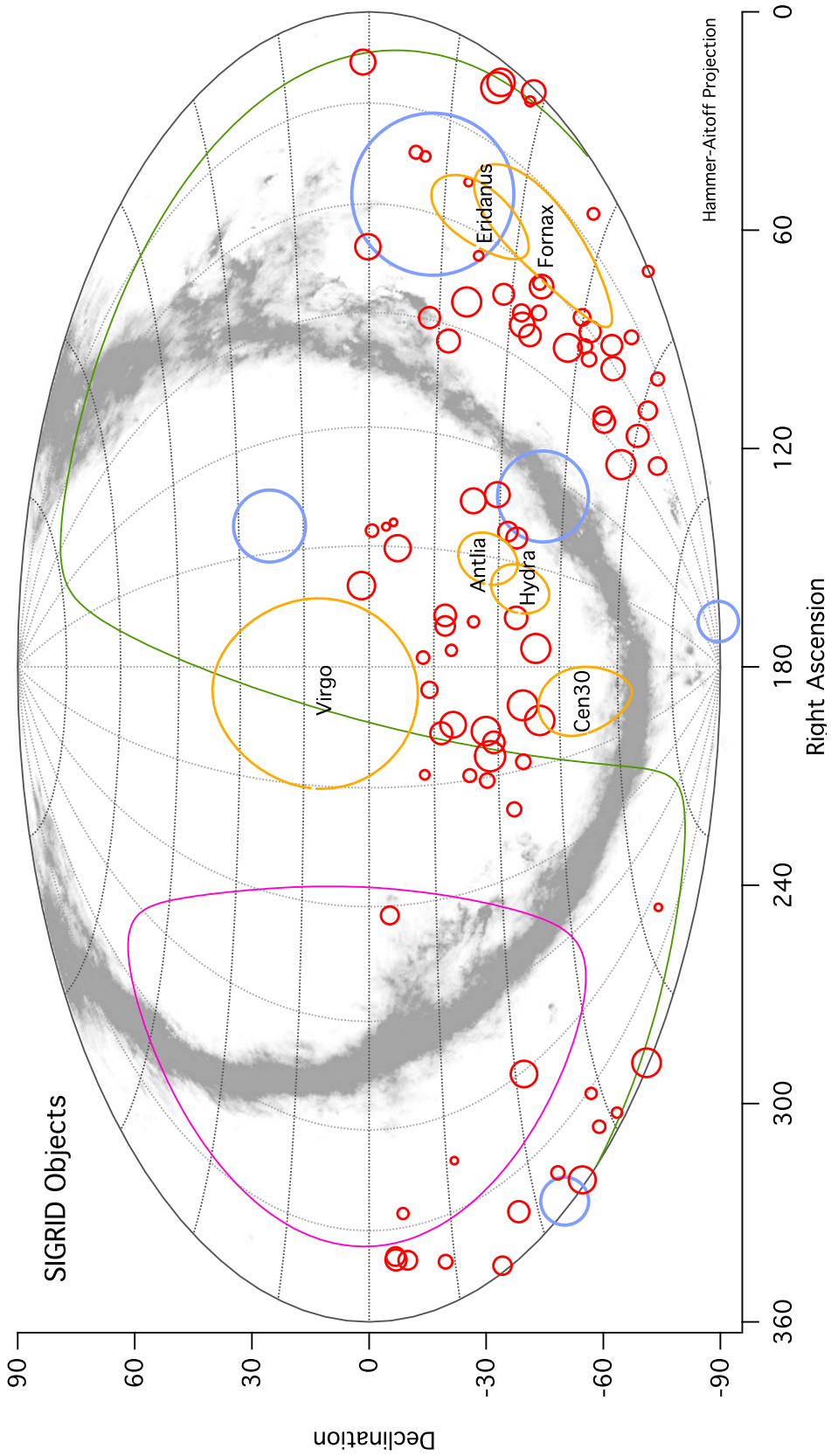


Figure 2.3 SIGRID galaxies with voids, galaxy clusters and MW dust absorption. SIGRID objects are plotted (red) with closer objects shown larger; the Local (Tully) Void is plotted with a radius of 50 (magenta); Local mini-voids are shown as simple circles proportional to their size (blue); Galaxy clusters are plotted with radius values listed in Table 2.2 (yellow); MW dust absorption is from [Schlegel et al. \(1998\)](#)

2.6. Sample images

To illustrate the range of objects included in the SIGRID sample, we present here six images from the SINGG survey (figures 4 to 9). These show the diversity of objects in the sample, from the active starburst region in Figure 5 to the faint $H\alpha$ regions in Figure 7; and the various distribution morphologies of the $H\text{ II}$ regions.

The $H\text{ II}$ region morphologies of the objects in our sample may be classified as follows:

- (i) single or few $H\text{ II}$ regions;
- (ii) multiple $H\text{ II}$ regions but centrally clumped;
- (iii) multiple dispersed $H\text{ II}$ regions; or
- (iv) separate $H\text{ II}$ regions or dwarf galaxy pairs

Each object can be characterised in addition by the ratio of its $H\alpha$ and R-band fluxes, although this does not correlate exactly with the visual appearance in the SINGG images.

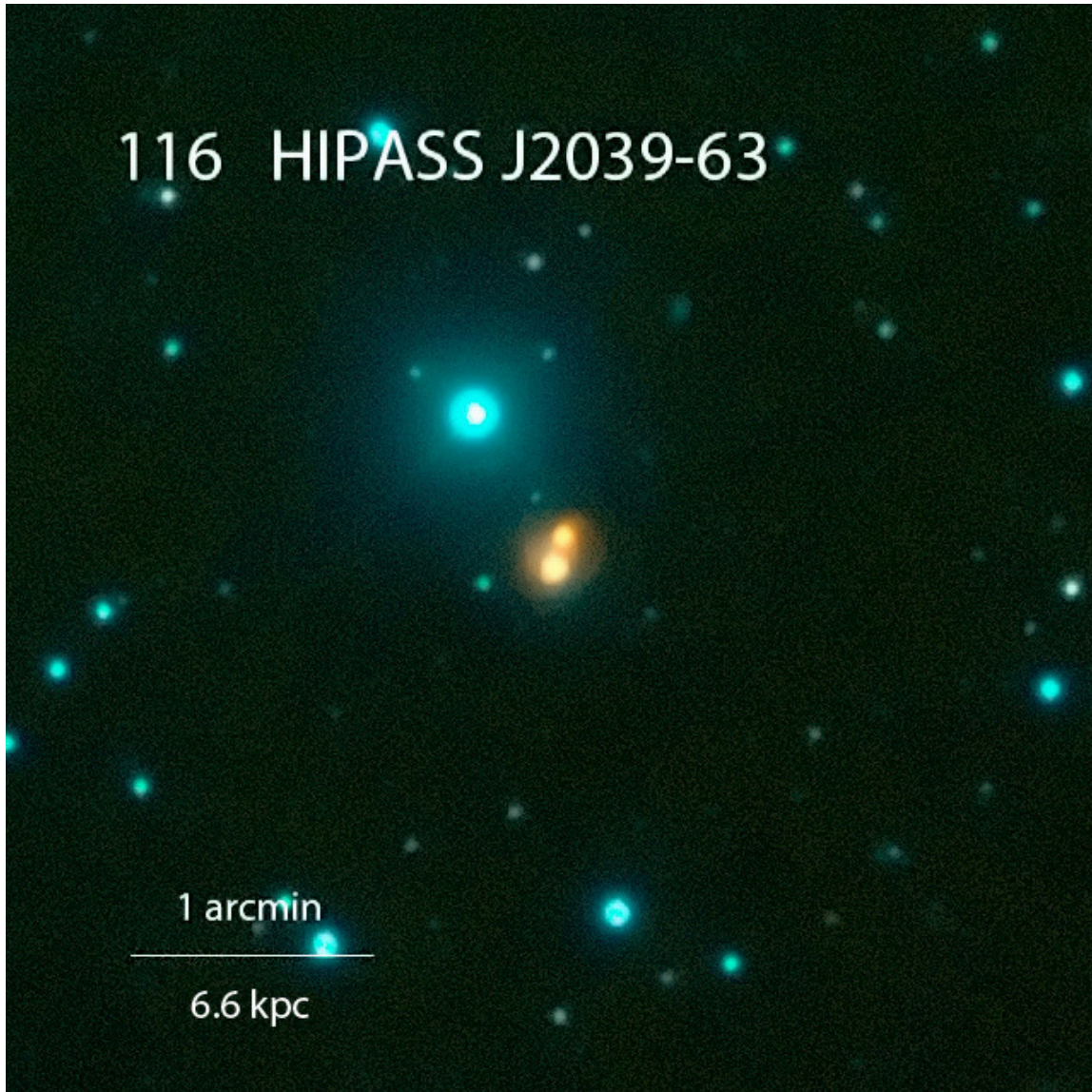


Figure 2.4 Type (i): Centrally condensed H α region(s)

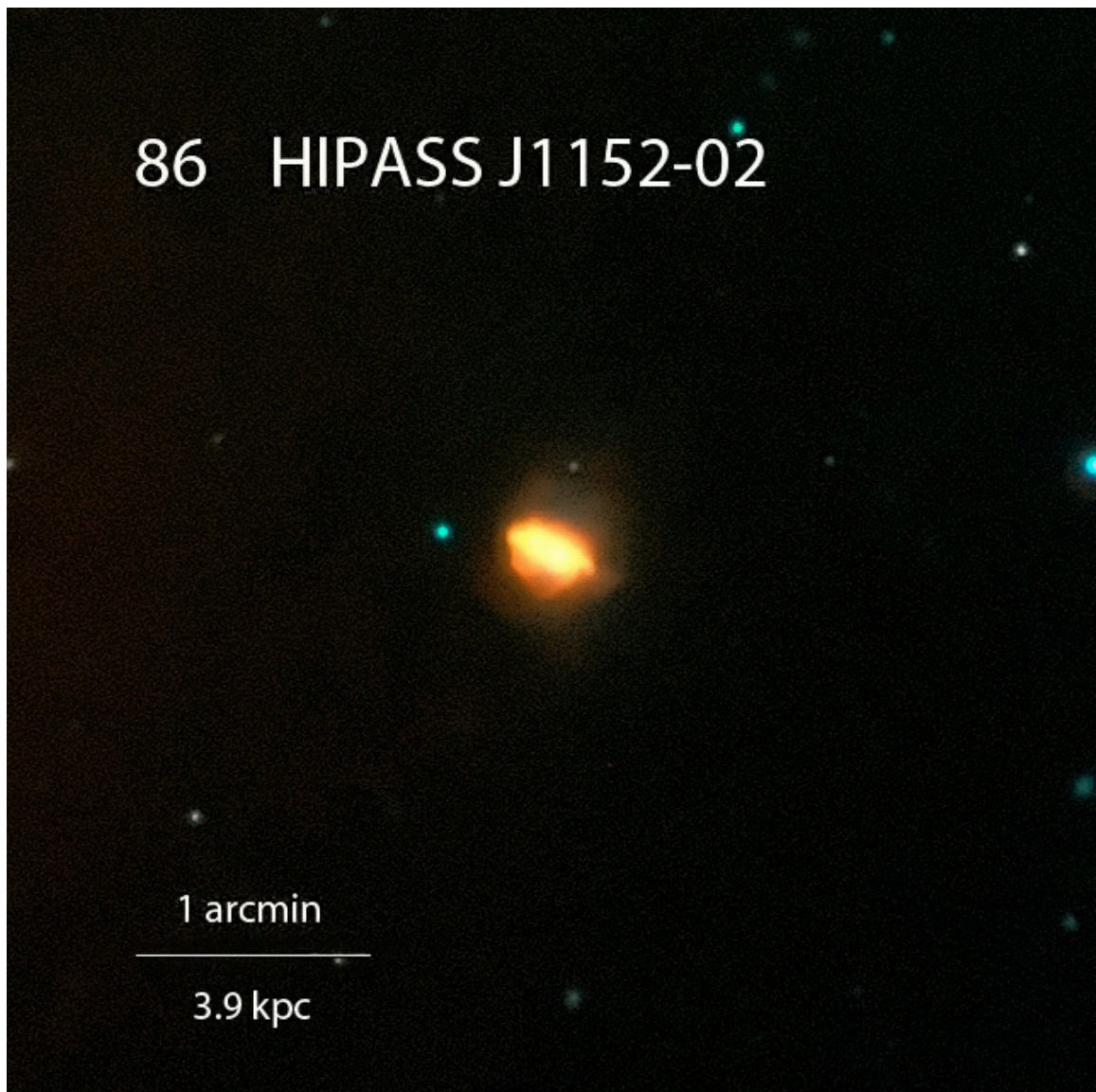


Figure 2.5 Type (i): Bright $H\alpha$ showing active starburst and outflows

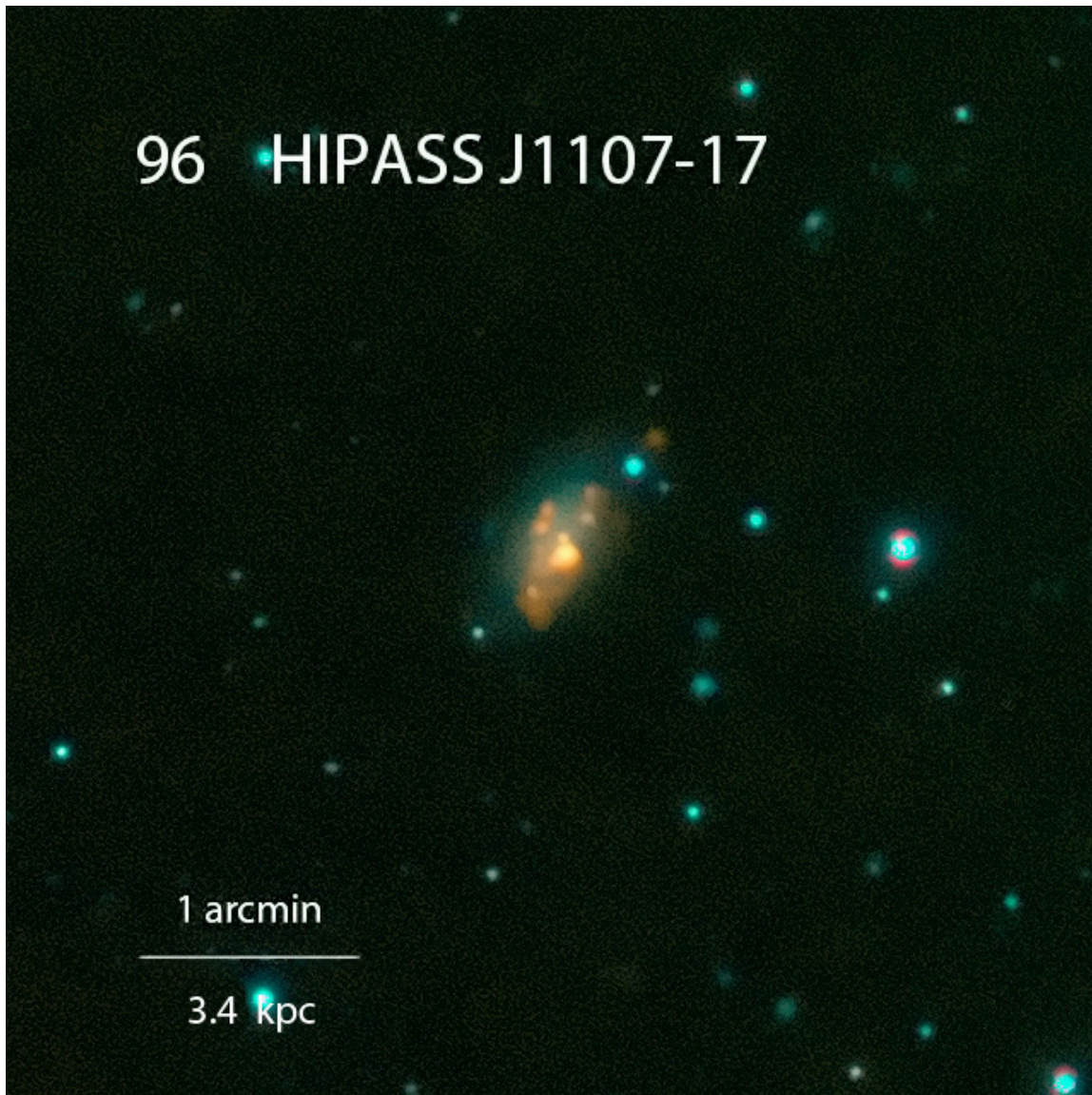


Figure 2.6 Type (ii): Centrally clumped multiple H α regions

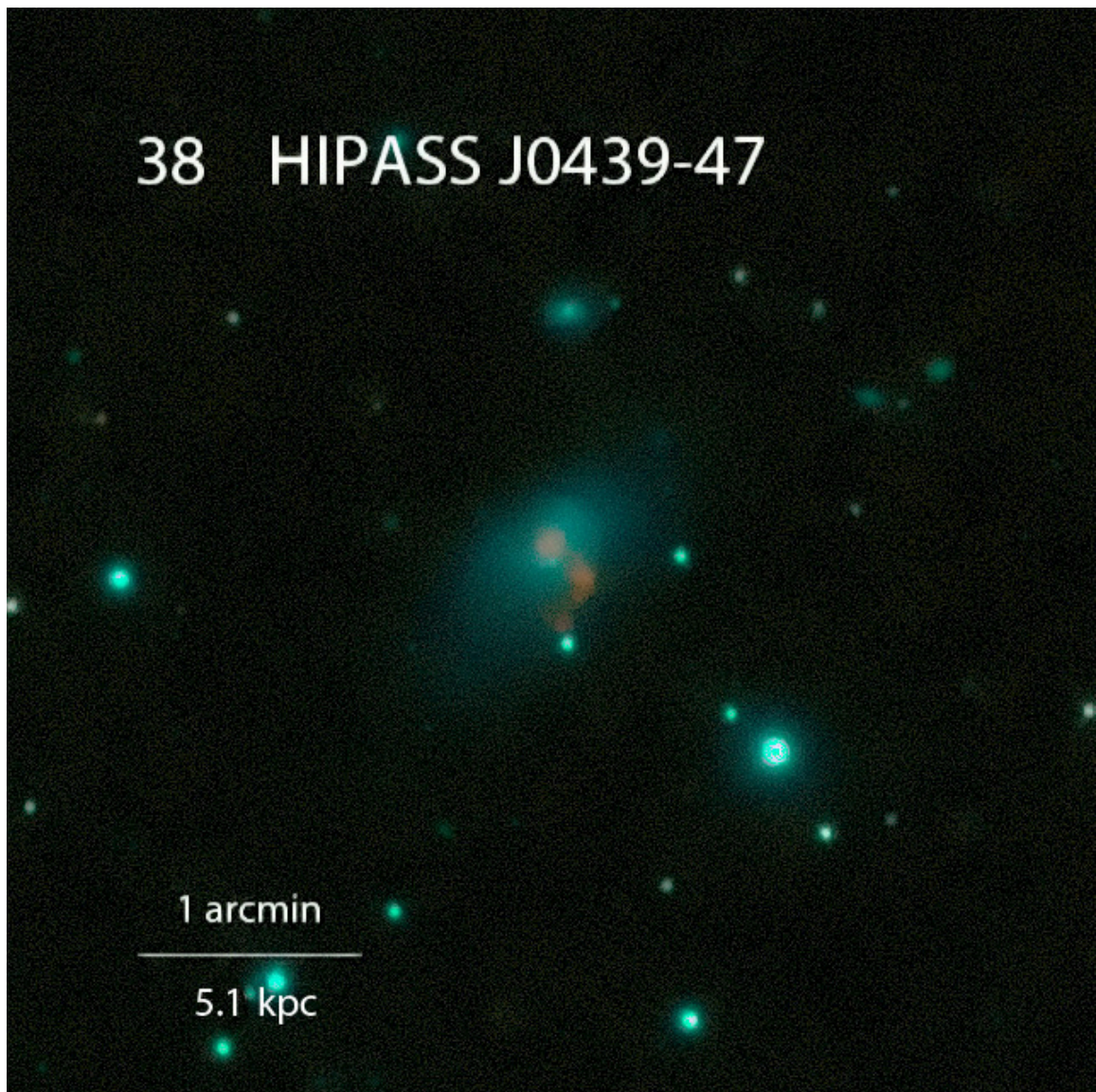


Figure 2.7 Type (ii): Faint H α compared to R-band

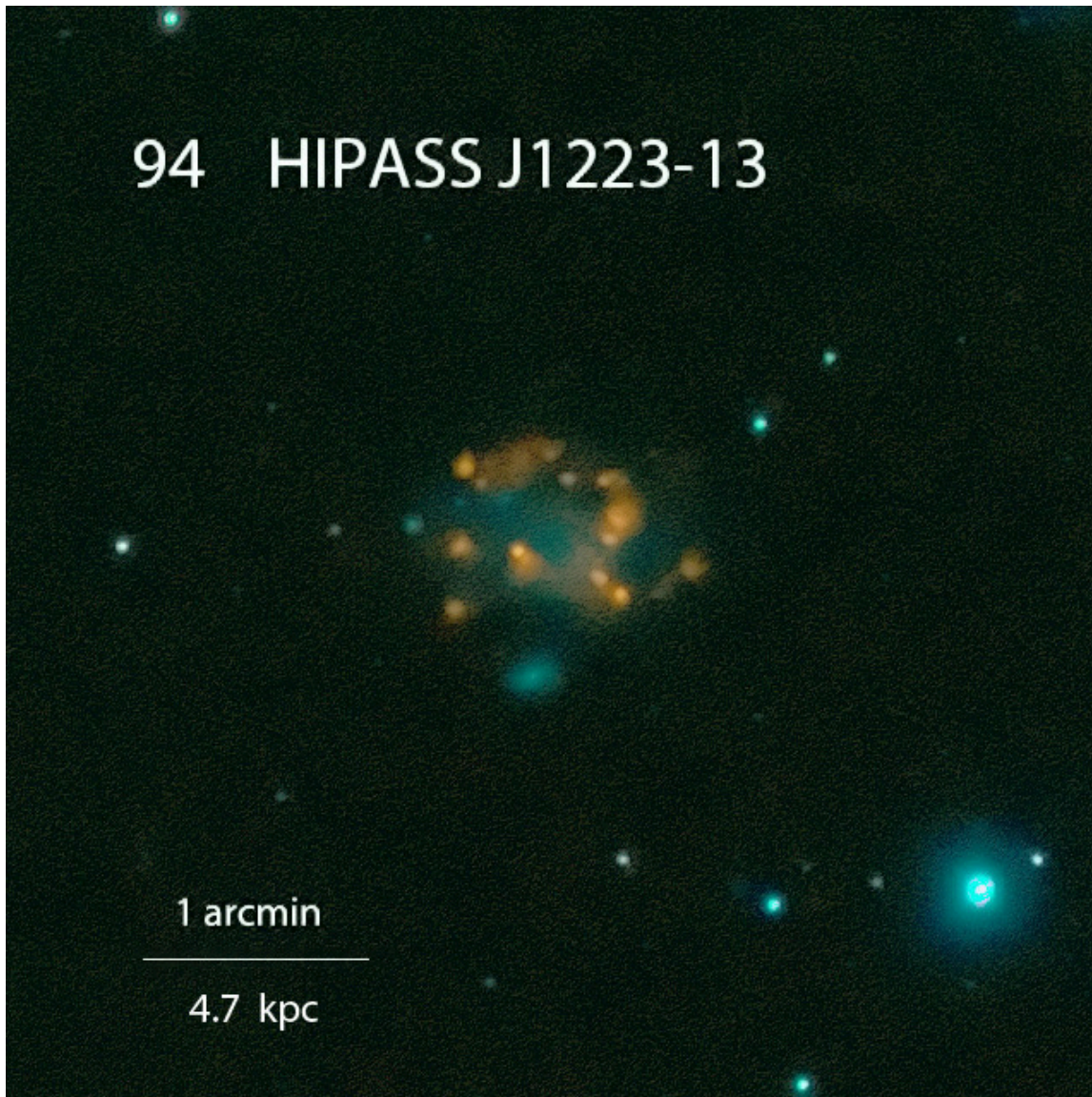


Figure 2.8 Type (iii): Dispersed H α regions

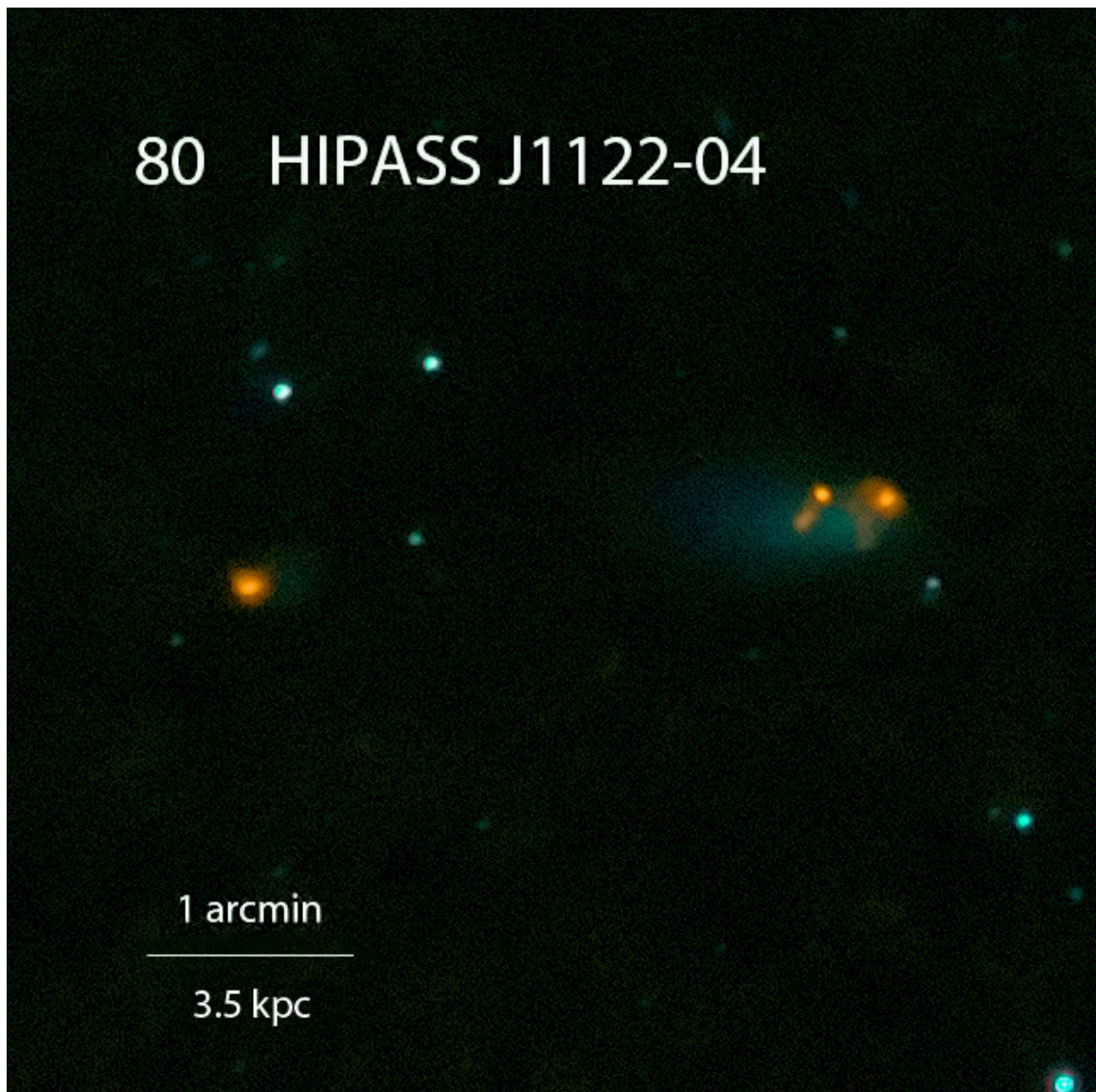


Figure 2.9 Type (iv): Separate neighbouring $H\alpha$ regions

2.7. Isolation

A key aspect of the SIGRID sample is that it consists of isolated objects, implying that current star formation is intrinsic to the galaxy's environment and evolutionary processes, rather than triggered by tidal influences of nearby larger galaxies. Isolation is also important because we wish to investigate galaxies that have formed from an intergalactic medium that is as far as possible pristine, or at least unenriched by outflows from large galaxies in recent times.

Thus there are two aspects of isolation we need to consider: isolation from nearby larger galaxies which could cause tidal effects; and isolation from galaxy clusters which might have enriched the IGM from which the dwarf galaxy formed. We have tackled this in three ways: visual inspection of optical and ultraviolet survey images; calculation of tidal potentials arising from galaxies in the same general region; and identification of objects that might have large peculiar radial velocities arising from infall into and through clusters.

2.7.1. Visual inspection of survey images

The initial identification of isolated targets involved visual inspection of DSS and GALEX images to exclude objects obviously proximate to larger galaxies. This process provided evidence of any nearby large neighbours within a few arc minutes, which was followed up using redshift data to estimate physical separation. More distant influences were evaluated using estimates of association with galaxy clusters and calculation of tidal influences from larger galaxies beyond the range of the visual inspection. An example of where the visual process was important occurred with HIPASS J1158-19b (ESO572-G034). While the initial tidal calculations did not suggest any significant effects, the DSS2 image showed it was within ~ 16 arc minutes of line-of-sight of two large galaxy/galaxy pairs, NGC 4027 and NGC 4038/9 (the Antennae galaxies). The standard NED data for distance (on which the tidal calculations are based, §6.3) suggest that the difference in redshifts (1114 and ~ 1650 km s^{-1}) and the fact that they are not part of a large cluster should take the small galaxy out of range of the larger ones. However, there is evidence from T_{rgb} distances that the larger galaxies are much closer, ie 13.3 Mpc (~ 970 km s^{-1}) (Saviane et al. 2008). The closer distance implies a significantly greater prospect for tidal effects, and could explain the strong starburst and outflows apparent in the SINGG image of the dwarf galaxy.

2.7.2. Excluding candidate galaxies due to proximity to galaxy clusters

When identifying possible candidates for the SIGRID sample we need to consider whether objects close to the same line-of-sight as more distant galaxy clusters (Centaurus, Eridanus, Fornax etc.) are in fact foreground objects, or whether they are members of the cluster with large peculiar velocities due to infall. Using recession velocity as a proxy for distance to determine the degree of isolation and absolute magnitude does not work in cluster environments, due to our inability to distinguish between normal Hubble flow recession and peculiar velocities due to cluster infall. We may therefore need to exclude from the sample objects located in the direction of nearby clusters. The size of the 'exclusion zone'

depends on the redshift of the cluster centre and size parameters such as the virial and zero-infall (turnaround) radii of the cluster and the velocity dispersion within the cluster.

[Karachentsev & Nasonova \(Kashibadze\) \(2010\)](#) investigated blueshifted galaxies in the Virgo Cluster, which they explain in terms of high infall peculiar velocities of objects located beyond the cluster centre. They found that these objects are confined to line-of-sight locations within the projected virial radius of the cluster (6°). They also found that 80% of such objects have young populations (S, BCD or dIr). They interpreted this as indicating these galaxies are still in the process of falling into the cluster, from beyond the cluster.

This suggests that galaxies with young stellar populations in the same line-of-sight as a galaxy cluster might be infalling from the far side of the cluster. This is important in the SIGRID context as all members have young stellar populations. Even if they exhibit apparent redshifts much lower than the cluster average, and thus appear to be closer than the cluster, it is not possible to say conclusively that they are not distant infalling objects, blueshifted against the Hubble flow trend. An example of this may be galaxy CCC026, identified as a member of the Cen30 Cluster ([Jerjen & Dressler 1997](#)). Its heliocentric recession velocity is 1438 km s^{-1} . The recession velocity of the Cen30 cluster is $3397 \pm 139 \text{ km s}^{-1}$ and its velocity dispersion σ is $933 \pm 118 \text{ km s}^{-1}$ ([Stein et al. 1997](#)). If CCC026 has a peculiar velocity $\sim 2\sigma$ this object may be a cluster member infalling from beyond the cluster centre, on which basis it has been excluded from the SIGRID sample.

The distortion of the flow velocity is well illustrated in calculations by [Tonry et al. \(2000\)](#) (their Figure 1) which show an ‘s-curve’ velocity variation with distance for Virgo Cluster infalling galaxies. The non-monotonic behaviour leads to three possible distance solutions for objects in direct line-of-sight with a cluster, but the effect falls off with increasing angular separation from the cluster centre. Near the centre of the cluster the effect is capable of reducing substantially the apparent recession velocity/redshift distance of infalling cluster members. At the 2σ level, the model shows that objects with apparent heliocentric recession velocities as low as 250 km s^{-1} can readily be found near the Virgo cluster centre, falling in from beyond the cluster. The blue-shifted galaxies reported by [Karachentsev & Nasonova \(Kashibadze\) \(2010\)](#) are extreme cases of this phenomenon. Such infalling galaxies are thus much more distant than if their redshifts were due solely to Hubble expansion. This effect was also explored by [Tully & Shaya \(1984\)](#) for the Virgo Cluster, who showed that objects as far as 26 from the cluster centre can exhibit anomalous redshifts (their Figure 4). In these circumstances, redshift cannot be used as a distance measure for estimating isolation or absolute magnitudes.

The Virgo Cluster also affects the SIGRID sample membership despite its northern location. While the cluster centre lies over 10 from the nearest potential SIGRID object, its zero infall radius (taken here as 25 based on several literature values) extends well into the southern hemisphere. On this basis, 14 candidate objects have been excluded from the sample. All objects in the final sample lie at or outside the projected zero infall velocity radius for the cluster ([Karachentsev & Nasonova 2010](#)), implying that they are not bound by the cluster’s gravitational potential.

The question of potential infall into a cluster is also important for objects in line-of-sight with the Centaurus30, Fornax, Antlia and Eridanus clusters. To exclude rogue galaxies with high peculiar velocities, we have adopted a selection criterion to exclude any sample

candidate that lies within the circle of the projected zero-infall (turnaround) radius of a nearby cluster, where the candidate’s recession velocity is within $\pm 3\sigma$ of the cluster recession velocity. Information on the zero-infall radius for all the relevant clusters is not available from published information, but we have adopted the values shown in Table 2.2. We have attempted to err on the side of caution. We have also confirmed that the objects are not associated with any of the Southern Compact Groups (Iovino 2002).

Table 2.2 Values used for projected cluster exclusion radii and velocity dispersions

Cluster	RA (J2000) (deg)	Dec (deg)	V_h (km s ⁻¹)	Excluded radius [†] (°)	σ (km s ⁻¹)	Excluded
Virgo	186.75	12.72	1059	25	757	14
Fornax	45.63	-35.45	1583	15	429	11
Eridanus	54.50	-22.32	1657	10	179	1
Antlia	157.50	-35.32	2797	7	469	2
Cen30	192.00	-51.80	3397	12	933	1
Hydra	150.61	-27.53	3777	7	608	1

[†] The Exclusion Radius figures are based where available on best estimates of the zero-infall radius. Where the zero-infall radius is at best known only poorly, a conservative estimate has been adopted. σ is the cluster velocity dispersion. ‘Excluded’ indicates the number of candidates that would otherwise be in the sample that are within the exclusion radii. All cluster centre values are approximate.

We have further considered whether candidates are outlying members of smaller association of galaxies—galaxy groups or sheets—and whether this should rule them out as sample members. As there are numbers of gas-rich dwarf galaxies in the Local Group with distances from the major galaxies > 270 kpc—implying they have had little opportunity to lose their gas through interaction with larger group members—(Grcevich & Putman 2009), in general we have not excluded from the sample galaxies that may be associated with the outer regions of groups and sheets.

Because the virial and zero-infall radii are less well defined for groups and associations (e.g. the NGC5128/NGC5236 group), they are not a good guide to interactions. In this case, we need to calculate the tidal influences to indicate likely present or past interactions with larger galaxies. To explore this we have used a ‘disturber index’ (§6.3 below) to check whether the tidal effects of adjacent galaxy group members are significant.

2.7.3. Tidal indices

Lack of apparent optical correlation of SIGRID objects with larger neighbours does not rule out the existence of potential tidal disturbers outside the fields from DSS and GALEX that could otherwise be identified visually. Thus it is important to identify potential disturber galaxies by calculating the tidal effect of galaxies in the same general region as the targets. We have investigated several ways of calculating this.

It should be noted that the purpose of calculating a disturbance index is not to obtain precise values for tidal forces, which in many cases is impossible, but to flag potential sample members which may have been tidally influenced in the past. As a result, a precise value for tidal strength is not required, and approximate methods can be used.

Karachentsev & Makarov (1999) (also Karachentsev et al. 2004) developed the ‘tidal index’ Θ as a way of estimating the isolation of a galaxy from the effects of tidal disturbance. Their work looked at nearby galaxies with heliocentric recession velocity $V_h < 720 \text{ km s}^{-1}$, where the distances to the target galaxies and to potential tidal disturbers are known through direct measurement. They used estimates of the masses of the galaxies based on their distances and H I rotational velocities, allowing evaluation of an expression of the form

$$\Theta = \log(M \times d^{-3}) + C$$

where M is the disturber galaxy mass, d is the separation between disturber and target and C is an arbitrary constant, evaluated by setting the ‘cyclic Keplerian period’ to the Hubble time, a point beyond which galaxies could be deemed not to have interacted (Karachentsev & Makarov 1999). For each target, Θ was taken as the maximum value of the index for all disturbers.

For the SIGRID galaxies, many of which are at greater distances (V_h up to $\sim 1650 \text{ km s}^{-1}$) than the Karachentsev catalog, the set of disturbers identified using the NASA/IPAC Extragalactic Database (NED) is incomplete due to optical bias effects. Most SIGRID distances are greater than measurable by direct methods (for example, measuring the Cepheid or RR Lyrae variable stars, or estimating distances using the tip of the red giant branch) and can usually only be estimated from redshifts or the Tully-Fisher relation. More important, H I rotation curves are not available for many of the potential disturbing galaxies, making a direct measurement of mass difficult or impossible. This implies that Θ cannot be calculated reliably, or at all, for the SIGRID galaxies. As a result, we have explored other disturbance measures.

There are a number of possible measures of interaction between target and disturber. The simplest is to calculate a hypothetical ‘time of last contact’, based on the distance between disturber and target and assuming a velocity of separation of 100 km s^{-1} ($\sim 100 \text{ kpc/Gyr}$). We have also taken a more sophisticated approach, based on the Karachentsev tidal index, to develop a simple alternative tidal index to estimate isolation for the galaxies in the SIGRID sample.

We define a ‘disturber index’, Δ , as:

$$\Delta = C_1 \times \left(\log_{10} \left(\frac{L_B}{d_{\text{Mpc}}^3} \right) - C_2 \right)$$

where L_B is the disturber absolute luminosity (B band) and d_{Mpc} is the separation between the disturber and target galaxy in Mpc. C_1 and C_2 are constants (see below). Δ is computed from NED data for all disturbers within the 10 degree ‘near name lookup’ NED limit from the target, and within the range of recession velocities $V_h(\text{target}) \pm 250 \text{ km s}^{-1}$. Typically this search generates a list of between 1 and 50 potential disturber galaxies for a target galaxy, for each of which a value of Δ is calculated. As with the Θ index of Karachentsev et al., the disturber index for a target galaxy is the maximum of the individual tidal potentials for all the possible disturbers identified by NED. This index has the great virtue that the necessary information on magnitudes and heliocentric recession velocities is readily available.

L_B is used as a proxy for disturber galaxy mass, so Δ is in effect a measure of the tidal potential at the target galaxy due to the disturber, following the approach described by

Karachentsev & Makarov (1999). The R- or I-band magnitudes might provide a better stellar mass estimate, but these are not available for the majority of NED listings. 2MASS magnitudes would provide even better mass estimates but are not available for most objects. The distances from the observer to the target and disturber galaxies were initially calculated assuming V_h is a measure of actual distance due to Hubble expansion and contains no peculiar velocity or local flow component. Angular separation and the V_h of the target galaxy are used to calculate lateral separation. The total separation for each galaxy pair is then calculated using Pythagoras. Thus Δ is a proxy for Θ and can be calculated from NED data.

The constants C_1 and C_2 are evaluated by deriving a linear best fit for Δ to Θ for 16 galaxies common to the Karachentsev and an earlier extended SIGRID list. The values $C_1 = 0.894$ and $C_2 = 13.0$ have been adopted. They give values for Δ which indicates isolation when $\Delta < 0$. Table 2.3 compares values of Θ and Δ calculated for the galaxies common to SIGRID and the Karachentsev et al. catalog (2004). Objects not part of the final SIGRID list are included in Table 2.3 to allow better comparison between the two methods. They were excluded from the SIGRID list for reasons such as cluster line-of-sight proximity discussed earlier (§6.2).

While the relationship between Θ and Δ is not completely consistent, Δ does appear to be a reasonable substitute for Θ . Both the Θ and Δ indices identify the possibility of disturbance of the target galaxy by the disturber, but because we do not know, for most objects, their actual locations and velocities, a positive value of the index does not guarantee that there has been interaction. The methods are approximate, but negative values of Θ and Δ are a good indication of isolation, and this is their purpose. The ‘time of last contact’ can be used to clarify marginal cases.

It should also be noted that this approach is limited by the available 10 radius of available NED data. As a result, potential disturbers outside this radius will be missed. However, the ready availability of reasonably consistent and complete data makes this a useful technique. The more analytically based technique of Karachentsev & Makarov (1999) is itself limited by the accuracy of available distance measurements, and may be best suited to objects closer than $V_h \sim 720 \text{ km s}^{-1}$.

2.7.4. Absolute magnitude bias for low luminosity objects

In the lists of possible disturbers generated for each target galaxy, the majority are usually faint objects, with a few larger (typically NGC catalog) objects. We need to take care to estimate the masses of the fainter objects carefully to identify those that, while small, may be close enough to disturb the target galaxy tidally.

As Mateo (1998) has shown, the King formalism in which mass follows light leads to an underestimate of mass for low luminosity objects ($L \lesssim 10^8 L_\odot$). Adopting the finding by Strigari et al. (2008) that there is a common mass scale that applies to dwarf Milky Way satellites, indicating a minimum integrated mass (dark + baryonic) of $10^7 M_\odot$ within 300pc of galactic centre for galaxies with luminosities $< 10^8 L_\odot$, we have found that taking into account very low luminosity objects that are relatively close to our targets makes little difference to the estimated maximum tidal potentials experienced by SIGRID objects, as the potentials are dominated by larger more distant galaxies.

2.7.5. Dust reddening corrections to distance and luminosity

We have corrected SIGRID apparent magnitudes for Milky Way dust absorption using the dust maps from [Schlegel et al. \(1998\)](#). NED also provides E(B-V) values for these objects using the same dust maps. At the time of this work, there were slight discrepancies between NED values and values calculated directly using current Schlegel et al. code, but they do not materially influence the results.

2.7.6. Local flow corrections to distance and luminosity

Bearing in mind that precise values of the disturber index are not required, how accurately must distances be known to estimate magnitudes suitable for use in the disturber index? In practice the potential disturbers are experiencing similar flow fields to the SIGRID targets, so it is reasonable to use the apparent recession velocities V_h of both as the basis for approximate absolute magnitude calculations in the disturbance index. This has the virtue that the values are readily available using the NED ‘near name’ search. Using flow-corrected velocities we recalculated the tidal indices for a 10% subset of SIGRID objects. It makes no significant difference to the isolation calculations whether we use the flow corrected distances or the simple V_h distances, confirming our assumption.

The flow model takes into account corrections to the measured heliocentric recession velocities, V_h , arising from the motion of the Sun around the Galaxy, our motion towards the Local Group barycentre, and flows induced by mass concentrations in the local Universe, such as the Virgo Cluster, the Great Attractor and the Shapley Supercluster.

Flow models investigated (following the approach used by [Meurer et al. \(2006\)](#) for the SINGG survey), were those published by [Mould et al. \(2000\)](#) and [Tonry et al. \(2000\)](#). The Mould et al. model turns out to give the better results when compared to directly measured distances.

Of the mass concentrations that could influence recession velocities, the Virgo Cluster at 17 Mpc ([Jerjen et al. 2004](#)) appears to have the greatest effect. This is not surprising because of the distance limit imposed on the SIGRID sample, $V_h < 1650 \text{ km s}^{-1}$. However, in estimating absolute magnitudes, we have used the flow corrections for Virgo, Great Attractor and Shapley Supercluster in fall as these give the best fit to direct distance measurements (where available). Twenty-one of the SIGRID sample have such distances listed. We have also used the *Extragalactic Distance Database* ([Tully et al. 2009](#)) as an additional source of independently measured distances. The closer objects have tip of the red giant branch measurements and some of the more distant objects have distances estimated using the Tully-Fisher relation. We conclude that the flow corrected velocities give reliable distance values for use in absolute magnitude calculations and that any peculiar velocity effects are minor, but as recommended in the NED database documentation, we have used the direct distance measurements when available instead of the flow model values in calculating absolute magnitudes.

We have also considered how to deal with the effects of anomalous velocities of galaxies away from voids, explored by [Tully et al. \(2008\)](#) and [Nasonova & Karachentsev \(2011\)](#). Understanding the details of the flow away from such voids and the uncertainties in the size and location of voids, makes a complete understanding of local flow patterns extremely

complex. As our aim in this work is to select a sample of galaxies that are isolated, we have assumed the simpler flow-model approach as the principle means of avoiding disturbed objects.

We conclude that the SIGRID galaxies have not experienced significant tidal influences from larger adjacent galaxies within at least the last 5 Gyr—in many cases, ever—and therefore that their recent star formation episodes are intrinsic to the galaxies themselves.

Table 2.3 Comparison of tidal indices

SIGRID ID	Object	RA (J2000) h m s	Dec (d m s)	V_h [†] (km s ⁻¹)	Θ tidal	Δ	T_{last} (Gyr)	Disturbers ($< 15\text{Gyr}$)
5	IC1574	00 43 03.8	-22 15 01	363	-0.1	-1.0	5.7	3
36	ESO121-G020	06 15 54.5	-57 43 35	583	-1.6	-1.9	9.6	1
	ESO489-G?056	06 26 17.0	-26 15 56	492	-2.1	-0.7	3.6	1
	ESO308-G022	06 39 32.7	-40 43 15	821	-2.6	-1.8	20	0
51	ESO320-G014	11 37 53.4	-39 13 14	654	-1.2	-0.9	10.6	3
	ESO379-G007	11 54 43.0	-33 33 29	640	-1.3	-1.0	4.9	3
	ESO321-G014	12 13 49.6	-38 13 53	615	-0.3	-1.6	5.0	5
55	ESO381-G018	12 44 42.7	-35 58 00	625	-0.6	-1.3	6.0	6
57	[KK98]182	13 05 02.9	-40 04 58	620	1.2	0.0	6.5	5
59	AM1306-265	13 09 36.6	-27 08 26	684	-0.6	-0.6	7.9	5
	[KK98]195	13 21 08.2	-31 31 47	567	-0.2	0.2	5.6	15
	UGCA365	13 36 30.8	-29 14 11	570	2.1	0.4	2.9	11
66	ESO444-G084	13 37 20.2	-28 02 46	587	1.7	0.0	2.6	11
	HIPASSJ1337-39	13 37 25.1	-39 53 52	492	-0.3	0.4	4.4	11
	ESO272-G025	14 43 25.5	-44 42 19	631	-1.5	-1.8	7.6	2
83	ESO149-G003	23 52 02.8	-52 34 39	574	-1.7	-6.7	-	0

[†] Notes: V_h is the target galaxy's heliocentric recession velocity and T_{last} is the most recent possible interaction time between the object and its possible disturbers, assuming a separation velocity of 100 km s⁻¹ for each object pair. The disturber index Δ is the largest value of the index for the set of disturbers identified from NED. Δ is thus arbitrary, but, like Θ , indicates isolation when less than zero.

2.8. Sample completeness

It is worth noting that completeness in the normal sense is not essential to the SIGRID sample, but isolation is important. Our purpose is to obtain a sample for spectroscopic study that can be reasonably argued to be isolated. By setting stringent sample selection criteria, we automatically exclude numbers of dwarf galaxies that would be present in a full set of Local Volume dwarf galaxies. However, it is of interest to consider how complete the base set is from which the SIGRID sample has been selected.

The completeness of the set of gas-rich dwarf galaxies in the Local Volume identified in this way is determined by the completeness of the HIPASS survey, i.e. 95% or better for an integrated 21cm flux of 9.4 Jy.km s^{-1} (Zwaan et al. 2004). Thus the set of dwarf galaxies is largely complete for galaxies of the SMC neutral hydrogen mass to a distance of $\sim 1250 \text{ km s}^{-1}$. Beyond this distance for SMC-size objects, and closer for smaller galaxies, there does exist a bias, but this is measurable and understood. Figure 10 shows M_R plotted against distance for the SIGRID galaxies. An unbiased sample would show a horizontal line. The top of the distribution is reasonably flat due in part to sample cut-off, but the base shows some bias, arising from the H I detection limit of the HIPASS catalog.

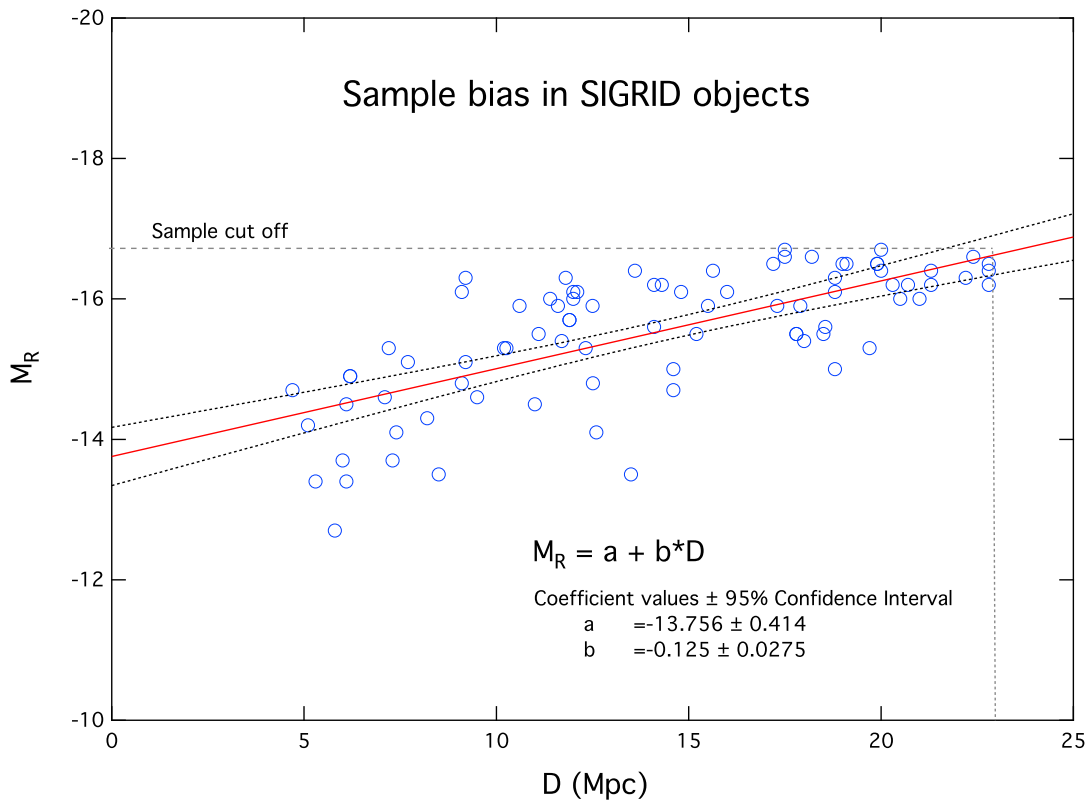


Figure 2.10 Sample bias for the SIGRID objects

Figure 11 shows the HIPASS sample completeness contours computed from a formula derived from that given by Zwaan et al. (2004):

$$\log_{10}(m_{HI}) = \log_{10}\left(\frac{\text{erf}^{-1}(C)}{0.12} - 6.4\right) + 5.371 + \log_{10}(D^2)$$

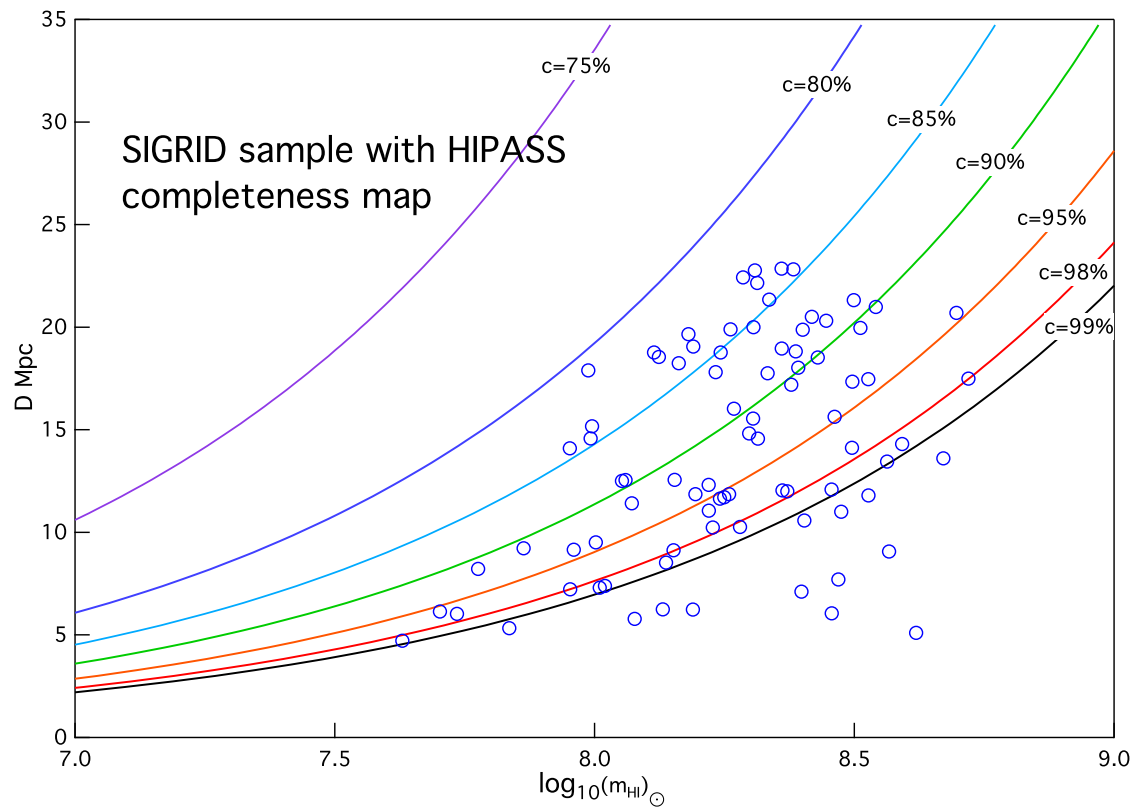


Figure 2.11 SIGRID sample plotted over HIPASS completeness contours

where D is the distance in Mpc and C is the sample completeness. Over 40% of the SIGRID sample lies above the HIPASS 95% completeness level.

2.9. Metallicity

Metallicity, the abundance of elements heavier than Helium, is an important parameter that controls many aspects of the formation and evolution of stars and galaxies (Kunth & Östlin 2000). Observations show that larger galaxies have higher metallicities than smaller galaxies, the so-called “mass-metallicity relation”. A major aim in our measurements of nebular metallicities is to improve understanding of the mass-metallicity relation for low mass, low luminosity isolated dwarf galaxies.

The mass-metallicity relation has been well studied for higher mass galaxies, but low luminosity objects have received much less attention (Tremonti et al. 2004; Lee et al. 2006; Guseva et al. 2009). There has so far been no complete or systematic study of the metallicity distribution in low mass isolated gas rich dwarf galaxies in the Local Volume.

In this work we have identified a number of previously unstudied low mass, low luminosity objects, where we are using a single observational base to increase consistency and reduce scatter. The main focus of this work is to measure the metallicities of this sample, using strong line and, where possible, direct metallicity techniques (Kewley & Dopita 2002; Kewley & Ellison 2008). In all our measurements to date (see §9 below), excellent S/N data have been obtained on the standard nebular emission lines.

In addition, in a few objects, a number of He I and He II lines have been detected. Intense OH airglow lines make observing longer wavelength faint nebular lines difficult in these objects, as integration times for the objects are typically 1 to 2 hours. The time variability of both the intensity and, particularly, the relative rotational level populations in the atmospheric OH molecules (Nicholls et al. 1972) makes the removal of such interference problematic, although the ‘nod and shuffle’ technique used by the WiFeS spectrograph works very well.

Gas-rich dwarf galaxies characteristically show substantially lower nebular metallicities than larger galaxies, implying a much lower chemical yield from any previous star formation episodes. The low metallicities may be explained in several ways:

First, the star-formation chronology (Lee et al. 2009; McQuinn et al. 2009, 2010):

- Star formation only early, mainly prior to re-ionisation;
- Continuous star formation at a low rate since the formation of the galaxy;
- Occasional, irregular short bursts of star formation, fed by cold inflows of near-pristine gas; or
- Only relatively recent commencement of star formation.

Second, evolutionary factors (e.g. Kunth & Östlin 2000):

- Low retention of enrichment by supernova outflows due to shallow gravitational potential and low efficiency of retention of outflows within the local H II region;
- Dilution of nebular metallicity by pristine gas inflows; and
- Lack of interactions, mergers, tidal effects or active galactic nuclei to stimulate strong star burst and consequent enrichment.

It is plausible that all of these have contributed to the chemical enrichment in the galaxies in our sample, and we anticipate that our measurements will help clarify the relative importance of these processes. [Disney et al. \(2008\)](#) have suggested that galaxy evolution may be simpler than it appears, but have not been able to identify the “controlling parameter” that describes the process.

We do, however, tend to favour the idea that, after some initial star formation before or around the re-ionisation era, later star forming episodes in dwarf galaxies have been sporadic, with durations of perhaps 0.5Gyr, resulting from inflows of cold pristine H I (i.e. “cold phase” gas), whose frequency depends on the availability of such inflows. This would imply that more isolated galaxies, arising in regions with a scarcity of gas suitable for cold inflows and initial galaxy formation, should show lower metallicity on average than those in more densely populated regions, where the IGM would have had more initial enrichment, and where the cold inflows would have been more frequent. Although not stated by [Pustilnik & Kniazev \(2007\)](#), this is an implication that could be drawn from their observations of blue compact galaxies in local voids.

SIGRID sample objects exhibit H II emission, implying current star formation with a time-frame of ~5 Myr, and clear evidence of UV emission from GALEX observations, implying a significant population of O and B stars, and consequent star formation over ~50 Myr. There is also evidence in initial observations with WiFeS (§9 below) in a few objects of Balmer absorption lines in the associated stellar continuum, implying a robust intermediate age A star population, evidence of star formation for ~400 Myr, similar to that found for NGC 839 ([Rich et al. 2010](#)).

This is fully consistent with the findings of [McQuinn et al. \(2009\)](#) that dwarf gas rich galaxies show evidence of star formation over periods of 200-400 Myr. As those authors have also found, this demonstrates that star formation in a dwarf galaxy can occur for protracted periods of at least 0.4 Gyr, and that star formation can occur over all time scales in that period, ruling out global “self-quenching” of starbursts over shorter periods ([McQuinn et al. 2009, 2010](#)).

2.10. WiFeS and nebular abundance measurements

The WiFeS spectrograph is a new double beam image slicing IFS, designed specifically to maximise throughput from the ANU 2.3m telescope at Siding Spring. It covers the spectral range 320 to 950nm, at resolutions of 3000 and 7000. It has a science field of view of 25x38 arc seconds ([Dopita et al. 2007](#)).

As many of the SIGRID objects subtend angles less than its FOV, WiFeS is an ideal instrument to measure nebular metallicities in the ionised hydrogen star forming regions. The instrument generates a data cube which allows exploration of nebular and continuum spectra in different regions of the target objects. Typically even in poor seeing WiFeS resolves SIGRID object star formation regions easily, making possible exploration of excitation and abundances in different regions of each object.

Figure 12 shows a slice through the data cube of object HIPASS J1609-04 in [O III] 5007Å. The star forming regions are typically 5 arc seconds across, corresponding to a diameter of

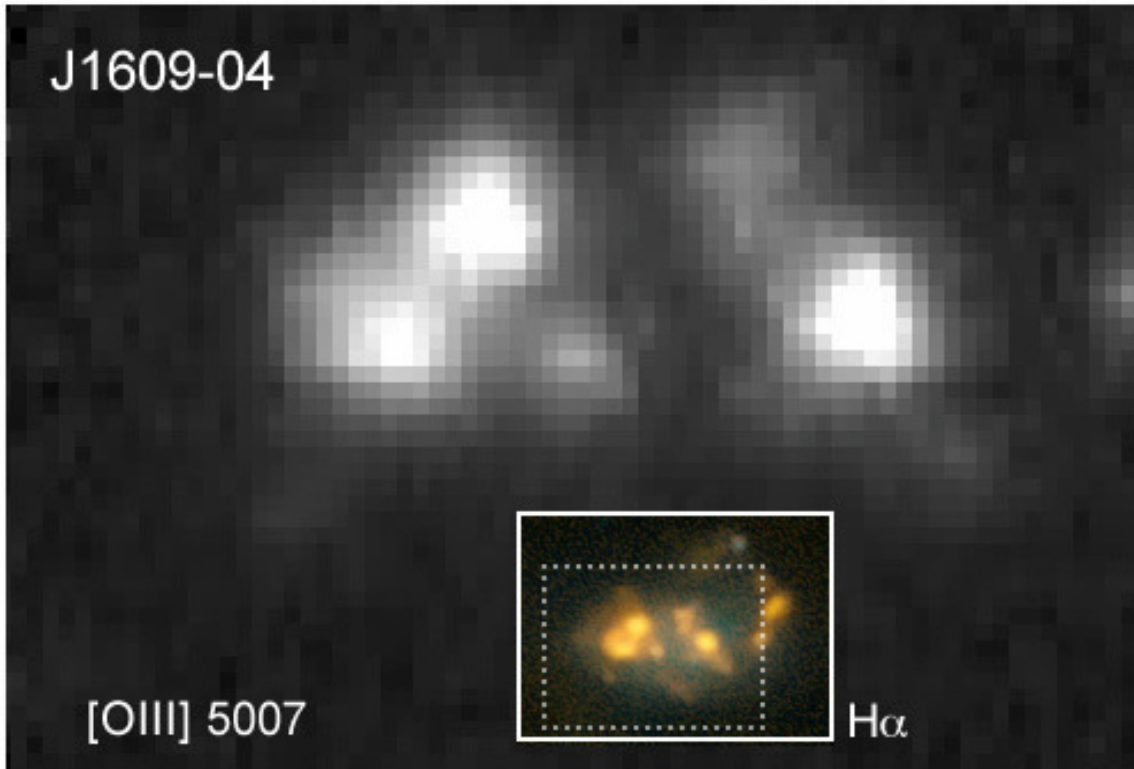


Figure 2.12 WiFeS datacube image of HIPASS J1609-04 at [O III] 5007Å, with SINGG image inset, showing WiFeS aperture

~300pc at 13.5 Mpc.

Inset in the figure is a composite image from the SINGG observations covering a slightly larger area, showing the H α regions orange and the stellar continuum (R-band) as cyan (Meurer et al. 2006).

At this scale, the data cube allows spectra to be obtained for complete H II regions around individual star-forming areas in a single observation. This will eliminate the bias toward high excitation regions at the centres of HII regions which are present in single-slit observations, and will allow for the derivation of more accurate chemical abundances from either the strong-line technique, or the direct electron temperature based techniques. A further benefit is that photometry can be undertaken using an image from an appropriately weighted wavelength slice.

An additional benefit of IFU spectroscopy is that it avoids fibre-size sampling errors that can occur with surveys such as the Sloan Digital Sky Survey, where fibre diameters have a 3 arc second size on the sky (York et al. 2000), and may miss important regions within a complex object such as illustrated in Figures 6, 8, and 9.

2.11. 'Sub-dwarf' galaxies?

When we undertook visual inspection of the DSS and GALEX image fields, some potential SIGRID objects appeared to be associated with one or more adjacent small UV-bright star forming regions. Few if any of these apparent star forming regions have been catalogued,

so it is not possible without additional spectroscopy to determine whether they are associated with the SIGRID objects, or random line-of-sight associations with more distant objects. However, consistent with this hypothesis, several SINGG objects do appear to have companions with active star formation regions—see for example, Figure 9.

If the objects are physically associated, it is possible that some of them may be extended loosely associated star-forming regions in otherwise extremely faint dwarf galaxies. [Warren et al. \(2007\)](#) concluded that there was a minimum number of stars a galaxy could form based on its initial baryonic mass, but as there appears to be no lower limit on initial masses, there should be no reason to impose a lower limit on the size of dwarf galaxies. If a power law describes the sizes of newly formed galaxies, one might expect regions with localised star-forming regions, where the IGM has condensed into numbers of very small ‘sub-dwarf’ galaxies. In isolated regions, such low luminosity objects would have been catalogued only by chance, consistent with the objects discussed here.

[Werk et al. \(2010\)](#) have identified what they term “ELdots”—emission line dots—small isolated regions of H II emission near galaxy-centred H II sources. However, the isolated star forming regions reported here (should they be such) are unlikely to be the same phenomenon as ELdots, as the latter are unresolved sources associated with highly disturbed regions.

We have not excluded from the SIGRID sample potential members adjacent to these regions, where the objects are clearly isolated from other sources of tidal disturbance. We propose to explore such regions further, as they may cast light on the formation of galaxies at the smallest scales.

2.12. ‘Bloaters’

Another phenomenon we have found during visual inspection of SIGRID candidates we term ‘bloaters’—dwarf irregular galaxies with typically low absolute R-band magnitude and low H I mass, but which appear to have a much larger physical extent than expected (typically 10 kpc or greater). These objects give the appearance of having been disrupted by tidal interaction, but since they are isolated, as far as can be determined, recent gas inflow may explain them. Even if these objects were initially larger galaxies that have undergone strong starburst and have ejected most of their gas, they would still be intriguing objects.

An example is shown in Figure 13 from DSS1 imagery. This shows galaxy UGCA051 (HIPASS J0315-19; SIGRID 18). Calculating its distance from its flow-corrected recession velocity as 22.2 Mpc (assuming $H_0 = 73 \text{ km s}^{-1} \text{ Mpc}^{-1}$) gives a maximum linear dimension of ~ 16 kpc, which is much larger than one would expect for a normal dwarf galaxy of this luminosity and neutral hydrogen mass ($M_R = -16.3$; $\log_{10}(m\text{H I}) = 8.3(M_\odot)$). The possibility of it being a faint side-on LSB galaxy is unlikely, given the low HIPASS rotational velocity measurement $w_{50} = 48.7 \text{ km s}^{-1}$. It has been classified variously as dIrr, IB(s)m and LC V-VI.

There are several cases of ‘bloaters’ in the SIGRID sample, but it will be necessary to undertake quantitative isophotal evaluation of the images to obtain reliable estimates of their size, to validate the visual observations. Whether one considers these as single larger faint objects, or as a small group of merging dwarf galaxies, may be a matter of interpretation. Certainly they are much more extended than, for example, 1Zw18 ([van Zee et al. 1998c](#)). We

are tempted to speculate that objects such as [KK98]246 (SIGRID 68) which show extended HI regions around a much smaller stellar core (Kreckel et al. 2011) may be the precursors of these bloated objects.

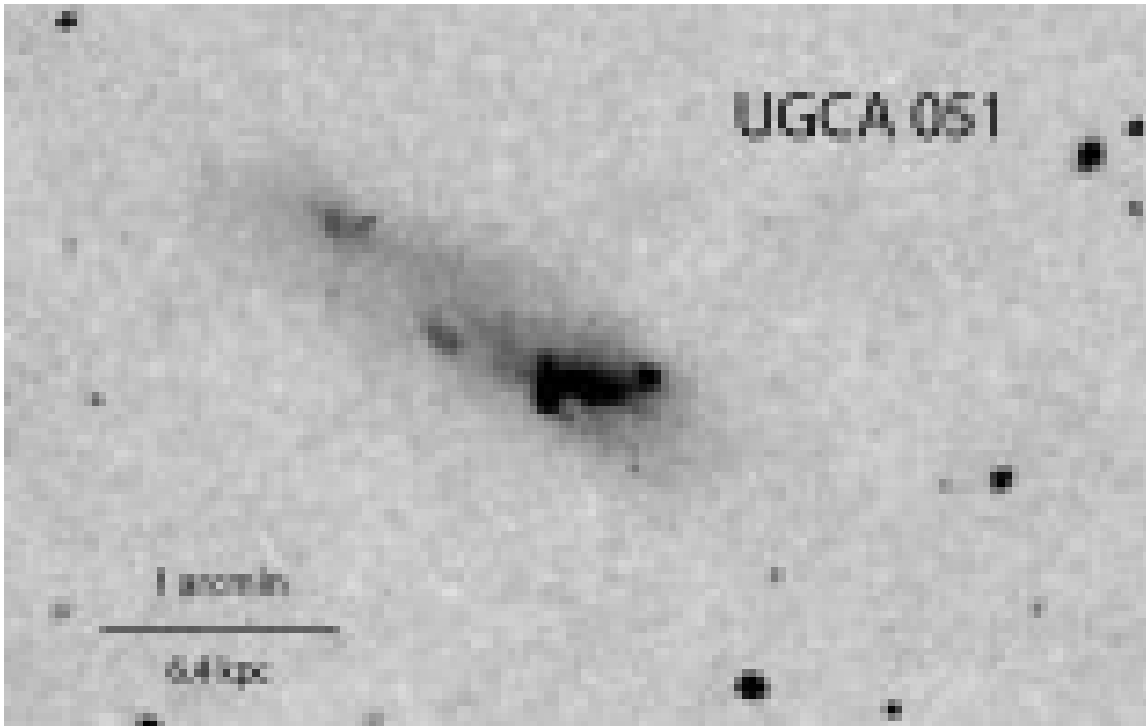


Figure 2.13 Example ‘bloater’: a dwarf irregular galaxy with absolute R-band magnitude = -16.3, $\log(H\text{ I})$ mass = $8.31(M_{\odot})$, $D = 22.2$ Mpc, which appears to have a much larger physical extent than expected. Its H I rotational velocity $w_{50} = 48.7$ km s⁻¹ suggests it is unlikely to be a large side-on galaxy.

2.13. A Blue Compact Dwarf excess?

Blue Compact Dwarf (BCD) galaxies are an important class of dwarf galaxy exhibiting current active star formation. They have attracted considerable attention over the past 30 years as they harbor examples with the lowest nebular metallicity yet recorded and also provide information on the level of primordial helium (Izotov & Thuan 2004b; Izotov et al. 2007). However, BCDs are not common among galaxy surveys (e.g. Izotov et al. 2004) and are believed to be rare in groups and clusters (Cellone & Buzzoni 2007).

First identified by Sargent & Searle (1970), BCDs have been categorised in several ways, without clear consensus on consistent parameters (Loose & Thuan 1986; Sung et al. 2002, e.g.). The simplest definition is that BCDs are “dwarf irregular galaxies whose optical presence is exemplified by active region(s) of star formation” (Sung et al. 2002). To this should be added the requirement that the galaxy and its star formation areas be centrally condensed rather than dispersed (i.e. compact). To formalise the qualitative description, Gil de Paz et al. (2003) used a quantitative approach to the classification of BCD galaxies based on stellar mass, peak surface brightness and colour. However, the formal definition of “BCD” remains to be settled.

Due to the previously accepted scarcity of BCDs, it came as a surprise that 23% of the dwarf galaxies identified in the SIGRID sample in our initial visual investigation could be

described as BCDs. Examples of two possible BCD candidates for which SINGG images are available are shown in Figures 4 and 5.

To take these visual evaluations further, a more quantitative approach such as that used by [Gil de Paz et al. \(2003\)](#) will be necessary. We also propose to refine the ‘BCD yield’ estimate by measuring ‘compactness’ analytically, e.g. as per [Cellone & Buzzoni \(2007\)](#). Although it is probable that some of these objects may not warrant the BCD classification after more careful measurement, our provisional conclusion is that using optically blind neutral hydrogen sampling methods may provide an efficient method for finding BCD galaxies.

2.14. Conclusion

We present a sample of 83 small isolated gas-rich dwarf irregular galaxies identified using their neutral hydrogen 21cm signatures and presence of star formation. The sample consists of galaxies with lower neutral hydrogen masses and lower R-band luminosities than the SMC. They are located in the southern sky with heliocentric recession velocities between 350 and 1650 km s⁻¹. We are observing these objects using the WiFeS integral field spectrograph on the ANU 2.3m telescope at Siding Spring, to measure nebular metallicities. We intend to use this data to explore the mass-metallicity relation at the low mass end of the spectrum, and to see if there is evidence for a metallicity floor in the IGM. The sample appears to include a higher percentage of Blue Compact Dwarf Galaxies than expected from other optical surveys, and a number of unusual extended dwarf objects.

CHAPTER 3

Resolving the electron temperature discrepancies in H II Regions and Planetary Nebulae: κ -distributed electrons

Just because something bears the aspect of the inevitable one should not, therefore, go along willingly with it.

Philip K. Dick, in *The Transmigration of Timothy Archer*

*This chapter was previously published as 'Resolving the electron temperature discrepancies in H II regions and Planetary Nebulae: κ -distributed electrons', Nicholls, D. C., Dopita, M. A., Jerjen, H., & Meurer, G. R. 2011, *AJ*, 142, 83. The work developed from long discussions with my thesis supervisor, Mike Dopita. The written work is my own apart from Sections 3.6.1, 3.6.2 and 3.8, which were written by Mike Dopita, and taking into account suggestions from my co-authors. Minor typographical errors have been corrected, and sections, tables and figures have been renumbered to conform with the layout of the thesis.*

3.1. Chapter summary

The measurement of electron temperatures and metallicities in H II regions and Planetary Nebulae (PNe) has—for several decades—presented a problem: results obtained using different techniques disagree. What it worse, they disagree consistently. There have been numerous attempts to explain these discrepancies, but none has provided a satisfactory solution to the problem. In this paper, we explore the possibility that electrons in H II regions and PNe depart from a Maxwell-Boltzmann equilibrium energy distribution. We adopt a “ κ -distribution” for the electron energies. Such distributions are widely found in Solar System plasmas, where they can be directly measured. This simple assumption is able to explain the temperature and metallicity discrepancies in H II regions and PNe arising from the different measurement techniques. We find that the energy distribution does not need to depart dramatically from an equilibrium distribution. From an examination of data from H II regions and PNe it appears that $\kappa \gtrsim 10$ is sufficient to encompass nearly all objects. We argue that the kappa-distribution offers an important new insight into the physics of

gaseous nebulae, both in the Milky Way and elsewhere, and one that promises significantly more accurate estimates of temperature and metallicity in these regions.

3.2. Introduction

Over forty years ago, [Vasyliunas \(1968\)](#) measured the electron energy distributions in the Earth's magnetosphere using the OGO1 and OGO3 satellites and found that there was a significant high energy ('suprathermal') excess, when compared to an equilibrium Maxwell-Boltzmann distribution. The best fit to this high energy tail was a power law. He introduced the " κ -distribution"—a generalised Lorentzian distribution—which described well the complete measured electron energy distribution.

Since then, κ -distributions have been the subject of considerable interest in Solar System physics. They have been found by direct measurement of electron energies by satellites and space probes in the outer heliosphere, the magnetospheres of all the gas-giant planets, Mercury and the moons Titan and Io, the Earth's magnetosphere, plasma sheet and magneto-sheath and in the Solar Wind (see references in [Pierrard & Lazar \(2010\)](#)). Evidence is also emerging from IBEX observations that energetic neutral atoms in the interstellar medium, where it interacts with the heliosheath, exhibit κ -distributions ([Livadiotis et al. 2011](#)). More than 5000 papers in many disciplines on the applications of κ -distributions had been published prior to 2011 ([Livadiotis & McComas 2011](#)). In Solar System plasmas, κ -distributions arise whenever the plasma is being continually pumped by an energy input of a non-thermal or supra-thermal nature, or by energy transport from elsewhere, so that the system cannot relax to a classical Maxwell-Boltzmann distribution.

To date, despite the extensive adoption of κ -distributions in analysing Solar System plasmas—where they are the rule rather than the exception—the possibility that electron energies are distributed in a non-thermal manner in the photoionised plasma of H II regions, Planetary Nebulae, or in the photoionised regions around active galaxies, does not appear to have been considered. Indeed the assumption that the electrons are in Maxwell-Boltzmann equilibrium dates back over 70 years; see for example, [Hebb & Menzel \(1940\)](#).

There are good reasons to question the basis on which temperatures and metallicities are measured in H II regions and PNe: for example, there have been consistent discrepancies between direct electron temperature (T_e) estimates and those obtained using recombination lines. None of the earlier attempts to solve the problem is fully satisfactory—for example, the " t^2 " temperature fluctuation method, ([Peimbert 1967](#))—and some have been completely abandoned ([Stasińska 2004](#)).

In this paper, we explore the implications of electron energies following a κ -distribution in these photoionised plasmas. We show that assuming a κ - electron energy distribution is a simple and elegant way to resolve many of the difficulties, and should lead to more consistent temperature measurements and metallicity estimates in H II regions and PNe.

The paper is organised as follows. In Section 3.3 we provide the key definitions and formulae for the κ -distribution. In Section 3.4 we show that there is a sound basis for H II regions and PNe having κ -distributed electrons. In Section 3.5 we examine the dependence of collisional excitation rates on excitation energy and the value of κ , and apply this to a detailed study

of the particular case of the [O III] $\lambda\lambda(4949 + 5007)/4363$ line ratio, the most important ratio used in the determination of electron temperatures in photoionised plasmas. In Section 3.6 we examine the observational data from H II regions and Planetary Nebulae to discover how well the value of κ can be constrained by requiring that different methods of measuring the electron temperature yield the same answer. Appendix (A) presents additional evidence for the presence of magnetic fields in H II regions which can give rise to hot-tailed electron energy distributions. In Appendix (B), we examine the relationship between the “ t^2 ” method for measuring the effect of temperature fluctuations and the κ -distribution.

3.3. The κ -distribution

3.3.1. Properties and Definitions

Initially, κ -distributions were used as an empirical fit to directly measured electron energies in Solar System plasmas, and were criticised as lacking a theoretical basis. More recently, the distribution has been shown to arise from entropic considerations. See, for example, [Tsallis et al. \(1995\)](#); [Treuermann \(1999\)](#); [Leubner \(2002\)](#), and the comprehensive analysis by [Livadiotis & McComas \(2009\)](#). They explored the so-called q -nonextensive entropy statistics in which the entropies of adjacent samples of plasma are not simply additive, and have shown that κ -energy distributions arise naturally in such plasmas. The requirement for this to occur is that there be long-range interactions between particles, in addition to the short-range Coulombic forces that give rise to Maxwell-Boltzmann equilibration. Although there is ongoing debate over whether the Tsallis statistical mechanics is the best generalisation of Boltzmann-Gibbs statistics, it provides a sound physical basis for the overtly successful use of the κ -distribution in plasma physics.

There are a number of slightly differing expressions for the energy distributions that can arise from q -nonextensive entropy, but the forms are generally similar. Here we adopt the Vasyliunas form of the distribution as representative of the possible variants. This is referred to by [Livadiotis & McComas \(2009\)](#) as a κ -distribution of the “second kind”. The successful use of the κ -distributions to describe physical phenomena in many disciplines, and especially in Solar System physics, provides ample justification for exploring their use in H II regions and PNe.

The κ -velocity distribution can be expressed (after Vasyliunas, 1968) as:

$$n(v)dv = \frac{4N}{\sqrt{\pi}w_0^3} \left(\frac{\Gamma(\kappa + 1)}{\kappa^{3/2}\Gamma(\kappa - \frac{1}{2})} \right) \frac{v^2}{(1 + v^2 / [(\kappa - \frac{3}{2})w_0^2])^{\kappa+1}} dv, \quad (3.1)$$

where $n(v)$ is the number of electrons with speeds between v and $v + dv$. The velocity w_0 is related to w_{mp} , the most probable speed (i.e. the velocity value at the distribution peak) by:

$$w_0 = w_{mp} \sqrt{\frac{\kappa}{(\kappa - \frac{3}{2})}}. \quad (3.2)$$

and related to the “physical temperature” of the system, T_U , as defined in [Livadiotis & McComas \(2009\)](#):

$$w_0 = \sqrt{\frac{2k_B T_U}{m_e}}, \quad (3.3)$$

where m_e is the electron mass and k_B is the Boltzmann constant.

κ is a parameter that describes the extent to which the distribution departs from an equilibrium distribution. In the Vasyliunas form, $\frac{3}{2} < \kappa \leq \infty$. In the limit as $\kappa \rightarrow \infty$, the velocity distribution reverts to the standard Maxwell-Boltzmann (M-B) form,

$$n(v)dv = \frac{4N}{\sqrt{\pi}w_0^3}v^2 \exp\left[-\frac{v^2}{w_0^2}\right]dv. \quad (3.4)$$

The physical temperature, T_U , also referred to as the kinetic temperature, is a generalisation of the Maxwell-Boltzmann equilibrium temperature, and is related to the energy density (system kinetic energy), U , which for a monatomic gas is the internal energy of the system:

$$U = \frac{3}{2}k_B T_U. \quad (3.5)$$

Figure 3.1 shows a family of κ -velocity distributions with a M-B distribution.

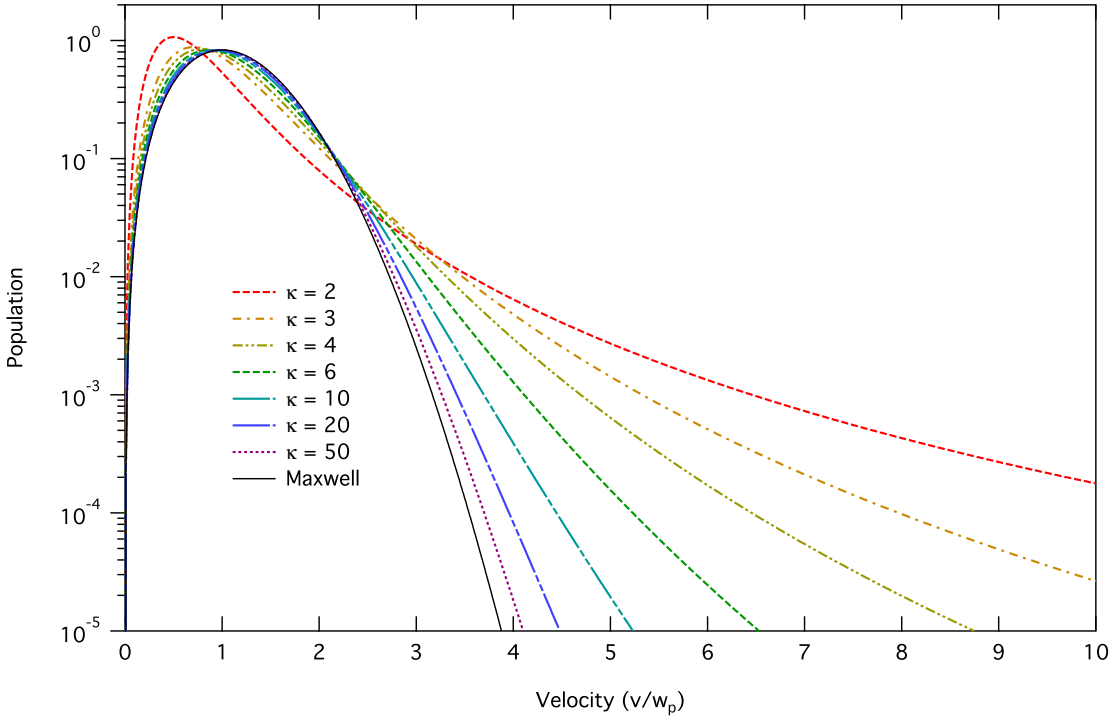


Figure 3.1 κ -velocity distributions (log scale) for κ from 2 to 50, with Maxwell-Boltzmann distribution.

Expressed in energy terms, the κ -distribution becomes:

$$n(E)dE = \frac{2N}{\sqrt{\pi}} \left(\frac{\Gamma(\kappa + 1)}{(\kappa - \frac{3}{2})^{3/2} \Gamma(\kappa - \frac{1}{2})} \right) \frac{\sqrt{E}}{(k_B T_U)^{3/2} (1 + E/[(\kappa - \frac{3}{2})k_B T_U])^{\kappa+1}} dE. \quad (3.6)$$

Again, the κ -energy distribution tends in the limit as $\kappa \rightarrow \infty$ to the Maxwell-Boltzmann,

$$n(E)dE = \frac{2N}{\sqrt{\pi}} \frac{\sqrt{E} \exp[-E/k_B T]}{(k_B T)^{3/2}} dE. \quad (3.7)$$

A family of normalised κ -energy distributions is shown in Figure 3.2, together with a Maxwell-Boltzmann (M-B) equilibrium distribution. Note that the peak of the M-B energy

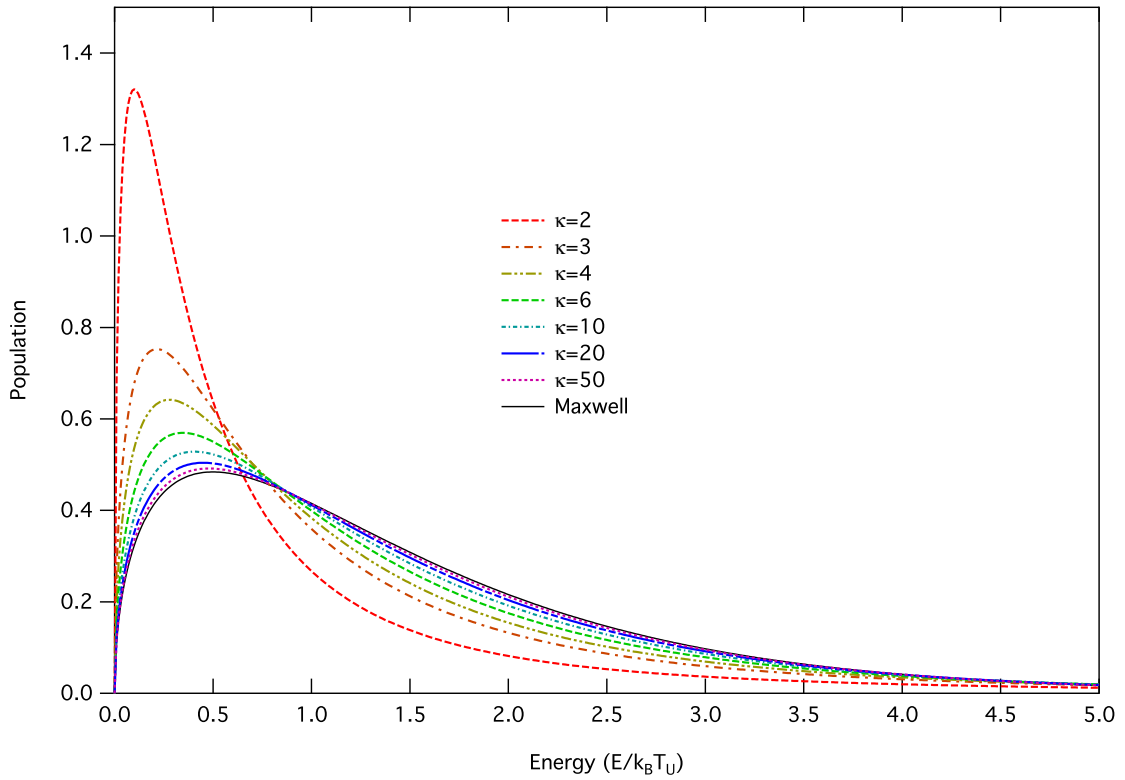


Figure 3.2 κ - energy distributions (linear scale) for κ from 2 to 50, with Maxwell-Boltzmann distribution.

distribution occurs at $E = \frac{1}{2}k_B T_U$ whereas κ -distributions with the same internal energy peak at $E = \frac{1}{2}k_B T_U (2\kappa - 3)/(2\kappa + 1)$.

The same distributions are shown in Figure 3.3 but plotted on a log scale. The high energy power-law tail of the κ -distributions is clearly shown.

Figures 3.1–3.3 illustrate the key characteristics of the κ -distribution: the peak of the distribution moves to lower energies; at intermediate energies there is a population deficit relative to the M-B distribution; and at higher energies the “hot tail” again provides a population excess over the M-B. The κ distribution behaves as a M-B distribution at a lower temperature, but with a significant high energy excess.

This can be seen in Figure 3.4, where a M-B distribution is peak-fitted to a $\kappa=2$ distribution. The peak-fitted “core” M-B distribution is in fact at a lower physical temperature than the κ -distribution to which it is fitted. The relationship between the physical temperature of the κ -distribution, T_U , and the equilibrium temperature of the “core” M-B, T_{core} , as implied by equation 3, is:

$$T_{core} = T_U \left(\frac{\kappa - \frac{3}{2}}{\kappa} \right). \quad (3.8)$$

For physical processes that involve low energy electrons such as recombination line excitation, reactions “see” the cool M-B core distribution. In other words, any physical property sensitive to the region of the electron energy distribution around or below the distribution peak will interact with an effective M-B electron energy distribution at a lower temperature than the M-B distribution with the same total internal energy as the κ -distribution.

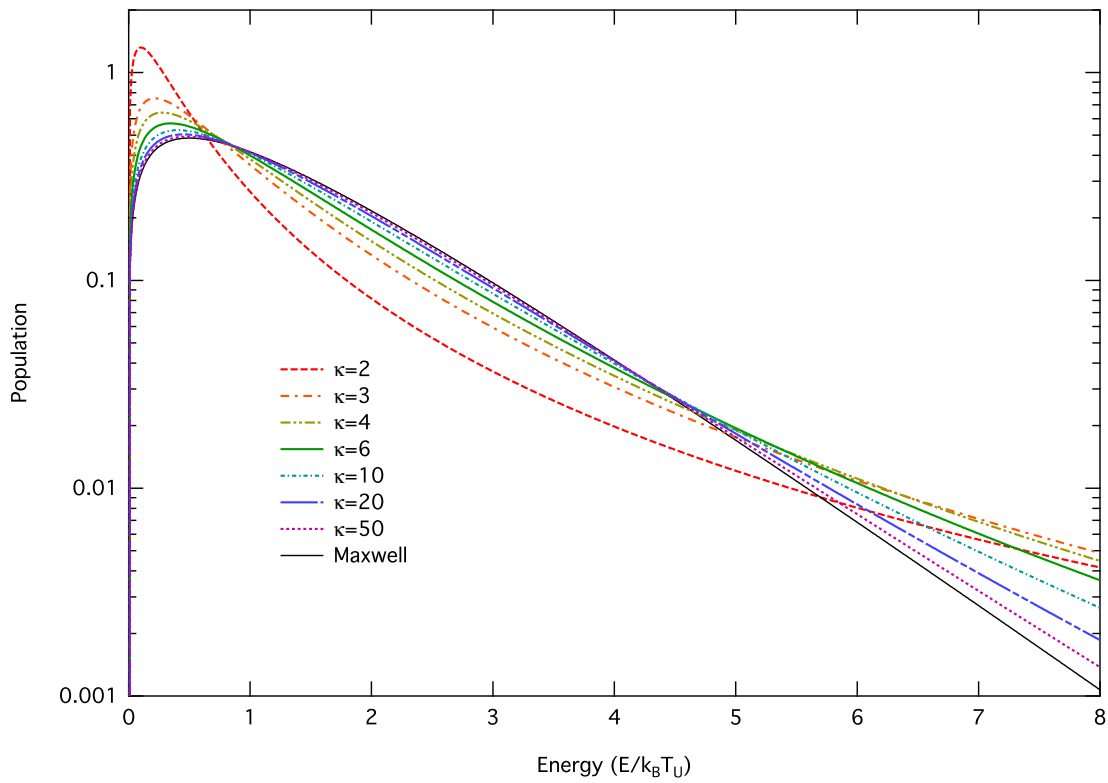


Figure 3.3 κ -energy distributions (log scale) for κ from 2 to 50, with Maxwell-Boltzmann distribution.

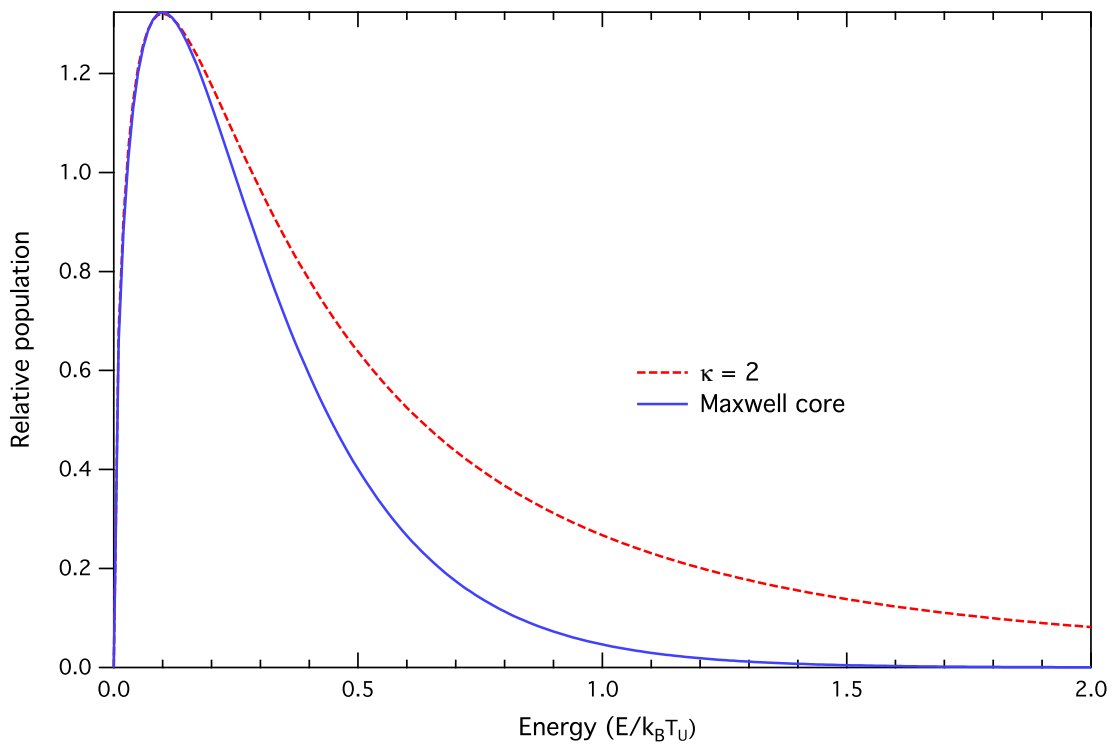


Figure 3.4 $\kappa = 2$ energy distribution with peak-fitted Maxwell-Boltzmann distribution core.

Conversely, in processes that depend on the high energy end of the distribution, such as collisional line excitation, the κ -distribution behaves like a M-B distribution at a higher temperature than one with the same total internal energy. In other words, physical properties sensitive to energies above the peak will behave as if they were interacting with a hotter distribution. The κ -distribution thus exhibits a “split personality”, depending on the physical process involved. We show below that this behaviour resolves many of the discrepancies between different nebular temperature measurement techniques.

3.4. What might give rise to κ -distributions in H II regions?

Given the plausibility of κ -distributions in H II regions, can we find mechanisms capable of maintaining the hot tails? The answer is, clearly, yes. A high-energy tail in the energy distribution will occur whenever the population of energetic electrons is being pumped in a timescale as short, or of the same order, as the energy re-distribution timescale of the electron population. Such effects may be long-range in nature, such as magnetic reconnection followed by the migration of high-energy electrons along field lines, and by the development of Inertial Alfvén Waves. We explore additional evidence for the existence of magnetic fields in galactic H II regions in Appendix A1.

Pumping of high energy tails can also be more local in character such as local shocks (driven either by the collision of bulk flows or by supersonic turbulence), or, most simply, by the injection of high-energy electrons through the photoionisation process itself. Normal photoionisation produces supra-thermal electrons on a timescale similar to the recombination timescale.

Energetic electrons can also be generated by the photoionisation of dust (Dopita & Sutherland 2000). Alternatively, X-ray ionisation can produce highly energetic (\sim keV) inner-shell (Auger process) electrons (e.g. Shull & van Steenberg (1985); Aldrovandi & Gruenwald (1985); Petrini & da Silva (1997), and references therein). Processes based on photoionisation should become more effective where the source of the ionising photons has a “hard” photon spectrum. Thus, the likelihood of the ionised plasma having a κ -electron energy distribution would be high in the case of either photoionisation by an Active Galactic Nucleus (AGN), or the case of PNe, in which the effective temperature of the exciting star could range up to \sim 250,000 K.

Thus, we have no shortage of possible energy injection mechanisms. The main consideration is whether feeding the energetic population can occur on a timescale which is short compared with the collisional re-distribution timescale, τ . Because this timescale increases very rapidly with energy, $\tau \propto \exp(E^{3/2})$, we would expect there to be a threshold energy above which any non-thermal electrons have a long residence timescale. These can then feed continually down towards lower energies, maintaining a κ -electron energy distribution. It seems more likely therefore that *all* photoionised plasmas will show departures from a Maxwell-Boltzmann distribution to some degree. The key question is, is this departure important, and does it produce observable effects in the plasma diagnostics on which we have relied upon hitherto? Again, yes, as we show in Section (4) below.

3.4.1. Are κ -distributions stable in their own right?

In addition to the energy injection mechanisms capable of maintaining the excitation of suprathermal distributions, several authors (Livadiotis & McComas (2011) and references therein; Shizgal (2007); Treumann (2001)) have investigated the possibility that the κ -distribution may remain stable against thermalisation longer than conventional thermalisation considerations would suggest (e.g. Spitzer (1962)). In particular, distributions with $2.5 \gtrsim \kappa > 1.5$ appear to have the capacity, through increasing entropy, of moving to values of lower κ (Livadiotis & McComas 2011) i.e. away from (Maxwell-Boltzmann) equilibrium. While the physical application of this aspect of κ -distributions remains to be explored fully, it suggests that where q -nonextensive entropy conditions operate, the suprathermal energy distributions produced exist in "stationary states" where the behaviour is, at least in the short term, time-invariant (Livadiotis & McComas 2010). These states may have longer lifetimes than expected classically. This is fully consistent with the numerous observations that in Solar System plasmas, κ - electron and proton energy distributions are the norm. It seems reasonable to expect that such conditions will also be present in H II regions and PNe.

3.5. The effect of κ -distributions on collisional excitation in H II regions

3.5.1. Collisional excitation rates

Consider the collisional excitation of an atomic species from energy level 1 to energy level 2. The rate of collisional population of the upper energy level per unit volume is given in terms of the collision cross-section, $\sigma_{12}(E)$, by:

$$R_{12} = n_e N_1 \int_{E_{12}}^{\infty} \sigma_{12}(E) \sqrt{\frac{2E}{m_e}} f(E) dE . \quad (3.9)$$

We separate out the strong energy dependence of the collision cross-section $\sigma_{12}(E)$, by expressing it in terms of the collision strength, Ω_{12} and the energy, E :

$$\sigma_{12}(E) = \left(\frac{h^2}{8\pi m_e E} \right) \frac{\Omega_{12}}{g_1} , \quad (3.10)$$

where h is the Planck Constant, m_e is the electron mass, and g_1 is the statistical weight of the lower energy state.

The collisional population rate now becomes:

$$R_{12} = n_e N_1 \frac{h^2}{8\pi m_e g_1} \sqrt{\frac{2}{m_e}} \int_{E_{12}}^{\infty} \frac{\Omega_{12}}{\sqrt{E}} f(E) dE , \quad (3.11)$$

where the appropriate form of the distribution is substituted, giving the well-known collisional population rate formula for a Maxwell-Boltzmann distribution:

$$R_{12}(\text{M} - \text{B}) = \frac{n_e N_e}{g_1} \frac{h^2}{(2\pi m_e k_B T_U)^{3/2}} \int_{E_{12}}^{\infty} \Omega_{12}(E) \exp\left[-\frac{E}{k_B T_U}\right] dE \quad (3.12)$$

For a κ -distribution, the corresponding rate is:

$$R_{12}(\kappa) = \frac{n_e N_e}{g_1} \frac{h^2}{(2\pi m_e k_B T_U)^{3/2}} \frac{\Gamma(\kappa + 1)}{(\kappa - \frac{3}{2})^{3/2} \Gamma(\kappa - \frac{1}{2})} \int_{E_{12}}^{\infty} \frac{\Omega_{12}}{(1 + E/[(\kappa - \frac{3}{2})k_B T_U])^{\kappa+1}} dE. \quad (3.13)$$

Adopting the approximation that Ω_{12} is independent of energy, the integral parts of the above equations (after taking a $k_B T_U$ factor outside the integrals) reduce to:

$$\exp\left[-\frac{E_{12}}{k_B T_U}\right] \quad (3.14)$$

and

$$\left(1 - \frac{3}{2\kappa}\right) \left(1 + \frac{E_{12}}{(\kappa - \frac{3}{2})k_B T_U}\right)^{-\kappa}, \quad (3.15)$$

respectively. Note that in the limit as $\kappa \rightarrow \infty$, equation (3.15) transforms into equation (3.14), as it should.

It is useful to compare the relative rates of population to an upper state for M-B and κ -distributions. Taking equations (3.12) and (3.13) and assuming constant Ω s, we can derive an analytical equation that expresses the ratio of the population rates:

$$\frac{R_{12}(\kappa)}{R_{12}(\text{M-B})} = \frac{\Gamma(\kappa + 1)}{(\kappa - \frac{3}{2})^{3/2} \Gamma(\kappa - \frac{1}{2})} \left(1 - \frac{3}{2\kappa}\right) \exp\left[\frac{E_{12}}{k_B T_U}\right] \left(1 + \frac{E_{12}}{(\kappa - \frac{3}{2})k_B T_U}\right)^{-\kappa}. \quad (3.16)$$

Figure 3.5 shows the effect of equation (3.16) in the enhancement of the collisional excitation rate for $\kappa: 2 \rightarrow 100$ compared to the Maxwell-Boltzmann rate for an electron distribution having the same internal energy. Very similar curves were obtained by [Owocki & Scudder \(1983\)](#) in the context of collisional ionisation rates in the solar corona. Data for Figure 3.5 for an extended energy ratio range are given in Table 3.2.

The implication is that collisionally excited UV lines—with higher excitation energies—should show strong enhancements compared to standard theory, while lines in the optical and IR would be relatively little changed, unless the region has a low kinetic temperature. Collisionally excited lines of un-ionised species such as [O I] $\lambda\lambda 6300, 63$ or [N I] $\lambda\lambda 5198, 5200$ will be differently affected, since the collision strength has a strong energy dependence, increasing above threshold. For these ions the degree of enhancement in the collisional excitation rate compared with the Maxwell-Boltzmann case will be much larger than shown in Figure 3.6. This could explain a long-standing problem in H II region models, which tend to systematically underestimate the strength of these lines, compared to observations. New data on the collision strengths of OI and NI, in the context of the κ -distribution, has implications for using the lines of these neutral species as low-temperature diagnostics in partially ionised regions. We will explore this in a future paper.

3.5.2. Effect of κ on [O III] electron temperatures

The direct method of estimating electron temperature in H II regions relies on measuring the flux ratios of different excited states from the same atomic species. Most often used are collisional excitation to the 1D_2 and 1S_0 states of [O III], which give rise to the forbidden

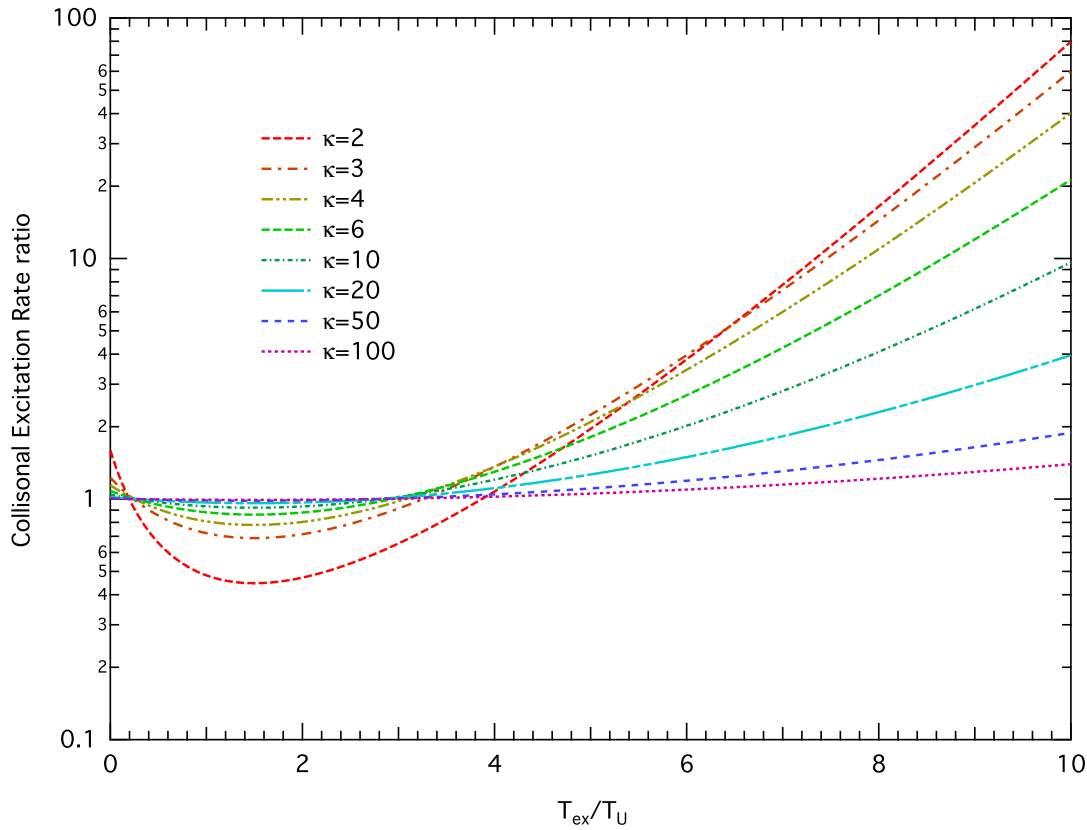


Figure 3.5 The collisional excitation enhancement ratio over a Maxwell-Boltzmann distribution for different κ -distributions plotted as a function of the excitation threshold energy (expressed as an equivalent temperature) over the kinetic temperature T_U , equation (3.16). For the κ -distributions very large enhancements in the collisional excitation rate are possible for high values of T_{ex}/T_U . (Extended data in Table 3.2)

nebular lines at 5007Å and 4959Å, and the “auroral” line at 4363Å. Lines of [O II], [N II], [S II], [Ne III], [Ar III] and [S III] are also used, when the relevant lines can be observed. The threshold excitation energies for the upper states in these species are different, so the degree of enhancement in a κ -distribution of electrons will differ from one ion to the next. This fact provides a possible resolution of the discrepancies encountered when measuring temperatures using these different atomic species.

As a specific and important example, we consider here the excitation of the O III ion. For reference, the configuration of the lower states which give rise to the forbidden lines used in temperature determinations is illustrated in Figure 3.6. The threshold excitation temperatures of the excited states are 29,130 K (1D_2) and 62,094 K (1S_0). For a κ -distribution at temperature $T_U = 10,000$ K from Figure 3.5 the excitation rate to the lower state will be little changed, while the collision excitation rate to the upper state will be strongly enhanced, leading to an overestimate of the true electron temperature computed by formulae such as given by Osterbrock & Ferland (2006). We now proceed to quantify this remark.

For an equilibrium electron energy distribution, the relative population rates can be calculated using equation (3.11) for the upper and lower excited states. If one assumes for simplicity that the Ω values are energy-independent, the ratio of the two population rates in the M-B case is simply:

$$\frac{R_{13}}{R_{12}} = \frac{\Omega_{13}}{\Omega_{12}} \exp\left[-\frac{E_{23}}{k_B T_U}\right]. \quad (3.17)$$

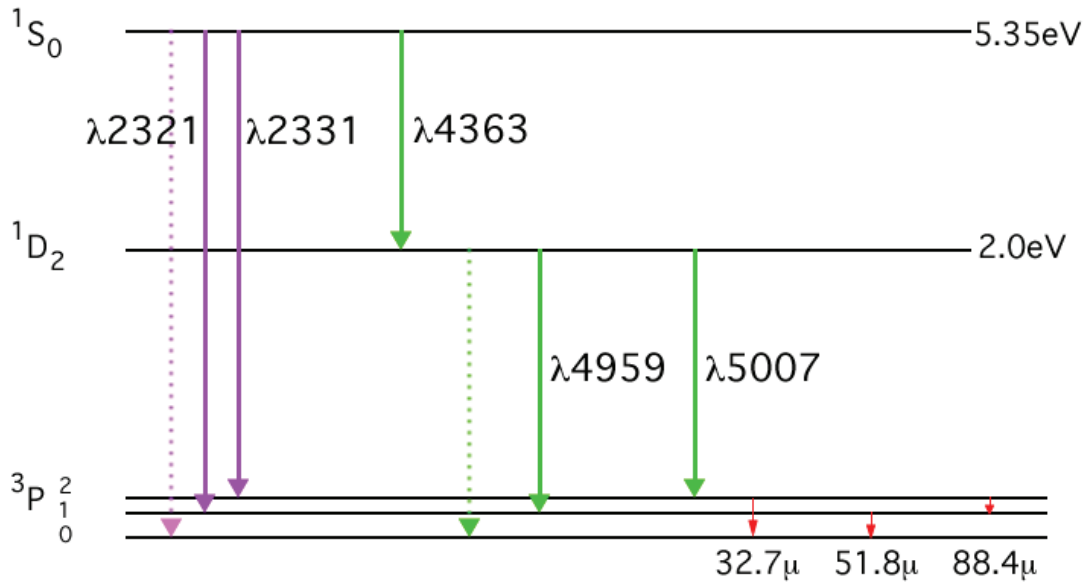


Figure 3.6 The lower energy levels and forbidden transitions for the O III ion.

In a more accurate analysis, the collision strength Ω is integrated over the energy range E_{12} to ∞ as per equation (3.11), to give the effective (temperature averaged) collision strength, Υ .

Allowing for other transitions from the $1S_0$ state via the branching ratio and correcting for the energies of the two lower state transition photons, the ratio of the fluxes of the ($\lambda 5007 + \lambda 4959$) to $\lambda 4363$ give a direct measure of the population rates to the two excited states, and therefore of the electron temperature of the energy distribution. Following Osterbrock & Ferland (2006) we can derive a simple equation for the electron temperature, T_e , in terms of the line fluxes, for low density plasmas:

$$\frac{j_{5007} + j_{4959}}{j_{4363}} = 7.90 \exp\left[\frac{32900}{T_e}\right]. \quad (3.18)$$

This formula is, of course, an approximation, as it assumes the values Ω_{12} and Ω_{13} (and therefore of Υ_{12} and Υ_{13}) do not depend on temperature. A more accurate iterative formula was given by Izotov et al. (2006). Values of the effective collision strength Υ assuming constant Ω differ slightly from those computed numerically, taking into account the detailed collisional cross section resonances. To identify what effect this would have on determining the electron temperature, we compared electron temperatures derived using constant Ω , the Izotov iterated formula, and the values computed using the detailed collision strengths from Lennon & Burke (1994) and Aggarwal (1993).

Figure 3.7 shows the relationship between the flux ratio and the electron temperature, using the Osterbrock equation, the Izotov iteration and computed numerically from the Lennon & Burke (1994) and Aggarwal (1993) Ω data. (The values in most common use for Υ_{12} are those published by Lennon & Burke (1994), available online via TIPbase (Hummer et al. 1993); or the data from Aggarwal & Keenan (1999), but the latter are only available in abbreviated tabular form.)

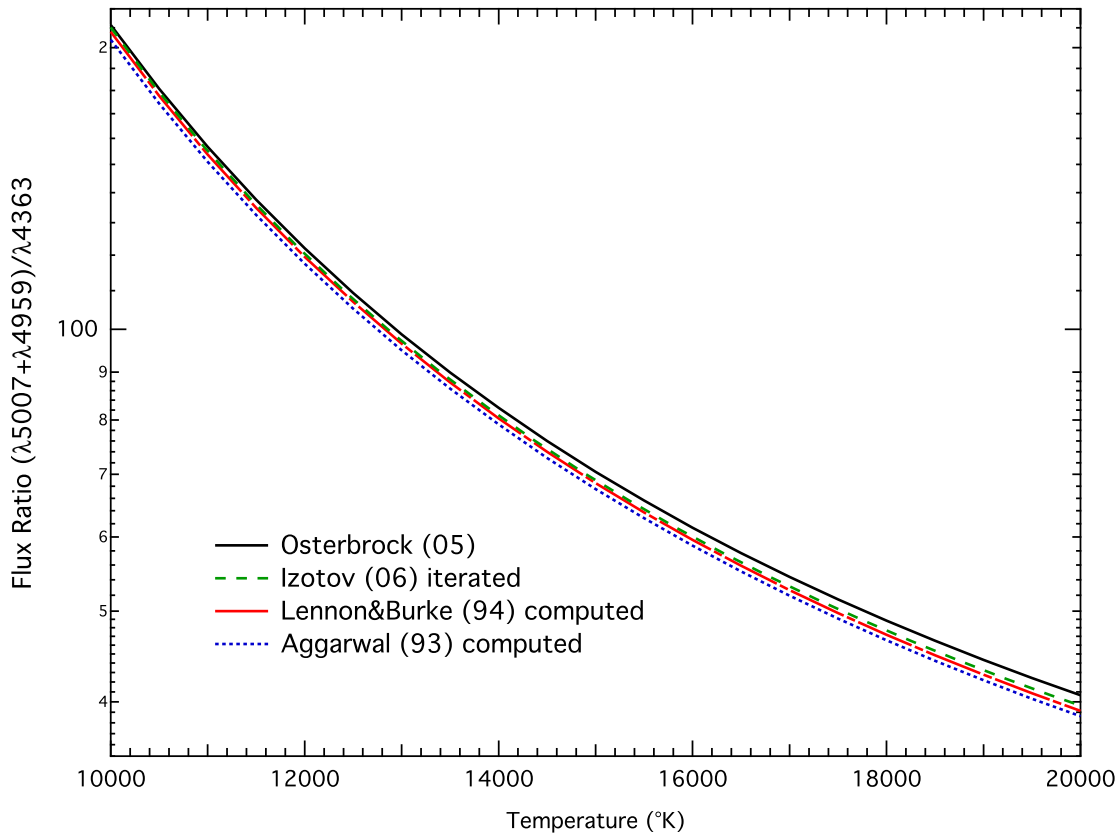


Figure 3.7 [O III] line flux ratio versus temperature for M-B distributed electrons computed from different methods and by different authors

For M-B energy distributions, the use of a constant Ω gives a slightly higher T_e than is obtained using the [Lennon & Burke \(1994\)](#) data, and higher still compared to the data from [Aggarwal \(1993\)](#). At an equilibrium temperature of 20,000 K, the difference between the Izotov value and the L&B data is 130 K and for the Aggarwal data, 285 K.

These differences are of minor import. An altogether different result occurs when we use a κ -distribution instead of the M-B to calculate the line ratio versus T_U graph. The results are shown in [Figure 3.8](#). For $\kappa=100, 50, 20,$ and 10 the kinetic temperature differences from the M-B equilibrium value at $T_U=20,000$ K are 180 K, 385 K, 980 K and 2,100 K. Data for the extended temperature range 5,000 to 20,000 K are given in [Table 3.1](#). The data are calculated using the detailed collision efficiencies (from [Lennon & Burke \(1994\)](#)), but assuming constant Ω s makes very small differences for $\kappa > 6$.

As can be seen in [Figures 3.2 and 3.3](#), these values of κ are visually relatively minor deviations from the M-B distribution, but they have a considerable effect. This implies that even κ -distributions which diverge slightly from equilibrium can have a significant effect on electron temperatures measured using the [O III] lines. The same result is true for other collisionally excited lines, [O II], [S II] and [N II], but to differing extents, owing to the different collisional excitation energy thresholds for the upper and lower states. The differences in apparent electron temperatures calculated using different collisionally excited species allow us to obtain an estimate of the effective value of κ for remote H II regions, as we show in [Section \(2.5\)](#) below.

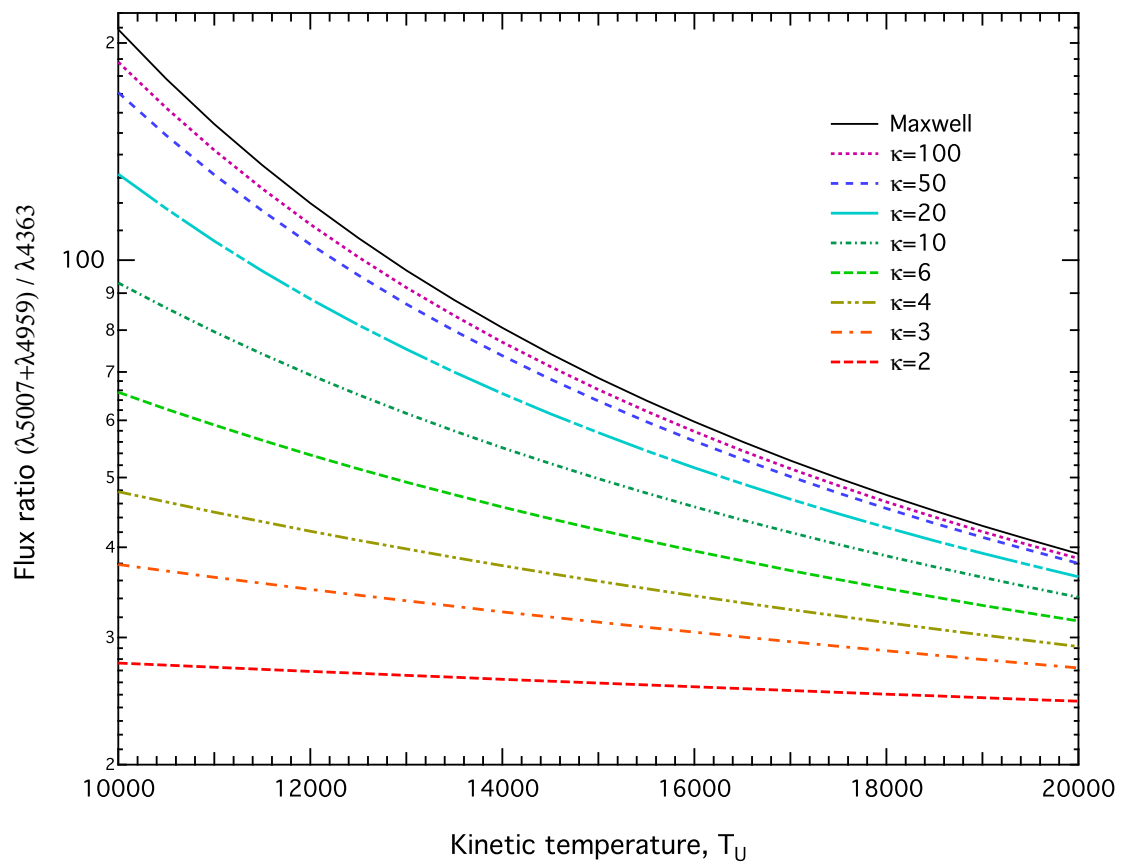


Figure 3.8 [O III] line flux ratio versus kinetic temperature for the range $\kappa = 2 \rightarrow 100$, compared to the computed [Lennon & Burke \(1994\)](#) equilibrium data, labeled Maxwell in the figure. (Extended data in Table 3.1)

Table 3.1 O III Line flux ratios vs kinetic temperature T_U —see Figure 3.8

T_U (K)	$\kappa = 2$	$\kappa = 3$	$\kappa = 4$	$\kappa = 6$	$\kappa = 10$	$\kappa = 20$	$\kappa = 50$	$\kappa = 100$	Maxwell ¹
5000	29.7012	48.1983	72.5995	138.179	322.942	914.582	2365.64	3551.70	5678.96
5500	29.4789	46.8930	69.0278	125.368	270.262	674.143	1513.02	2121.70	3117.32
6000	29.2609	45.6613	65.7814	114.480	229.899	515.460	1032.33	1372.76	1891.11
6500	29.0469	44.4974	62.8208	105.148	198.350	406.285	741.598	945.508	1238.84
7000	28.8369	43.3962	60.1122	97.0852	173.257	328.495	555.442	684.565	861.973
7500	28.6308	42.3530	57.6269	90.0701	152.988	271.388	430.514	516.106	629.358
8000	28.4285	41.3637	55.3402	83.9261	136.389	228.376	343.322	402.263	477.847
8500	28.2299	40.4242	53.2305	78.5127	122.629	195.251	280.418	322.330	374.680
9000	28.0348	39.5313	51.2794	73.7162	111.094	169.241	233.734	264.362	301.772
9500	27.8433	38.6815	49.4707	69.4446	101.329	148.467	198.235	221.147	248.601
10000	27.6551	37.8721	47.7904	65.6223	92.9877	131.622	170.664	188.154	208.767
10500	27.4702	37.1003	46.2259	62.1868	85.8035	117.779	148.851	162.440	178.225
11000	27.2886	36.3637	44.7665	59.0863	79.5699	106.266	131.311	142.033	154.330
11500	27.1102	35.6602	43.4024	56.2774	74.1239	96.5858	117.002	125.577	135.302
12000	26.9348	34.9875	42.1252	53.7234	69.3362	88.3683	105.179	112.119	119.912
12500	26.7623	34.3438	40.9273	51.3936	65.1029	81.3305	95.2955	100.973	107.292
13000	26.5928	33.7274	39.8019	49.2613	61.3397	75.2547	86.9487	91.6369	96.8137
13500	26.4262	33.1366	38.7429	47.3043	57.9780	69.9709	79.8335	83.7378	88.0182
14000	26.2623	32.5699	37.7450	45.5029	54.9612	65.3451	73.7166	76.9927	80.5612
14500	26.1012	32.0260	36.8034	43.8406	52.2424	61.2705	68.4173	71.1849	74.1819
15000	25.9426	31.5035	35.9135	42.3027	49.7824	57.6609	63.7940	66.1462	68.6799
15500	25.7867	31.0013	35.0715	40.8766	47.5483	54.4468	59.7342	61.7444	63.8991
16000	25.6333	30.5183	34.2739	39.5513	45.5125	51.5708	56.1483	57.8745	59.7166
16500	25.4823	30.0534	33.5173	38.3170	43.6512	48.9858	52.9635	54.4524	56.0347
17000	25.3338	29.6057	32.7988	37.1652	41.9444	46.6528	50.1207	51.4099	52.7748
17500	25.1876	29.1742	32.1158	36.0884	40.3747	44.5389	47.5714	48.6915	49.8733
18000	25.0437	28.7582	31.4658	35.0798	38.9272	42.6167	45.2751	46.2514	47.2781
18500	24.9020	28.3569	30.8466	34.1336	37.5891	40.8628	43.1986	44.0517	44.9463
19000	24.7625	27.9695	30.2562	33.2444	36.3492	39.2574	41.3137	42.0609	42.8424
19500	24.6252	27.5953	29.6926	32.4074	35.1975	37.7835	39.5966	40.2524	40.9365
20000	24.4900	27.2337	29.1543	31.6185	34.1256	36.4266	38.0273	38.6038	39.2038

¹ Maxwell figures computed using Lennon & Burke (1994) Ω data.

3.6. The Determination of κ

3.6.1. H II regions

As noted earlier, a κ -distribution with kinetic temperature T_U can be characterised at low electron energies below the peak of the distribution by a Boltzmann distribution with an effective temperature $T_B = (\kappa - 3/2)T_U/\kappa$. Since T_B ($\equiv T_{core}$ in Figure 3.4) is systematically lower than T_U , and as it is the energy distribution of these low-energy electrons that determines the recombination temperature ($T_{rec} \equiv T_B$), it is clear that in a κ -distribution the recombination rate is systematically enhanced. These same low-energy electrons also determine the size of the Balmer and Paschen discontinuities of Hydrogen, so that the measured Balmer and Paschen break temperatures will reflect T_B , rather than T_U .

At the same time, lines with excitation temperatures comparable to T_U may be either mildly enhanced or suppressed in a κ -distribution, but lines with excitation temperatures well above T_U are strongly enhanced by the power-law tail of high energy electrons present in the κ -distribution. As shown earlier, the effect of this is to enhance the apparent electron temperature inferred using well-known temperature-sensitive line ratios such as [O III] 4363Å/5007,4959Å , [S II] 4069,76Å/6717,31Å , [N II] 5755Å/6548,84Å or [O II] 7318,24Å/3726,29Å . However, the degree of enhancement of the inferred temperature compared with T_U is strongly dependent on the excitation temperature, T_{ex} , of the upper levels involved in these transitions. Those ions in which T_{ex} is much greater than T_U will have their inferred collisional excitation temperature, T_{CEL} , very strongly enhanced over T_U , while those for which T_{ex} is comparable to T_U will show little change ($T_{CEL} \sim T_U$).

These properties of the κ -distribution can be used as the basis for the determination of κ from spectrophotometric observations of both H II regions and Planetary Nebulae. Indeed, precisely these kinds of temperature discrepancies between the various ions has been observed in both classes of objects; the recombination temperatures (derived from the Balmer and Paschen jumps) are systematically lower than temperatures derived from collisionally excited line ratios.

Systematic differences in temperature are also observed between collisionally excited line ratios of different ionic species (García-Rojas & Esteban 2007; Izotov et al. 2006). This results in systematically different chemical abundances derived by optical recombination lines (ORLs) and collisionally excited lines (CELs), a problem dating back to Wyse (1942), and first discussed in detail by Torres-Peimbert & Peimbert (1977). There are also systematic differences between abundances determined using either direct measurements of ionic temperatures, correcting observed ionic abundances for unseen ionisation stages (the T_e method) or using the intensities of strong emission lines relative to the Hydrogen recombination lines (the strong line method). These issues are collectively known as the abundance discrepancy problem (García-Rojas et al. 2006; García-Rojas & Esteban 2007).

The confusion surrounding this issue has been well summarised by Stasińska (2004):

“It has been known for several decades that optical recombination lines [ORL] in PNe and H II regions indicate higher abundances than collisionally excited lines [CEL]. ... The ORL abundances are higher than CEL abundances by

factors of about 2 for most PNe, discrepancies over a factor 5 are found in about 5% of the PNe and can reach factors as large as 20. For a given nebula, the discrepancies for the individual elements C,N,O,Ne are found to be approximately of the same magnitude.

The explanations most often invoked are: i) temperature fluctuations, ii) incorrect atomic data, iii) fluorescent excitation, iv) upward bias in the measurement of weak line intensities, v) blending with other lines, vi) abundance inhomogeneities. None of them is completely satisfactory, some are now definitively abandoned."

The possibility that the abundance discrepancy problem could be generated by the techniques of measurement was recently investigated by [López-Sánchez et al. \(2012\)](#) using a grid of theoretical models to eliminate any systematics of observational errors. Although systematic errors were found in a number of empirical strong line techniques, the classical electron temperature + ionisation correction factor technique works surprisingly well. Clearly this technique itself is not at fault.

Perhaps the most successful attempt to account for the abundance discrepancy problem has been to postulate the existence of small-scale temperature fluctuations as first proposed by [Peimbert & Costero \(1969\)](#) and applied widely since; see *e.g.* [Peimbert \(2003\)](#) and references therein. In some sense electron temperature fluctuations (if real) act in a similar way to a κ -distributed electron population, in that both weight CELs towards higher temperature. However, we are missing an obvious physical explanation of why micro-fluctuations in temperature should exist and persist in the first place. The relationship between that approach and the κ -distribution is explored further in Appendix (B).

We can test the κ -distribution hypothesis using the excellent echelle spectrophotometry which has been gathered by a number of authors in recent years. For Galactic H II regions we have data in M 42 ([Esteban et al. 2004](#)), NGC 3576 ([García-Rojas et al. 2004](#)), S311 ([García-Rojas et al. 2005](#)), M20 & NGC 3603 ([García-Rojas et al. 2006](#)), M 8 & M 17 ([García-Rojas & Esteban 2007](#)). For the extragalactic H II regions we have data for 30 Dor ([Peimbert 2003](#)), NGC595 ([López-Sánchez et al. 2007](#)), NGC 595, NGC 604, VS 24, VS 44, NGC 2365 and K 932 ([Esteban et al. 2009](#)).

One of the strongest tests of the validity of the κ -distribution is the comparison of the [O II] 7318,24Å/3726,29Å and [S II] 4069,76Å/6717,31Å temperatures. These ions have very similar ionisation potentials and are therefore distributed in a very similar way in the nebula. The photoionisation models used by ([López-Sánchez et al. 2012](#)) have line emission weighted temperatures in the O II and S II zones which differ from each other by less than 400 K over the abundance range 0.3 – 3.0 times solar. However the excitation temperatures of the lines are quite different. For the [S II] 4069,76Å lines, $T_{\text{ex}} = 35,320$ K, and for the [S II] 6717,31Å $T_{\text{ex}} = 21,390$ K. In the case of [O II] 7318,24Å, $T_{\text{ex}} = 58,220$ K while for the 3726,29Å lines, $T_{\text{ex}} = 38,590$ K. Thus the [O II] lines are much more sensitive to the high-energy tail of the κ -distribution than are the [S II] lines. On this basis, one would expect higher temperatures to be derived from the [O II] line ratios than from the [S II] line ratios, in the presence of a κ -distribution.

We have computed the effect that a κ -distribution has on the inferred collisional excitation temperature, T_{CEL} of these ions. This is shown in Fig. 3.9, panel (a). The observations

suggest that the [O II] temperatures are indeed higher than the [S II] temperatures, and that this difference can be accounted for in most of the H II regions by $20 \gtrsim \kappa \gtrsim 10$.

As an alternative approach, we show on Fig. 3.9, panel (b) the average of the inferred collisional excitation temperatures for the [O II] and [N II] ions compared with that of the [S II] ion. For the [O II] and [N II] ions the sensitivity to κ is not so great as for the [O II] lines alone, but the errors in the temperature determination produced by assumptions about the dust extinction curve are reduced. Again, the [S II] temperatures are lower. The inferred range of κ is somewhat wider, but most H II regions are still consistent with $20 \gtrsim \kappa \gtrsim 10$.

Because the recombination temperature, T_B , is appreciably lower than the kinetic temperature T_U which is itself lower than the excitation temperature for collisionally excited line ratios, T_{ex} , a comparison of recombination temperatures and inferred line temperatures is strongly sensitive to the choice of κ . The recombination temperatures, T_{REC} , should be significantly lower than the collisionally excited line temperatures, T_{CEL} , in the presence of a κ -distribution. Again, this is clearly shown in the analysis of the observed H II region spectra.

In Figure 3.9, panels (c) and (d) we show this comparison for the H II regions, using the excitation temperature given by the average of the [O II] and [N II] line ratios and by the [O III] line ratio, respectively. How well these determine κ depends on which of the ionic species is the dominant ionisation stage in the nebula. For cooler exciting stars, [O II] and [N II] line ratios are the better ones to use, but when the central star(s) is hot enough to ionise helium to He II in the bulk of the nebula, then the [O III] line ratio is the better one to use. From Figure 3.9, panels (c) and (d) it would appear that $\kappa \sim 20$, or even higher. Because the upper state of [OIII] has the highest excitation temperature, it is the most sensitive of all the ions to the high energy electrons, and therefore lower values of κ have greater effects.

3.6.2. Planetary Nebulae

High quality spectrophotometry also exists for many PNe, although published values of electron temperatures for many ions is rather sparse. However, rather complete data exist for temperatures determined from the Balmer discontinuity and from the [O III] line ratio. The direct comparison of these should be fairly reliable as a means to estimate κ , since the O III ion is most often the dominant ionisation stage in PNe.

We have taken data from Tsamis et al. (2003); Liu et al. (2004); Zhang et al. (2004); Wesson et al. (2005); Wang & Liu (2007) and Fang & Liu (2011). These data are plotted in Figure 3.10, along with the expectation for $\kappa = 6, 10$ and 20 . The points with error bars are from Zhang et al. (2004). Again the results are consistent with $\kappa > 10$ in most cases, i.e. a mild departure from an equilibrium electron energy distribution. A few points lie above the line of equality of temperatures shown by the dotted line, corresponding to $\kappa = \infty$. However, many of these are consistent with no departure from a Maxwell-Boltzmann distribution, within the observational errors.

There is a tendency for the cooler objects to show greater deviations from equilibrium (smaller inferred κ). These objects will tend to be more metal rich, and/or of lower excitation class. Why this should lead to a greater departure from equilibrium energy distributions is not yet clear, and worth investigating. Of course, it is likely that local temperature and

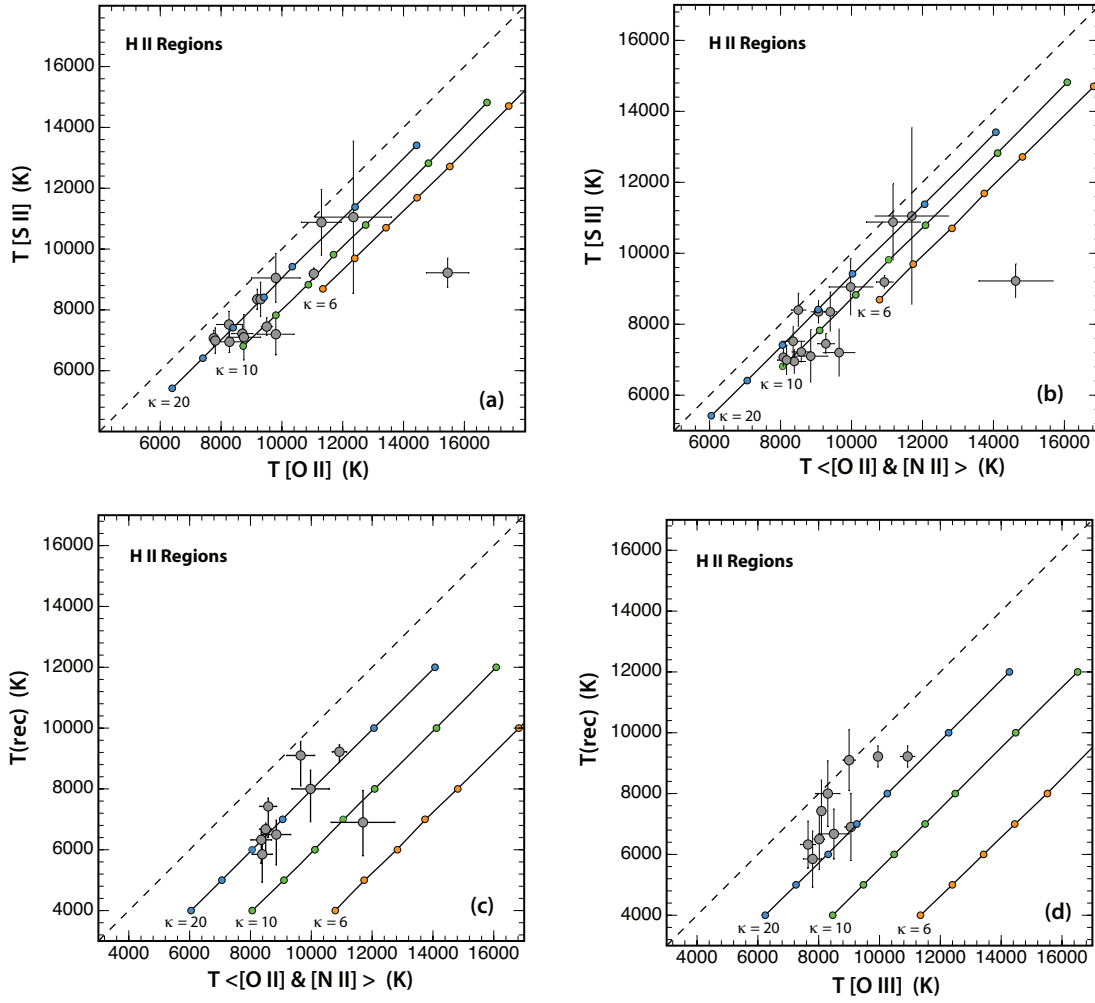


Figure 3.9 Measured temperatures in H II regions compared with what would be expected if the electrons have a κ -distribution. Panel (a) compares the inferred excitation temperatures of the [O II] and [S II] ions, panel (b) the average of the [O II] and [N II] ions with the [S II] ion. Panel (c) and (d) compare the recombination temperatures given by the mean of the Balmer and the Paschen break temperatures with the mean excitation temperature given by the average of the [O II] and [N II] line ratios, panel (c), and that of the [O III] line ratio. Most H II regions seem to have $20 \gtrsim \kappa \gtrsim 10$.

density fluctuations in the PNe contribute to the measured results, and it is not clear what the balance is between the various effects.

The results for both PNe and H II regions are consistent with mild departures from equilibrium ($\kappa \gtrsim 10$). It is interesting to note that in the analysis of the observed spectra, extreme values of κ are not required. The implied departures from a Maxwell-Boltzmann distribution are quite small, but their effect on the nebular diagnostics is quite gross, with serious implications for the chemical abundance determinations in both classes of object. Large departures from the Maxwell-Boltzmann distribution in either PNe or H II regions (lower values of κ) would in any case not be expected, since at the peak of the energy distribution the mean collision time between electrons is short.

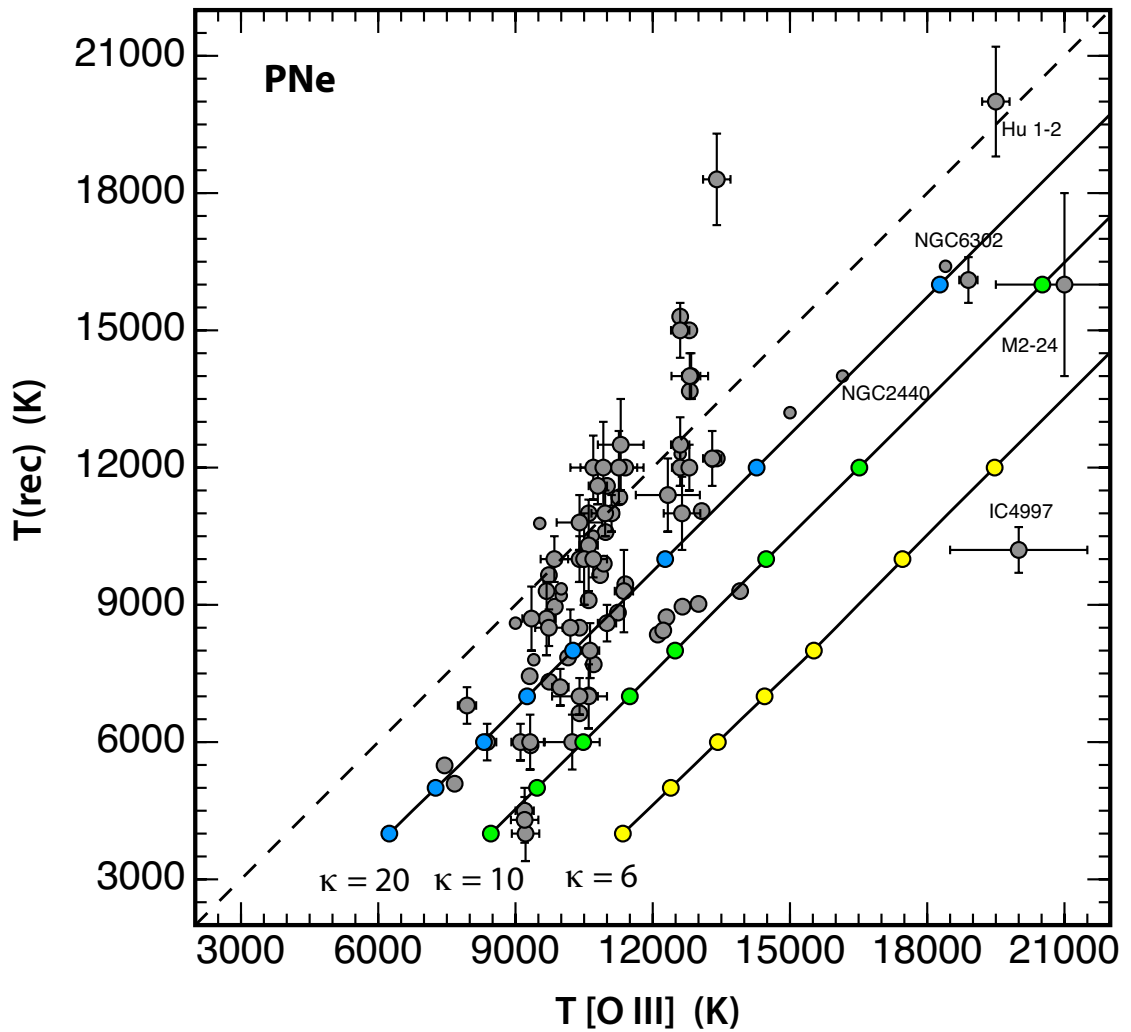


Figure 3.10 As figure 9, panel (d), but for planetary nebulae.

3.7. Conclusion

In this paper we have explored the implications for temperature and metallicity measurement in H II regions and PNe of assuming a non-equilibrium κ -electron energy distribution. We have shown that κ -distributions provide apparent electron temperatures measured from forbidden line ratios which are systematically higher than the kinetic temperature T_U . Assuming κ -distributed electron energies appears to resolve the long standing discrepancies in temperatures measured using the collisional excitation lines of different atomic species, and those calculated using the bound-free recombination continuum. Using high quality published spectra, we have shown that for objects where the spectra of more than one appropriate atomic species is identifiable, it is possible to estimate a value for the effective value of κ . $\kappa \sim 20$ is a good fit to many of the measurements. This value does not require a substantial redistribution of the population to achieve, meaning that any of several means of generating high energy electrons should be capable of sustaining the non-equilibrium distribution.

The κ -distribution offers an important new insight into the physics of gaseous nebulae, both in the Galaxy and elsewhere. It is implausible that thermal equilibrium applies throughout in H II regions and PNe, and the fact that the κ -distribution is able to explain long standing discrepancies is a strong indication that non-equilibrium is a valid assumption. It should enable more accurate estimates of temperature and metallicity in these regions. A detailed investigation into the implications for metallicity measurements will be provided in a future paper.

3.8. Evidence for magnetic fields in Milky Way H II regions

In order for magnetic energy to be an important source of non-thermal electrons, we require β , the ratio of the thermal to magnetic energy, to be less than unity. Direct measurements of β have been made for H II regions using Faraday rotation observations (Harvey-Smith et al. 2011; Rodríguez et al. 2012). These reveal values of $\beta \sim 5$. However, these measurements do not reveal the full strength of the magnetic field if there is turbulence, they indicate only the size of the organised field. They should therefore be taken as imposing a lower bound on the true magnetic field. However, recent evidence on the warm ionised medium (Gaensler et al. 2011) suggests that magnetic turbulence dominates at small scales. Finally, it is generally believed that the magnetic turbulence in the H I phase leads to equipartition ($\beta \sim 1$). Let us take this as a working hypothesis and ask what happens across an ionisation front in an H II region.

Let the H I region be characterised by a density ρ_0 , temperature T_0 , pressure P_0 , magnetic field \vec{B}_0 and sound speed $c_0 = (\gamma P_0 / \rho_0)^{1/2}$. The Alfvén velocity in the gas is $v_A^2 = B_0^2 / 4\pi\rho$. In the H I region ahead of the ionisation front, we if we assume that the gas is turbulently supported, $\beta_0 \sim 1$ *i.e.* $(2/\gamma)(c_0/v_A)^2 \sim 1$, on average. We can resolve the magnetic field into components parallel to the gas flow, $B_0^{\parallel} \sim B_0 / \sqrt{3}$ and perpendicular to the gas flow (in the plane of the ionisation front), $B_0^{\perp} \sim B_0 \sqrt{2/3}$. These components will fluctuate on the scale of the pressure-supported turbulent cells in the H I region, so they relate to the mean field only in a stochastic fashion.

Now consider what happens on the other side of the ionisation front, where the sound speed is c_1 , the outflow Mach number is \mathcal{M} and the hydrodynamic variables are ρ_1 , P_1 , T_1 , B_1^{\parallel} and B_1^{\perp} . The ratio of the densities is obtained by equating the pre-ionisation pressure to the post-ionisation pressure, accounting for the recoil momentum of the ionised plasma;

$$\frac{\rho_0 c_0^2}{\gamma} = \frac{\rho_1 c_1^2}{\gamma} + \mathcal{M}^2 \rho_1 c_1^2. \quad (3.19)$$

The component of the magnetic field perpendicular to the flow direction is stretched (reduced) in the post-ionisation zone by the ratio ρ_1/ρ_0 , and the local gas pressure is decreased in the ratio $1/(1 + \gamma\mathcal{M}^2)$. Therefore:

$$\beta_1^{\perp} \sim \frac{3}{2} \left(\frac{1}{1 + \gamma\mathcal{M}^2} \right) \left(\frac{\rho_0}{\rho_1} \right)^2. \quad (3.20)$$

Thus, all magnetic pressure support is effectively lost in this plane. However, parallel to the

flow, the post-shock magnetic field is unchanged by the ionisation, and therefore

$$\beta_1^{\parallel} \sim 3 \left(\frac{1}{1 + \gamma \mathcal{M}^2} \right) < 1. \quad (3.21)$$

Thus, the magnetic pressure dominates the thermal pressure in this direction. The turbulent origin of the magnetic field in the molecular cloud ensures that β_1^{\parallel} is rapidly fluctuating both in magnitude and direction, which will naturally assist magnetic reconnection and inertial Alfvén wave formation.

This magnetic field, highly aligned to the flow direction and showing strong fluctuations on the small scale provides the natural explanation for the filamentary structure of the ionised plasma seen very clearly in the η Carina and M17 H II regions observed by the Advanced Camera for Surveys (ACS) on the Hubble Space Telescope (HST) (see Figure 3.11, below). In the case of η Carina, the ionised filaments are seen as bright “hairs” originating at the ionisation front. These bright regions correspond to the regions of low magnetic field, given that the gas flow from the ionisation front has to be force free in the plane of the ionisation front. In the case of M17, we are seeing un-ionised regions of low magnetic field and high dust optical depth “combed out” by the expanding ionised plasma. These filaments are only a few AU in diameter, and have an aspect ratio of up to 50 : 1. The implied atomic densities are of order 10^5 atoms cm^{-3} .

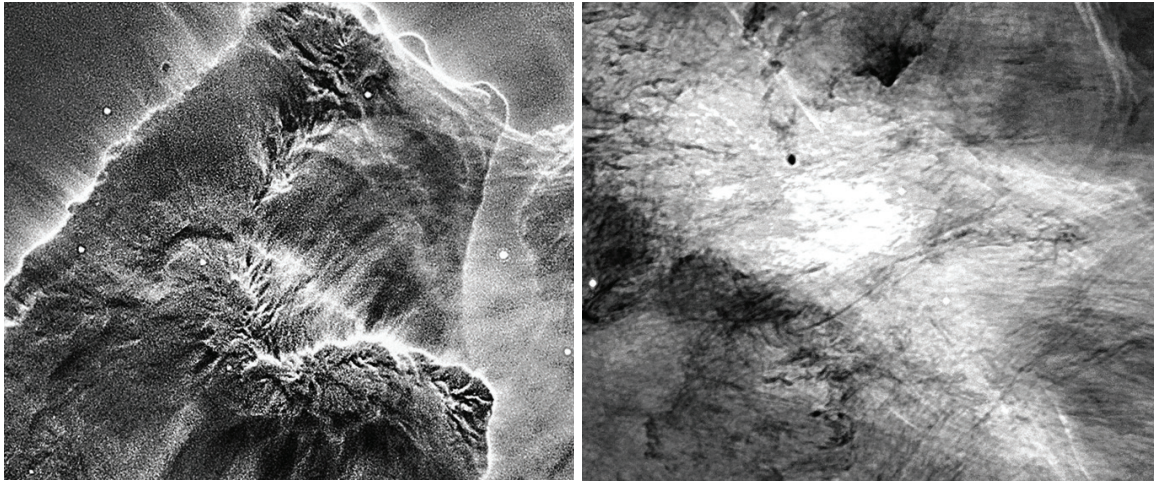


Figure 3.11 Portions of HST images of the η Carina nebula (left) and M17 (right) taken with the ACS. These images have been processed by an unsharp mask to bring up the microstructure. Both images display magnetically-dominated microstructures aligned with the outflow direction. The scales of these microfilaments is of order of the size of the solar system.

3.9. The κ -distribution and the temperature fluctuation (“ t^2 ”) method

As early as 1967, Peimbert proposed that abundance discrepancies might be explained by spatial temperature variations within an H II region (Peimbert 1967). The approach is characterised by a parameter, t^2 , the mean square fractional temperature fluctuation (assumed to have a Gaussian distribution in space). While it is certain that there are spatial variations in temperature, those caused naturally by the radial temperature variation in the H II region are usually insufficient to explain observations, and the cause of the larger values

of t^2 implied by the observations remains unknown. However, the t^2 approach has been widely used, with mixed success (e.g. Peña-Guerrero et al. (2012); García-Rojas & Esteban (2007); Esteban (2002); Kingdon & Ferland (1995)). Detailed discussions of the technique are given in Stasińska (2004) and Kingdon & Ferland (1995).

The t^2 parameter is estimated by solving equations involving the collisionally excited line temperature(s) and the recombination line temperature (Kingdon & Ferland 1995). But as Kingdon & Ferland (1995) also argued, “while temperature fluctuations may result in non-negligible abundance corrections in some objects, they are insufficient to resolve the abundance discrepancy”.

There is, however, a connection between the t^2 method for resolving abundance discrepancies and the κ -distribution. Livadiotis et al. (2011) noted that “ κ -distributions can be derived from the superposition of Maxwellian distributions, by considering a non-fixed temperature that is characterised by a certain (continuous or discrete) density distribution of temperatures”. Thus:

$$f_{\kappa}(E, T_U, \kappa) = \sum_{i=0}^{\infty} \Phi(f_{Max}(E, T_i), \kappa), \quad (3.22)$$

where Φ can, in theory, be determined from the expressions in equations 6 and 7. The necessity to include Maxwellian distributions in the series with extreme temperatures to provide the suprathermal tail at high energies, is, of course, non-physical, and the series needs to be truncated. Nonetheless, expressed this way, the κ -distribution can be seen as a generalisation of the t^2 method.

The κ approach has major advantages over the t^2 method: it is simple; it is consistent over many objects and atomic species; it arises directly from Tsallis q-nonextensive statistics; the physics of ionised plasmas in H II regions and PNe provides several mechanisms capable of generating the suprathermal distribution tails; it has been shown to describe accurately numerous directly measured electron energy distributions in the Solar System; and it explains behaviour over an energy range of at least 3 orders of magnitude, from low energy recombination line electrons to the high ionisation energies in the solar corona.

3.10. Collision Excitation Rate ratios

Table 3.2 Collisional Excitation Rate ratios—see Figure 3.5

T_{ex}/T_U	$\kappa = 2$	$\kappa = 3$	$\kappa = 4$	$\kappa = 6$	$\kappa = 10$	$\kappa = 20$	$\kappa = 50$	$\kappa = 100$
0.0	1.596E+00	1.228E+00	1.142E+00	1.081E+00	1.043E+00	1.020E+00	1.008E+00	1.004E+00
0.1	1.225E+00	1.119E+00	1.079E+00	1.047E+00	1.026E+00	1.012E+00	1.005E+00	1.002E+00
0.2	9.944E-01	1.031E+00	1.025E+00	1.017E+00	1.010E+00	1.005E+00	1.002E+00	1.001E+00
0.3	8.414E-01	9.596E-01	9.795E-01	9.905E-01	9.956E-01	9.982E-01	9.994E-01	9.997E-01
0.4	7.348E-01	9.017E-01	9.408E-01	9.672E-01	9.828E-01	9.921E-01	9.970E-01	9.985E-01
0.5	6.577E-01	8.544E-01	9.079E-01	9.469E-01	9.713E-01	9.866E-01	9.949E-01	9.975E-01
0.6	6.008E-01	8.157E-01	8.800E-01	9.293E-01	9.612E-01	9.817E-01	9.929E-01	9.965E-01
0.7	5.579E-01	7.841E-01	8.566E-01	9.141E-01	9.523E-01	9.774E-01	9.912E-01	9.957E-01
0.8	5.254E-01	7.584E-01	8.370E-01	9.011E-01	9.446E-01	9.736E-01	9.897E-01	9.949E-01
0.9	5.006E-01	7.377E-01	8.209E-01	8.902E-01	9.380E-01	9.703E-01	9.884E-01	9.943E-01
1.0	4.820E-01	7.213E-01	8.080E-01	8.813E-01	9.326E-01	9.676E-01	9.873E-01	9.937E-01
1.1	4.682E-01	7.086E-01	7.978E-01	8.742E-01	9.282E-01	9.654E-01	9.864E-01	9.933E-01
1.2	4.583E-01	6.993E-01	7.902E-01	8.688E-01	9.248E-01	9.636E-01	9.857E-01	9.929E-01
1.3	4.518E-01	6.930E-01	7.849E-01	8.650E-01	9.225E-01	9.624E-01	9.852E-01	9.927E-01
1.4	4.481E-01	6.894E-01	7.818E-01	8.628E-01	9.211E-01	9.617E-01	9.849E-01	9.925E-01
1.5	4.470E-01	6.882E-01	7.808E-01	8.620E-01	9.206E-01	9.614E-01	9.848E-01	9.925E-01
1.6	4.481E-01	6.893E-01	7.818E-01	8.628E-01	9.211E-01	9.617E-01	9.849E-01	9.925E-01
1.7	4.512E-01	6.926E-01	7.846E-01	8.649E-01	9.224E-01	9.624E-01	9.852E-01	9.927E-01
1.8	4.562E-01	6.979E-01	7.893E-01	8.683E-01	9.247E-01	9.636E-01	9.857E-01	9.929E-01
1.9	4.631E-01	7.053E-01	7.956E-01	8.731E-01	9.278E-01	9.652E-01	9.864E-01	9.933E-01
2.0	4.716E-01	7.145E-01	8.037E-01	8.792E-01	9.318E-01	9.674E-01	9.873E-01	9.937E-01
2.1	4.819E-01	7.257E-01	8.135E-01	8.866E-01	9.367E-01	9.700E-01	9.884E-01	9.942E-01
2.2	4.939E-01	7.387E-01	8.249E-01	8.953E-01	9.424E-01	9.730E-01	9.896E-01	9.949E-01
2.3	5.075E-01	7.536E-01	8.381E-01	9.054E-01	9.490E-01	9.765E-01	9.911E-01	9.956E-01
2.4	5.229E-01	7.704E-01	8.529E-01	9.167E-01	9.565E-01	9.805E-01	9.927E-01	9.965E-01
2.5	5.400E-01	7.892E-01	8.694E-01	9.293E-01	9.648E-01	9.850E-01	9.946E-01	9.974E-01
2.6	5.589E-01	8.099E-01	8.877E-01	9.432E-01	9.740E-01	9.899E-01	9.966E-01	9.984E-01
2.7	5.797E-01	8.327E-01	9.077E-01	9.585E-01	9.841E-01	9.953E-01	9.989E-01	9.996E-01
2.8	6.024E-01	8.575E-01	9.296E-01	9.752E-01	9.951E-01	1.001E+00	1.001E+00	1.001E+00
2.9	6.272E-01	8.845E-01	9.533E-01	9.932E-01	1.007E+00	1.008E+00	1.004E+00	1.002E+00
3.0	6.541E-01	9.138E-01	9.790E-01	1.013E+00	1.020E+00	1.014E+00	1.007E+00	1.004E+00
3.1	6.833E-01	9.455E-01	1.007E+00	1.034E+00	1.034E+00	1.022E+00	1.010E+00	1.005E+00
3.2	7.149E-01	9.796E-01	1.037E+00	1.056E+00	1.048E+00	1.030E+00	1.013E+00	1.007E+00
3.3	7.491E-01	1.016E+00	1.069E+00	1.080E+00	1.064E+00	1.038E+00	1.017E+00	1.009E+00
3.4	7.859E-01	1.056E+00	1.103E+00	1.106E+00	1.081E+00	1.047E+00	1.020E+00	1.010E+00
3.5	8.257E-01	1.098E+00	1.140E+00	1.134E+00	1.099E+00	1.056E+00	1.024E+00	1.012E+00
3.6	8.686E-01	1.144E+00	1.179E+00	1.163E+00	1.118E+00	1.066E+00	1.028E+00	1.014E+00
3.7	9.147E-01	1.193E+00	1.221E+00	1.194E+00	1.137E+00	1.076E+00	1.032E+00	1.016E+00
3.8	9.645E-01	1.245E+00	1.266E+00	1.227E+00	1.159E+00	1.087E+00	1.037E+00	1.019E+00
3.9	1.018E+00	1.301E+00	1.313E+00	1.262E+00	1.181E+00	1.099E+00	1.041E+00	1.021E+00
4.0	1.076E+00	1.361E+00	1.364E+00	1.299E+00	1.204E+00	1.111E+00	1.046E+00	1.023E+00
4.1	1.138E+00	1.425E+00	1.418E+00	1.339E+00	1.229E+00	1.123E+00	1.051E+00	1.026E+00
4.2	1.204E+00	1.493E+00	1.476E+00	1.380E+00	1.255E+00	1.137E+00	1.057E+00	1.029E+00
4.3	1.276E+00	1.566E+00	1.537E+00	1.424E+00	1.282E+00	1.150E+00	1.062E+00	1.031E+00
4.4	1.353E+00	1.644E+00	1.603E+00	1.471E+00	1.311E+00	1.165E+00	1.068E+00	1.034E+00
4.5	1.437E+00	1.728E+00	1.672E+00	1.520E+00	1.341E+00	1.180E+00	1.074E+00	1.037E+00
4.6	1.526E+00	1.817E+00	1.746E+00	1.572E+00	1.373E+00	1.196E+00	1.080E+00	1.040E+00
4.7	1.622E+00	1.913E+00	1.825E+00	1.627E+00	1.406E+00	1.212E+00	1.087E+00	1.044E+00
4.8	1.726E+00	2.015E+00	1.909E+00	1.685E+00	1.441E+00	1.229E+00	1.093E+00	1.047E+00
4.9	1.837E+00	2.124E+00	1.998E+00	1.747E+00	1.478E+00	1.247E+00	1.100E+00	1.050E+00
5.0	1.957E+00	2.241E+00	2.092E+00	1.812E+00	1.516E+00	1.265E+00	1.107E+00	1.054E+00

Table 3.2 Collisional Excitation Rate ratios—see Figure 3.5 (continued)

T_{ex}/T_U	$\kappa = 2$	$\kappa = 3$	$\kappa = 4$	$\kappa = 6$	$\kappa = 10$	$\kappa = 20$	$\kappa = 50$	$\kappa = 100$
5.1	2.087E+00	2.365E+00	2.193E+00	1.881E+00	1.557E+00	1.285E+00	1.115E+00	1.057E+00
5.2	2.226E+00	2.499E+00	2.300E+00	1.953E+00	1.599E+00	1.305E+00	1.122E+00	1.061E+00
5.3	2.376E+00	2.642E+00	2.414E+00	2.030E+00	1.643E+00	1.325E+00	1.130E+00	1.065E+00
5.4	2.537E+00	2.794E+00	2.535E+00	2.110E+00	1.689E+00	1.347E+00	1.138E+00	1.069E+00
5.5	2.712E+00	2.958E+00	2.665E+00	2.196E+00	1.738E+00	1.369E+00	1.146E+00	1.073E+00
5.6	2.899E+00	3.133E+00	2.802E+00	2.286E+00	1.789E+00	1.393E+00	1.155E+00	1.077E+00
5.7	3.102E+00	3.320E+00	2.948E+00	2.382E+00	1.842E+00	1.417E+00	1.164E+00	1.081E+00
5.8	3.320E+00	3.520E+00	3.104E+00	2.482E+00	1.898E+00	1.442E+00	1.173E+00	1.086E+00
5.9	3.555E+00	3.735E+00	3.270E+00	2.589E+00	1.956E+00	1.468E+00	1.183E+00	1.090E+00
6.0	3.809E+00	3.965E+00	3.447E+00	2.702E+00	2.017E+00	1.495E+00	1.192E+00	1.095E+00
6.1	4.083E+00	4.211E+00	3.636E+00	2.821E+00	2.081E+00	1.523E+00	1.202E+00	1.100E+00
6.2	4.379E+00	4.475E+00	3.836E+00	2.947E+00	2.148E+00	1.552E+00	1.213E+00	1.105E+00
6.3	4.698E+00	4.758E+00	4.050E+00	3.080E+00	2.219E+00	1.582E+00	1.223E+00	1.110E+00
6.4	5.043E+00	5.061E+00	4.279E+00	3.221E+00	2.292E+00	1.613E+00	1.234E+00	1.115E+00
6.5	5.415E+00	5.386E+00	4.522E+00	3.369E+00	2.369E+00	1.645E+00	1.245E+00	1.120E+00
6.6	5.818E+00	5.735E+00	4.781E+00	3.527E+00	2.450E+00	1.679E+00	1.257E+00	1.126E+00
6.7	6.252E+00	6.109E+00	5.058E+00	3.694E+00	2.535E+00	1.713E+00	1.268E+00	1.131E+00
6.8	6.722E+00	6.510E+00	5.354E+00	3.870E+00	2.624E+00	1.749E+00	1.281E+00	1.137E+00
6.9	7.229E+00	6.941E+00	5.669E+00	4.057E+00	2.717E+00	1.787E+00	1.293E+00	1.143E+00
7.0	7.778E+00	7.403E+00	6.005E+00	4.255E+00	2.814E+00	1.825E+00	1.306E+00	1.148E+00
7.1	8.371E+00	7.900E+00	6.365E+00	4.464E+00	2.917E+00	1.865E+00	1.319E+00	1.154E+00
7.2	9.013E+00	8.433E+00	6.748E+00	4.686E+00	3.024E+00	1.907E+00	1.332E+00	1.161E+00
7.3	9.707E+00	9.006E+00	7.158E+00	4.921E+00	3.136E+00	1.950E+00	1.346E+00	1.167E+00
7.4	1.046E+01	9.621E+00	7.596E+00	5.170E+00	3.254E+00	1.995E+00	1.360E+00	1.173E+00
7.5	1.127E+01	1.028E+01	8.064E+00	5.434E+00	3.378E+00	2.041E+00	1.375E+00	1.180E+00
7.6	1.215E+01	1.099E+01	8.565E+00	5.714E+00	3.508E+00	2.089E+00	1.390E+00	1.187E+00
7.7	1.310E+01	1.176E+01	9.100E+00	6.010E+00	3.644E+00	2.139E+00	1.405E+00	1.194E+00
7.8	1.413E+01	1.258E+01	9.672E+00	6.325E+00	3.787E+00	2.190E+00	1.421E+00	1.201E+00
7.9	1.525E+01	1.346E+01	1.028E+01	6.659E+00	3.937E+00	2.244E+00	1.437E+00	1.208E+00
8.0	1.646E+01	1.441E+01	1.094E+01	7.013E+00	4.094E+00	2.299E+00	1.453E+00	1.215E+00
8.1	1.777E+01	1.544E+01	1.164E+01	7.389E+00	4.259E+00	2.356E+00	1.470E+00	1.223E+00
8.2	1.919E+01	1.654E+01	1.239E+01	7.787E+00	4.433E+00	2.416E+00	1.488E+00	1.230E+00
8.3	2.073E+01	1.773E+01	1.319E+01	8.211E+00	4.615E+00	2.478E+00	1.505E+00	1.238E+00
8.4	2.240E+01	1.900E+01	1.405E+01	8.660E+00	4.807E+00	2.542E+00	1.524E+00	1.246E+00
8.5	2.421E+01	2.038E+01	1.497E+01	9.138E+00	5.008E+00	2.608E+00	1.542E+00	1.254E+00
8.6	2.617E+01	2.186E+01	1.596E+01	9.645E+00	5.219E+00	2.677E+00	1.562E+00	1.263E+00
8.7	2.829E+01	2.345E+01	1.702E+01	1.018E+01	5.441E+00	2.748E+00	1.581E+00	1.271E+00
8.8	3.060E+01	2.517E+01	1.815E+01	1.076E+01	5.675E+00	2.822E+00	1.601E+00	1.280E+00
8.9	3.310E+01	2.702E+01	1.936E+01	1.137E+01	5.921E+00	2.899E+00	1.622E+00	1.288E+00
9.0	3.582E+01	2.902E+01	2.066E+01	1.201E+01	6.179E+00	2.979E+00	1.643E+00	1.297E+00
9.1	3.877E+01	3.117E+01	2.206E+01	1.270E+01	6.450E+00	3.062E+00	1.665E+00	1.307E+00
9.2	4.196E+01	3.350E+01	2.356E+01	1.343E+01	6.736E+00	3.148E+00	1.687E+00	1.316E+00
9.3	4.544E+01	3.600E+01	2.516E+01	1.421E+01	7.037E+00	3.237E+00	1.710E+00	1.325E+00
9.4	4.920E+01	3.870E+01	2.689E+01	1.504E+01	7.353E+00	3.329E+00	1.733E+00	1.335E+00
9.5	5.330E+01	4.161E+01	2.874E+01	1.592E+01	7.686E+00	3.426E+00	1.757E+00	1.345E+00
9.6	5.774E+01	4.476E+01	3.072E+01	1.686E+01	8.037E+00	3.525E+00	1.782E+00	1.355E+00
9.7	6.257E+01	4.815E+01	3.285E+01	1.786E+01	8.406E+00	3.629E+00	1.807E+00	1.365E+00
9.8	6.781E+01	5.182E+01	3.514E+01	1.893E+01	8.794E+00	3.736E+00	1.833E+00	1.376E+00
9.9	7.351E+01	5.577E+01	3.760E+01	2.006E+01	9.204E+00	3.848E+00	1.859E+00	1.386E+00
10.0	7.970E+01	6.004E+01	4.024E+01	2.127E+01	9.635E+00	3.964E+00	1.886E+00	1.397E+00

Table 3.2 Collisional Excitation Rate ratios—see Figure 3.5 (continued)

T_{ex}/T_U	$\kappa = 2$	$\kappa = 3$	$\kappa = 4$	$\kappa = 6$	$\kappa = 10$	$\kappa = 20$	$\kappa = 50$	$\kappa = 100$
10.1	8.643E+01	6.466E+01	4.308E+01	2.256E+01	1.009E+01	4.085E+00	1.914E+00	1.408E+00
10.2	9.374E+01	6.964E+01	4.613E+01	2.393E+01	1.057E+01	4.210E+00	1.942E+00	1.420E+00
10.3	1.017E+02	7.503E+01	4.940E+01	2.539E+01	1.107E+01	4.340E+00	1.972E+00	1.431E+00
10.4	1.103E+02	8.084E+01	5.293E+01	2.695E+01	1.161E+01	4.475E+00	2.001E+00	1.443E+00
10.5	1.197E+02	8.713E+01	5.671E+01	2.861E+01	1.217E+01	4.616E+00	2.032E+00	1.455E+00
10.6	1.300E+02	9.393E+01	6.079E+01	3.038E+01	1.276E+01	4.762E+00	2.063E+00	1.467E+00
10.7	1.411E+02	1.013E+02	6.517E+01	3.228E+01	1.338E+01	4.913E+00	2.096E+00	1.479E+00
10.8	1.532E+02	1.092E+02	6.988E+01	3.429E+01	1.404E+01	5.071E+00	2.129E+00	1.492E+00
10.9	1.663E+02	1.178E+02	7.495E+01	3.645E+01	1.474E+01	5.235E+00	2.162E+00	1.504E+00
11.0	1.806E+02	1.271E+02	8.040E+01	3.875E+01	1.547E+01	5.406E+00	2.197E+00	1.517E+00
11.1	1.962E+02	1.371E+02	8.627E+01	4.120E+01	1.625E+01	5.584E+00	2.232E+00	1.531E+00
11.2	2.131E+02	1.480E+02	9.259E+01	4.382E+01	1.706E+01	5.768E+00	2.269E+00	1.544E+00
11.3	2.316E+02	1.598E+02	9.940E+01	4.662E+01	1.793E+01	5.961E+00	2.306E+00	1.558E+00
11.4	2.516E+02	1.725E+02	1.067E+02	4.961E+01	1.884E+01	6.161E+00	2.344E+00	1.572E+00
11.5	2.735E+02	1.863E+02	1.146E+02	5.280E+01	1.980E+01	6.369E+00	2.384E+00	1.586E+00
11.6	2.973E+02	2.012E+02	1.231E+02	5.622E+01	2.082E+01	6.585E+00	2.424E+00	1.601E+00
11.7	3.232E+02	2.173E+02	1.323E+02	5.986E+01	2.190E+01	6.811E+00	2.465E+00	1.616E+00
11.8	3.514E+02	2.348E+02	1.421E+02	6.376E+01	2.303E+01	7.045E+00	2.507E+00	1.631E+00
11.9	3.821E+02	2.538E+02	1.528E+02	6.793E+01	2.423E+01	7.290E+00	2.551E+00	1.646E+00
12.0	4.156E+02	2.743E+02	1.642E+02	7.238E+01	2.551E+01	7.544E+00	2.595E+00	1.662E+00
12.1	4.520E+02	2.965E+02	1.766E+02	7.715E+01	2.685E+01	7.809E+00	2.641E+00	1.678E+00
12.2	4.917E+02	3.205E+02	1.899E+02	8.224E+01	2.827E+01	8.086E+00	2.688E+00	1.694E+00
12.3	5.349E+02	3.466E+02	2.042E+02	8.769E+01	2.977E+01	8.373E+00	2.736E+00	1.711E+00
12.4	5.821E+02	3.748E+02	2.197E+02	9.352E+01	3.136E+01	8.673E+00	2.785E+00	1.727E+00
12.5	6.334E+02	4.054E+02	2.364E+02	9.977E+01	3.305E+01	8.985E+00	2.835E+00	1.744E+00
12.6	6.894E+02	4.386E+02	2.544E+02	1.064E+02	3.483E+01	9.311E+00	2.887E+00	1.762E+00
12.7	7.504E+02	4.746E+02	2.739E+02	1.136E+02	3.671E+01	9.650E+00	2.940E+00	1.780E+00
12.8	8.169E+02	5.136E+02	2.948E+02	1.213E+02	3.871E+01	1.000E+01	2.995E+00	1.798E+00
12.9	8.894E+02	5.558E+02	3.175E+02	1.294E+02	4.082E+01	1.037E+01	3.051E+00	1.816E+00
13.0	9.684E+02	6.017E+02	3.419E+02	1.382E+02	4.306E+01	1.076E+01	3.108E+00	1.835E+00
13.1	1.055E+03	6.514E+02	3.682E+02	1.476E+02	4.543E+01	1.116E+01	3.167E+00	1.854E+00
13.2	1.149E+03	7.053E+02	3.967E+02	1.577E+02	4.794E+01	1.158E+01	3.227E+00	1.873E+00
13.3	1.251E+03	7.638E+02	4.274E+02	1.685E+02	5.060E+01	1.201E+01	3.289E+00	1.893E+00
13.4	1.363E+03	8.272E+02	4.606E+02	1.801E+02	5.342E+01	1.247E+01	3.353E+00	1.913E+00
13.5	1.485E+03	8.960E+02	4.964E+02	1.925E+02	5.641E+01	1.294E+01	3.418E+00	1.934E+00
13.6	1.618E+03	9.707E+02	5.351E+02	2.057E+02	5.958E+01	1.344E+01	3.485E+00	1.955E+00
13.7	1.763E+03	1.052E+03	5.770E+02	2.200E+02	6.294E+01	1.396E+01	3.554E+00	1.976E+00
13.8	1.921E+03	1.140E+03	6.221E+02	2.353E+02	6.650E+01	1.450E+01	3.625E+00	1.998E+00
13.9	2.094E+03	1.235E+03	6.709E+02	2.516E+02	7.028E+01	1.506E+01	3.697E+00	2.020E+00
14.0	2.282E+03	1.339E+03	7.237E+02	2.692E+02	7.429E+01	1.565E+01	3.772E+00	2.042E+00
14.1	2.487E+03	1.451E+03	7.807E+02	2.881E+02	7.854E+01	1.627E+01	3.848E+00	2.065E+00
14.2	2.712E+03	1.574E+03	8.423E+02	3.083E+02	8.305E+01	1.691E+01	3.927E+00	2.089E+00
14.3	2.957E+03	1.706E+03	9.089E+02	3.300E+02	8.784E+01	1.758E+01	4.007E+00	2.112E+00
14.4	3.224E+03	1.850E+03	9.810E+02	3.532E+02	9.292E+01	1.828E+01	4.090E+00	2.137E+00
14.5	3.516E+03	2.007E+03	1.059E+03	3.782E+02	9.832E+01	1.901E+01	4.175E+00	2.161E+00
14.6	3.834E+03	2.177E+03	1.143E+03	4.050E+02	1.040E+02	1.978E+01	4.262E+00	2.186E+00
14.7	4.182E+03	2.362E+03	1.234E+03	4.338E+02	1.101E+02	2.058E+01	4.352E+00	2.212E+00
14.8	4.561E+03	2.562E+03	1.333E+03	4.647E+02	1.166E+02	2.142E+01	4.444E+00	2.238E+00
14.9	4.976E+03	2.780E+03	1.439E+03	4.979E+02	1.234E+02	2.229E+01	4.539E+00	2.264E+00
15.0	5.428E+03	3.017E+03	1.555E+03	5.336E+02	1.307E+02	2.321E+01	4.636E+00	2.291E+00

Table 3.2 Collisional Excitation Rate ratios—see Figure 3.5 (continued)

T_{ex}/T_U	$\kappa = 2$	$\kappa = 3$	$\kappa = 4$	$\kappa = 6$	$\kappa = 10$	$\kappa = 20$	$\kappa = 50$	$\kappa = 100$
15.1	5.923E+03	3.274E+03	1.679E+03	5.719E+02	1.385E+02	2.416E+01	4.736E+00	2.319E+00
15.2	6.462E+03	3.554E+03	1.814E+03	6.130E+02	1.467E+02	2.516E+01	4.839E+00	2.347E+00
15.3	7.052E+03	3.858E+03	1.961E+03	6.572E+02	1.554E+02	2.621E+01	4.944E+00	2.376E+00
15.4	7.696E+03	4.189E+03	2.119E+03	7.047E+02	1.647E+02	2.730E+01	5.053E+00	2.405E+00
15.5	8.399E+03	4.548E+03	2.290E+03	7.557E+02	1.746E+02	2.845E+01	5.164E+00	2.434E+00
15.6	9.168E+03	4.939E+03	2.475E+03	8.106E+02	1.851E+02	2.965E+01	5.279E+00	2.464E+00
15.7	1.001E+04	5.364E+03	2.676E+03	8.696E+02	1.963E+02	3.090E+01	5.396E+00	2.495E+00
15.8	1.092E+04	5.826E+03	2.893E+03	9.330E+02	2.082E+02	3.221E+01	5.517E+00	2.526E+00
15.9	1.193E+04	6.328E+03	3.129E+03	1.001E+03	2.208E+02	3.359E+01	5.642E+00	2.558E+00
16.0	1.302E+04	6.874E+03	3.384E+03	1.074E+03	2.343E+02	3.503E+01	5.770E+00	2.591E+00
16.1	1.422E+04	7.468E+03	3.660E+03	1.153E+03	2.486E+02	3.653E+01	5.901E+00	2.624E+00
16.2	1.553E+04	8.115E+03	3.959E+03	1.238E+03	2.638E+02	3.811E+01	6.036E+00	2.658E+00
16.3	1.695E+04	8.818E+03	4.283E+03	1.329E+03	2.800E+02	3.976E+01	6.176E+00	2.692E+00
16.4	1.852E+04	9.583E+03	4.634E+03	1.427E+03	2.972E+02	4.150E+01	6.319E+00	2.727E+00
16.5	2.022E+04	1.042E+04	5.014E+03	1.533E+03	3.156E+02	4.331E+01	6.466E+00	2.763E+00
16.6	2.209E+04	1.132E+04	5.427E+03	1.647E+03	3.351E+02	4.521E+01	6.617E+00	2.799E+00
16.7	2.413E+04	1.231E+04	5.873E+03	1.769E+03	3.559E+02	4.720E+01	6.773E+00	2.836E+00
16.8	2.636E+04	1.338E+04	6.357E+03	1.900E+03	3.781E+02	4.929E+01	6.933E+00	2.874E+00
16.9	2.880E+04	1.455E+04	6.882E+03	2.042E+03	4.017E+02	5.147E+01	7.098E+00	2.913E+00
17.0	3.147E+04	1.582E+04	7.451E+03	2.195E+03	4.268E+02	5.377E+01	7.267E+00	2.952E+00
17.1	3.438E+04	1.720E+04	8.068E+03	2.359E+03	4.536E+02	5.617E+01	7.442E+00	2.992E+00
17.2	3.757E+04	1.871E+04	8.737E+03	2.536E+03	4.821E+02	5.869E+01	7.621E+00	3.033E+00
17.3	4.105E+04	2.034E+04	9.462E+03	2.726E+03	5.125E+02	6.134E+01	7.806E+00	3.074E+00
17.4	4.487E+04	2.213E+04	1.025E+04	2.931E+03	5.449E+02	6.411E+01	7.996E+00	3.116E+00
17.5	4.904E+04	2.407E+04	1.110E+04	3.152E+03	5.795E+02	6.702E+01	8.192E+00	3.160E+00
17.6	5.360E+04	2.619E+04	1.203E+04	3.390E+03	6.163E+02	7.007E+01	8.393E+00	3.204E+00
17.7	5.858E+04	2.849E+04	1.303E+04	3.647E+03	6.556E+02	7.327E+01	8.601E+00	3.248E+00
17.8	6.404E+04	3.100E+04	1.412E+04	3.923E+03	6.975E+02	7.663E+01	8.814E+00	3.294E+00
17.9	7.001E+04	3.374E+04	1.530E+04	4.221E+03	7.421E+02	8.015E+01	9.034E+00	3.341E+00
18.0	7.654E+04	3.671E+04	1.658E+04	4.541E+03	7.897E+02	8.385E+01	9.261E+00	3.388E+00
18.1	8.368E+04	3.996E+04	1.797E+04	4.887E+03	8.405E+02	8.774E+01	9.494E+00	3.437E+00
18.2	9.149E+04	4.349E+04	1.948E+04	5.260E+03	8.947E+02	9.182E+01	9.734E+00	3.486E+00
18.3	1.000E+05	4.734E+04	2.112E+04	5.662E+03	9.525E+02	9.610E+01	9.981E+00	3.537E+00
18.4	1.094E+05	5.153E+04	2.290E+04	6.095E+03	1.014E+03	1.006E+02	1.024E+01	3.588E+00
18.5	1.196E+05	5.610E+04	2.483E+04	6.563E+03	1.080E+03	1.053E+02	1.050E+01	3.640E+00
18.6	1.308E+05	6.108E+04	2.692E+04	7.066E+03	1.150E+03	1.103E+02	1.077E+01	3.694E+00
18.7	1.431E+05	6.651E+04	2.920E+04	7.610E+03	1.225E+03	1.155E+02	1.105E+01	3.748E+00
18.8	1.565E+05	7.242E+04	3.167E+04	8.196E+03	1.305E+03	1.210E+02	1.133E+01	3.804E+00
18.9	1.712E+05	7.887E+04	3.435E+04	8.828E+03	1.391E+03	1.267E+02	1.163E+01	3.860E+00
19.0	1.873E+05	8.589E+04	3.726E+04	9.510E+03	1.482E+03	1.328E+02	1.194E+01	3.918E+00
19.1	2.048E+05	9.355E+04	4.042E+04	1.025E+04	1.580E+03	1.391E+02	1.225E+01	3.977E+00
19.2	2.241E+05	1.019E+05	4.385E+04	1.104E+04	1.684E+03	1.458E+02	1.257E+01	4.037E+00
19.3	2.452E+05	1.110E+05	4.758E+04	1.190E+04	1.795E+03	1.528E+02	1.291E+01	4.099E+00
19.4	2.682E+05	1.209E+05	5.163E+04	1.282E+04	1.914E+03	1.602E+02	1.325E+01	4.161E+00
19.5	2.935E+05	1.317E+05	5.603E+04	1.382E+04	2.041E+03	1.679E+02	1.361E+01	4.225E+00
19.6	3.211E+05	1.435E+05	6.081E+04	1.490E+04	2.176E+03	1.761E+02	1.397E+01	4.290E+00
19.7	3.514E+05	1.564E+05	6.600E+04	1.606E+04	2.321E+03	1.847E+02	1.435E+01	4.356E+00
19.8	3.845E+05	1.704E+05	7.164E+04	1.731E+04	2.476E+03	1.937E+02	1.474E+01	4.424E+00
19.9	4.208E+05	1.857E+05	7.777E+04	1.867E+04	2.642E+03	2.032E+02	1.514E+01	4.493E+00
20.0	4.606E+05	2.024E+05	8.444E+04	2.013E+04	2.819E+03	2.132E+02	1.555E+01	4.564E+00

CHAPTER 4

Measuring nebular temperatures—the effect of new collision strengths with equilibrium and κ -distributed electron energies

Dans nos plus extrêmes démenances, nous rêvons d'un équilibre que nous avons laissé derrière nous et dont nous croyons ingénument que nous allons le retrouver au bout de nos erreurs.¹

Albert Camus - *L'exil d'Hélène*

*This chapter was previously published as 'Measuring nebular temperatures: the effect of new collision strengths with equilibrium and κ -distributed electron energies', Nicholls, D. C., Dopita, M. A., Sutherland, R. S., Kewley, L. J., & Palay, E., *ApJS*, 207, 21. The work is entirely my own, apart from the numerical values in Tables 3.4 and 3.5, which were calculated by Mike Dopita, and comments and suggested modifications from my co-authors. Minor typographical errors have been corrected, and sections, tables and figures have been renumbered to conform with the layout of the thesis.*

4.1. Chapter summary

In this paper we develop tools for observers to use when analysing nebular spectra for temperatures and metallicities, with two goals: to present a new, simple method to calculate equilibrium electron temperatures for collisionally excited line flux ratios, using the latest atomic data; and to adapt current methods to include the effects of possible non-equilibrium “ κ ” electron energy distributions. Adopting recent collision strength data for [O III], [S III], [O II], [S II], and [N II], we find that existing methods based on older atomic data seriously overestimate the electron temperatures, even when considering purely Maxwellian statistics.

¹In our wildest aberrations we dream of an equilibrium we have left behind and which we naively expect to find at the end of our errors.

If κ distributions exist in H II regions and planetary nebulae as they do in solar system plasmas, it is important to investigate the observational consequences. This paper continues our previous work on the κ distribution (Nicholls et al. 2012).

We present simple formulaic methods that allow observers (1) to measure equilibrium electron temperatures and atomic abundances using the latest atomic data, and (2) to apply simple corrections to existing equilibrium analysis techniques to allow for possible non-equilibrium effects. These tools should lead to better consistency in temperature and abundance measurements, and a clearer understanding of the physics of H II regions and planetary nebulae.

4.2. Introduction

Fundamental to all methods of measuring temperatures and abundances in gaseous nebulae are the atomic data for the ionised nebular species. In particular, an accurate knowledge of the collision strengths for the excitation of ionised nebular species is critical to obtaining reliable information on the conditions in these plasmas. Unfortunately, computing these collision strengths is a lengthy and complex process, placing considerable demands on computational power. Many current nebular abundance analysis methods make use of atomic data computed over 20 years ago. In this work we assemble the best available modern data to investigate the effects on temperature and abundance measurement. We find that the latest data makes a considerable difference to the answers obtained.

All previous approaches have used “effective collision strengths”, where the detailed computed collision strengths are convolved with Maxwell-Boltzmann (M-B) electron energy distributions at fixed temperatures. In this work, we use the detailed collision strengths whose energy dependence has not been convolved with an electron energy distribution. Our approach has enabled us to build simple formulas which will allow the observer to calculate (equilibrium) electron temperatures, based on the most recent atomic data.

We also return to the subject of our previous paper (Nicholls et al. 2012, hereafter, NDS12), the non-equilibrium κ electron energy distribution. These distributions have been widely detected in solar system plasmas (Pierrard & Lazar 2010), and Tsallis et al. (1995) have explained from entropy considerations why and how such distributions can occur. As previous analyses have assumed equilibrium energy distributions in H II regions and planetary nebulae (PNe), we revisit our reasons for considering non-equilibrium electron energy distributions in these objects.

In this paper we take the exploration of the κ distribution further. Using the un-convolved collision strengths, we explore in detail the effects of the κ distribution. We derive formulae to simplify calculating the effects of a κ distribution from conventional equilibrium results. In this way, observers can investigate the effect of any κ -type divergence from equilibrium electron energies.

Our aim is to provide the observer with a set of tools to (1) take advantage of the latest atomic data for equilibrium calculations; and (2) using the κ electron energy distribution, to correct apparent temperatures measured from temperature sensitive line ratios or recombination continua for subsequent abundance analyses.

The paper is organised as follows. In Section 4.3, we present a rationale for considering non-equilibrium electron energy distributions in gaseous nebulae. In Section 4.4, we describe the κ distribution for electron energies and compare the collisional excitation rates for the κ and M-B distribution. In Section 4.5, we discuss the factors involved in obtaining accurate collisionally excited line (CEL) equilibrium electron temperatures from theoretical collision strengths. In particular we point out the errors resulting from inaccuracies in the collision strengths used as the bases for most current direct electron temperature techniques. We show that for non-equilibrium electron energy distributions, it is necessary to use detailed collision strengths for atomic species of interest, as distinct from the thermally averaged *effective* collision strengths that are usually published; we discuss the effect of premature truncation of collision strength computation at high energies; and we list the sources for the collision strength data we have used. In Section 4.6 we explore the effect of the κ distribution on recombination processes, and how to calculate the effects of a κ distribution on the apparent temperature and density of the recombining electrons; and we calculate the degree to which recombination lines are enhanced by the κ distribution. In Section 4.7, we describe in detail the effect of the κ distribution on CELs. Using a general expression for the collisional excitation rate ratio between the κ and M-B distributions, we derive the relative intensity enhancements for different atomic species, and detailed equations for temperature sensitive line flux ratios. We show typical flux ratio versus kinetic temperature plots for [O III] and [S III] for a range of values of κ , based on direct calculation from recently published collision strengths.

Section 4.8 is the main focus of the paper, where we present a new, simple method for calculating equilibrium electron temperatures from line flux ratios using the most recent collision strength data, including density corrections; tools for measuring true (kinetic) CEL electron temperatures, using conventionally calculated equilibrium electron temperatures as a starting point; and a simple linear equation for converting between conventional measurement results and κ -corrected temperatures. In Section 4.9 we discuss briefly the effect of κ on strong line methods. In Section 4.10 we present ways to determine κ and point out the need for and progress with implementing κ effects in photoionisation modelling codes. In Section 4.11 we summarise our conclusions. In the appendix we list the temperature-sensitive lines for the most common atomic species found in H II regions and PNe; the transition probabilities for these transitions; and the various factors appearing in the formulae in Section 4.6 which allow the temperature-sensitive line ratios to be computed for any internal energy temperature and value of κ .

4.3. Rationale for considering non-equilibrium electron energies.

It has long been held that the electrons in H II regions and PNe are in thermal equilibrium. Analytical calculations of electron velocity distributions in gaseous nebulae were presented by Bohm & Aller (1947). Their work led them to state that the velocity distribution is “very close to Maxwellian”. Spitzer (1962, Ch.5) also examined the thermalisation process for electron energies in plasmas and found that electron energies equilibrate rapidly through collisions. This early work has lead later authors to assume the electrons in gaseous nebulae are always in thermal equilibrium. However, Spitzer’s analysis showed that the equilibration

time of an energetic electron is proportional to the cube of the velocity, so even using equilibrium theory, plasmas with very high energy electrons take much longer to equilibrate than those excited by normal UV photons from stars found in H II regions.

In more recent times, the electron energies in solar system plasmas have been measured directly by satellites and space probes. This began with [Vasyliunas \(1968\)](#), who found that the electron energies in the Earth's magnetosphere departed substantially from the Maxwellian, and resembled a Maxwellian with a high energy power law tail. He showed that this distribution could be well described by what he called the " κ distribution". Since then, κ distributions have been widely detected in solar system plasmas and are the subject of considerable interest in solar system physics.² They have been detected in the outer heliosphere, the magnetospheres of all the gas-giant planets, Mercury, the moons Titan and Io, the Earth's magnetosphere, plasma sheet and magnetosheath and the solar wind (see references in [Pierrard & Lazar 2010](#)). There is also evidence from IBEX observations that energetic neutral atoms in the interstellar medium, where it interacts with the heliosheath, exhibit κ energy distributions ([Livadiotis et al. 2011](#)). In solar system plasmas, the κ distribution is the norm, and the M-B distribution is a rarity. So we are confronted with the fact that despite the early theoretical work suggesting that the electrons in such plasmas should be in thermal equilibrium, they are almost always not.

Initially, κ distributions were used as empirical fits to observed energies, and were criticised as lacking a theoretical basis. Subsequently, the distribution has been shown to arise naturally from entropy considerations. See, for example, [Tsallis et al. \(1995\)](#); [Treumann \(1999\)](#); [Leubner \(2002\)](#), and the comprehensive analysis by [Livadiotis & McComas \(2009\)](#). They have explored "q non-extensive statistical mechanics" and have shown that κ energy distributions arise as a consequence of this entropy formalism, in the same way as the M-B distribution arises from Boltzmann-Gibbs statistics. The requirement for this to occur is that there be macroscopic interactions between particles, in addition to the shorter-range Coulombic forces that give rise to M-B equilibration. Tsallis statistics provide a sound basis for the overtly successful use of the κ distribution in describing solar system plasmas. κ distributions appear to arise whenever the plasma is being pumped rapidly with high energy non-thermal electrons, so that the system cannot relax to a classical M-B distribution. [Collier \(1993\)](#) has also shown that κ -like energy distributions can arise as a consequence of normal power-law variations of physical parameters such as density, temperature, and electric and magnetic fields.

It is plausible that such conditions are also present in H II regions and PNe—solar system plasma parameters span many of the conditions found in gaseous nebulae, and, as in the solar system, H II region plasmas can be magnetically dominated ([Arthur et al. 2011](#); [Nicholls et al. 2012](#))—so it is important to investigate the effects of non-equilibrium energy distributions with high-energy tails occurring in gaseous nebulae, should they occur.

Such non-Maxwellian energies may occur whenever the population of energetic electrons is being pumped in a timescale shorter than, or of the same order as the normal energy re-distribution timescale of the electron population. Suitable mechanisms include magnetic

²Over 400 papers on the applications of κ distributions in astrophysics had been published prior to 2009 ([Livadiotis & McComas 2009](#)) and over 5000 in physics in general had been published prior to 2011 ([Livadiotis & McComas 2011](#)).

reconnection followed by the migration of high-energy electrons along field lines, the development of inertial Alfvén waves, local shocks (driven either by the collision of bulk flows or by supersonic turbulence), and, most simply, by the injection of high-energy electrons through the photoionisation process itself. Normal photoionisation produces supra-thermal electrons on a timescale similar to the recombination timescale. However, energetic electrons can be generated by the photoionisation of dust (Dopita & Sutherland 2000), and X-ray ionisation can produce highly energetic (\sim keV) inner-shell (Auger process) electrons (e.g., Shull & van Steenberg (1985); Aldrovandi & Gruenwald (1985); Petrini & da Silva (1997), and references therein). These photoionisation-based processes should become more effective where the source of the ionising photons has a “hard” photon spectrum. Thus, the likelihood of the ionised plasma having a κ electron energy distribution would be high in the case of either photoionisation by an Active Galactic Nucleus (AGN), or the case of PNe, where the effective temperature of the exciting star could range up to $\sim 250,000$ K.

So we have no shortage of possible energy injection mechanisms capable of feeding the energetic population on a timescale which is short compared with the collisional re-distribution timescale. The rate of equilibration falls rapidly with increasing energy, and we would expect there to be a threshold energy above which any non-thermal electrons have a long residence time. These can then feed continually down towards lower energies through conventional collisional energy redistribution, thus maintaining a κ electron energy distribution.

In addition to the energy injection mechanisms capable of maintaining the excitation of suprathermal distributions, several authors (Livadiotis & McComas (2011) and references therein; Shizgal (2007); Treumann (2001)) have investigated the possibility that the κ distribution may remain stable against equilibration longer than conventional thermalisation considerations would suggest. In particular, distributions with $2.5 \gtrsim \kappa > 1.5$ —detected, for example, in Jupiter’s magnetosphere—appear to have the capacity, through increasing entropy, of moving to values of lower κ (Livadiotis & McComas 2011) i.e., away from (M-B) equilibrium. While the physical application of this aspect of κ distributions remains to be explored fully, it suggests that where q non-extensive entropy conditions operate, the suprathermal energy distributions produced exist in “stationary states” where the behaviour is, at least in the short term, time-invariant (Livadiotis & McComas 2010). These states may have longer lifetimes than expected classically. This is consistent with the numerous observations in solar system plasmas, that κ electron and proton energy distributions are the norm.

It is likely, therefore, that photoionised plasmas in gaseous nebulae will show departures from a Maxwell distribution to some degree. The key questions are, is this important, and does it produce observable effects in the nebular diagnostics which we have relied upon hitherto?

The answer to both questions appears to be ‘yes’. For several decades, systematic discrepancies have plagued abundance measurements derived from observations of emission lines and emission continua in H II regions and PNe. In particular, abundances determined from CELs for different ions differ from one another, and temperatures determined from Hydrogen and Helium bound-free continuum spectra are consistently lower than those obtained from CELs. As a consequence, chemical abundances determined from the optical recombination lines (ORLs) are systematically higher than those determined from CELs.

These discrepancies are often referred to as the “abundance discrepancy problem” and are sometimes even parameterised as the “abundance discrepancy factor” (ADF). The problem was first observed 70 years ago and has been discussed regularly in the literature for 40 years. See, for example, Wyse (1942); Peimbert (1967); Liu et al. (2000); Stasińska (2004); García-Rojas & Esteban (2007).

A number of attempts have been made to explain these differences. The earliest attempt appears to be by Peimbert (1967), who proposed small temperature inhomogeneities through the emitting regions as the cause. Later, Liu et al. (2000) suggested the presence of a two-phase “bi-abundance” structure, where the emitting regions contain cool, metal-rich, hydrogen poor inclusions. However, neither explanation appears to be fully satisfactory: the temperature fluctuation model often requires large fluctuations to explain the observed discrepancies, without suggesting how these fluctuations could arise. The bi-abundance model requires proposing inhomogeneities where, in some cases, none are observed, or where the physical processes militate against the stability of such inhomogeneities. The reader is referred to the detailed discussion by Stasińska (2004). Further, in neither of these mechanisms is the discrepancy between different CEL species explained. More recently, Binette et al. (2012) have suggested that shock waves may contribute to the apparent discrepancies, but they state that the mechanism needs to be explored further before it can be considered an explanation. A common feature of all these approaches is that they assume the electrons involved in collisional excitation and recombination processes are in thermal equilibrium.

In our previous paper (NDS12) we showed that a non-equilibrium κ electron energy distribution is capable of explaining both the ORL/CEL discrepancy, and the differences between electron temperatures obtained using different CEL species. The mechanism has been shown, for example, to provide an explanation in the case of [O III] and [S III] CEL lines (Binette et al. 2012). It is interesting to note that extreme departures from an equilibrium electron energy distribution are not required to accomplish this, and if there is pumping of electron energies by mechanisms clearly likely to occur in gaseous nebulae, such distributions may not be difficult to achieve.

In this paper, we continue to explore the implications of κ energy distributions, using recently published collision strength data for key nebular species to model the effects the κ distribution will have, if present, on the physics of H II regions and PNe.

4.4. The κ distribution

The κ distribution resembles the M-B distribution at lower energies but has a high energy power law tail. Expressed in energy terms, the κ distribution is (NDS12):

$$n(E)dE = \frac{2N_e}{\sqrt{\pi}} \left(\frac{\Gamma(\kappa + 1)}{(\kappa - \frac{3}{2})^{3/2} \Gamma(\kappa - \frac{1}{2})} \right) \frac{\sqrt{E}}{(k_B T_U)^{3/2} (1 + E / [(\kappa - \frac{3}{2}) k_B T_U])^{\kappa+1}} dE. \quad (4.1)$$

The parameter κ describes the extent to which the energy distribution differs from the M-B. Its values lie in the range $[\frac{3}{2}, \infty]$. In the limit as $\kappa \rightarrow \infty$, the energy distribution reduces to

the equilibrium M-B distribution:

$$n(E)dE = \frac{2N_e}{\sqrt{\pi}} \frac{\sqrt{E} \exp[-E/k_B T_U]}{(k_B T_U)^{3/2}} dE. \quad (4.2)$$

where T_U is the “kinetic” or “internal energy” temperature, defined in terms of the energy density of the system, as per [NDS12](#), Equation 5; N_e is the electron density; and k_B is the Boltzmann constant. For an M-B energy distribution, T_U is simply the thermodynamic temperature. Thus the M-B distribution is a special case of the κ distribution, where there is no long-range pumping of electron energies at timescales similar to the collisional relaxation time.

It can readily be shown by integration with respect to energy between the limits $[0, \infty]$ that the area under the curves given in Equations (4.1) and (4.2) is N_e , the electron density, in both cases, and in the case of $\kappa \rightarrow \infty$ the internal energy temperature is identically equal to the classical electron temperature.

As shown by [NDS12](#), the collisional excitation rate from level 1 to level 2 for an M-B distribution is given by

$$R_{12}(\text{M-B}) = \frac{n_e N_e}{g_1} \frac{h^2}{(2\pi m_e k_B T_U)^{3/2}} \int_{E_{12}}^{\infty} \Omega_{12}(E) \exp\left[-\frac{E}{k_B T_U}\right] dE, \quad (4.3)$$

and for a κ -distribution, the corresponding rate is:

$$R_{12}(\kappa) = \frac{n_e N_e}{g_1} \frac{h^2}{(2\pi m_e k_B T_U)^{3/2}} \frac{\Gamma(\kappa + 1)}{(\kappa - \frac{3}{2})^{3/2} \Gamma(\kappa - \frac{1}{2})} \int_{E_{12}}^{\infty} \frac{\Omega_{12}}{(1 + E/[(\kappa - \frac{3}{2})k_B T_U])^{\kappa+1}} dE. \quad (4.4)$$

where Ω_{12} is the collision strength for collisional excitations from level 1 to level 2, E_{12} is the energy gap between levels 1 and 2, g_1 is the statistical weight of the lower state, and Γ is the gamma function.

As a first order approximation, we can assume that the collision strength from excitations from level 1 to 2, Ω_{12} , is independent of energy. For this case the ratio of the rates of collisional excitation from level 1 to level 2 for a κ distribution can be expressed analytically ([NDS12](#)) as:

$$\frac{R_{12}(\kappa)}{R_{12}(\text{M-B})} = \frac{\Gamma(\kappa + 1)}{(\kappa - \frac{3}{2})^{3/2} \Gamma(\kappa - \frac{1}{2})} \left(1 - \frac{3}{2\kappa}\right) \exp\left[\frac{E_{12}}{k_B T_U}\right] \left(1 + \frac{E_{12}}{(\kappa - \frac{3}{2})k_B T_U}\right)^{-\kappa}. \quad (4.5)$$

Detailed plots and values for this equation for a range of values of κ are given in [NDS12](#), Figure 5 and Table 1.

Electron temperatures are generally measured using the line ratio of two emission lines with well-separated excitation energies, of which the best known is the $\lambda\lambda 4363/5007$ ratio for [O III]. As shown in [NDS12](#), Equations (12) and (13)³, for an M-B electron energy distribution, considering a simplified three-level atom, the ratio of the collisional excitation rate from

³The error in [NDS12](#), equations 9, 11, 12 and 13, where a factor of $\sqrt{2/m_e}$ was missing, has been corrected here and in Chapter 3. This omission disappeared in the ratio process, however, and had no effect on the conclusions.

level 1 to level 3 to the rate from level 1 to level 2, for the constant Ω case, is given by the well-known formula:

$$\frac{R_{13}}{R_{12}} = \frac{\Omega_{13}}{\Omega_{12}} \exp\left[-\frac{E_{23}}{k_B T_U}\right]. \quad (4.6)$$

where the collision strengths are once again considered to be independent of energy.

For a κ electron energy distribution, again for the constant Ω case, the collisional excitation rate ratio is given by:

$$\frac{R_{13}}{R_{12}} = \frac{\Omega_{13}}{\Omega_{12}} \left[\frac{E_{13} + (\kappa - \frac{3}{2})k_B T_U}{E_{12} + (\kappa - \frac{3}{2})k_B T_U} \right]^{-\kappa}, \quad (4.7)$$

where T_U is the kinetic or internal energy temperature.

4.5. Collision strength considerations

4.5.1. “Non-averaged” and Effective Collision Strengths

Equations (4.3) and (4.4) emphasise the importance of a knowledge of the collision strength over all energies. In all the current literature, an M-B distribution has been assumed, and the effective collision strengths used are the collision strengths averaged over M-B energy distributions at different temperatures. It should be noted that this averaging process is calculated for a fixed population of electrons, N_e . Thus the full equation for deriving the effective collision strengths, Υ_{12} , from the collision strengths, Ω_{12} , for collisional excitations from level 1 to level 2 is:

$$\Upsilon_{12}(T) = \frac{\int_{E=E_{12}}^{\infty} \Omega_{12}(E) \exp\left(\frac{-E}{kT}\right) d\left(\frac{E}{kT}\right)}{\int_{E=E_{12}}^{\infty} \exp\left(\frac{-E}{kT}\right) d\left(\frac{E}{kT}\right)}. \quad (4.8)$$

where E_{12} is the threshold energy for excitation from level 1 to level 2.

In the case of a κ -distribution, the weighting with energy in the integral is quite different, c.f. Equation (4.4), and a knowledge of the behaviour of the collision strength at high energy becomes much more important. It is therefore necessary to use the raw (non-energy averaged) collision strengths. While effective collision strengths have been published for almost all atomic species relevant to H II regions and PNe, the raw collision strength data are much harder to find.

For this work we have collated modern computed “raw” collision strength data for O I, N II, O III, S III, and O II, and older or limited data for S II, Ne III, Ar V, Ne IV, Ar IV, and Ne V. We have no raw collision strength data for N I. Our data sources are listed in Table 4.1.

An example of the complexity of the raw collision strength data is shown for the 1D_2 and 1S_0 levels of O III in Figure 4.1, where the data is taken from Palay et al. (2012, hereafter, PNPE12). Note the numerous resonances and edges, and the systematic variation with energy seen in the $^3P - ^1D_2$ transition.

The calculation of raw collision strengths is a very complex exercise, involving the coupling of many electrons, relativistic corrections, and a host of other computational issues. In

Table 4.1 Collision strength data sources

Species	Authors	Reference	URL/source
O III	Palay et al.	2012, MNRAS, 423, L35	Data from authors
O III	Aggarwal	1993, ApJS, 85, 197	Data digitised from paper
O III	Aggarwal & Keenan	1999, ApJS, 123, 311	Effective collision strengths only
O III	Lennon & Burke	1994, A&AS, 103, 273	TIPbase ¹
S III	Hudson et al.	2012, ApJ, 750, 65	Data from authors
Ar III	Galavís et al.	1995, A&AS, 111, 347	TIPbase
Ne III	Butler & Zeippen	1994, A&AS 108, 1	TIPbase
O II	Tayal	2007, ApJS, 171, 331	Data from author
N II	Hudson & Bell	2004, MNRAS, 348, 1275	APARC ²
N II	Tayal	2011, ApJS, 195,12	Data from author
S II	Tayal & Zatsarinny	ApJS, 2010,188, 32	Data from authors
O I	Barklem	2007, A&A, 462, 781	Data from author
Ar IV	Ramsbottom et al.	1997, MNRAS, 284, 754	APARC
Ar V	Galavís et al.	1995, A&AS, 111, 347	TIPbase

¹ The Iron Project database (TIPbase): <http://cdsweb.u-strasbg.fr/tipbase>

² APARC website: <http://web.am.qub.ac.uk/apa>

general, there has been a steady improvement in the techniques of computation, so we need to be careful in using data from older sources. Given that an accurate knowledge of collision strengths is essential for determining electron temperatures and elemental abundances in nebulae, the errors that may be present in published data sets is a concern. In the following sub-sections we consider the possible effects of truncation of the energy range of the computed collision strengths, errors in the computed excitation energies, and absolute errors in the computed collision strengths on the collisional excitation rates.

4.5.2. Errors in computed collision strengths

Our knowledge of the absolute value of the collision strengths feeds directly into measurements of electron temperatures and elemental abundances. Because of the complexity of calculating the collision strengths and the wide range of atomic species for which they are needed, these parameters are frequently only available at present from a single source, if at all. An exception to this is O III, but even for this important species, they have only been computed four times in the past two decades, and only once in the past decade (Aggarwal 1993; Lennon & Burke 1994; Aggarwal & Keenan 1999; Palay et al. 2012). Further, non-averaged collisions strengths (i.e., not convolved with M-B distributions) are difficult for the end user to obtain. See Table 4.1 above for details of the sources used.

These computations vary considerably in their details, the upper energy limit of the computations (the truncation energy), and what physics is taken into account. For O III, the most recent computations by PNPE12 appear much the most reliable, as they take into account relativistic effects and have a much higher truncation energy (178.2eV, c.f. 43.5eV for Aggarwal (1993) and 54.4eV for Lennon & Burke (1994)). For this reason the currently used values (see, e.g., Osterbrock & Ferland 2006) for calculating line flux ratios, and resultant electron temperatures, need to be revised, independently of any κ -distribution considerations.

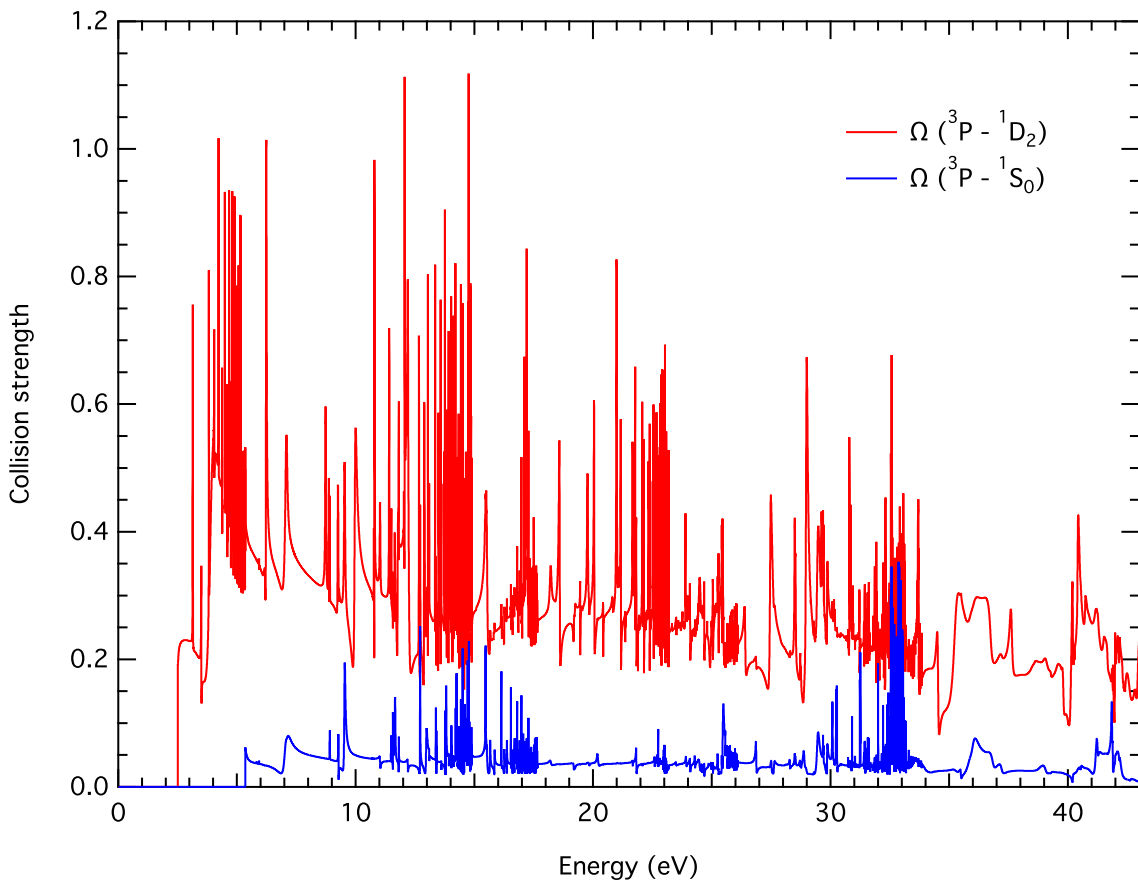


Figure 4.1 Computed collision strength data for O III from PNPE12, shown here to 43 eV. Note the numerous resonances and edges, and the variation with energy in the $^3P - ^1D_2$ transition.

We use the PNPE12 data and detailed numerical integration as the baseline. This became available only after the finalisation of our earlier paper. The differences between these and earlier computations can lead to considerable differences in electron temperatures computed from CEL flux ratios, even for M-B equilibrium electron energy distributions. Figure 4.2 shows that use of the earlier data sources leads to systematic overestimates of [O III] electron temperatures for temperatures between 5,000 and 30,000 K. The IRAF 2.14 results were obtained using the nebular/temden routine, which for the 11/2008 release adopts the Lennon & Burke (1994) effective collision strengths⁴.

The overestimate of [O III] electron temperatures implied by Figure 4.2 has a profound impact upon all previous abundance analyses of PNe and H II regions, even before taking into account the effect of non-equilibrium κ electron energy distributions. Wherever the T_e + ionisation correction factor (ICF) method has been used, the overestimate in T_e will result in a significant under-estimate in the chemical abundance. The strong line techniques are also liable to revision, as the collision strength for the [O III] $^3P - ^1D_2$ transition is enhanced by about 30% over the previous estimates. The effect on the strong line methods is discussed briefly in Section 8, below, but these and other strong line effects will be the subject of a later paper.

⁴PyNeb, a revised and extended Python-based version of the IRAF nebular/temden routines has been developed (Luridiana et al. 2012) that uses more recent collision strength data than the older IRAF code. While it incorporates the O III data from Palay et al. (2012), this needs to be set as the default, manually.

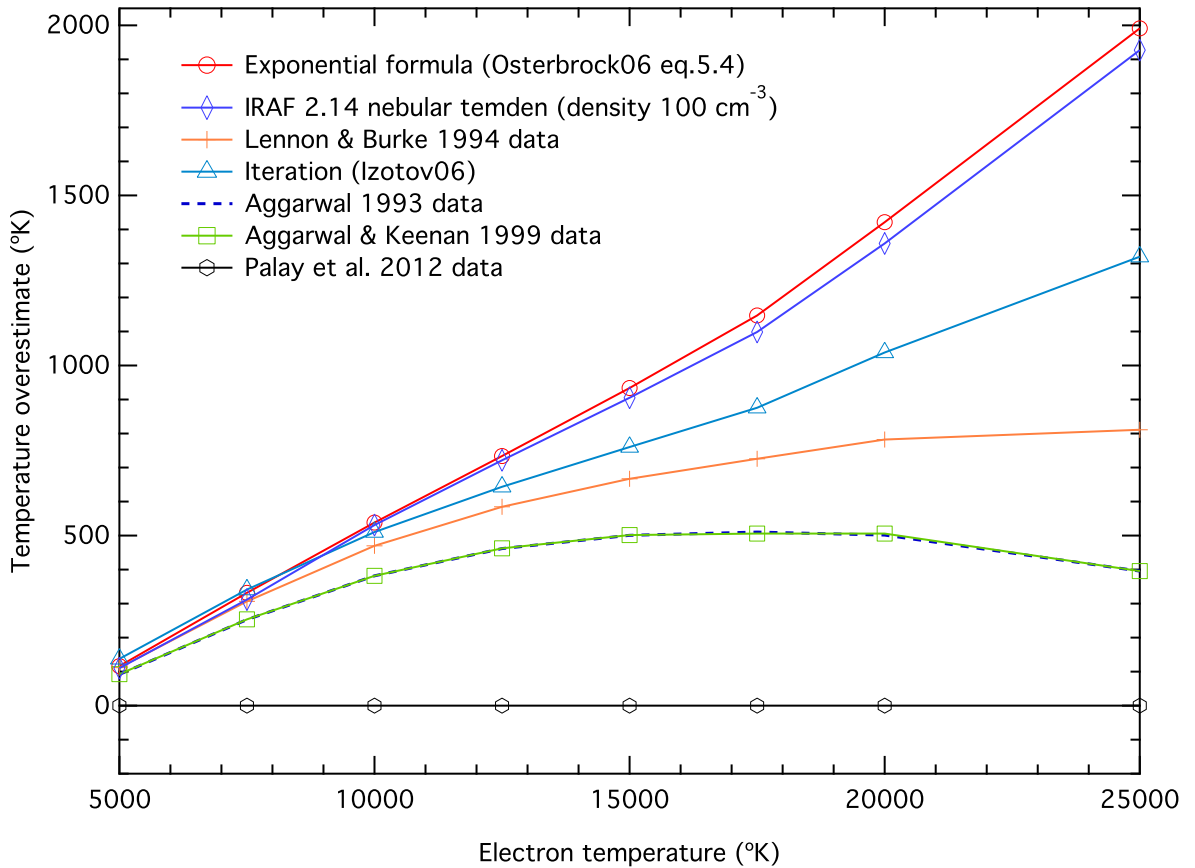


Figure 4.2 Temperature excesses resulting from computing (M-B equilibrium) electron temperatures from [O III] flux ratios, using older effective collision strength data, and approximate methods, compared to the results obtained using effective collision strengths derived from the latest data from PNPE12.

4.5.3. Errors in computed excitation energies

Also critical to the accurate estimation of collision strength effects are errors in the computed threshold energies of the excited states. In some computations (e.g., Aggarwal (1993); Aggarwal & Keenan (1999) for O III), there are non-trivial differences between the computed and the observed energies. PNPE12 note that although their computed energies for O III were quite close to the experimentally determined values, errors in effective collision strengths can arise from threshold energy discrepancies for low temperature excitations dominated by near-threshold resonances. They minimise these by adjusting the threshold energies to match the observed excitation energies. In the case of κ distribution, where we integrate the raw collision strengths directly, it is essential that the threshold energies used in the integration (E_{12} and E_{13} in Equation (4.7)) correspond exactly to the values expressed in the collision strength data. Using a threshold energy from a standard source that differs from the threshold indicated by the particular collision strength computations, can introduce errors in the excitation rate ratios, and, therefore, in the abundances determined assuming M-B equilibrium and the enhancement effects of a κ distribution.

4.5.4. Truncation of collision strength computations

Finally, we need to consider the effect of truncating computations of collision strengths at high energies. Collision cross sections are calculated between the species excitation threshold energy and a computationally mandated upper limit. For the cross sections of O III published in the past 20 years, this upper limit has ranged between 43.5eV (Aggarwal 1993) and 178.2eV (Palay et al. 2012). Effective collision strengths are computed by convolving the raw collision strengths with an M-B distribution, as in Equation (4.8). For temperatures typically found in H II regions and PNe, the population in the M-B distribution at high energies is sufficiently small that the truncation point for the raw collision strengths has little effect on the value of the effective collision strength. However, κ distributions can have significant populations at higher energies compared to the M-B, and the effect of truncating the collision strength computation can become much more apparent.

To demonstrate this effect, using an extreme case with $\kappa=2$, we adopt a simple model collision cross section: $\Omega =$ zero below the excitation threshold, Ω constant ($=1$) up to the truncation energy, and zero above that. Specifying an excitation threshold energy allows us to explore the effect of truncating the upper energy bound for the collision strength. In this case we use 3.0eV, which sets the temperature of the point where $\Delta E/k_B T = 1.0$ to $T_{exc}=34,814\text{K}$. We compare the computed truncated solution with the untruncated analytical solution, Equation (4.5), in which Ω is constant to ∞ . Figure 4.3 shows the percentage difference between the computed values and the analytical value at low values of the parameter $\Delta E/k_B T$ (i.e., at high temperatures), truncating at 20, 50, 100 and 200eV.

The effect is minor at low temperatures; for truncations above $\sim 50\text{eV}$ and temperatures typically found in H II regions and PNe; and for values of $\kappa \gtrsim 10$. In the EUV and in some supernova remnants, and for extreme values of $\kappa \gtrsim 1.5$, the effect may need to be considered, both for κ and M-B energy distributions.

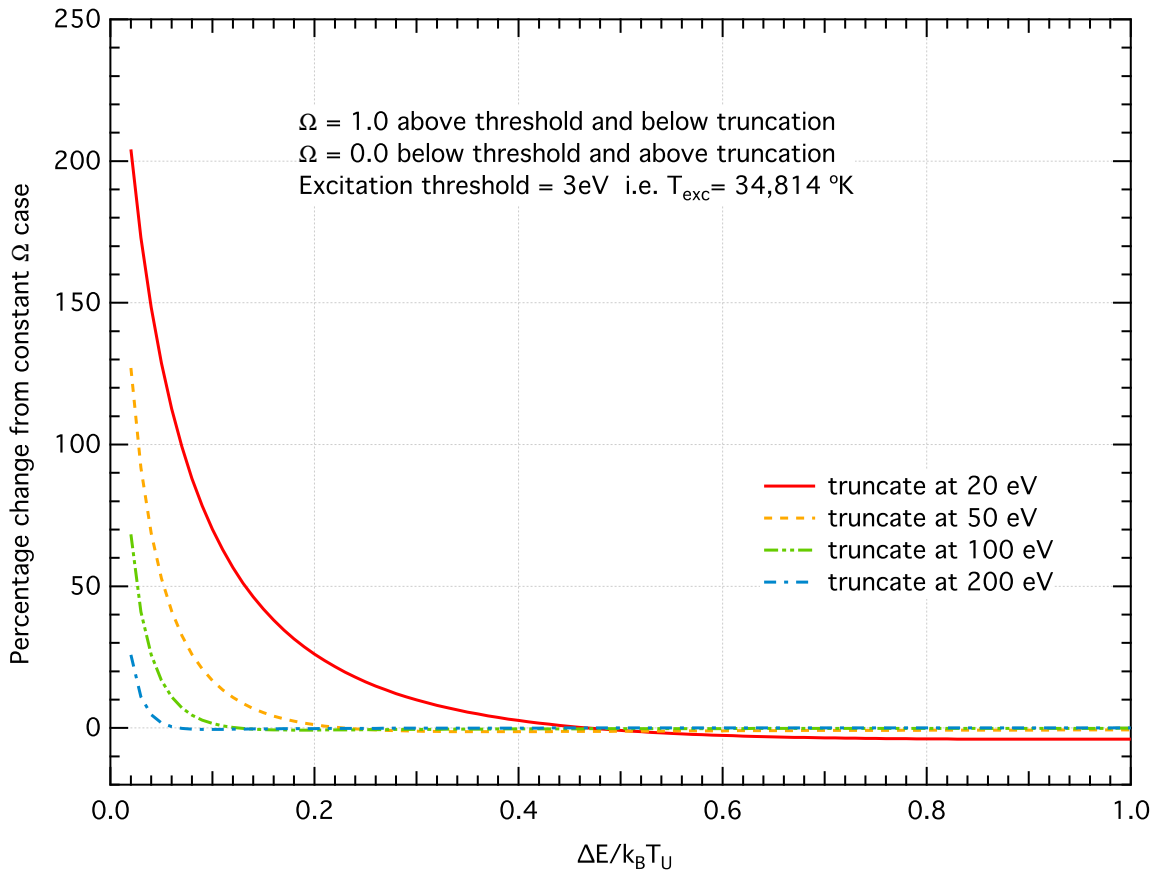


Figure 4.3 Effect on the excitation rate of truncating the collision strength computations at a range of energies, for a $\kappa=2$ distribution.

4.6. The Effect of κ on recombination processes

In this section, we examine first the effect of the κ -distribution on the recombination process. This links directly to the shape of the bound-free continuum which is used to determine recombination temperatures of H and He, and to the observed intensity of the recombination lines of heavy elements, which are used to determine chemical abundances.

4.6.1. Recombination line effects

One major consequence of adopting a κ distribution for electron energies arises when comparing abundances determined using ORLs and CELs. In the vast majority of H II regions and PNe, the ORL abundance is systematically higher than the abundance derived from CEL measurements, the so called “abundance discrepancy factor”, or ADF. This has been known for decades and not satisfactorily explained (see, e.g., [Stasińska 2004](#)). As [NDS12](#) have pointed out, the κ distribution provides a simple and automatic explanation of the abundance “discrepancy”. The reason for this can be understood by comparing the form of the κ distribution to that of the M-B distribution.

The key characteristics of the κ distribution, compared to an M-B distribution of the same internal energy, are that the peak of the distribution moves to lower energies; at intermediate energies there is a population deficit relative to the M-B distribution; and at higher energies

the “hot tail” again provides a population excess over the M-B. (See Figures 1-3 of [NDS12](#)). The κ distribution behaves as an M-B distribution at a lower peak temperature, but with a significant high energy excess.

The two distributions peak at different values of the energy, E . The peak of the Maxwell distribution (for the energy form of the distribution) is at $E = \frac{1}{2}k_B T_U$. For the κ distribution, the peak occurs at $\frac{1}{2}k_B T_U(2\kappa - 3)/(2\kappa + 1)$ ([NDS12](#)). Thus, for all valid values of κ ($\frac{3}{2} < \kappa < \infty$), the κ distribution peaks at a lower energy than the M-B. This is illustrated in Figure 4.4, for $\kappa = 2$.

For recombination, or any other physical process that is primarily sensitive to the low energy electrons, the critical point to note is that the form of the κ distribution at lower energies (up to and just past the peak energy) is very similar indeed to an M-B distribution. This is shown in Figure 4.4, where an M-B distribution (blue solid curve) has been peak-fitted to a $\kappa = 2$ distribution (red, dashed curve), adjusting the M-B temperature to $T_{core} = T_U(1 - \frac{3}{2\kappa})$ and matching peak heights. The total area under the M-B “core” is less than the area under the κ curve.

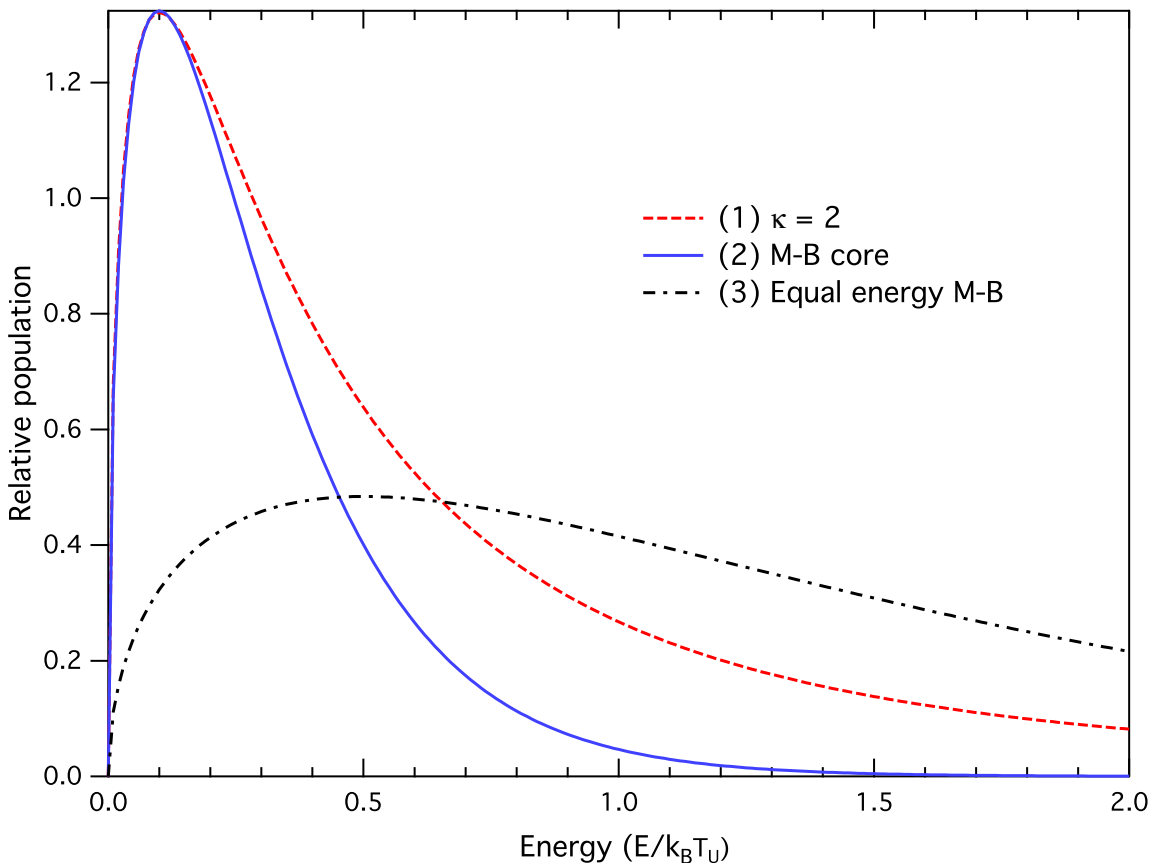


Figure 4.4 κ , best-fit M-B and equal energy M-B distributions: (1) Red dashed curve: $\kappa = 2$ distribution; (2) blue curve: “core” M-B distribution fitted to the κ peak; (3) black dash/dot curve: M-B distribution with the same internal energy as the κ . The areas under the red (dashed) and black (dot-dashed) curves (i.e., the total electron densities) are equal, and greater than the area under the blue curve.

For any physical process that involves mainly the low energy electrons, such as recombination line emissions, reactions “see” the cool M-B core distribution. In other words, any physical property sensitive to the region of the electron energy distribution around or below

the distribution peak will interact with a κ electron energy distribution as if it were an M-B distribution at a lower temperature than the M-B with the same kinetic temperature and electron density as the κ distribution, and with a slightly lower total internal energy than the κ -distribution.

So how does this impact on recombination line abundances and temperatures? In order of importance, the first effect of the kappa distribution on ORLs is the difference between the apparent temperature of the low energy part of the energy distribution that is most important in determining the intensities of the recombination lines, compared to the true internal energy temperature. The second effect arises from the population of electrons in the energy peak of a kappa distribution, compared to the total population. The third effect is the slight difference in shape between the peak of a kappa distribution and the best fit M-B distribution.

4.6.2. Correcting the recombination temperature

First, the most obvious effect of a kappa distribution is that it shifts the peak of the energy distribution to lower energies, compared to an M-B distribution with the same kinetic temperature. The recombination rate falls off strongly with increasing energy—for hydrogen below the photoionisation threshold, the recombination rate depends on ν^{-3} (e.g., [Osterbrock & Ferland 2006](#)). This means that the low energy electrons play the dominant role in recombination processes. Recombination processes experience the κ distribution as an M-B distribution at a temperature T_{core} . Thus, in using recombination temperatures in the presence of κ distributions to estimate the kinetic or internal energy temperature, T_U , we need to increase the apparent recombination line temperature by a factor:

$$T_U/T_{core} = \kappa/(\kappa - 3/2). \quad (4.9)$$

The difference between the distributions is visually slight for higher kappa values (smaller deviation from thermal equilibrium), but even minor deviations from equilibrium can be sufficient to explain the ADF.

4.6.3. Correcting the electron density

Second, we need to apply a correction to the apparent electron density. The reason for this is that an M-B distribution at a temperature T_{core} and with the *same* total energy as the κ distribution with a kinetic temperature T_U will have a peak at a *higher* value of $n(E)$ than the κ . To fit the M-B distribution to the κ —in other words, to simulate what recombination processes react to when they meet a κ distribution—it is necessary to reduce the total electron density by a factor that depends on κ .

We can calculate the electron density correction analytically by equating the peak of the M-B electron energy distribution $n(E)$ at a temperature T_{core} to the peak value of the κ distribution at a temperature T_U . It is relatively straight forward to show that the effective (apparent) electron density, $N_e(\text{eff})$ is related to the actual electron density N_e , by:

$$\frac{N_e(\text{eff})}{N_e} = \frac{((\kappa + 1)/(\kappa + \frac{1}{2}))^{\kappa+1} \sqrt{(\kappa + \frac{1}{2})(\kappa - \frac{3}{2})} \Gamma(\kappa - \frac{1}{2})}{\Gamma(\kappa + 1) \sqrt{e}}. \quad (4.10)$$

For values of $\kappa \gtrsim 10$, this factor is close to unity, and in most conditions likely to be found in H II regions and PNe (NDS12) is unlikely to substantially affect the physics. The correction factor is shown in Figure 4.5 as a function of κ . The recombination process “sees” a lower electron density for all values of κ , but for typical values ~ 10 , the difference between effective and true electron densities is less than 10%.

For computational purposes, the curve can be fitted with a simple power law (reciprocal), also shown in Figure 4.5:

$$\frac{N_e(\text{eff})}{N_e} = 1.0 - 0.8/(\kappa - 0.72). \quad (4.11)$$

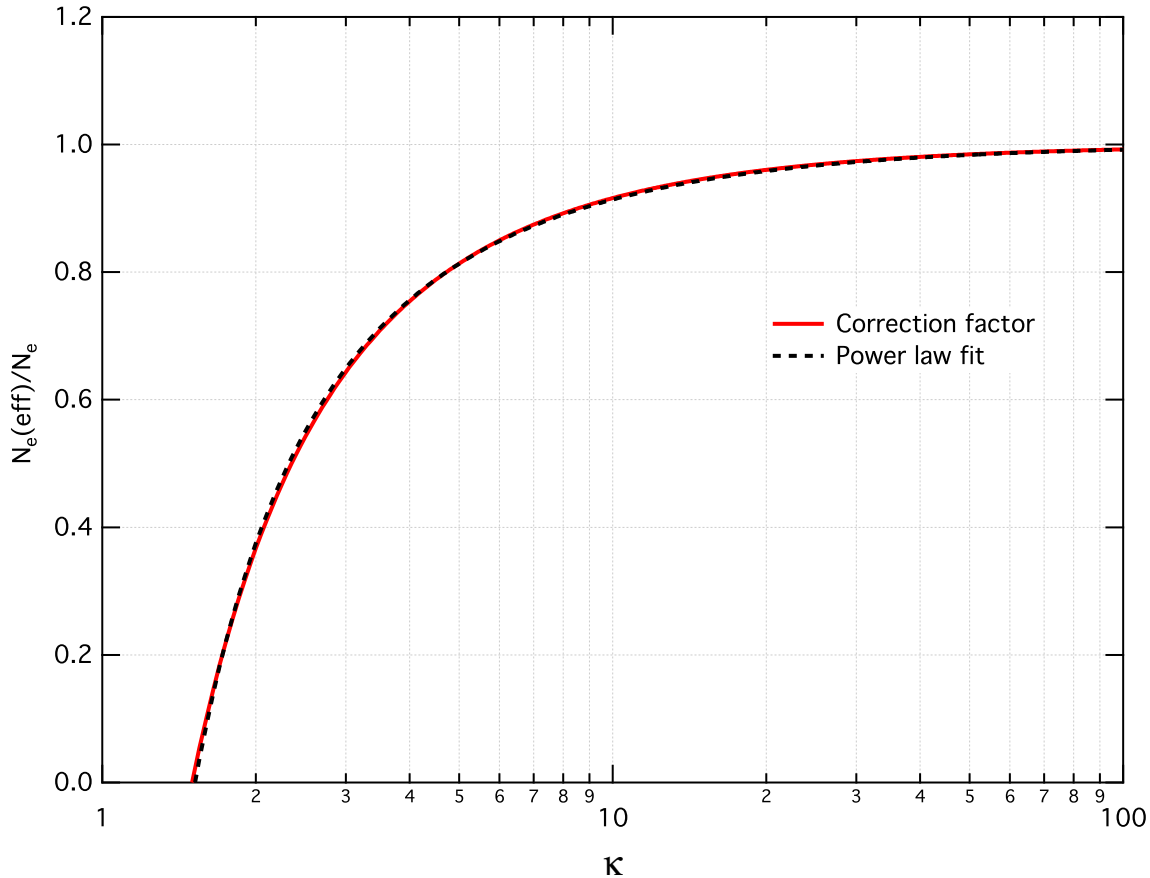


Figure 4.5 Electron density correction as a function of κ

4.6.4. Correcting the low energy shape of the distribution

The third effect is that the shape of the “fitted” M-B distribution differs slightly from the peak of the κ distribution. Figure 4.6 shows the difference in recombination electrons as a function of $\Delta E/k_B T_U$, using a weighting factor of $1/E$ to account for a typical energy dependence of the recombination process, and normalised so that the total number of electrons at the distribution peaks are the same. It shows that for a typical value of κ of 10, the difference in the κ distribution and the fitted M-B leads to an error of less than 2%.

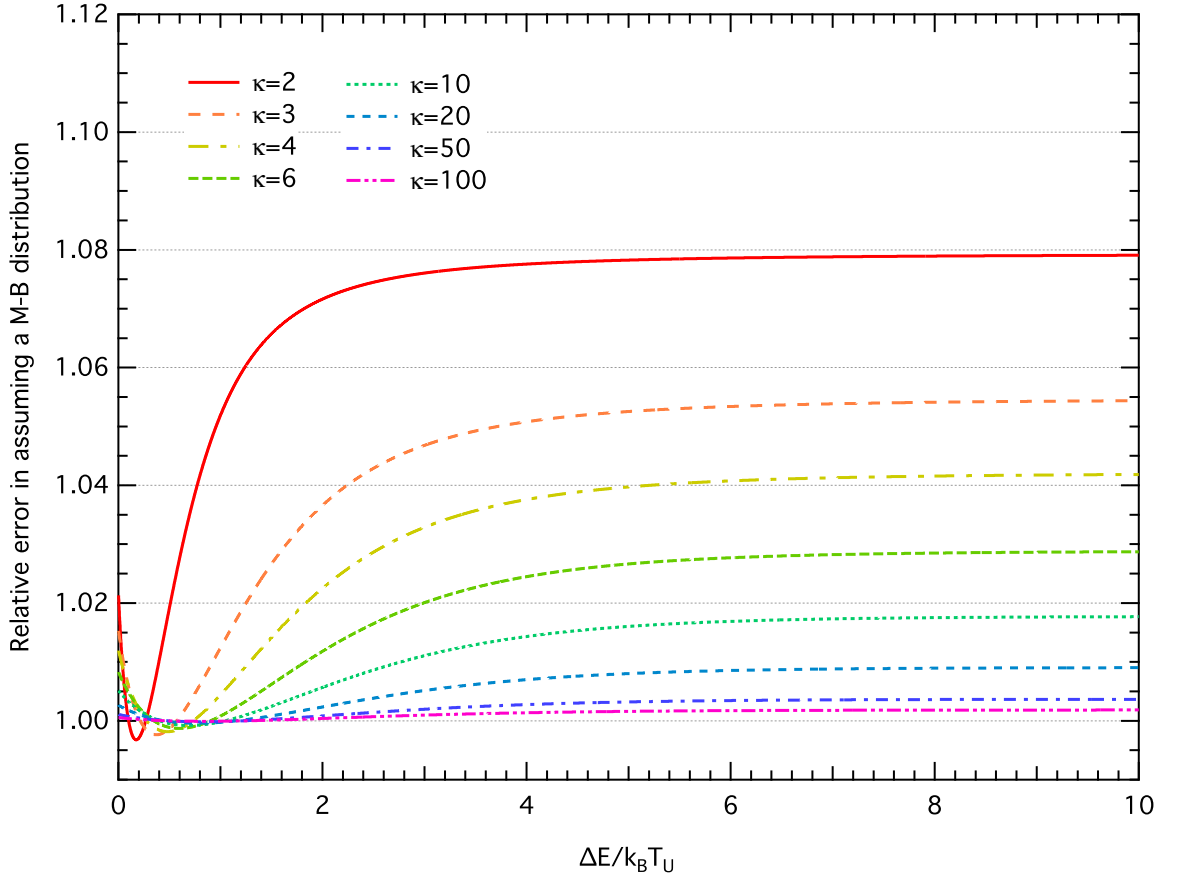


Figure 4.6 Error in assuming a fitted M-B distribution instead of a κ distribution, as a function of $\Delta E/k_B T_U$ and κ

4.6.5. Effect of κ on recombination rates

The recombination rate (in $\text{s}^{-1} \text{cm}^{-3}$) for hydrogen ions combining with electrons is given by $N_e N_p \alpha$, where N_e and N_p are the densities of electrons and protons and α is the recombination rate, which for an electron energy distribution $f(E)dE$ is given by:

$$\alpha = \int_0^{\infty} \sqrt{\frac{2}{m_e}} \sqrt{E} \sigma(E) f(E) dE, \quad (4.12)$$

where $\sigma(E)$ is the recombination cross section. It is related via the Milne Relation to the ionisation cross section a_ν by:

$$\sigma(E) = \frac{g_1}{g_2} \frac{2h^2 \nu^2}{m_e c^2} \frac{1}{E} a_\nu, \quad (4.13)$$

where $g_{1,2}$ are the statistical weights of the lower and upper levels, h is the Planck constant, m_e is the electron mass, c is the speed of light and ν is the photon energy above the threshold (expressed as a frequency).

For hydrogen, a_ν can be expressed approximately as:

$$a_\nu = a_T \left(\frac{\nu}{\nu_T} \right)^{-3}, \quad (4.14)$$

where a_T is the threshold value of the ionisation cross section and ν_T is the threshold frequency.

Inserting these values into Equation (4.12) and gathering the energy-independent components outside the integral we get:

$$\alpha = \sqrt{\frac{2}{m_e}} \frac{g_1}{g_2} \frac{2h^2 v^2}{m_e c^2} a_T \left(\frac{v}{v_T}\right)^{-3} \int_0^\infty \frac{1}{\sqrt{E}} f(E) dE \quad (4.15)$$

We can calculate the ratio of the recombination rates for a κ distribution to an M-B distribution by substituting the appropriate forms for $f(E)$:

$$\frac{\alpha_\kappa}{\alpha_{M-B}} = \int_0^\infty \frac{1}{\sqrt{E}} f_\kappa(E) dE \bigg/ \int_0^\infty \frac{1}{\sqrt{E}} f_{M-B}(E) dE \quad (4.16)$$

This simplifies to a form similar to the analytical expression for collisional excitation with a constant collision strength from Equation (4.5), but in this case with $E_{12} = 0$:

$$\frac{\alpha_\kappa}{\alpha_{M-B}} = \frac{\Gamma(\kappa + 1)}{(\kappa - \frac{3}{2})^{3/2} \Gamma(\kappa - \frac{1}{2})} \left(1 - \frac{3}{2\kappa}\right) \quad (4.17)$$

This implies the hydrogen ion recombination rates are enhanced, but for a typical value, $\kappa=10$, only by 4.3%. Typical values for the recombination rate ratios are given in Table 4.2:

Table 4.2 Recombination rate ratios as a function of κ

κ	2	3	4	6	10	20	50	100
$\alpha_\kappa/\alpha_{M-B}$	1.59577	1.22842	1.14184	1.08073	1.04338	1.02011	1.00771	1.0038

4.6.6. Recombination lines: summary

In summary, when interpreting a κ distribution as if it were an M-B distribution: (1) apparent recombination temperatures need to be increased by a factor $\kappa/(\kappa - 3/2)$; (2) apparent electron densities need to be divided by the correction factor in Equation (4.10), to get the true electron densities and kinetic temperatures; (3) the “shape” correction is sufficiently small that it can be neglected; and (4) recombination rates are slightly enhanced, as per Table 4.2 and Equation (4.17). Note that the corrections to the recombination rate are only applicable to recombination of ions with recombination coefficients similar to hydrogen.

4.7. Collisionally Excited Lines

4.7.1. Effect on CEL Intensities

In Figure 4.7 we show, for $\kappa = 10$ and a kinetic (internal energy) temperature $T_U=10,000$ K, the relative collisional excitation rate relative to an M-B distribution as a function of T_{exc}/T_U for the [O III] λ 4363 auroral line, computed using the detailed collisions strengths for O III from PNPE12. Any other CEL would produce a similar curve, so Figure 4.7 provides a

generic description of the effects of a κ -distribution on CEL intensities. Note that for a fixed kinetic temperature T_U , positions along the x-axis correspond to values of the CEL excitation temperature in units of 10^4K . The axis could equally well be looked at by scaling the kinetic temperature for a fixed excitation temperature, but here we want to differentiate the effects of κ on lines with different excitation temperatures at a fixed kinetic temperature.

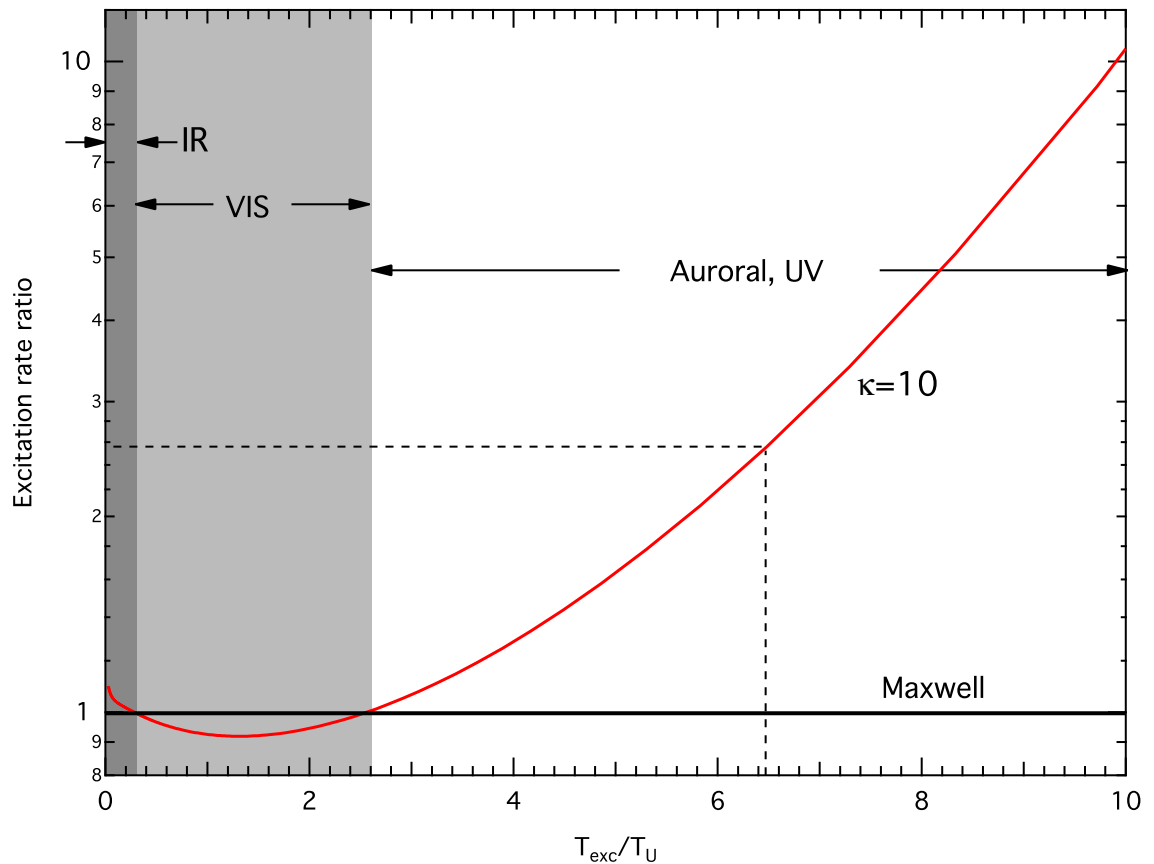


Figure 4.7 The collisional excitation rate for $\kappa=10$ compared to an M-B distribution, plotted as a function of the excitation threshold energy (expressed as an equivalent temperature) divided by the kinetic temperature T_U . Setting the kinetic temperature T_U to a typical nebular temperature of 10^4K allows us to locate the excitation temperature of the $\text{O III } ^1S_0$ level. It is marked by the vertical dashed line. Where this intercepts the κ curve shows the enhancement of the excitation rate ratio (and therefore, of the population in that level, relative to the M-B population). This illustrates the generic behaviour of all CELs. When T_{exc}/T_U is low, such as for transitions in the IR and FIR, the emission line intensities are slightly enhanced (dark grey area). In the central (light-grey) region typical of transitions giving rise to lines at optical wavelengths, a mild reduction in line intensity is expected. For $T_{exc}/T_U \gtrsim 3$, appropriate UV or “auroral” line intensities are either enhanced or strongly enhanced.

So what does this mean for different atomic species, energy levels and radiative transitions? Figure 4.7 can be divided into three parts, marked in different shades. The left-most dark grey segment corresponds to fine-structure levels with low excitation energy. These typically correspond to far infrared lines. For such levels, the population rate is slightly enhanced, leading to slightly higher line fluxes.

The middle section (mid-gray) corresponds to the excitation of the strong visible transitions, with excitation energies of a few eV. An example would be the $[\text{S II}]$ lines at 6731\AA and 6716\AA , with excitation temperatures of $\sim 21,400\text{K}$ (for $T_U=10,000\text{K}$, this corresponds to $x=2.14$

in Figure 4.7). The collisional excitation rates for these lines are mildly reduced in a κ -distribution compared to an M-B distribution.

The third, right-most section shows the excitation energies where the population rate will be enhanced or strongly enhanced by the κ distribution, compared to the M-B. This region is appropriate to either highly-excited UV lines, or the “auroral” lines in the visible spectrum. Examples include the [O III] UV lines at 2321, 2331Å and the auroral line at 4363Å, with an excitation temperature of $\sim 62,000$ K corresponding to $x=6.2$ in Figure 4.7.

In summary then, for a κ distribution the far-IR transitions are slightly enhanced, and the strong emission lines used in the optical to obtain CEL abundances will be mildly reduced. However, we expect the UV lines, such as the important C II or C III intercombination lines, to be strongly enhanced, and the “auroral” lines used in temperature diagnostics also to show strong enhancements in more metal-rich H II regions.

The relative effect of κ at different metallicities is interesting to consider. Plasmas with higher metallicities cool faster than plasmas with low metallicities. If we set the kinetic temperature for Figure 4.7 to 20,000 K, i.e., to a lower metallicity, the excitation temperatures are now scaled in units of 2×10^4 K. Thus for the O III 1S_0 level, the excitation temperature occurs at $x \sim 3.1$, and at this point on the curve, the excitation enhancement by the κ distribution is much lower, ~ 1.1 , c.f. ~ 2.6 . The precise effect on the line flux ratio used to measure the electron temperature depends as well on the relative enhancement of the 5007Å and 4959Å lines, which will also fall with lower metallicities. The process is not simple because of the interconnected effects, and is best explored with photoionisation models that take the κ effects into account. We have extensively updated the Mappings photoionisation code to take into account both the κ effects and the latest atomic data. We explore these effects in a subsequent paper (Dopita et al. 2013) using this code.

In the following section we explore the explicit effects of the κ distribution on line flux ratios.

4.7.2. Temperature-sensitive line ratios

CEL ratios are central to the measurement of electron temperatures in H II regions and PNe. Most frequently, the ratio of optical forbidden lines of O III at 5007Å, 4959Å to the “auroral” transition at 4363Å has been employed. However, many others can be used when bright lines are observed, such as the [N II], [O II], [S II], [S III], [Ar III], [Ar IV], [Ar V], or [Cl III] forbidden line ratios (see, e.g., Peimbert 2003). The measurement of electron temperatures depends on having two well-separated excited fine-structure energy levels for which an equation of the form of Equation (4.6) or (4.7) applies. An idealised three energy level arrangement is shown in Figure 4.9(a), which illustrates the transitions involved in the formation of temperature-sensitive line ratios.

Among the species actually employed to measure electron temperatures, there are two principal energy level structures. The first of these are the p^2 ions such as O III, and the p^4 ions such as O I, which have a very similar fine-structure level configuration, as shown in the second panel of Figure 4.8 (case a). The second group consists of the p^3 ions, such as O II, which has a doublet structure in the excited states as shown in the third panel of Figure 4.8 (case b). These ions are most frequently used to determine electron densities since the

closely spaced excited states have different transition probabilities, and undergo collision de-excitation at different densities.

The p^2 and p^4 ions have a triplet ground state ($^3P_0, ^3P_1, ^3P_2$) and singlet upper states, 1D_2 (lower) and 1S_0 (upper). Examples include N II, O III, S III, Ne V and Ar V (p^2 configuration) and O I, Ne III, and Ar III (p^4 configuration). The p^3 ions have a single ground state (usually $^4S_{3/2}$) and a pair of closely spaced doublet upper states, usually $^2D_{3/2}, ^2D_{5/2}$ (lower) and $^2P_{1/2}, ^2P_{3/2}$ (upper). Examples of this form include N I, O II, S II, Ar IV, and Ne IV.

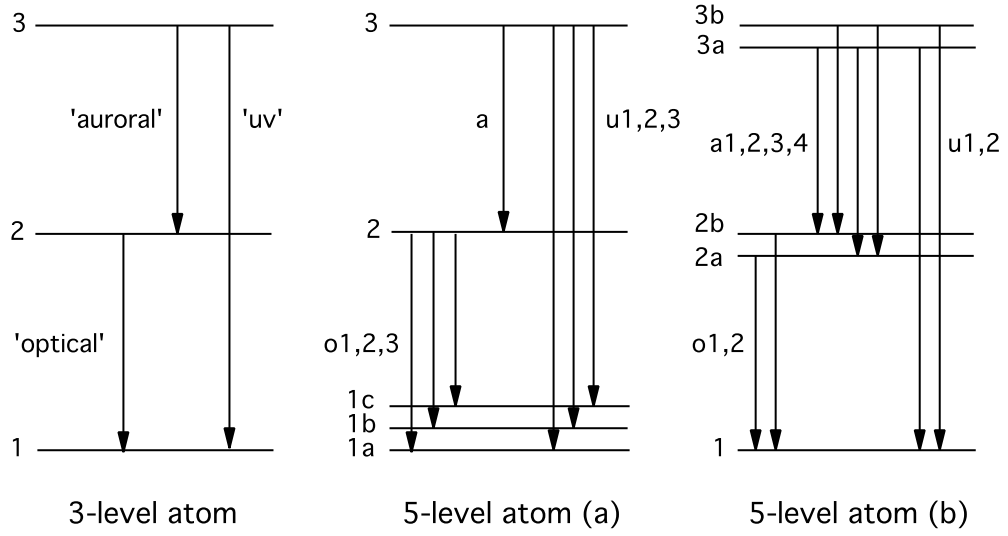


Figure 4.8 Energy level arrangements for temperature-sensitive line ratios. The left diagram illustrates the simplified three-level arrangement illustrating the lines involved. The centre diagram represents the level configuration for p^2 and p^4 ions, and the right hand panel, p^3 . The doublet and triplet spacings are not drawn to scale. Some lines arise from doubly-forbidden transitions with very low transition probabilities.

To calculate the flux ratio, we must take into account the branching ratio for transitions from the uppermost state, the summed transition probabilities for transitions to multiple ground states, and the transition-probability-averaged energies for the multiple optical lines. For the p^2 or p^4 ions (case a), the general expression for the ratio of flux of the auroral line from level 3 to 2 to the fluxes of the optical lines from level 2 to 1b and 2 to 1c (ignoring the doubly forbidden line from level 2 to 1a) is given by the a generalised inverse of Equation 5.1 in [Osterbrock & Ferland \(2006\)](#):

$$\frac{j_{\lambda a}}{j_{\lambda o2} + j_{\lambda o3}} = \frac{\bar{\Upsilon}_{13}}{\bar{\Upsilon}_{12}} \left[\frac{A_a}{A_a + \Sigma A_u} \right] \frac{(A_{o2} + A_{o3})\nu(\lambda_a)}{A_{o2}\nu(\lambda_{o2}) + A_{o3}\nu(\lambda_{o3})} \exp \left[\frac{-E_{23}}{k_B T} \right], \quad (4.18)$$

where E_{23} is the energy gap between the two singlet states, $\bar{\Upsilon}_{12}$ and $\bar{\Upsilon}_{13}$ are the (mean) effective collision strengths for collisional excitation from the triplet ground states to the lower and upper singlet states, given by (e.g.,):

$$\bar{\Upsilon}_{12} = \frac{\Upsilon_{1a \rightarrow 2} g_{1a} + \Upsilon_{1b \rightarrow 2} g_{1b} + \Upsilon_{1c \rightarrow 2} g_{1c}}{g_{1a} + g_{1b} + g_{1c}}, \quad (4.19)$$

and where g_{1a} , g_{1b} and g_{1c} are the statistical weights of levels 1a, 1b, and 1c; and ΣA_u is the total transition probability for the transitions between the upper singlet state (3) and the triplet ground states (1a, 1b and 1c),

$$\Sigma A_u = A_{u1} + A_{u2} + A_{u3} . \quad (4.20)$$

In practice, one of the transitions from the singlet upper state to one of the triplet ground states is doubly forbidden and its transition probability is negligible. The term in Equation (4.18) in the square brackets is the branching ratio, i.e., the fraction of atoms excited to level 3 that decay to level 2, and the term following that is the energy weighting for the transition probabilities.

For the p^3 ions, the expression for the flux ratio is similar to Equation (4.18):

$$\frac{\Sigma j_{\lambda a}}{j_{\lambda o1} + j_{\lambda o2}} = \frac{\Upsilon_{13}}{\Upsilon_{12}} \left[\frac{\Sigma A_a}{\Sigma A_a + \Sigma A_u} \right] \frac{(A_{o1} + A_{o2}) \bar{v}_a}{A_{o1} v_{o1} + A_{o2} v_{o2}} \exp \left[\frac{-E_{23}}{k_B T} \right] , \quad (4.21)$$

where

$$\bar{v}_a = \left(\frac{A_{a1} v_{a1} + A_{a2} v_{a2} + A_{a3} v_{a3} + A_{a4} v_{a4}}{\Sigma A_a} \right) , \quad (4.22)$$

and

$$\Sigma A_a = A_{a1} + A_{a2} + A_{a3} + A_{a4} , \quad (4.23)$$

and

$$\Upsilon_{12} = \Upsilon_{1 \rightarrow 2a} + \Upsilon_{1 \rightarrow 2b} , \quad (4.24)$$

with ΣA_u and Υ_{13} defined analogously.

For each of the ions we consider here, the values of the various constants entering in these equations are listed in the tables in the Appendix. As shown in Figure 4.8, the transitions ‘o1’ and ‘o2’ are the “optical” transitions, from the two middle levels to the ground state; transitions ‘a1’, ‘a2’, ‘a3’ and ‘a4’ are the four “auroral” lines from each of the upper levels to each of the middle levels; and transitions ‘u1’ and ‘u2’ are the “UV lines” from the upper two levels to the ground state (frequently in the optical, not the UV, spectrum). $\Sigma j_{\lambda a}$ is the total flux of the (four) auroral transitions, $j_{\lambda o1}$ and $j_{\lambda o2}$ are the fluxes of the two optical lines.

In some cases where wavelengths of the auroral lines are not well placed, it is more convenient to use the UV lines in combination with the optical lines to measure temperature dependent flux ratios. Examples where this is used in the IRAF/temden routine are S II, Ne IV and Ar IV. However, in principle, UV lines can be used equivalently to auroral lines. This can be useful at higher redshifts. As the UV and auroral lines both originate from the uppermost of the levels (3 or 3a, 3b in Figure 4.8), their relative fluxes are related via the branching ratio and the energies of the transitions. This may be expressed in general as a ratio:

$$\frac{\text{flux(UV)}}{\text{flux(auroral)}} = \frac{\sum_i (A_{ui} / \lambda_{ui})}{\sum_i (A_{ai} / \lambda_{ai})} \quad (4.25)$$

However, most of the p^3 ions are also strongly density sensitive, so flux ratios using these lines—auroral or UV—will only give useful temperatures at densities ($\lesssim 5 \text{ cm}^{-3}$).

4.7.3. Excitation rate ratios

The generalised version of Equations (4.6) and (4.7) for the energy-dependent Ω case are:

$$\frac{R_{13}}{R_{12}} = \frac{E_{13} \int_{E_{13}}^{\infty} \Omega_{13}(E) \exp[-E/k_B T_U] dE}{\int_{E_{12}}^{\infty} \Omega_{12}(E) \exp[-E/k_B T_U] dE} \quad (4.26)$$

for the M-B electron distribution and

$$\frac{R_{13}}{R_{12}} = \frac{E_{13} \int_{E_{13}}^{\infty} \Omega_{13}(E) / [1 + E / ((\kappa - \frac{3}{2})k_B T_U)]^{\kappa+1} dE}{\int_{E_{12}}^{\infty} \Omega_{12}(E) / [1 + E / ((\kappa - \frac{3}{2})k_B T_U)]^{\kappa+1} dE}, \quad (4.27)$$

for the κ -distribution.

We can now generalise the expression for the flux ratio for variable Ω s, using Equations (4.18) and (4.27):

$$\frac{j_{\lambda a}}{j_{\lambda o1} + j_{\lambda o2}} = f_1(A, \lambda) \frac{E_{13} \int_{E_{13}}^{\infty} \bar{\Omega}_{13}(E) / [1 + E / ((\kappa - \frac{3}{2})k_B T_U)]^{\kappa+1} dE}{\int_{E_{12}}^{\infty} \bar{\Omega}_{12}(E) / [1 + E / ((\kappa - \frac{3}{2})k_B T_U)]^{\kappa+1} dE}, \quad (4.28)$$

where

$$f_1(A, \lambda) = \left[\frac{A_a}{A_a + A_{u1} + A_{u2}} \right] \frac{(A_{o1} + A_{o2})\nu(\lambda_a)}{A_{o1}\nu(\lambda_{o1}) + A_{o2}\nu(\lambda_{o2})}, \quad (4.29)$$

and $\bar{\Omega}_{13}, \bar{\Omega}_{12}$ are the statistical weight averaged Ω s, defined analogously to Equation (4.19). This equation allows us to calculate the line ratios for any of the relevant atomic species and for any value of κ . The values of the parameter $f_1(A, \lambda)$ for several atomic species are given in Table 4.7 in the Appendix.

Similarly, Equation (4.21) can be generalised for non-M-B populations for the p^3 ions as:

$$\frac{j_{\lambda a}}{j_{\lambda o1} + j_{\lambda o2}} = f_2(A, \lambda) \frac{E_{13} \int_{E_{13}}^{\infty} \bar{\Omega}_{13}(E) / [1 + E / ((\kappa - \frac{3}{2})k_B T_U)]^{\kappa+1} dE}{\int_{E_{12}}^{\infty} \bar{\Omega}_{12}(E) / [1 + E / ((\kappa - \frac{3}{2})k_B T_U)]^{\kappa+1} dE}. \quad (4.30)$$

where

$$f_2(A, \lambda) = \left[\frac{\Sigma A_a}{\Sigma A_a + \Sigma A_u} \right] \frac{(A_{o1} + A_{o2})\bar{\nu}_a}{A_{o1}\nu_{o1} + A_{o2}\nu_{o2}}. \quad (4.31)$$

The values of the parameters for the p^3 ions are also given in Table 4.8 in the Appendix.

Tables 4.7 and 4.8 also show the values of $f_1(A, \lambda)$ and $f_2(A, \lambda)$ using the UV lines instead of the auroral lines.

4.7.4. Plotting the temperature-sensitive line ratios

The simplest way to determine the electron temperature T_e from the line ratios is to use the IRAF/SCSDS/nebular/temden routine (Shaw & Dufour 1995), or the more recent PyNeb code (Luridiana et al. 2012). Alternatively, one can use Osterbrock & Ferland (2006, Figure 5.1), reading off the temperature from the line ratio graph, using the inverse of Equation (4.12) above. This does not take into account that the collision strengths (and even the effective collision strengths) are not constant with temperature, but in general are complex functions of the energy above the threshold (see Figure 4.1). For an M-B distribution, one can use the effective collision strengths for each temperature, leading to a more accurate function of line ratio versus temperature. A further improvement to this process was used by Izotov et al. (2006) who derived an iterative formula to obtain T_e from the line ratio measurements.

However, current methods only apply where there is thermal equilibrium, and in the non-equilibrium κ distribution case, it is necessary to calculate the integrals in Equation (4.21) numerically, using the original collision strength data (not the thermally averaged values). This leads to a graph similar to that presented in Osterbrock & Ferland (2006), with a series of curves for each value of κ required. The result is simple to determine.

As noted for Equation (4.18), in this paper (except in section 3.7.1) we break with tradition and invert the equation, as it is easier to understand the correlation between an increasing upper state flux (j_{43}) and increasing electron temperature (T_e), and the plot is closer to a linear form.

Figure 4.9 shows the line flux ratio plotted against electron temperature for the forbidden transitions of [O III], for several values of κ .

Figure 4.10 is the same as Figure 4.9, but for the [S III] transitions. It differs noticeably from the [O III] case, owing to the lower excitation energy of the upper state of the 6312Å auroral line. The implication is that in extremely low metallicity, high electron temperature plasmas, above ~20,000 K, the effect of the κ distribution is to increase the kinetic temperature above the value suggested by assuming an M-B distribution, rather than the reverse which applies to [O III] transitions for similar metallicity and temperature environments.

Although it occurs at different temperatures for different atomic species, this crossover point in the line ratio flux plots appears to be a universal phenomenon, a point on the electron temperature scale where the collisional excitation generates a line flux ratio which is the same for any value of the parameter κ , including the M-B distribution.⁵

4.7.5. Comparison of [S III] and [O III] electron temperatures as a function of κ

Figures 4.9 and 4.10 above show that as κ varies, electron temperature measurements using the [S III] flux ratios will differ from equivalent measurements using the [O III] lines. Figure 4.11 shows how the two measurements relate to each other, and provides a means of estimating the value of κ and T_U by comparing the two measured electron temperatures.

⁵ A suitable term for the crossover is the 'isodierethitic point', from the (ancient) Greek ίσοσ(equal) and διερεθισις (excitation) (reference: Liddell, H. G. & Scott, R., rev. Jones, H. S. & McKenzie, R. 1940, *A Greek-English Lexicon* (Oxford: Clarendon Press)) Available at <http://stephanus.tlg.uci.edu/ljsj/#eid=1&context=lsj>

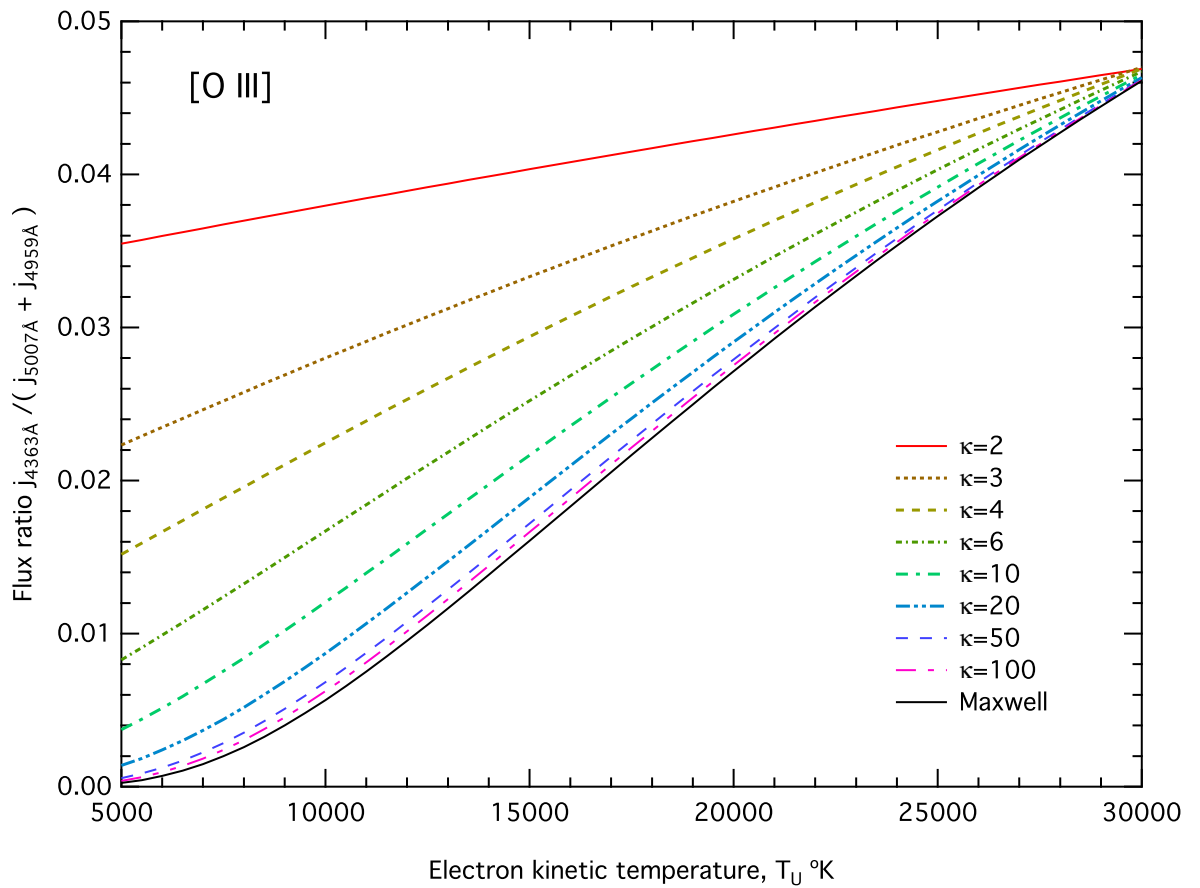


Figure 4.9 Temperature-sensitive line flux ratio curve for the O III forbidden lines using collision strength data from [PNPE12](#).

Values of the [S III] flux ratios determined assuming M-B equilibrium are plotted against similar values using the [O III] flux ratios, as a function of κ and the kinetic temperature, T_U . This demonstrates how the κ distribution can explain discrepancies between CEL temperatures from different species. See also Figure 7 from [Binette et al. \(2012\)](#).

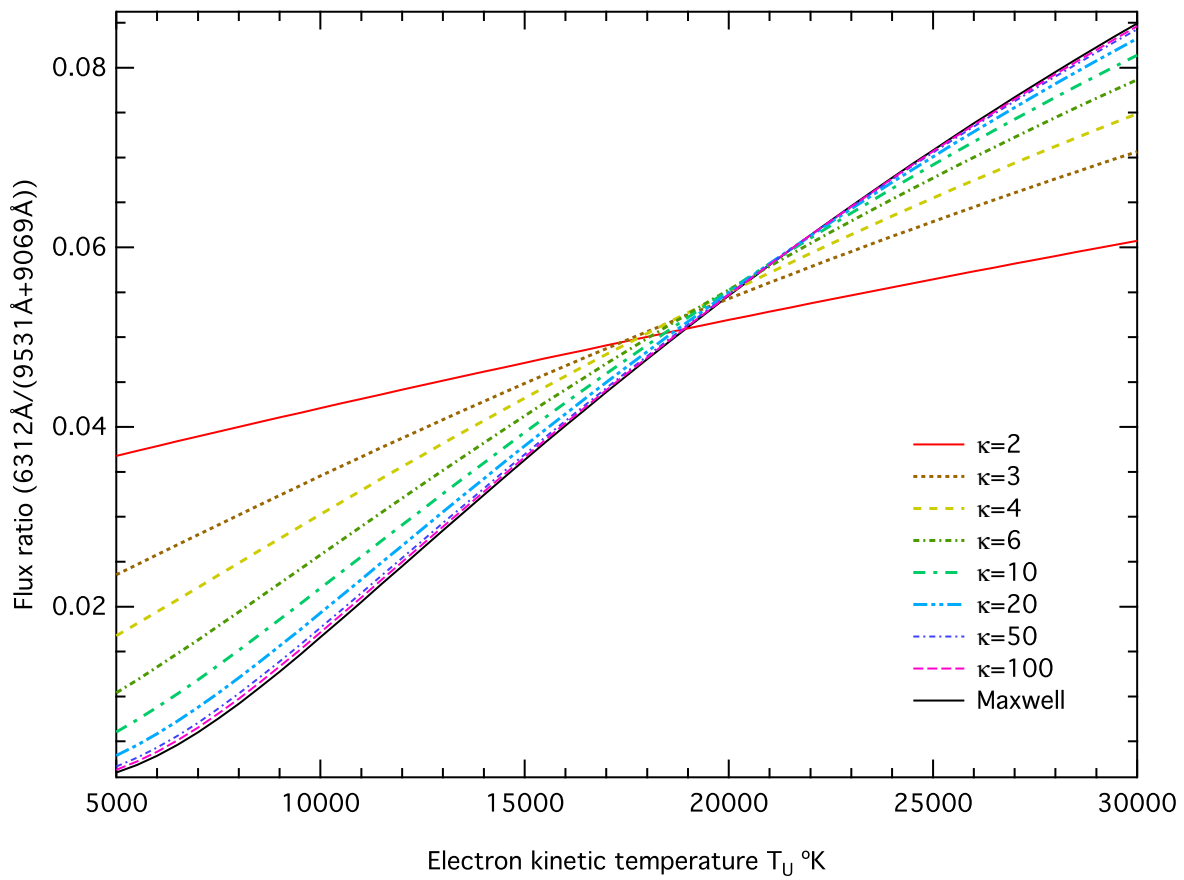


Figure 4.10 Temperature-sensitive line flux ratio curve for the S III forbidden lines using collision strength data from [Hudson et al. \(2012\)](#).

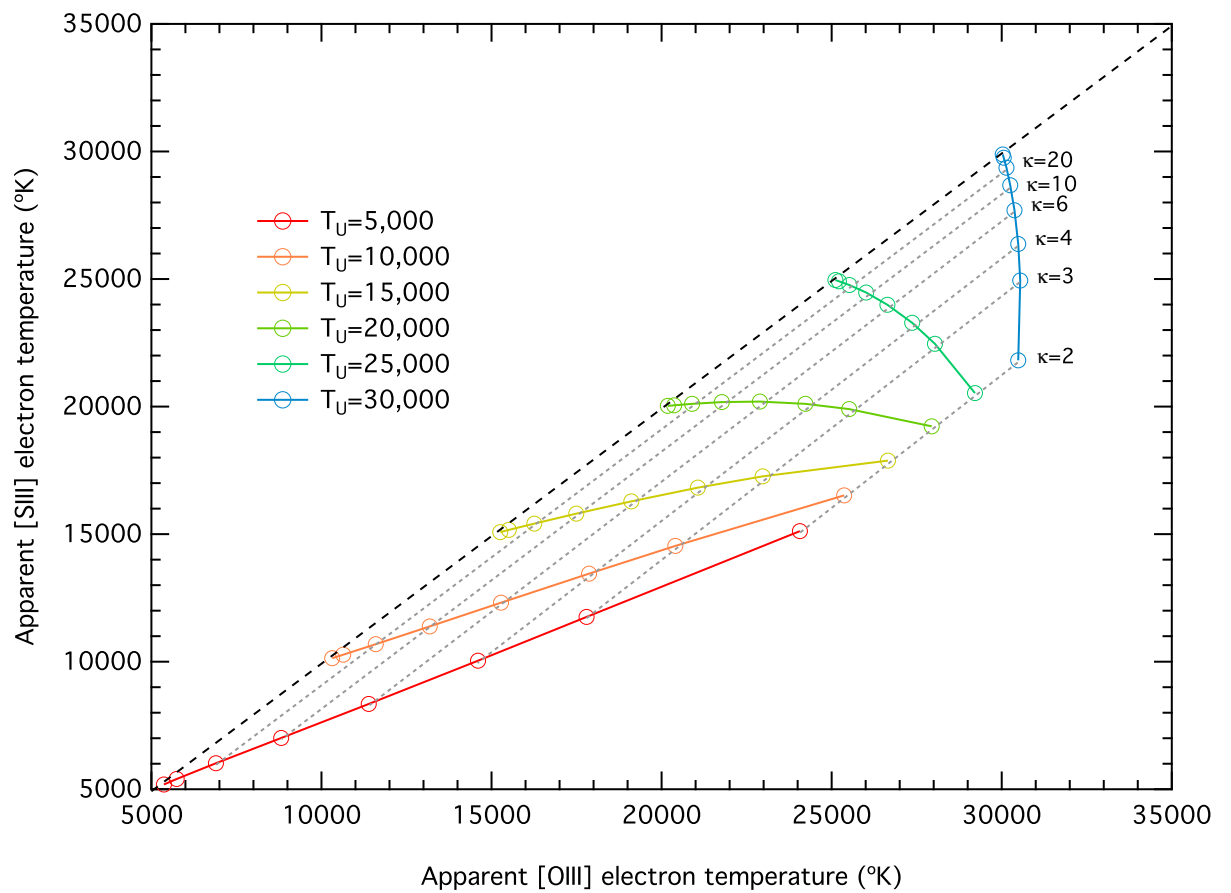


Figure 4.11 Locus of “apparent” electron temperatures measured using [S III] and [O III] flux ratios, as functions of κ and the kinetic (internal energy) temperature, T_U . With “equilibrium” measurements of electron temperatures from the two species, it is possible to estimate both κ and the true kinetic temperature.

4.8. Tools for measuring the equilibrium and true (kinetic) temperatures

4.8.1. Calculating equilibrium temperatures using the latest collision strengths

There are three methods commonly used to measure electron temperatures from CEL flux ratios. The first is to use the simple exponential expression (Equation 5.4, *et seq.*, [Osterbrock & Ferland 2006](#)), or the equivalent, using the flux ratio/temperature graphs, e.g., in Figure 4.10 or the inverse graphs given in [Osterbrock & Ferland \(2006\)](#). The second, in the case of O III, is to use the iterative process described by [Izotov et al. \(2006\)](#). The third is to use the IRAF STSDAS/nebular/temden routine ([Shaw & Dufour 1995](#)) or PyNeb ([Luridiana et al. 2012](#)). If we assume the electrons exhibit an M-B energy distribution, the accuracy of these methods depends (*inter alia*) on the accuracy of the collision strengths used, and all of these methods make use of older values for the effective collision strengths. For example, IRAF/temden by default uses O III data from [Lennon & Burke \(1994\)](#) and O II energy levels dating from 1960. In many cases, more recent and more accurate atomic data are available, and should be used in preference to older data.

To illustrate the differences that arise from using older data, for O III, we calculate the flux ratios using the M-B averaged detailed collision strengths from [PNPE12](#) for a range of equilibrium temperatures and an electron density of 100 cm^{-3} , and then use these flux ratios as input to the methods mentioned above. The results are given in Figure 4.12. The differences are considerable and point out the errors inherent in using old data. In this section we present a simple method for calculating equilibrium electron temperatures directly from observed line flux ratios, using the most recent atomic data.

Flux ratios of temperature sensitive CELs have been used for many years to measure electron temperatures. Most frequently used is the ratio of the [O III] nebular and auroral lines, but line flux ratios of several other species have been used. Table 4.3 lists line flux ratios (for which detailed collision strength data is available) that have been or can be used to estimate electron temperatures. Some species, for example, S II and O II, can be used to estimate both electron densities and temperatures.

The most accurate method for calculating the equilibrium electron temperature from line flux ratios is to compute the flux ratios as a function of temperature by convolving the collision strengths with the M-B distribution, using Equation (4.8). However, based on these calculations, a much simpler approach is possible, which allows the observer to calculate the M-B temperature directly from the line flux ratio measurements. This involves fitting a simple power law to the computed flux ratio versus equilibrium temperature curves.

An expression involving the flux ratio \mathcal{R} of the form:

$$T_{\text{MB}} = a (-\log_{10}(\mathcal{R}) - b)^{-c} \quad (4.32)$$

gives equilibrium temperatures accurate to within 0.5% of the computed collision strength values, where the flux ratio

$$\mathcal{R} = \frac{j_{\lambda a}}{j_{\lambda o1} + j_{\lambda o2}} \quad (4.33)$$

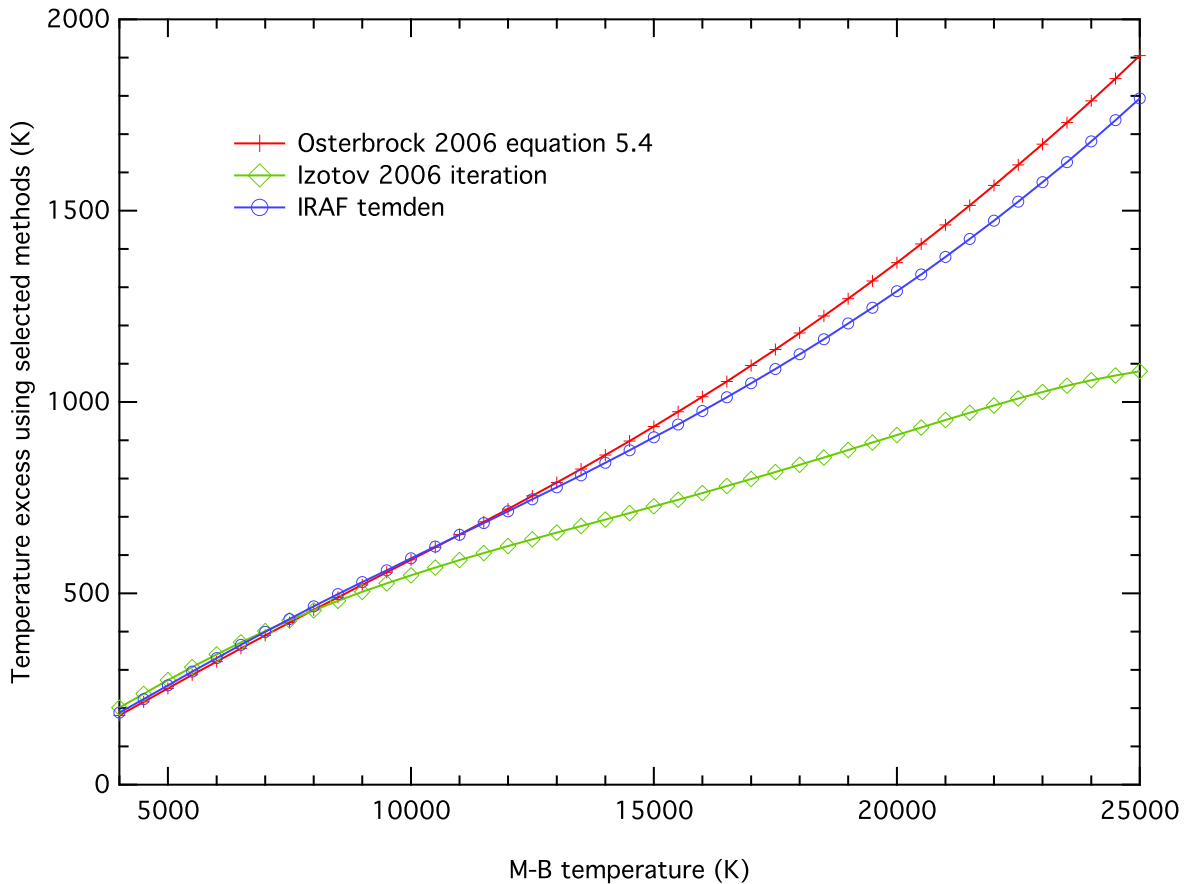


Figure 4.12 Errors arising from using old O III atomic data in conventional electron temperature estimates (electron density 100 cm^{-3}). c.f. Figure 4.2, which uses published effective collision strengths, rather than the numerically integrated collision strengths and resultant flux ratios, used here.

used in Equation (4.32) is as defined in Tables 4.3 and 4.4, and the inverse of the ratio used in Osterbrock & Ferland (2006, Equation (5.4)). The observer simply uses Equation (4.32) with the observed line flux ratio to calculate the electron temperature. The equation coefficients a , b , and c are given in Table 4.3. This method has the advantage that equilibrium electron temperatures can be calculated directly from the observed data, while making use of the latest collision strengths.

The p^2 and p^4 ions in Table 4.3 are those normally used for electron temperature measurement. It is quite feasible to use p^3 ions, but most of these are also strongly density sensitive, so flux ratios calculated simply from collision strength data for these lines—auroral or UV—will only give useful temperatures at densities $\lesssim 5 \text{ cm}^{-3}$. All ratios listed here increase in value as the electron temperature increases (the inverse of the conventional approach).

However, a more sophisticated approach is possible using the Mappings IV photoionisation code, which makes use of the latest collision strength and effective collision strength data, and takes into account densities. We discuss this in the following section.

4.8.2. The effect of densities on measured temperatures

All line ratios are ultimately dependent upon both temperature and density. For temperature sensitive ratios, a number of attempts have been made to account for the effect of electron

Table 4.3 Line ratios and M-B temperature fit coefficients from simple collision strength calculations

p^2, p^4 species				
Species	Line Ratio	a	b	c
[O I]	j(5577) / j(6300+6363)	8488.9	0.86645	0.9578
[N II]	j(5755) / j(6548+6583)	11187	0.85916	1.0259
[S III]	j(6312) / j(9069+9532)	11237	0.67368	1.0835
[O III]	j(4363) / j(4959+5007)	13748	0.87704	1.0064
[Ne III]	j(3342) / j(3869+3969)	14911	1.2619	1.0270
[Ar III]	j(5192) / j(7136+7751)	11899	0.96857	0.9897
p^3 ions				
Species	Line Ratio	a	b	c
[S II]	j(10287+10321+10336+10371) / j(6716+6731)	6965.6	0.64471	0.9960
[O II]	j(7319+7320+7330+7331) / j(3726+3729)	9090.5	0.87779	1.0161
[Ar IV]	j(7171+7238+7263+7332) / j(4711+4740)	9935.6	0.64612	1.1243

density on the temperatures measured using CEL ratios. For example see [Osterbrock & Ferland \(2006, Equations \(5.4\) through \(5.7\)\)](#) and the IRAF/temden routine provides a multi-level approach for the commonly used ions. Again, these procedures are approximations and/or are based on older atomic data⁶. Here we have used the newly revised Mappings IV photoionisation code to explore how electron density affects computed temperatures. Mappings IV takes into account the multi-level nature of the atomic species involved in generating the emission lines whose ratios are used to compute electron temperatures. The code uses the latest detailed collision strengths (see [Table 4.2](#)) or the latest available atomic data for effective collision strengths where detailed collision strengths are not available. It also uses a consistent set of transition probabilities ([Dopita et al. 2013](#)).

[Figure 4.13](#) shows the effect of density on the ratio of auroral to optical line fluxes for [S III], [N II], and [O III], calculated using Mappings IV, for an M-B temperature of 10,000 K. [Figure 4.14](#) shows what temperature these ratios would imply without any density correction. It is apparent that, for most ions, without correction, substantial errors will be made in the estimated M-B temperature, even at moderate densities.

In a more comprehensive approach to determining the M-B temperatures from ion flux ratios in the presence of changing densities, we have computed the temperature behaviour for several important and widely used line ratios, using Mappings IV, at a range of densities, from 1 to 10^4 cm^{-3} , and have derived simple linear fits as per [Equation \(4.32\)](#). The line ratios and the results of these fits are presented in [Table 4.4](#). Note that most of these ratios use the brightest and most spectroscopically convenient lines likely to be observed in nebular spectra. In general, we use simpler ratios than those in [Table 4.3](#), to make use of bright nebular lines and those least sensitive to density effects. However, the full ratio for [O III] is also presented for comparison with [Table 4.3](#).

The fit coefficients for [O III] differ somewhat from those in [Table 4.3](#), and show the effects of fully modelling excitation balances using multi-level atoms, rather than the simpler

⁶See footnote 3: PyNeb is a revised and extended Python-based version of the IRAF nebular/temden routines, developed by [Luridiana et al. \(2012\)](#)

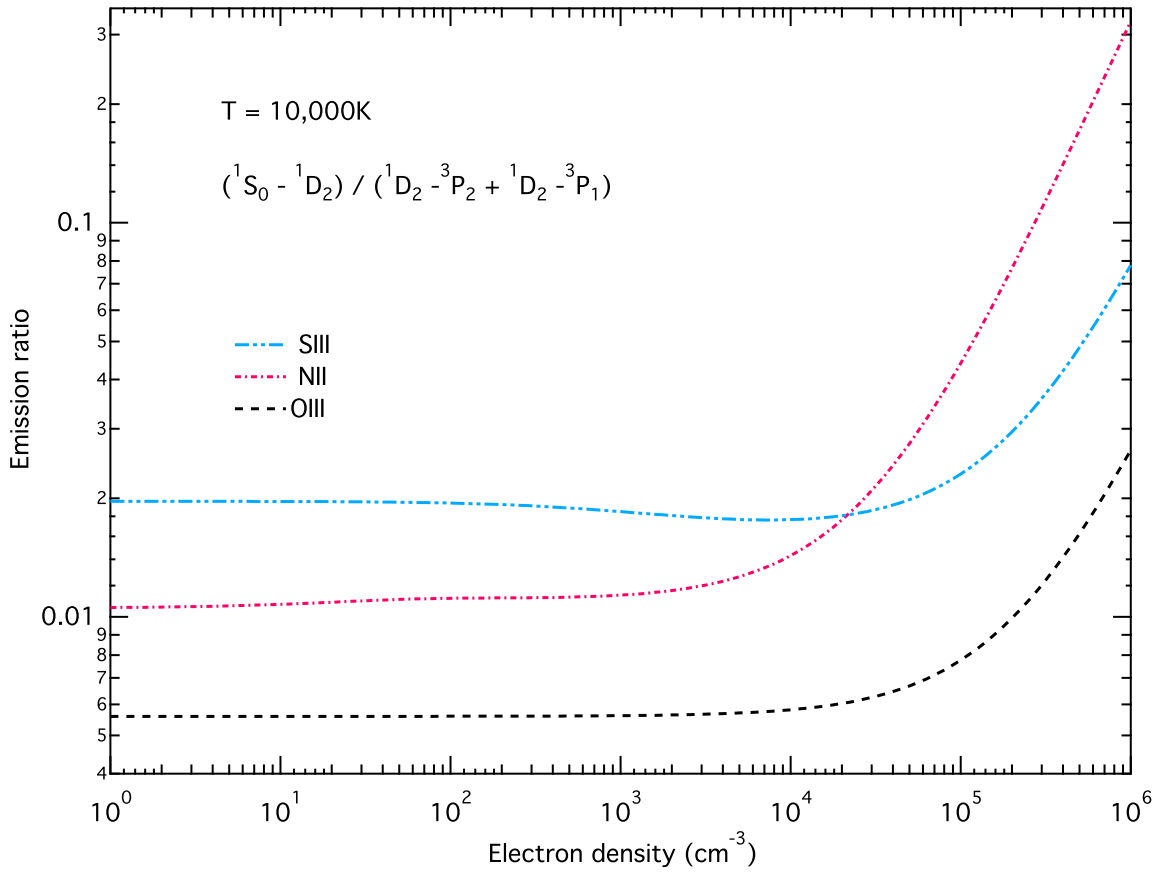


Figure 4.13 Effect of density on the flux emission ratios for the p^2 ions, S III, N II, and O III, plotted on a log-log scale. The flux ratio rises at high density due to collisional de-excitation of the $^1D_2 - ^3P$ transitions. Note the non-constant behaviour of the [N II] and [S III] line ratios below $n_e \sim 10^4$. This is due to collisional re-adjustment of the 3P levels before they are populated according to their statistical weights.

approach taken for Table 4.3. They should be used in preference to those in Table 4.3.

For all ions with the exception of N II and S III, the density effect can be accommodated by the inclusion of a term which quantifies the collisional de-excitation of the middle level. This takes the form used by Osterbrock & Ferland (2006):

$$\mathcal{R} = \frac{\mathcal{R}_{obs}}{1 + d (N_e/T^{1/2})}, \quad (4.34)$$

where d is a constant related to the critical density for the transition, $n_{crit} = (T^{1/2}/d)$. \mathcal{R} is the “corrected” value of the observed density \mathcal{R}_{obs} , such that the calculated temperature is the true M-B temperature. Because the density effects are complex, it is necessary in some cases to use two different values of the parameters for different density ranges. Table 4.5 shows the values of d for different density ranges, and for different species.

For N II and S III a more complex form must be chosen, since the collisional re-adjustment of the 3P levels with increasing density causes the peculiar behaviour seen in Figure 4.13. For N II an excellent fit can be obtained with two separate values of a , b and d , applicable over different density ranges, as indicated in the footnote to Table 4.5.

Combining Equations (4.32) and (4.34), one can use the a , b , c , and d parameters from Tables

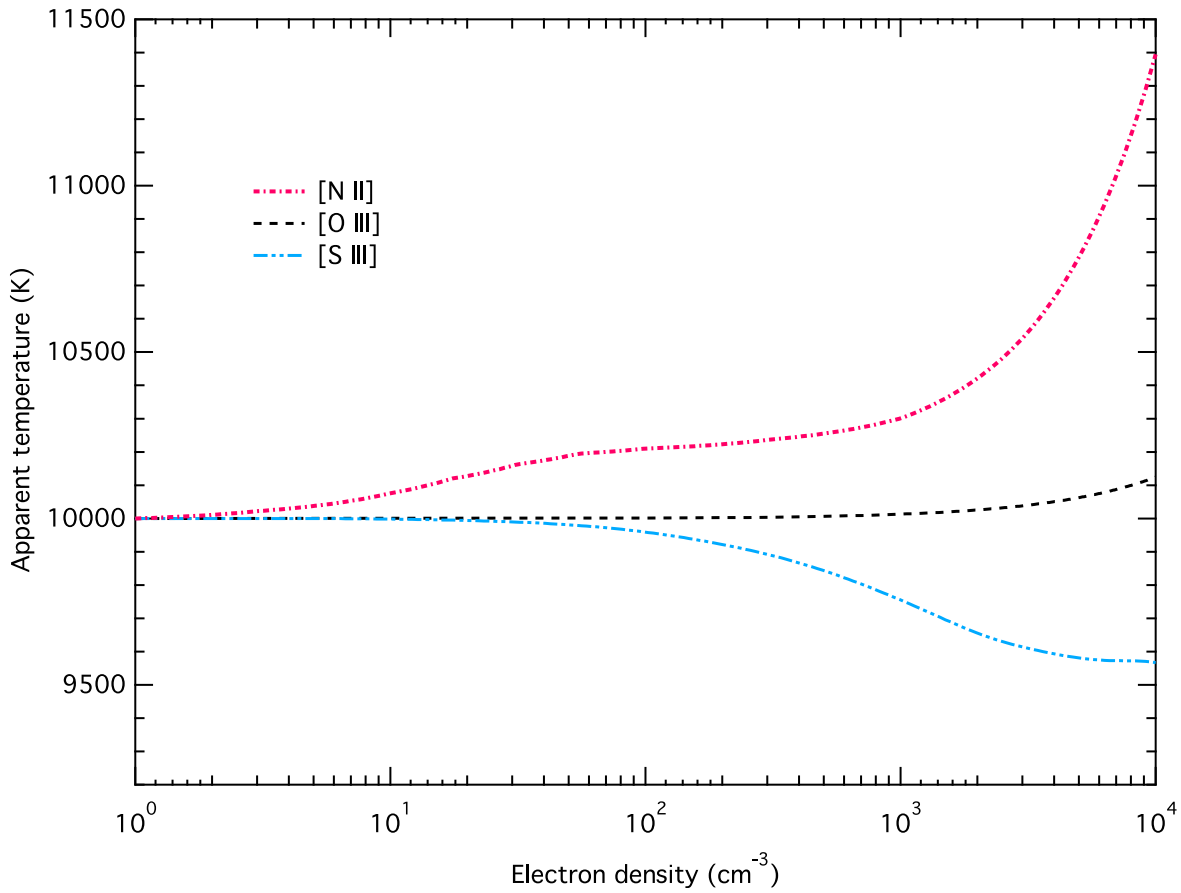


Figure 4.14 Errors arising in the M-B temperature calculations where no correction is made for density, for O III, S III, and N II, plotted on a linear-log scale. The non-constant behaviour of the [N II] and [S III] line ratios is more clearly shown in this graph.

4.4 and 4.5 to fit both densities and temperatures with a single equation,

$$T_{\text{MB}} = a \left[-\log_{10} \left(\frac{\mathcal{R}_{\text{obs}}}{1 + d (N_e/T^{1/2})} \right) - b \right]^{-c}. \quad (4.35)$$

4.8.3. Calculating κ dependence

In the above approach, we assume that the electron energies are in thermal equilibrium. No insight is given into the effects of non-equilibrium electron energies. To take the effects of a κ distribution into account, we can use Figures 4.9 and 4.10 to measure graphically the true kinetic temperature from the [O III] and [S III] CEL flux ratios for a range of values of the parameter κ . Similar graphs may be derived for other CEL species. However, an easier method is to derive a simple linear equation from the graph, that expresses the kinetic temperature in terms of the temperature measured using conventional M-B methods, such as the formula in Equation (4.32). This is based on the near-linearity of the curves in Figures 4.9 and 4.10 for temperatures between 4,000 K and 25,000 K.

For the range of temperatures ($4,000 < T_U < 25,000$ K) encountered in H II regions and many PNe, the relationship between the apparent (M-B) electron temperature T_e and the kinetic temperature T_U can be expressed to very good accuracy as a linear equation with

Table 4.4 Line ratios and M-B temperature fit coefficients from MAPPINGS IV

p^2, p^4 species				
Species	Line Ratio	a	b	c
[O I]	j(5577)/j(6300)	10512	0.87725	0.92405
[N II]	j(5755)/j(6583)	10873	0.76348	1.01350
[S III]	j(6312)/j(9069)	10719	0.09519	1.03510
[S III]	j(6312)/j(9069+9532)	10719	0.64080	1.03510
[Ar III]	j(5192)/j(7136)	11887	0.98752	0.99124
[O III]	j(4363)/j(5007)	13229	0.79432	0.98196
[O III]	j(4363)/j(4959+5007)	13229	0.92350	0.98196
[Ne III]	j(3342)/j(3869)	18419	1.01660	0.99815
[Ar V]	j(4626)/j(7006)	13131	0.67472	0.98282
[Ne V]	j(2975)/j(3426)	22471	1.00700	1.08260
p^3 species				
Species	Line Ratio	a	b	c
[S II]	j(4068+4076)/j(6731)	5483.8	0.25461	0.88515
[S II]	j(4068+4076)/j(6717+6731)	5483.8	0.65255	0.88515
[O II]	j(7320+7330)/j(3726+3729)	7935.2	0.98516	0.94679
[Ar IV]	j(7171)/j(4740)	12665	1.09820	1.18100
[Cl III]	j(3342+3358)/j(5517+5538)	6637.9	0.41953	0.91886

parameters that are quadratic functions of $1/\kappa$, for all values of κ , as follows:

$$T_U = a(\kappa) T_e + b(\kappa) \quad (4.36)$$

where

$$a = \left(a_1 + \frac{a_2}{\kappa} + \frac{a_3}{\kappa^2} \right) \quad (4.37)$$

and

$$b = - \left(b_1 + \frac{b_2}{\kappa} + \frac{b_3}{\kappa^2} \right) \quad (4.38)$$

and where T_e is derived from conventional equilibrium methods such as Equation (4.32). The equation coefficients can be derived for any CEL species for which non-averaged collision strengths are available. For the [O III] CELs, this equation is illustrated graphically for a range of values of κ in Figure 4.15. The parameters $a_1, a_2, a_3, b_1, b_2,$ and b_3 are given in Table 4.6, for several nebular atomic species.

Using the revised [O III] atomic data and a κ of 10, we see that an apparent [O III] electron temperature of 15,000 K derived via the IRAF/temden routine (with old atomic data) corresponds to a kinetic (internal energy) temperature of $\sim 11,000$ K.

Table 4.5 Density parameter d used in equations (4.34) and (4.35)

Log density (cm^{-3})	O III ^d	S III	N II ^b	O I	S II	O II	Ne III	Ar IV ^c
$0.0 < \log_{10}(N_e) < 2.0$	3.8895E-04	-6.50E-03	5.80E-02	2.20E-04	3.90E-02	1.05E-01	0.00E+00	2.90E-02
$2.0 < \log_{10}(N_e) < 3.0$	3.8895E-04	-6.50E-03	3.60E-03	2.20E-04	3.90E-02	8.90E-02	0.00E+00	2.90E-02
$3.0 < \log_{10}(N_e) < 3.5$	3.8895E-04	n/a^d	3.60E-03	2.20E-04	3.90E-02	8.90E-02	0.00E+00	2.90E-02
$3.5 < \log_{10}(N_e) < 4.0$	3.8895E-04	n/a^d	3.60E-03	2.20E-04	n/a^d	n/a^d	0.00E+00	2.90E-02

^a The fit with $d=3.8895$ is applicable up to $\log_{10}(N_e) < 5.3$ with an error of less than 10^{-4} .

^b Better fits to the density behaviour can be obtained for N II with the following parameters:

$0.0 < \log_{10}(N_e) < 1.5$: $a=10850$, $d=1.45E-01$; $1.5 < \log_{10}(N_e) < 5.2$: $a=10820$, $b=0.8762$, $d=3.0E-03$.

^c Better fits to the density behaviour can be obtained for Ar V with the following a parameters:

$\log_{10}(N_e) < 3.0$: $a=12665$, $4 > \log_{10}(N_e) > 3.0$: $a=14551$ (error $< 2 \times 10^{-3}$).

^d “ n/a ” means that the fits are not reliable for these species at these densities, so the parameter d is not available, and Equations (4.34) and (4.35) are not applicable in these situations.

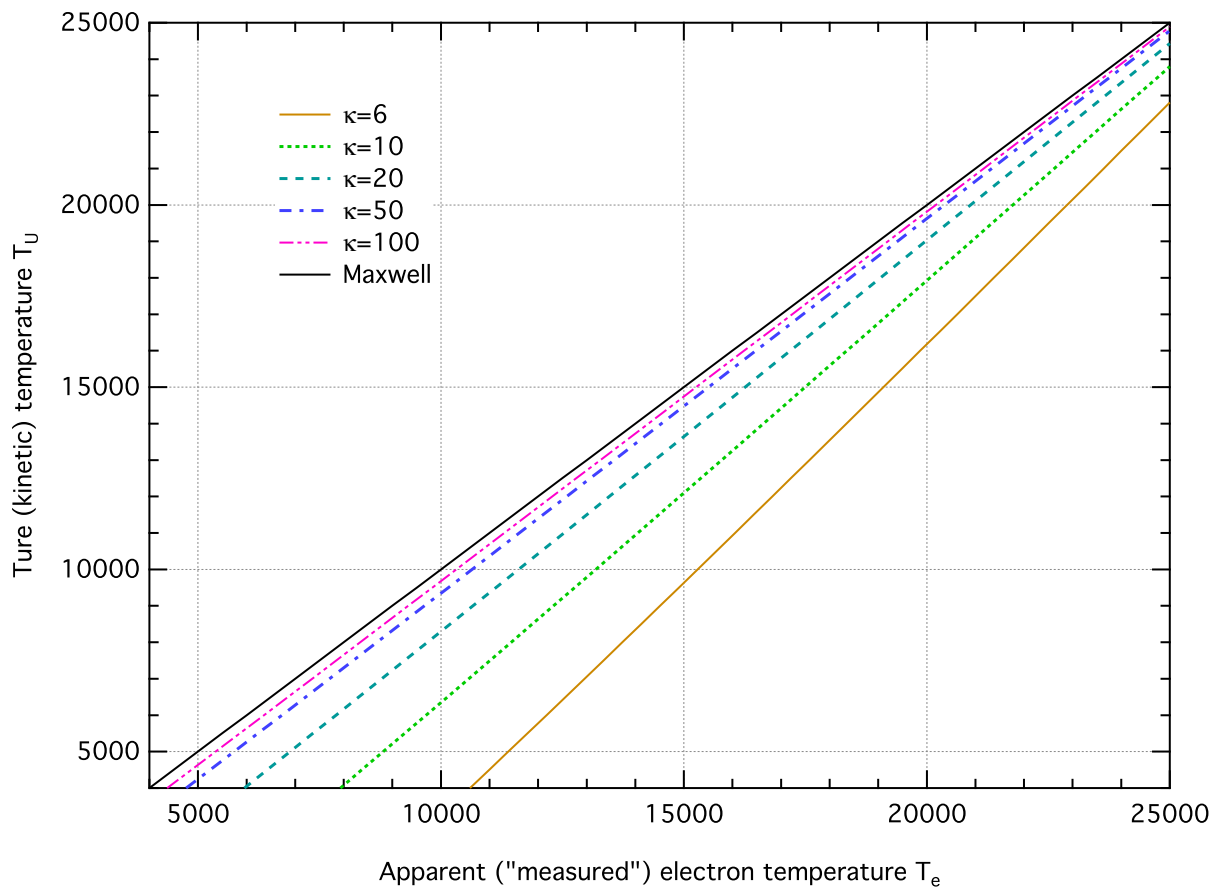


Figure 4.15 True kinetic temperature versus electron temperature for [O III] estimated using conventional methods. It shows the effect of the parameter κ in reducing the true kinetic temperature.

Table 4.6 Linear coefficients for $4\,000\text{ K} < T_U < 25\,000\text{ K}$

O III					
a_1	a_2	a_3	b_1	b_2	b_3
1.00036	1.27142	3.55371	21.1751	42693.5	103086
S III					
a_1	a_2	a_3	b_1	b_2	b_3
1.00075	1.09519	3.21668	13.3016	24396.2	57160.4
N II					
a_1	a_2	a_3	b_1	b_2	b_3
1.0008	1.26281	3.06569	19.432	31701.9	70903.4
O I*					
a_1	a_2	a_3	b_1	b_2	b_3
0.995398	1.02877	2.80919	-45.0544	38145.8	92736.3
Ne III					
a_1	a_2	a_3	b_1	b_2	b_3
1.00128	1.18331	2.01139	42.7545	50728.7	100311
Ar III					
a_1	a_2	a_3	b_1	b_2	b_3
1.00087	1.4561	3.62825	17.4001	32190	72395
Ar V					
a_1	a_2	a_3	b_1	b_2	b_3
1.00083	1.10823	3.15458	19.6749	31483.4	72117.8
O II					
a_1	a_2	a_3	b_1	b_2	b_3
0.999828	1.36062	2.99473	19.5715	47145	107673
S II					
a_1	a_2	a_3	b_1	b_2	b_3
0.998299	1.62932	3.9533	-17.6454	31513	73137.3
Ar IV					
a_1	a_2	a_3	b_1	b_2	b_3
0.99791	1.19881	3.82751	-13.2742	36490.7	98591.4

* For O I, the linear range is between 1 000 K and 20 000 K

4.9. Strong line techniques

Numerous methods have been developed using ratios of the strong lines in nebular spectra, which are important in the absence of direct electron temperature diagnostic lines. See, for example, [Kewley & Ellison \(2008\)](#) and [Kewley & Dopita \(2002\)](#). These methods make use of the line fluxes from a range of different atomic species, usually selected because they are readily measurable with low noise in most nebular spectra. However the impact of a κ distribution on these methods is not simple, as each species is affected to a different extent by the distribution. It is necessary to calculate and model each strong line index separately as a function of temperature. Initial investigations suggest that several of the methods will not be strongly affected by κ distributions, and in particular, measurements comparing [S II] 6716Å, 6731Å and [N II] 6548Å, 6583Å are not significantly affected, as the fluxes of both species are changed to a similar extent by a κ distribution.

As a simple illustration, we can consider the strong line ratio “ R_{23} ”. This flux ratio is given by:

$$R_{23} = ([\text{O II}]\lambda 3726 + [\text{O II}]\lambda 3729 + [\text{O III}]\lambda 4959 + [\text{O III}]\lambda 5007)/\text{H}\beta \quad (4.39)$$

The excitation temperatures for the [O II] and [O III] lines are $\sim 38,600\text{K}$ and $\sim 29,000\text{K}$ respectively. For a κ value of 10, and a kinetic temperature of 10,000 K, from [Figure 4.7](#), it is apparent that the [O II] lines are enhanced by $\sim 20\%$; the [O III] lines are not significantly affected; and, from the discussion earlier, $\text{H}\beta$ is enhanced by $\sim 4\%$. Thus the overall R_{23} ratio is slightly enhanced. A detailed analysis of strong line methods is best tackled using photoionisation models that take into account κ effects. While a detailed analysis of the impacts of κ distributions and new atomic data on strong line methods is beyond the scope of the present paper, it is explored in our next paper in this series ([Dopita et al. 2013](#)), which develops new strong line diagnostics that give significantly more consistent results when compared to direct T_e methods. The subject will be addressed further in subsequent papers. Nonetheless, it is apparent from this simple example that the effect of changes in the collision strengths and κ on derived strong line abundances is relatively small, but not insignificant.

4.10. Estimating κ

The kappa distribution uses a single parameter to describe the deviation from thermal equilibrium in electron energies. In any one temperature or abundance measurement, there is no unique way to estimate the value of κ , although a value of ~ 10 appears consistent with many of the observed spectra ([NDS12](#)). When more than one measurement is available—for example, electron temperatures obtained using different CEL species, or CEL and ORL-derived abundances—the value of kappa can be estimated by the requirement that the discrepancies be minimised. When several different methods are available such as in bright nebulae, it is possible to iterate to an optimum value of kappa and estimate errors and variance. [Figure 4.11](#) shows that measuring apparent (M-B) electron temperatures for [S III] and [O III] allows one to estimate both κ and the kinetic (internal energy) temperature.

Needless to say, in real nebulae there are likely to be kappa distributions spanning a range of values of κ , so specifying a single value is not always meaningful, but the concept can

help to avoid the large discrepancies that arise using equilibrium methods, and can augment values obtained using other contributing factors such as temperature and abundance inhomogeneities.

There will seldom be a single answer for temperature, abundances and κ for any real nebula, and using photoionisation models to explore the complex physics is critically important. For this reason, we have revised the Mappings III photoionisation code (Allen et al. 2008) to version IV, to incorporate both non-equilibrium κ effects and the most accurate available collision strengths and other atomic data. This work is the subject of our next paper (Dopita et al. 2013), where we use it to investigate the effect of κ distributions on temperatures and abundances estimated using the strong line methods, to develop a revised set of strong line diagnostics. The code development has been undertaken independently of the work on Mappings Ie (Binette et al. 2012), with which it shares a common origin but which has had a separate development.

4.11. Conclusions

In this paper we have explored further the ideas put forward in NDS12, where the non-equilibrium κ electron energy distribution widely encountered in solar system plasmas was found to explain the long standing abundance discrepancy problem that arises when temperatures and abundances are measured using spectra from different atomic species. We have discussed the factors involved in obtaining accurate CEL temperatures from theoretical collision strengths. We have also shown that significant errors in electron temperatures can arise unless one has access to the best possible collision strength data. We have examined the effects of the κ distribution on recombination processes, in particular how the κ distribution is able to resolve the long standing discrepancy between ORL and CEL abundances. We show that a typical κ distribution leads to a small enhancement of hydrogen recombination lines. We have examined in detail the effects of κ and newly available collision strength data affects the measurement of electron temperatures using CELs. We compare these effects on the forbidden lines of S III and O III. In the main thrust of the paper, we present simple techniques for calculating equilibrium electron temperatures from line flux ratios using the most up to date atomic data, and using these equilibrium temperatures to derive the actual kinetic (internal energy) temperatures resulting from non-equilibrium electron energy distributions. We outline future work on adapting photoionisation modelling programs and strong line methods to take into account the effects of the κ distribution.

4.12. Appendix: Supplementary Data Tables

4.12.1. Temperature-sensitive line ratio data

The tables in this appendix give the wavelengths, transition probabilities and line ratio multipliers (Equations 4.29 and 4.31), for transitions of the p^2 , p^4 and p^3 lines of nebular interest. For the meanings of the wavelength and transition probability symbols, see Sections 6.2 and 6.3.

Table 4.7 Line wavelengths (Å) (in air) and line strengths and line ratio multipliers for the p^2 and p^4 ions

Species	O I	N II	O III	S III	Ne III	Ar III	Ar v
λ_a (Å)	5577.3	5754.6	4363.2	6312.1	3342.2	5191.8	4625.4
λ_{o2} (Å)	6363.8	6548.0	4958.9	9068.6	3968.5	7751.1	6435.1
λ_{o3} (Å)	6300.3	6583.4	5006.8	9530.6	3868.8	7135.8	7005.8
λ_{u2} (Å)	2972.3	3062.8	2321.0	3721.6	1814.6	3109.2	2691.1
λ_{u3} (Å)	2958.4	3070.6	2331.4	3797.2	1823.7	3005.2	2786.0
A_a	1.26E+00	1.14E+00	1.71E+00	2.08E+00	2.65E+00	3.10E+00	3.80E+00
A_{o2}	1.82E-03	9.84E-04	6.21E-03	1.85E-02	5.40E-02	8.31E-02	2.26E-01
A_{o3}	5.65E-03	2.91E-03	1.81E-02	4.80E-02	1.74E-01	3.35E-02	5.20E-01
A_{u2}	7.54E-02	3.18E-02	2.15E-01	6.61E-01	2.06E+00	4.02E+00	6.80E+00
A_{u3}	2.42E-04	1.55E-04	6.34E-04	8.82E-03	4.00E-03	4.30E-02	8.10E-02
$f_1(A,\lambda)$	1.06824	1.11132	1.01650	1.12615	0.65458	0.63050	0.52476
$f_1(A,\lambda)_{uv}^*$	0.12034	0.05853	0.24096	0.61492	0.93727	1.38038	1.63260

* The final line in this table shows the $f_1(A,\lambda)$ line ratio multiplier for the UV-to-optical line ratios. They are related to the auroral-to-optical line ratios via the wavelength weighted branching ratios.

Table 4.8 Line wavelengths (Å) (in air) and line strengths and line ratio multipliers for the p^3 ions

Species	N I	S II	O II	Ne IV	Ar IV
λ_{a1}	10407.6	10370.5	7330.7	4725.6	7332.2
λ_{a2}	10407.2	10336.4	7329.7	4724.2	7263.3
λ_{a3}	10398.1	10320.5	7320.0	4715.7	7237.8
λ_{a4}	10397.7	10286.7	7318.9	4714.2	7170.7
λ_{o1}	5200.3	6730.8	3728.8	2424.4	4740.1
λ_{o2}	5197.9	6716.4	3726.0	2421.8	4711.3
λ_{u1}	3466.5	4076.3	2470.3	1601.1	2868.2
λ_{u2}	3466.5	4068.6	2470.2	1600.9	2853.7
A_{a1}	5.31E-02	6.81E-02	5.34E-02	3.89E-01	1.22E-01
A_{a2}	2.74E-02	1.42E-01	8.67E-02	4.36E-01	6.78E-01
A_{a3}	3.45E-02	1.57E-01	9.91E-02	1.10E-01	6.70E-01
A_{a4}	6.12E-02	1.15E-01	5.19E-02	3.01E-01	9.08E-01
A_{o1}	7.56E-06	6.84E-04	3.06E-05	5.80E-04	7.71E-02
A_{o2}	2.03E-05	2.02E-04	1.78E-04	5.47E-03	9.60E-03
A_{u1}	6.50E-03	7.72E-02	5.22E-02	5.30E-01	9.70E-01
A_{u2}	2.60E-03	1.92E-01	2.12E-02	1.33E+00	2.55E+00
$f_2(A,\lambda)$	0.47521	0.41815	0.40631	0.20480	0.26438
$f_2(A,\lambda)_{uv}^*$	0.07365	0.59216	0.30377	0.90891	0.98929

* Alternative flux ratios can be used for the p^3 ions, using the UV lines in place of the “auroral”. This is done, for example, in the IRAF/temden routine for S II, Ne IV and Ar IV. The final line in this table shows the $f_2(A,\lambda)$ line ratio multiplier for the UV-to-optical line ratios. They are related to the auroral-to-optical line ratios via the wavelength weighted branching ratios.

CHAPTER 5

Nebular metallicities in two isolated Local Void dwarf galaxies

...the Chaotic Voids outside of the Stars are measured by the Stars

William Blake, *Milton, A Poem, Book 2*

This chapter was previously published as ‘Nebular metallicities in two isolated Local Void dwarf galaxies’, Nicholls, D. C., Jerjen, H., Dopita, M. A., and Basurrah, H., ApJ, 780, 88. The work is entirely my own, taking into account suggestions from my co-authors. Minor typographical errors have been corrected, and sections, tables and figures have been renumbered to conform with the layout of the thesis.

5.1. Chapter summary

Isolated dwarf galaxies, especially those situated in voids, may provide insight into primordial conditions in the universe and the physical processes that govern star formation in undisturbed stellar systems. The metallicity of H II regions in such galaxies is key to investigating this possibility. From the SIGRID sample of isolated dwarf galaxies, we have identified two exceptionally isolated objects, the Local Void galaxy [KK98]246 (ESO 461-G036) and another somewhat larger dwarf irregular on the edge of the Local Void, MCG-01-41-006 (HIPASS J1609-04). We report our measurements of the nebular metallicities in these objects. The first object has a single low luminosity H II region, while the second is in a more vigorous star forming phase with several bright H II regions. We find that the metallicities in both galaxies are typical for galaxies of this size, and do not indicate the presence of any primordial gas, despite (for [KK98]246) the known surrounding large reservoir of neutral hydrogen.

5.2. Introduction

The physical isolation of a dwarf galaxy is often argued to be a major contributor in preserving evidence of intergalactic H I gas in its primordial condition. Isolated dwarf galaxies

are thought to be very slow to enrich their neutral gas clouds, compared to the much more rapid evolution of larger galaxies (e.g., [Mateo 1998](#)). Their relatively shallow potential wells are argued to be inefficient in retaining the heavy element abundances generated by supernovae (e.g., [Kunth & Östlin 2000](#)). This picture is consistent with the mass-metallicity relation (e.g., [Lee et al. 2003](#); [Tremonti et al. 2004](#); [Lee et al. 2006](#)), which shows that smaller galaxies generally exhibit lower nebular metallicity than larger ones. Investigating the nature of this relation was one of the motivations behind the SIGRID sample of isolated gas-rich dwarf galaxies ([Nicholls et al. 2011](#)), which, *inter alia*, seeks to clarify the behaviour of the mass-metallicity relation at low galactic masses. It has also been suggested that dwarf galaxies residing in low density environments (e.g., in voids) have lower metallicities, and in some cases, very low mass-to-light ratios, compared to similar objects in higher density regions ([Pustilnik & Kniazev 2007](#); [Pustilnik et al. 2011b,a](#)). Therefore it is useful to investigate whether spatially isolated galaxies in voids are in any way unusual, in terms of mass-to-light ratio or metallicity, compared to similar objects in denser environments.

We have identified two isolated gas-rich dwarf galaxies in the SIGRID sample located within the Local Void for investigation, [KK98]246 (ESO 461-G036), hereafter “KK246” and MCG-01-41-006 (HIPASS J1609-04), hereafter “J1609”. KK246 is relatively nearby (6.4 Mpc, [Tully et al. 2008](#)). J1609-04 is somewhat more massive and luminous, but is over twice as distant, at 14.82 Mpc ([Nicholls et al. 2011](#)). We present the spectra and nebular metallicity results for the two galaxies, and compare them with data from other investigations of void galaxies.

This paper is organised as follows. In Sections 5.3 and 5.4 we provide a summary of what is known about the two galaxies. In Section 5.5 we detail our observations. In Section 5.6 we present the flux-calibrated spectra from 3600Å to 7000Å at resolutions of 3000 (blue) and 7000 (red). In Section 5.7 we present the methods and results for our metallicity analyses; we list the observed line fluxes; and nebular metallicities and ionisation parameters using the revised strong line methods described in [Dopita et al. \(2013\)](#). In Section 5.8 we present comparisons with other surveys of similar galaxies for mass-to-light ratios and mass-metallicities. In Section 5.9 we discuss the implications for dwarf galaxy evolution of these observations. Section 5.10 presents our conclusions.

5.3. KK246

5.3.1. Description

KK246 is a particularly interesting object in the SIGRID sample as it has been identified as the most isolated dwarf galaxy known in the Local Volume ($D \lesssim 10$ Mpc; 2013AJ....145..101K). It is situated a few Mpc within the Local Void ([Tully et al. 2008](#); [Kreckel et al. 2011](#); [Nasonova & Karachentsev 2011](#)). This void is large, at least 23 Mpc in radius ([Tully et al. 2008](#)), and KK246 has no apparent neighbours within ~ 3 Mpc ([Karachentsev et al. 2004](#)). Assuming a spatial peculiar velocity of 100-200 km s⁻¹ this translates into a time of 15–30 Gyr since the last possible galaxy–galaxy encounter. As such, the object is an ideal laboratory in which to study galaxy evolution and self-enrichment in isolation. It is of particular interest in understanding the intrinsic evolutionary processes in the formation of this small galaxy, as almost certainly it has never been affected by tidal disruption by nearby large galaxies,

nor by enrichment of the intergalactic medium (IGM) from which it formed by outflows from such galaxies. It has no detectable adjacent dwarf galaxies, unlike the low metallicity low surface brightness (LSB) galaxies in the Lynx-Cancer void at 18 Mpc investigated by [Pustilnik et al. \(2011a\)](#).

Previous observations of KK246 have shown that the stellar component is embedded in a large surrounding H I cloud (2011AJ....141..204K) and contains an old stellar population ([Karachentsev et al. 2006](#)). Although it currently has only one small, low-luminosity star-forming H II region, we have been able to measure the nebular metallicity of that region using the WiFeS IFU spectrograph on the ANU 2.3 m telescope at Siding Spring Observatory. This paper reports the first measurement of the nebular spectrum and resultant nebular metallicities.

5.3.2. Location

Using Hubble Space Telescope (HST) imagery and photometry, [Karachentsev et al. \(2006\)](#) measured the TRGB distance to KK246 as 7.83 Mpc. [Tully et al. \(2008\)](#) use a more recent calibration of the T_{rgb} scale from [Rizzi et al. \(2007\)](#) and give a distance of 6.4 Mpc. With either distance value, KK246 is within the Void ([Tully et al. 2008](#)). In the calculations in this paper, we have used the value from Tully et al., but our conclusions do not depend on which value is adopted.

The object's isolation is indicated by the low value of the Tidal Index $\Theta = -2.2$ ([Karachentsev et al. 2004](#)) and the SIGRID Δ index (not measurable: no potential tidally effective objects within 10° or ~ 1.3 Mpc radius, [Nicholls et al. 2011](#)), implying no tidal interference from any nearest neighbour galaxy within a Hubble time¹. [Karachentsev et al. \(2004\)](#) have concluded that there are no potential interacting galaxies within 3 Mpc. KK246 is also listed in the "Local Orphan Galaxies" catalog ([Karachentsev et al. 2011](#)) as having the highest recorded isolation index ($\log_{10}(\text{ii}) = 3.22$) using an alternative isolation measure.

5.3.3. Extended H I region

KK246 is one of over 4500 H I objects detected in the HIPASS survey (HIPASS J2003-31, [Meyer et al. 2004](#)) and was identified with the optical counterpart galaxy ESO 461-G036 ([Doyle et al. 2005](#)). It was subsequently observed using the Very Large Array (VLA) at 21cm at higher resolution by [Kreckel et al. \(2011\)](#), who found that KK246 is surrounded by a very extended H I region, at least ten times the diameter of the stellar disk.

[Kreckel et al. \(2011\)](#) find a large dynamical mass ($4.1 \times 10^9 M_\odot$) and consequently one of the highest measured dynamic-mass-to-light ratios, $M_{\text{dyn}}/L_B = 89$, further emphasising the unusual nature of this galaxy. Other noteworthy high dynamic-mass-to-light ratio objects include NGC 2915 ($M_{\text{dyn}}/L_B = 76$, [Meurer et al. 1996](#)), ESO 215-G?009 ($M_{\text{dyn}}/L_B = 22$, [Warren et al. 2004](#)), and NGC 3741 ($M_{\text{dyn}}/L_B = 107$, [Begum et al. 2005](#)). However, these objects have H II regions (using GALEX FUV flux as a diagnostic) that are either much brighter (NGC 2915, 3741) or more spatially extended (ESO 215-G?009), than KK246.

¹ Θ takes into account galaxies whose mass is known, at large angular distances from the tidally influenced object, whereas Δ is sensitive to dwarf galaxies within 10° in the sky, whose mass has not been directly measured, but whose flow-corrected redshift and luminosity are known.

5.3.4. Stellar Population

As part of a survey of Local Volume galaxies aimed at measuring TRGB distances, [Karachentsev et al. \(2006\)](#) observed KK246 using the HST. The left panel of Figure 5.1 shows the composite F606W-band image, obtained from the HST archive, from those observations. The location of the H II regions observed in this work is marked.

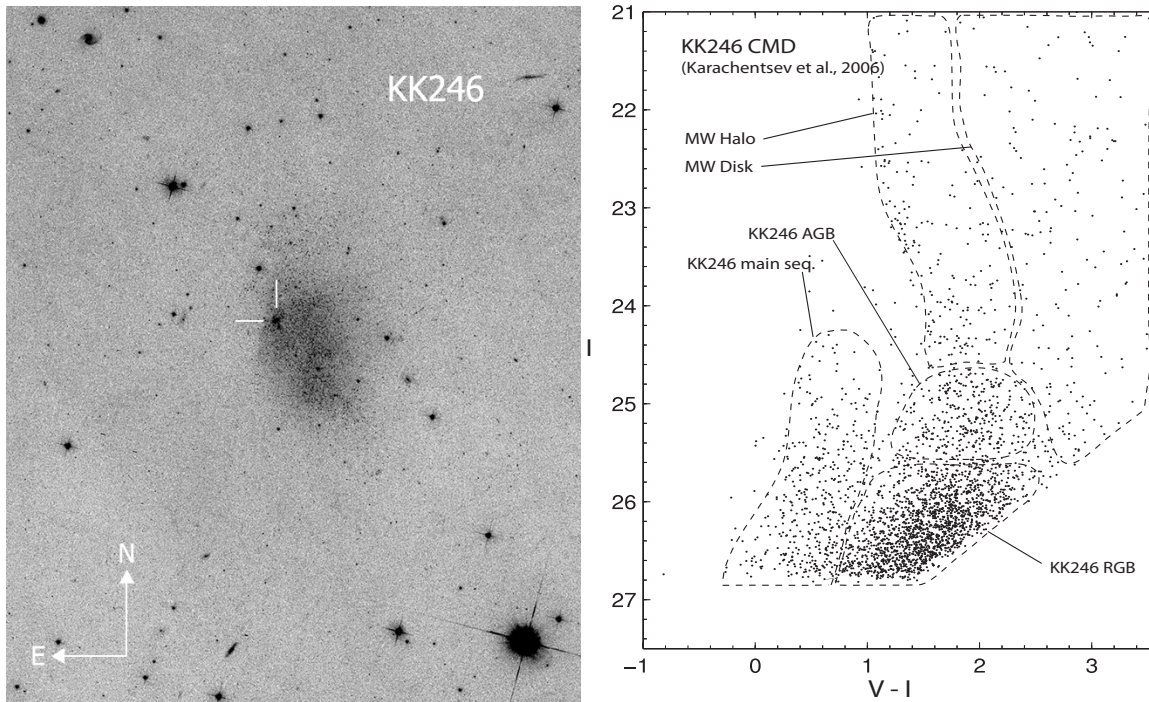


Figure 5.1 Left Panel: HST V-band image of KK246. The only H II region in the galaxy is marked to the NE of the centre. Right Panel: HST (V-I, I) colour magnitude diagram derived from [Karachentsev et al. \(2006\)](#), showing evidence of at least two stellar populations. The transition from the RGB to the AGB stars occurs around $I \sim 25.6$ mag.

[Karachentsev et al. \(2006\)](#) resolved the brightest two magnitudes of the colour magnitude diagram (CMD) for KK246 from HST WFC3 images, which shows clear evidence of an old stellar population. The large distance to KK246 makes star formation modelling difficult, which rules out calculating the star formation history in detail, but by comparing its CMD with the CMD data for 60 nearby dwarf galaxies in the ANGST survey from [Dalcanton et al. \(2009\)](#), and their star formation histories analysed by [Weisz et al. \(2011\)](#), it appears likely that KK246 has had at least three epochs of star formation, including the present one involving the H II region. The right panel of Figure 5.1 shows our interpretation of the CMD from [Karachentsev et al. \(2006\)](#).

5.3.5. UV, Visible, H α and H-band Imagery

KK246 is detected in both the NUV and FUV images from Galaxy Evolution Explorer (GALEX; see Table 1). The low FUV flux [luminosity] of $28.2 \mu\text{Jy}$ implies that there is only a small population of hot young stars currently present in the galaxy. Using Equations (17) and (18) from [Karachentsev et al. \(2013\)](#) we infer a star formation rate of $\log(\text{SFR}) = -2.43$. This is consistent with our H α observations (see below). Figure 5.2 (bottom, left) shows

the composite GALEX image. Although the resolution and sensitivity are marginal, it is apparent that the brightest UV object coincides with the H II region.

The same figure also shows the visible colour image from DSS2 (top left), the single H II region from a H α + R-band WiFeS data cube, (top right), and an H-band image from Kirby *et al.* (2008) (bottom right). The small H II region corresponds to the point marked in the HST image (Figure 5.1) above. The physical extent, spectrum (see below) and H α flux confirm that this is an H II region and not a planetary nebula, unlike the object discussed by Makarov *et al.* (2012) in the isolated dwarf spheroidal galaxy KKR25.

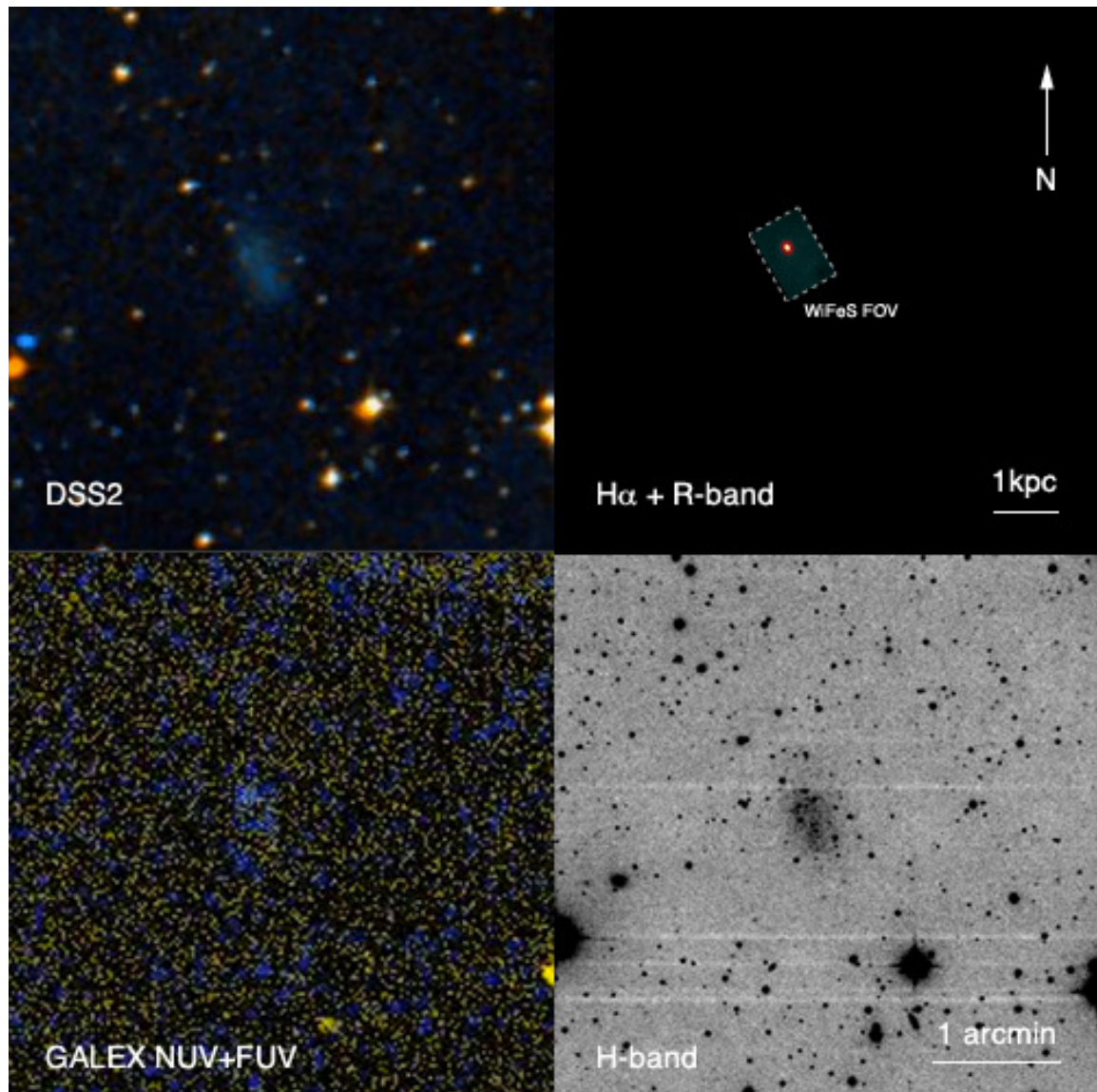


Figure 5.2 KK246 in Visible, H α /R-band, H-band, and GALEX NUV + FUV , all to the same scale

Table 5.1 summarises information available on KK246.

Table 5.1 Compendium of UV, Optical, Near-IR and HI Parameters for KK246

Parameter	Value	Reference
R.A. (J2000)	20 03 57.4	Lauberts (1982)
Decl. (J2000)	-31 40 54	Lauberts (1982)
l (deg)	9.72864	Derived from Lauberts (1982)
b (deg)	-28.36894	Derived from Lauberts (1982)
H II region R.A. (J2000)	20 03 57.7	This work
H II region Decl. (J2000)	-31 40 48	This work
Dist (Mpc)	6.4 ^a	Tully et al. (2008)
m _B (mag)	17.22	Tully et al. (2008)
A _B (mag)	1.10	Schlafly & Finkbeiner (2011)
E _{B-V} (mag.)	0.154	Schlafly & Finkbeiner (2011)
M _{B,0} (mag)	-12.91	This work
log ₁₀ (L _B /L _⊙)	7.524	This work
m _H (mag)	13.9±0.2	Kirby et al. (2008)
M _{H,0} (mag)	-15.9±0.3	Kirby et al. (2008)
FUV flux (μJy)	28.18±3.89	GALEX Data Release 6/7
NUV flux (μJy)	26.05±3.72	GALEX Data Release 6/7
Total H I flux (Jy km s ⁻¹)	7.3	Kreckel et al. (2011)
	7.5	Meyer et al. (2004)
W ₂₀ (km s ⁻¹)	93	Kreckel et al. (2011)
	104.5	Meyer et al. (2004)
W ₅₀ (km s ⁻¹)	71.6	Meyer et al. (2004)
log ₁₀ (M _{HI} /M _⊙)	8.02±0.03	Kreckel et al. (2011)
	8.03	Derived from Meyer et al. (2004)
log ₁₀ (M _* /M _⊙)	7.7±0.2	Kirby et al. (2008)
M _{HI} /L _B	4.656	This work
Θ tidal index	-2.2	Karachentsev et al. (2004)
Δ tidal index	(nil)	Nicholls et al. (2011)
log ₁₀ (ii) isolation index	3.32	Karachentsev et al. (2011)

^a [Tully et al. \(2008\)](#) use a more recent calibration of the T_{rgb} scale from [Rizzi et al. \(2007\)](#) and give a distance of 6.4 Mpc, compared to the value of 7.83 Mpc from [Karachentsev et al. \(2006\)](#). This does not affect the conclusions reached here.

5.4. HIPASS J1609-04

5.4.1. Description and location

Another interesting galaxy from the SIGRID sample in this context is HIPASS J1609-04. It is located on the edge of the Local Void, 7.65 Mpc from its centre ([Nasonova & Karachentsev 2011](#)). It is one of the more isolated galaxies in the SIGRID sample ([Nicholls et al. 2011](#)), with a Δ tidal index of -2.9. It has an isolation index of 2.38 ([Karachentsev et al. 2011](#)), compared to 3.22 for KK246. Its distance of 14.82 Mpc is estimated from local flow data for the Virgo, Shapley and GA fields. Its baryonic mass is about four times larger than KK246, and it is substantially more actively star forming.

5.4.2. UV, Visible, H α and H-band Imagery

Figure 5.3 shows the GALEX NUV+FUUV, visible, H α and R-band, and H-band images. There are several active star forming regions. The H-band image is from the VISTA Phase III survey (<http://www.eso.org/sci/observing/phase3.html>) and the H α + R-band is from the SINGG survey (Meurer et al. 2006).

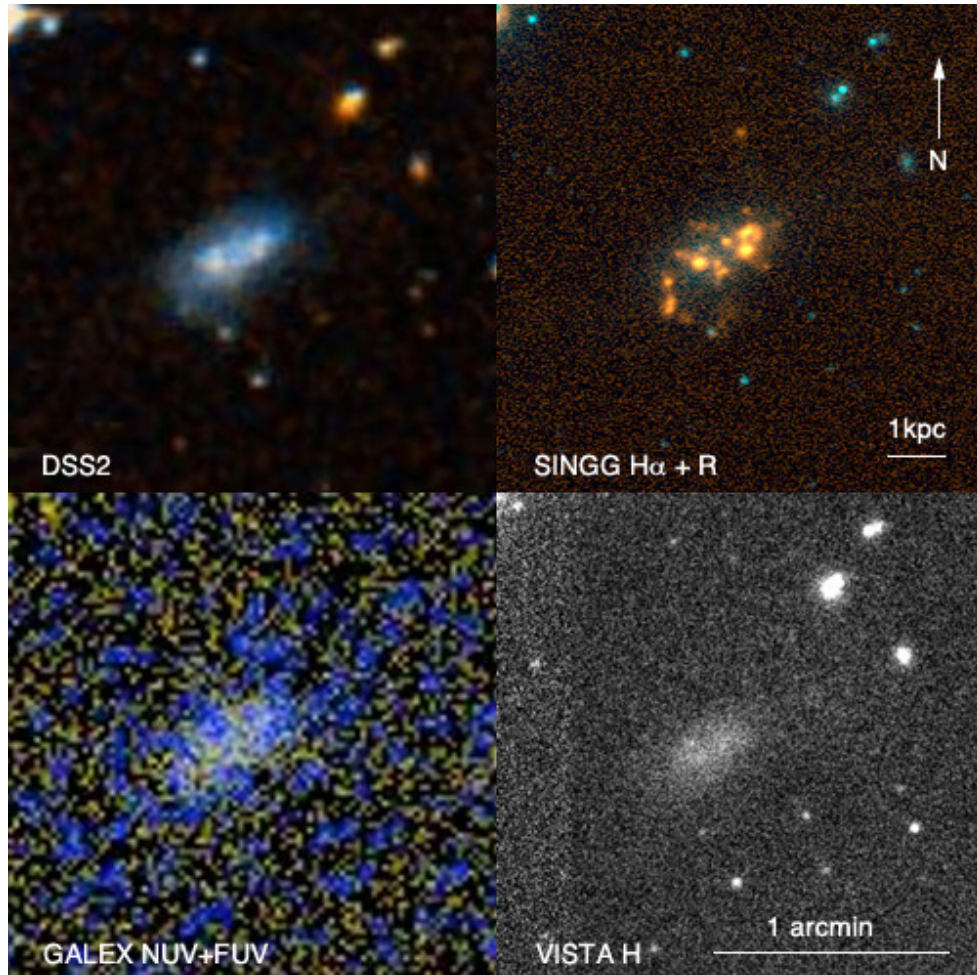


Figure 5.3 J1609 in UV, Visible, H α /R-band and H-band, all to the same scale

Table 5.2 summarises information available on J1609-04. Stellar masses were calculated using the methods discussed by Kirby et al. (2008), based on the stellar mass-to-light ratio models of Bell & de Jong (2001). They found that the major contributor to uncertainties in estimating total stellar mass from H- or other IR band magnitudes was the initial mass function (IMF). As this is not well known, we have adopted the same approach as Kirby et al. (2008). Drawing on their more extensive observational base, we assume the same mass-to-light ratio, $\Upsilon_*^H = 1.0 \pm 0.4$.

For the stellar mass and error estimates, photometry was performed on the VISTA H-band FITS image, using an elliptical aperture large enough to cover the complete galaxy to measure the total H-band flux. The same ellipse was used to measure the noise characteristics in five adjacent, signal free areas (no apparent stars or background galaxies). The errors quoted in Table 2 combine the effect of the (large) mass-to-light ratio uncertainties and the (small) average of the luminosity noise measurements.

Table 5.2 Compendium of UV, Optical, Near-IR and HI Parameters for J1609

Parameter	Value	Reference
R.A. (J2000)	16 09 36.8	NED
Decl. (J2000)	-04 37 12.6	NED
l (deg)	7.134450	Derived from Lauberts (1982)
b (deg)	32.607155	Derived from Lauberts (1982)
Dist (Mpc)	14.82	NED
m_B (mag)	15.35	Doyle et al. (2005)
A_B (mag)	0.862	Schlafly & Finkbeiner (2011)
E_{B-V} (mag.)	0.201	Schlafly & Finkbeiner (2011)
$M_{B,0}$ (mag)	-15.50	(Derived here)
$\log_{10}(L_B/L_\odot)$	8.39	From NED
m_H (mag)	13.26±0.06	From VISTA Phase III imagery ^a
$M_{H,0}$ (mag)	-17.59±0.06	From VISTA Phase III imagery
FUV flux (μJy)	361.26±29.68	GALEX Data Release 6/7
NUV flux (μJy)	345.87±17.19	GALEX Data Release 6/7
Total H I flux (Jy km s^{-1})	7.2	Meyer et al. (2004)
W_{20} (km s^{-1})	111.2	Meyer et al. (2004)
W_{50} (km s^{-1})	71.9	Meyer et al. (2004)
$\log_{10}(M_{\text{HI}}/M_\odot)$	8.55±0.03	Meurer et al. (2006) ^b
$\log_{10}(M_*/M_\odot)$	8.37±0.22	From VISTA Phase III imagery ^c
M_{HI}/L_B	1.45±0.10	(Derived here)
Δ tidal index	-2.9	Nicholls et al. (2011)
\log_{10} (ii) isolation index	2.38	Karachentsev et al. (2011)

^a The H-band magnitude was calculated from the VISTA image using the standard equation $m_H = -2.5 \log_{10}(\text{flux}) + \text{photozp}$.

^b Re-calculated using the flow-corrected distance taking into account the Virgo Cluster, the Great Attractor and the Shapley concentration.

^c The major part or the error (± 0.2) arises from uncertainties in determining the mass-to-light ratio from the H-band luminosity. See above.

5.5. Observations and Data Reduction

We observed both target galaxies using the WiFeS IFU spectrograph ([Dopita et al. 2007, 2010](#)) on the ANU 2.3 m telescope at Siding Spring Observatory. The WiFeS spectrograph is ideal for objects of this size, with a field of view of 25×38 arc sec. Data were obtained on 23–26 August 2011, under clear skies with seeing 1.6–2.4 arc sec, at resolutions of $R=3000$ ($\lambda < 5600\text{\AA}$) and 7000 ($5600 < \lambda < 7000\text{\AA}$), with signal-to-noise ratios typically 50 to 100:1 for the brighter lines. The total on-source integration time was 3.5 hr for KK246 and 1 hr for J1609-04, respectively. Figure 5.4 shows the 3 \AA -wide H α slices (6571 to 6574 \AA) from the data cubes, with overlaid flux contours obtained using IRAF/STSDAS/newcont.

Observed, reddening-corrected line fluxes are given in Table 5.3. Uncorrected data are shown in Table 5.4. The data were reduced using the revised WiFeS Python pipeline ([Childress et al. 2014](#)). This involves steps generally similar to those described in [Dopita et al. \(2010\)](#) for the older pipeline: bias modelling and subtraction, arc line identification and wavelength calibration, cosmic ray removal, sky-line subtraction using nod-and-shuffle, initial data cube construction and atmospheric dispersion correction, standard flux star calibration,

telluric correction, assembly into the final data cubes and combination of multiple cubes into a final object data cube. Spectral sampling was undertaken using a 3 arc sec radius circular spatial area centred on each H II region, through the full wavelength range of the data cube, to obtain spectra for each region. Line fluxes were measured from these spectra using IRAF/splot, and flux de-reddening was performed on the raw flux data using the dust models from [Fischer & Dopita \(2005\)](#), using a relative extinction curve with $R_V^A=4.3$, where $R_V^A = A_V/(E_{B-V})$ and A_V is the V-band extinction. See also the discussion in [Vogt et al. \(2013, Appendix 1\)](#). We used an initial Balmer decrement ratio of 2.82 for $H\alpha/H\beta$, then adjusted the apparent Balmer ratios by varying the value of A_V for the best fit to the $H\gamma/H\beta$ ratio, using the ratio $H\delta/H\beta$ as a check, fitting to the [Storey & Hummer \(1995\)](#) Case B Balmer ratios.

The raw fluxes are listed in [Table 5.4](#), and the de-reddening fits for the Balmer ratios of $H\alpha$ through $H\delta$ in [Table 5.5](#). The fit for region 3 of J1609-04 is not particularly satisfactory, possibly due to differential contamination of the sampled area from regions 1 and 2 in the red and blue channels. Other fits are good, and excellent in the case of KK246. The low value of the extinction, $A_V=0.032$, for KK246, implies very low dust content. For clarity the error estimates are omitted from [Table 5.4](#), but they may be calculated from those quoted in [Table 5.3](#).

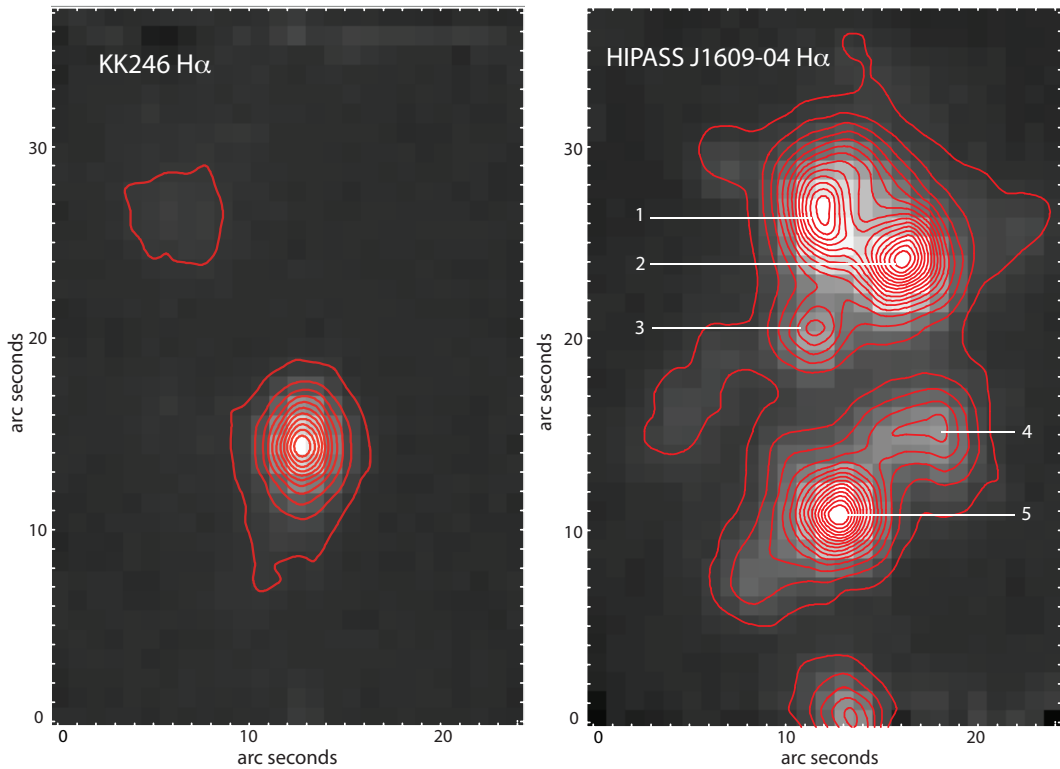


Figure 5.4 Left Panel: KK246 $H\alpha$ WiFeS IFU image with contours (logarithmic stretch, $6.2e-18$ to $1.76e-16$ erg $cm^{-2} s^{-1} \text{\AA}^{-1}$, at 0.125 dex intervals). Right Panel: J1609-04 $H\alpha$ WiFeS IFU image with contours (logarithmic stretch, $1.0e-18$ to $7.2e-16$ erg $cm^{-2} s^{-1} \text{\AA}^{-1}$, at 0.25 dex intervals). Numbers indicate the locations of the individual H II regions used in the analysis ([Tables 5.3–5.7](#)).

Table 5.3 Measured line fluxes for the H α regions in KK246 and HIPASS J1609-04, corrected for reddening, in units of $\text{erg s}^{-1}\text{cm}^{-2}\text{\AA}^{-1}$. Fluxes were measured using a 6 arc sec diameter sample centred on each arc sec.

Line	KK246	J1609(1)	J1609(2)	J1609(3)	J1609(4)	J1609(5)
SiII 6731	(2.26±0.16)E-16	(8.54±0.23)E-15	(1.18±0.02)E-15	(5.28±0.21)E-16	(4.55±0.18)E-16	(7.86±0.02)E-15
SiII 6716	(3.34±0.15)E-16	(1.21±0.24)E-15	(1.67±0.02)E-15	(7.78±0.21)E-16	(6.22±0.18)E-16	(1.15±0.02)E-15
NII 6584	(1.65±0.17)E-16	(4.65±0.17)E-16	(6.67±0.19)E-16	(3.41±0.19)E-16	(2.42±0.18)E-16	(5.92±0.19)E-16
H α 6563	(6.35±0.02)E-15	(1.33±0.01)E-14	(1.60±0.01)E-14	(6.31±0.02)E-15	(5.92±0.03)E-15	(1.18±0.00)E-14
OIII 5007	(5.65±0.03)E-15	(1.38±0.01)E-14	(1.50±0.01)E-14	(5.65±0.02)E-15	(5.82±0.02)E-15	(1.34±0.00)E-14
OIII 4959	(2.02±0.03)E-15	(4.63±0.03)E-15	(5.12±0.02)E-15	(1.88±0.02)E-15	(1.93±0.02)E-15	(4.62±0.02)E-15
H β 4861	(2.24±0.04)E-15	(4.76±0.11)E-15	(5.59±0.03)E-15	(2.27±0.02)E-15	(2.10±0.02)E-15	(4.20±0.02)E-15
OIII 4363	(1.34±0.15)E-16	(2.90±0.29)E-16
H γ 4340	(1.06±0.04)E-15	(2.26±0.03)E-15	(2.70±0.03)E-15	(9.65±0.26)E-16	(9.93±0.28)E-16	(1.97±0.03)E-15
H δ 4102	(5.82±0.06)E-16	(1.23±0.03)E-15	(1.48±0.04)E-15	(4.92±0.36)E-16	(5.19±0.38)E-16	(9.83±0.34)E-16
OIII 3729	(2.50±0.15)E-15	(7.54±0.07)E-15	(9.49±0.09)E-15	(3.67±0.10)E-15	(5.30±0.12)E-15	(6.44±0.07)E-15
OIII 3726	(1.37±0.15)E-15	(5.95±0.20)E-15	(8.50±0.09)E-15	(3.54±0.10)E-15	(3.92±0.12)E-15	(5.93±0.07)E-15

Table 5.4 Uncorrected fluxes ($\text{erg s}^{-1} \text{cm}^{-2} \text{\AA}^{-1}$). For errors see previous table.

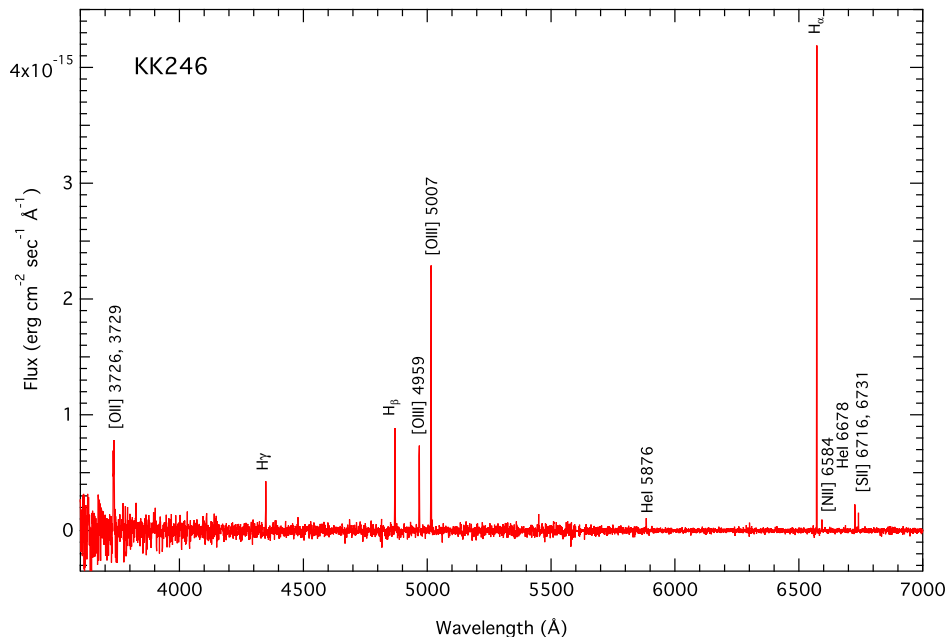
Line	KK246	J1609(1)	J1609(2)	J1609(3)	J1609(4)	J1609(5)
SII 6731	2.29E-16	1.39E-15	1.63E-15	7.55E-16	7.10E-16	1.24E-15
SII 6716	3.38E-16	1.96E-15	2.31E-15	1.11E-15	9.66E-16	1.80E-15
NIi 6584	1.67E-16	7.35E-16	9.08E-16	4.78E-16	3.68E-16	9.09E-16
H α	6.42E-15	2.10E-14	2.17E-14	8.82E-15	8.96E-15	1.81E-14
OIII 5007	5.66E-15	1.45E-14	1.55E-14	5.86E-15	6.09E-15	1.41E-14
OIII 4959	2.02E-15	4.79E-15	5.24E-15	1.93E-15	1.99E-15	4.76E-15
H β	2.24E-15	4.76E-15	5.59E-15	2.27E-15	2.10E-15	4.20E-15
OIII 4363	1.18E-16	2.42E-16
H γ	1.05E-15	1.84E-15	2.35E-15	8.30E-16	8.24E-16	1.63E-15
H δ	5.77E-16	9.01E-16	1.20E-15	3.91E-16	3.91E-16	7.35E-16
OII 3729	2.29E-15	4.63E-15	6.84E-15	2.56E-15	3.40E-15	4.08E-15
OII 3726	1.37E-15	3.65E-15	6.12E-15	2.47E-15	2.51E-15	3.75E-15

Table 5.5 Corrected Balmer line ratios and corresponding A_v values

Object	KK246	J1609(1)	J1609(2)	J1609(3)	J1609(4)	J1609(5)
A_v	0.032	1.250	0.840	0.920	1.140	1.170
$H\alpha/H\beta$	2.833	2.802	2.861	2.782	2.820	2.818
$H\gamma/H\beta$	0.471	0.475	0.483	0.425	0.473	0.470
$H\delta/H\beta$	0.260	0.258	0.265	0.217	0.247	0.234

5.6. Spectra

Figure 5.5 shows the flux-calibrated spectrum of KK246 in the range $3600 < \lambda < 7000\text{\AA}$ derived from the data cubes using spatial pixels within a 6 arc sec diameter aperture. The principle atomic lines are: [OII] 3726,27 \AA , $H\gamma$, $H\beta$, [OIII] 4959 \AA , [OIII] 5007 \AA , HeI 5876 \AA , $H\alpha$, [NII] 6584 \AA , HeI 6678 \AA , and [SII] 6716,31 \AA . It is noteworthy that the intensity of the [OIII] 4959 \AA line is less than the $H\beta$, the intensity of the [OIII] 5007 \AA line is considerably less than the $H\alpha$, and there is no evidence of the [OIII] 4363 \AA auroral line. This suggests a reasonably low metallicity, and possibly the tail-end of an episode of star formation, and hence relatively low ionisation. No stellar continuum is apparent.

**Figure 5.5** Flux-calibrated spectrum of KK246 with principle atomic lines labelled.

Five separate, reasonably bright, star forming regions were observed in HIPASS J1609-04, and spectra for each of these were obtained. The regions are identified in Figure 5.4, right panel. The spectra are shown in Figure 5.6. The auroral line is apparent in the two brightest regions, 2 and 5. The bottom right panel of Figure 5.6 is a composite spectrum of regions 2 and 5, with the main spectral lines labeled.

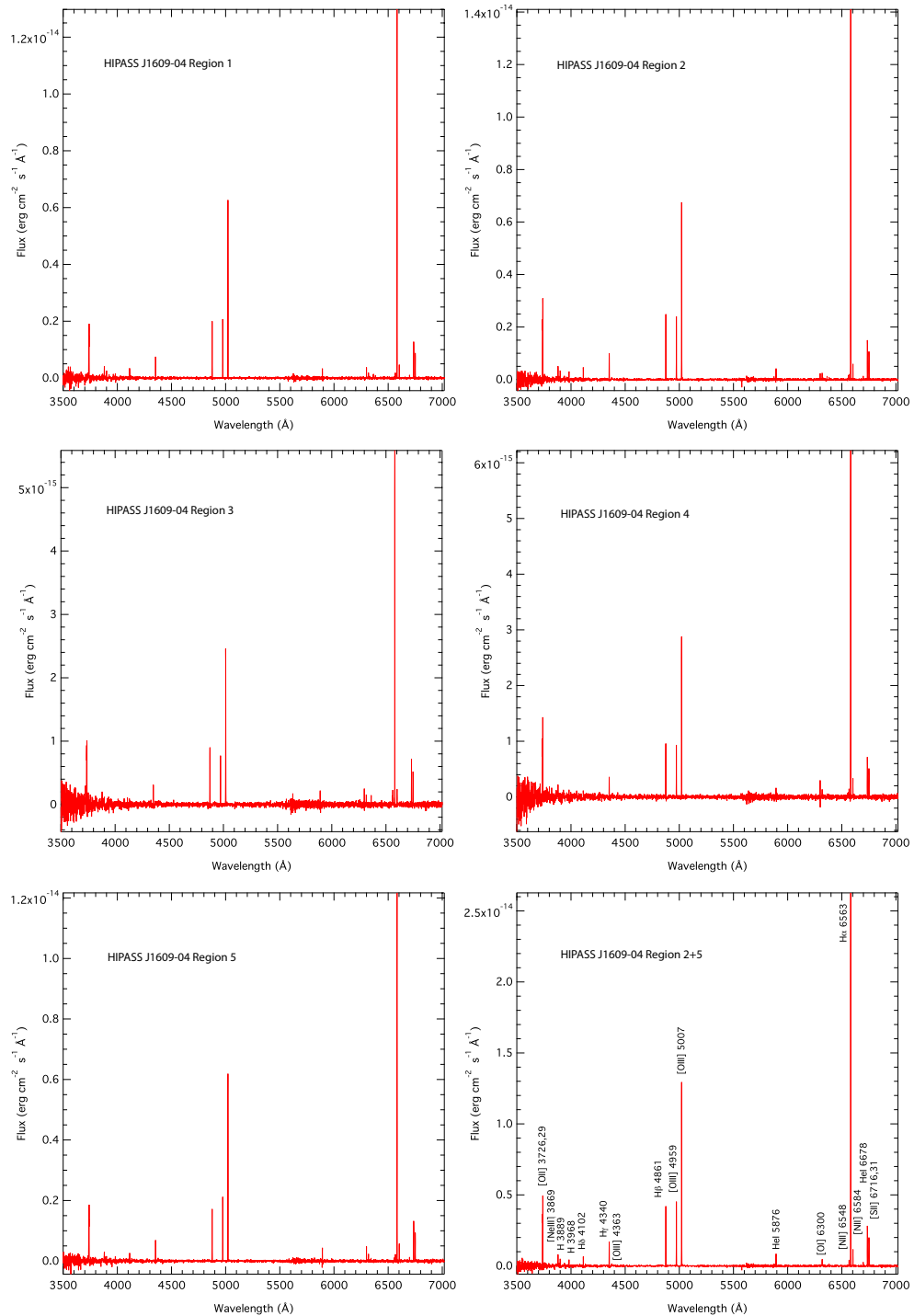


Figure 5.6 Spectra of five individual H II regions in HIPASS J1609-04, and a combined spectrum from regions 2 and 5, with line identification.

5.6.1. Comments on Spectra

The spectra of both KK246 and J1609-04 show, at most, only faint stellar continua, and as a result measurement of equivalent widths of the spectral lines is unreliable. The brighter H II regions 2 and 5 in J1609-04 exhibit faint broad stellar absorption underlying the H β , γ and δ nebular emission lines, but the stellar continuum is faint. Measurement noise makes it difficult to estimate the equivalent widths of the absorption features, but they have been taken into account in estimating emission line fluxes. In addition, our reduction pipeline does not currently allow accurate rendering of the absolute continuum for faint continua at the short wavelength end of the blue spectrum, below 4200Å.

Equivalent widths for emission lines are similarly problematic. The low stellar continuum creates large EW values for the bright lines 2008ApJ...681.1183K, e.g. EW [O III 5007] = 135 for J1609-04(5), with reliable errors difficult to estimate. For the UV [O II] lines, the measurement noise is sufficiently large that EW estimates are meaningless. For this reason we have not included EW measurements in this paper.

5.7. Nebular metallicities

The most important insight into the evolutionary stage of the two objects is provided by their (nebular) metallicities. This tells us about the enrichment of the star-forming regions by previous generations of stars, and the degree to which the heavier elements are retained by the gravitational potential of the galaxies. In general, the mass–metallicity relation shows that there is a trend to lower metallicities for lower mass galaxies (e.g., Tremonti et al. 2004). The primary finding of this paper relates to metallicity measurements.

A key method for determining nebular temperatures and metallicities is the electron temperature, or T_e method. This is possible only if one of the “auroral” lines is observed, usually [O III] 4363Å. This line was detected in only two of the five regions in J1609-04, but was absent in the spectrum of KK246, so we have used strong line methods to determine metallicities (e.g., Dopita et al. 2013; Kewley & Dopita 2002; Kewley & Ellison 2008). López-Sánchez et al. (2012) evaluated the reliability of several of the conventional strong line methods in reproducing theoretically constructed emission line data. They found that some of the commonly used techniques cannot be relied on to give consistently accurate results for nebular metallicity, and that the T_e method gave consistently lower metallicities than the (reliable) strong line methods, by ~ 0.2 - 0.25 dex. Subsequently, Nicholls et al. (2012, 2013) showed that non-equilibrium (κ) electron distributions can affect the diagnostic results. This, and the advent of much improved atomic data, led us (Nicholls et al. 2013; Dopita et al. 2013) to revise the strong line diagnostic methods and the photoionisation modelling code. The strong line diagnostics used here are derived from the newly revised Mappings photoionisation modelling code (version IV; Dopita et al. 2013), resulting in substantially more consistent metallicity values, as demonstrated in Table 5.6, which shows the results of that analysis. The diagnostic grids on which the analysis is based are shown in Figures 5.7 and 5.8.

Earlier strong line methods did not solve explicitly for the ionisation parameter, $\log(q)$, and thus did not take fully into account the ionisation gradients present in H II regions

(see, e.g., [Dopita et al. 2013](#)). In the analysis used in Mappings IV, we solve separately for the metallicity Z ($= 12 + \log(\text{O}/\text{H})$) and ionisation parameter $\log(q)$, thus avoiding most of the degeneracies present in older strong line diagnostic methods. The diagnostics chosen here are also relatively insensitive to non-equilibrium (κ) electron energy distributions, especially for values of $\kappa > 20$, i.e., values which give the best fit in resolving the abundance discrepancy ([Stasińska 2004](#); [Nicholls et al. 2012](#)).

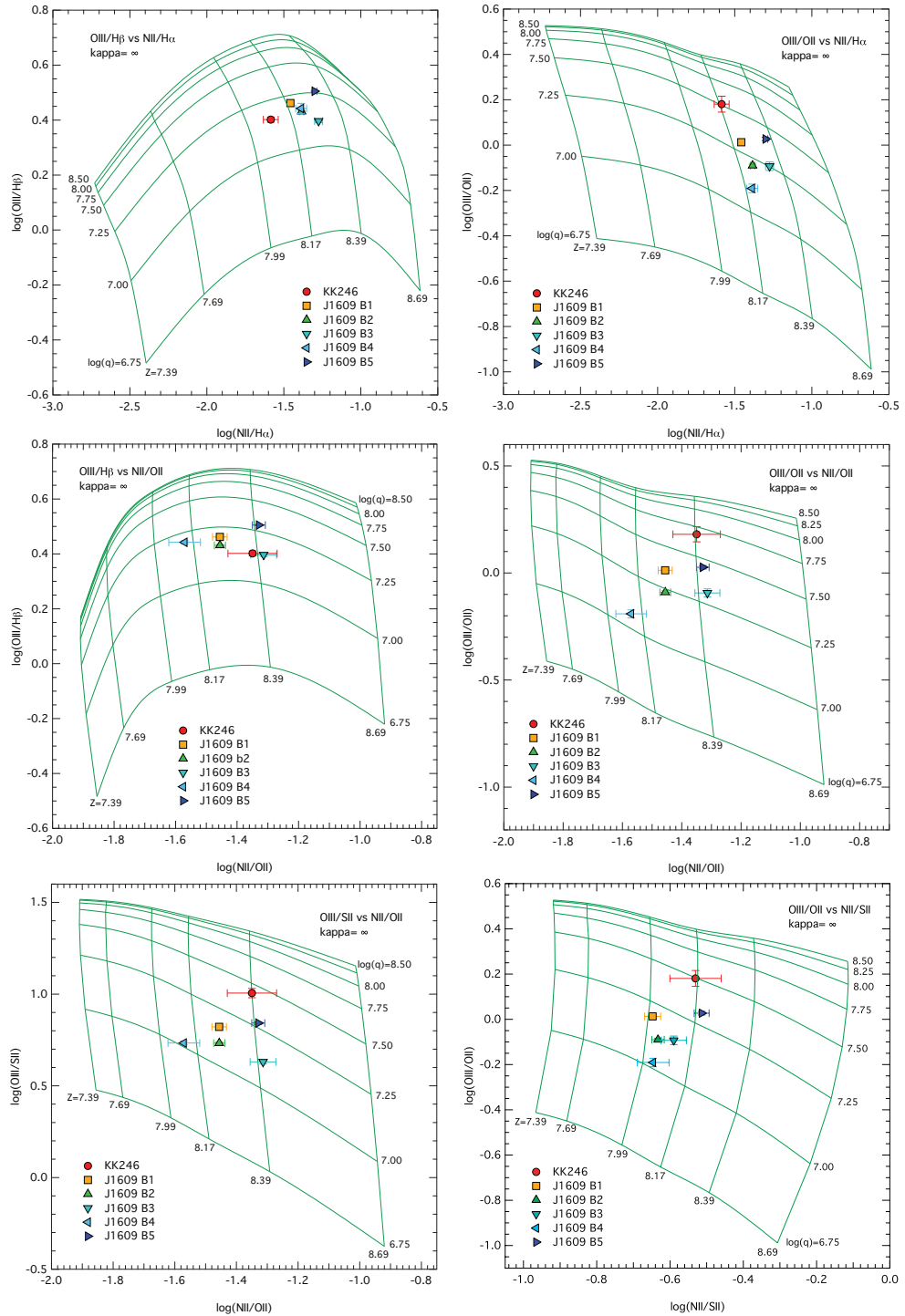


Figure 5.7 Strong line diagnostic grids, showing flux ratios for KK246 and the five regions in J1609-04 (grids computed using data from [Dopita et al. 2013](#)).

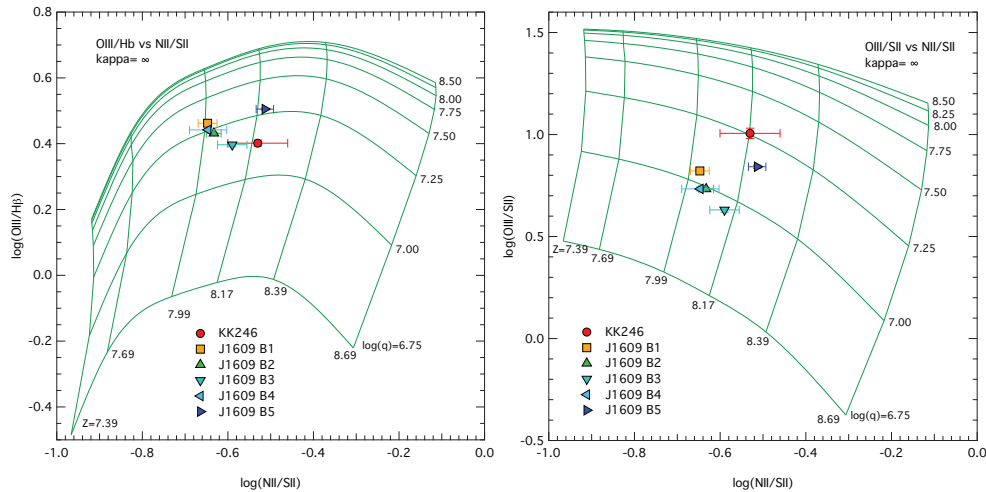


Figure 5.8 Strong line diagnostic grids, continued, showing flux ratios for KK246 and the five regions in J1609-04 (grids computed using data from [Dopita et al. 2013](#)).

5.7.1. Direct T_e Method Metallicity

For the two brightest regions in J1609-04 (2 and 5), the [O III] auroral line $\lambda 4363$ is evident. For these we can measure the metallicity using the direct T_e method. To improve the signal-to-noise ratio, we have combined the spectra of the two regions. Using the models presented in [Dopita et al. \(2013\)](#); [Nicholls et al. \(2013\)](#), we calculate the [O III] electron temperature from the combined spectra, as: $T_e = 12,806 \pm 556$ K. Using the methods described in [Izotov et al. \(2006\)](#), the oxygen ([O III]+[O II]) metallicity calculated from the electron temperature of the combination of regions 2 and 5 of J1609-04 is 7.96 ± 0.06 . As is characteristic of metallicities derived conventionally from the T_e method ([López-Sánchez et al. 2012](#)), this value is lower by ~ 0.2 dex than the value determined using the latest strong line methods ([Dopita et al. 2013](#)).

5.7.2. Metallicity Results (Strong Line)

Table 5.6 shows the complete line ratios for $\kappa = \infty$, with two sets of averages. The first set takes the means over all strong line diagnostics. The second, significantly more precise, uses only the mean values of diagnostic ratios using [N II]/[S II]. The latter diagnostic ratios accurately return input values from test spectra generated by the Mappings IV code, whereas the diagnostic ratios involving [N II]/[O II] return significantly higher values, in some cases. It is not clear yet whether this indicates a problem with the diagnostic itself, or, more likely, whether the interpolation process ([Dopita et al. 2013](#)) is at fault. Further work is necessary. In any case, as shown in Figures 7 and 8, the errors in observed flux ratios are significantly greater for ratios involving [O II]. For this reason we adopt values for Z and $\log(q)$ using only diagnostics involving [N II]/[S II]. Other ratios including [N II]/[H α] tend to confirm the [N II]/[S II] values.

As shown in Table 5.6, the metallicity for KK246, assuming an equilibrium electron energy distribution, is 8.17 ± 0.01 , and for the H II regions in J1609-04, the metallicity values span a range between 8.02 and 8.20. For a non-equilibrium κ electron energy distributions with $\kappa = 50$ and 20, the metallicities are virtually identical, a consequence of choosing strong

Table 5.6 Metallicity and ionisation parameter values

	KK246	J1609(1)	J1609(2)	J1609(3)	J1609(4)	J1609(5)
$\kappa = \infty$						
<hr/>						
N _{II} /S _{II} vs O _{III} /S _{II}						
z	8.172	8.027	8.066	8.144	8.038	8.211
log(q)	7.256	7.051	6.993	6.973	6.990	7.157
N _{II} /S _{II} vs O _{III} /H _b						
z	8.187	8.00	8.031	8.111	8.001	8.195
log(q)	7.142	7.304	7.242	7.154	7.257	7.294
N _{II} /O _{II} vs O _{III} /O _{II}						
z	8.373	8.250	8.284	8.398	8.079	8.408
log(q)	7.637	7.316	7.242	7.277	7.025	7.449
N _{II} /O _{II} vs O _{III} /S _{II}						
z	8.367	8.240	8.273	8.388	8.076	8.401
log(q)	7.420	7.156	7.101	7.109	7.002	7.281
N _{II} /S _{II} vs O _{III} /O _{II}						
z	8.162	8.008	8.042	8.112	8.035	8.194
log(q)	7.474	7.184	7.123	7.132	7.005	7.318
N _{II} /O _{II} vs O _{III} /H _b						
z	8.351	8.244	8.280	8.390	8.102	8.403
log(q)	7.134	7.209	7.166	7.130	7.212	7.296
N _{II} /H _a vs O _{III} /H _b						
z	8.095	8.196	8.244	8.303	8.245	8.334
log(q)	6.560	6.754	7.181	7.012	7.194	7.212
N _{II} /H _a vs O _{III} /O _{II}						
z	8.176	8.218	8.252	8.333	8.203	8.361
log(q)	7.482	7.294	7.221	7.234	7.088	7.420
Mean z	8.24 ± 0.11	8.15 ± 0.11	8.18 ± 0.12	8.27 ± 0.13	8.10 ± 0.09	8.31 ± 0.10
Mean log(q)	7.26 ± 0.33	7.16 ± 0.19	7.16 ± 0.09	7.13 ± 0.10	7.10 ± 0.11	7.30 ± 0.10
Adopted mean z	8.17 ± 0.01	8.01 ± 0.01	8.05 ± 0.02	8.12 ± 0.02	8.03 ± 0.02	8.20 ± 0.01
Adopted mean log(q)	7.29 ± 0.17	7.18 ± 0.13	7.11 ± 0.12	7.09 ± 0.10	7.08 ± 0.15	7.26 ± 0.09

line diagnostics that are not especially sensitive to κ , and which therefore result in very consistent metallicities.

The interpretation of the new diagnostic ratios used here is explored in depth by [Dopita et al. \(2013\)](#), but there is scope for further work. In the meantime, especially for low metallicity H II regions, diagnostics involving [N II]/[S II] appear to offer very consistent results.

Table 5.6 Metallicity and ionisation parameter values (continued)

	KK246	J1609(1)	J1609(2)	J1609(3)	J1609(4)	J1609(5)
$\kappa = 50$						
Mean z	8.25 ± 0.10	8.17 ± 0.13	8.20 ± 0.13	8.29 ± 0.14	8.11 ± 0.12	8.32 ± 0.11
Mean $\log(q)$	7.36 ± 0.15	7.24 ± 0.13	7.20 ± 0.11	7.18 ± 0.10	7.15 ± 0.16	7.33 ± 0.10
Adopted mean z	8.17 ± 0.01	8.02 ± 0.02	8.05 ± 0.02	8.12 ± 0.02	8.03 ± 0.02	8.20 ± 0.01
Adopted mean $\log(q)$	7.32 ± 0.12	7.25 ± 0.20	7.18 ± 0.18	7.13 ± 0.13	7.16 ± 0.23	7.30 ± 0.13
$\kappa = 20$						
Mean z	8.28 ± 0.09	8.18 ± 0.15	8.19 ± 0.14	8.26 ± 0.15	8.08 ± 0.13	8.29 ± 0.11
Mean $\log(q)$	7.43 ± 0.09	7.37 ± 0.23	7.28 ± 0.20	7.24 ± 0.16	7.19 ± 0.28	7.38 ± 0.19
Adopted mean z	8.17 ± 0.01	8.02 ± 0.02	8.05 ± 0.03	8.12 ± 0.04	8.03 ± 0.03	8.21 ± 0.02
Adopted mean $\log(q)$	7.39 ± 0.08	7.40 ± 0.40	7.29 ± 0.31	7.23 ± 0.22	7.29 ± 0.39	7.40 ± 0.25

5.8. Comparison with similar samples

5.8.1. $\log(N/O)$ Values

One of the more important parameters in understanding galactic evolution is the nitrogen abundance, and in particular, the ratio of nitrogen to oxygen. The observations reported here include good measurements of both $[N\text{II}]$ and $[O\text{II}]$, allowing us to explore the values of $\log(N/O)$ for each $H\text{II}$ region. To calculate the value of N/O from $[N\text{II}]$ and $[O\text{II}]$ line fluxes, we use empirical formulae from [Izotov et al. \(2006\)](#), Equations (3) and (6). These reduce to:

$$\log\left(\frac{N}{O}\right) = \log\left(\frac{N\text{II } 6584 + 6548}{O\text{II } 3726 + 3729}\right) + 0.273 - 0.726/T_{e4} + 0.007 * T_{e4} - 0.02 * \log(T_{e4}), \quad (5.1)$$

where T_{e4} is the electron temperature in units of 10,000 K. This equation differs only by a small constant offset (0.033) from that quoted by [Pagel et al. \(1992\)](#), Equation (9)). We assume the same electron temperature for $O\text{II}$ and $N\text{II}$ (reasonable, as they both arise primarily from the outer parts of the $H\text{II}$ region), and further, that $N^+/O^+ = N/O$, following [Pilyugin et al. \(2010\)](#) and others. The errors from these assumptions are likely to be of the same order as the measurement uncertainties. The results are shown in Table 5.7.

The values of $\log(N/O)$ for these regions are uniformly low, and similar to the value adopted by [Lebouteiller et al. \(2013\)](#) for 1Zw18, -1.61 ± 0.10 .

5.8.2. Mass–metallicity

Mass versus metallicity behaviour is one of the important evolutionary diagnostics for galaxies. It has been extensively mapped for larger galaxies (e.g., [Tremonti et al. 2004](#)), but it is less well known for dwarf galaxies ([Lee et al. 2006](#)). Exploring it was one of the motivations

Table 5.7 $\log(N/O)$ calculated from $[NII]/[OII]$ flux ratios using equation (7.1), for T_e in units of 10,000K. (The measurement errors apply to all ratios.)

	KK246	J1609(1)	J1609(2)	J1609(3)	J1609(4)	J1609(5)
$\log[NII]/[OII]$	-1.352	-1.303	-1.249	-1.325	-1.420	-1.320
\pm error	0.156	0.036	0.028	0.042	0.082	0.021
$\log(N/O)_{T_{e4}=1}$	-1.80	-1.75	-1.70	-1.77	-1.86	-1.77
$\log(N/O)_{T_{e4}=1.25}$	-1.65	-1.60	-1.55	-1.63	-1.72	-1.62

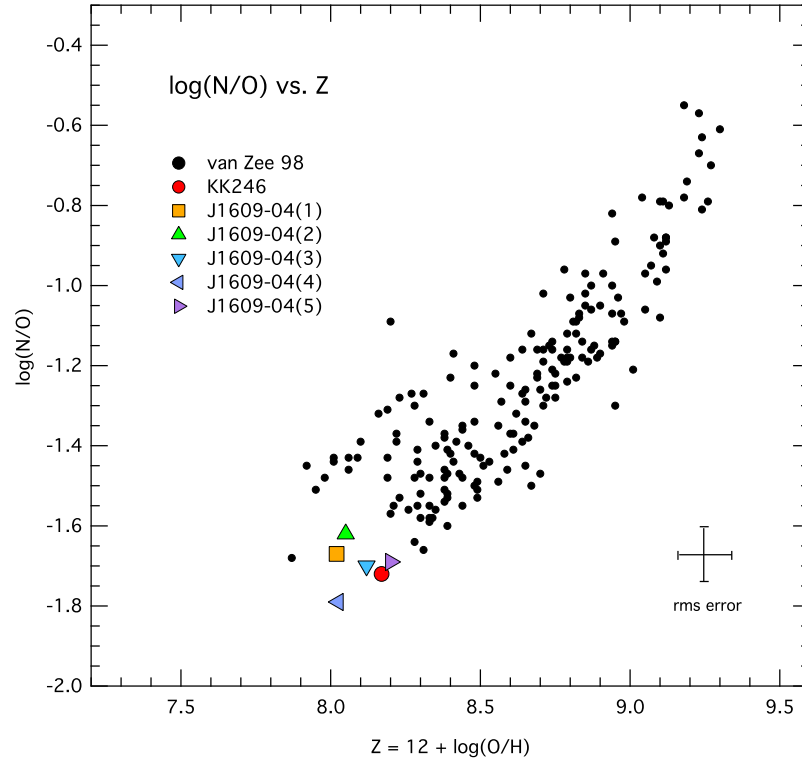


Figure 5.9 $\log(N/O)$ versus oxygen metallicity for the objects observed here and data from [van Zee et al. \(1998c\)](#). Values of $\log(N/O)$ shown here correspond to an electron temperature of 11,250K. The error bars indicate the rms error averaged over all observations.

for the SIGRID sample ([Nicholls et al. 2011](#)). Figure 5.10 shows the stellar masses versus metallicities for KK246 (red) and J1609-04 (yellow, summed over all regions) plotted with data on similar low mass objects from [Lee et al. \(2006\)](#) for comparison. Metallicity for the Lee objects was taken from several sources of good quality spectra, estimated using the T_e method (and older atomic data). The values for KK246 and J1609-04 have been reduced by 0.2 dex to compensate for the typical difference between strong line and T_e method metallicities. Figure 5.10 shows that KK246 and J1609-04 follow the same trend as Lee et al.'s non-void dwarf objects, although, as has been found for void galaxies ([Pustilnik et al. 2011b](#)), J1609-04 falls a little below the trend.

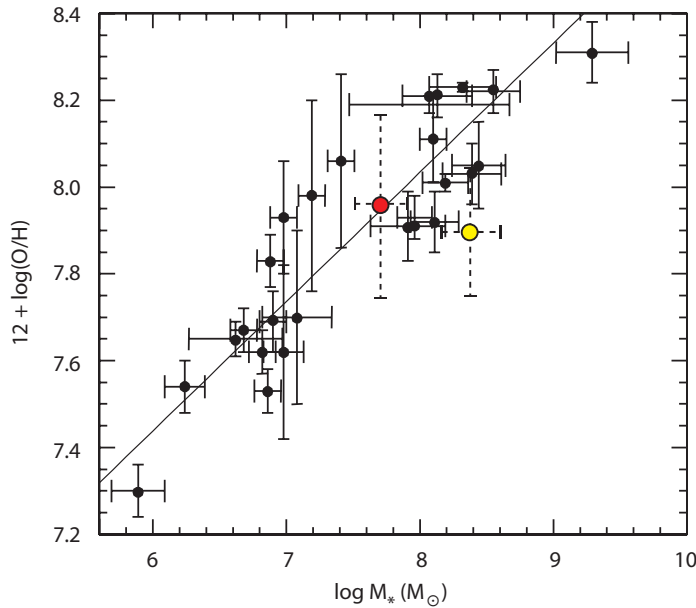


Figure 5.10 Oxygen abundance versus stellar mass for KK246 (red) and J1609-composite (yellow), plotted with T_e method data for 25 nearby ($D < 5$ Mpc) dwarf irregular galaxies from Lee et al. (2006). Our metallicity measurements are offset by -0.2 dex to compensate for the systematic difference between strong line and T_e methods. The least-squares fit (solid line) applies only to the Lee et al. data.

5.8.3. Mass versus light

Another question of interest is how the mass to light ratio versus absolute magnitudes of these two galaxies compare with other similar galaxies. Are they intrinsically low luminosity objects? Values for M_{HI}/L_B are shown in Tables 1 and 2: for KK246 the value is 4.66 and for J1609-04, 1.45. In Figure 5.11 we plot KK246 and J1609-04 on data from Figure 2 from Warren et al. (2007). The shaded area shows 752 more luminous galaxies from the HIPASS Bright Galaxy Catalog. The dashed line shows the locus of an upper limit for the H I mass-to-light ratio, as a function of luminosity. The individual galaxies marked with error bars are those discussed by Warren et al. (2007) and comprise late-type galaxies with a wide range of physical parameters. It is clear that there is nothing extreme about the two objects presented here—their M_{HI}/L_B ratios are typical of the 38 late-type galaxies with a range of mass-to-light ratios discussed by Warren et al. (2007).

5.8.4. Other studies of void galaxies

The subject of galaxies in voids in the Local Volume has received increasing attention recently. Pustilnik et al. (2011a,b) have investigated galaxies in the Lynx-Cancer Void using their own and SDSS data, and find that in general, the metallicities are lower by $\sim 30\%$ than for higher density regions. In a study using Sloan Digital Sky Survey (SDSS) data for galaxies in Local Volume voids, van de Weygaert et al. (2011) and Kreckel et al. (2012) found that, despite predictions from simulations, there was no significant population of H I-rich low-luminosity galaxies filling the voids. They also found evidence of cold-mode accretion of H I in some objects. Both studies included late-type spiral galaxies as well as dwarf irregulars. For 48 Lynx-Cancer Void galaxies from Pustilnik et al. (2011b), the listed metallicity varies between 7.14 and 8.36. These values are measured using the T_e method, or using a semi-empirical

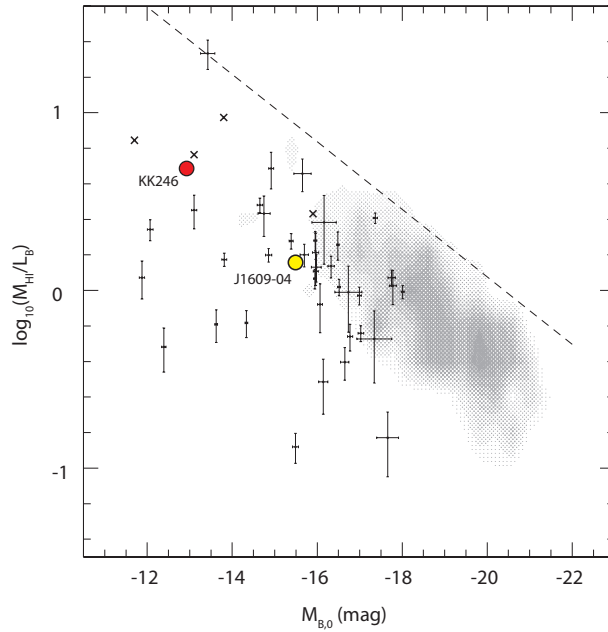


Figure 5.11 Mass-to-light ratio versus absolute magnitude: $\log_{10}(\mathcal{M}_{\text{HI}}/L_B)$ versus $M_{B,0}$ for KK246 (red) and J1609-composite (yellow), plotted on data from Figure 2 from Warren et al. (2007). Error bars for KK246 and J1609-04 are within the plotted circles. The grey hatched area shows the HIPASS Bright Galaxy Catalog objects, the objects with error bars are from Warren et al., and the crosses are other objects from Warren et al. from the literature.

method based on it, using older atomic data, and are likely underestimated by ~ 0.2 dex compared to strong line metallicities (López-Sánchez et al. 2012; Nicholls et al. 2013).

Figure 5.12 shows metallicity versus $M_{B,0}$ for KK246 and J1609-04 plotted in the data for 42 Lynx-Cancer Void galaxies from Pustilnik et al. (2011b). The metallicities for KK246 and J1609-04 have been reduced by 0.2 dex to reflect the discrepancy between T_e metallicities and strong line metallicities. The dashed line is for dI galaxies from Lee et al. (2003). J1609-04 is typical of the other galaxies plotted, and lies near the trend defined by the dIrrs. KK246 is somewhat more metal rich, or conversely, less luminous in the B-band, than the others. This may be explained if the galaxy is nearing a “post-starburst” phase, with fewer blue stars present than would be expected from the current metallicity.

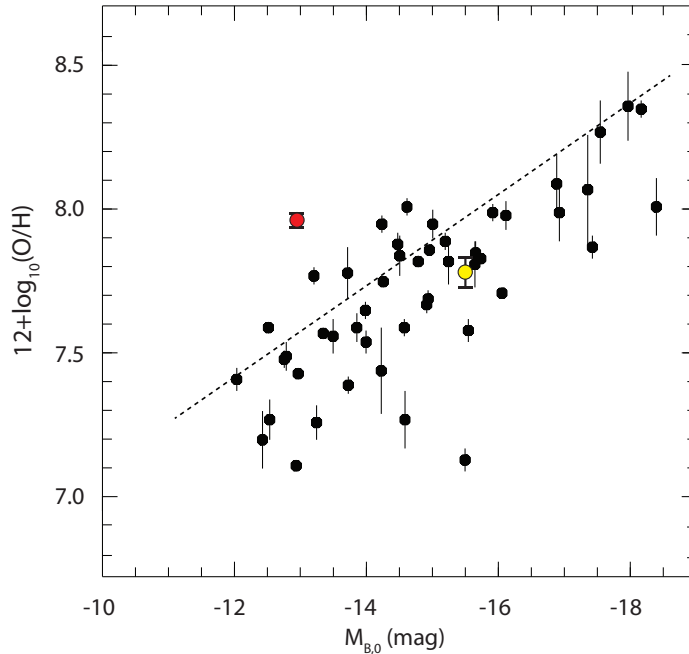


Figure 5.12 Metallicity versus $M_{B,0}$ for KK246 (red) and J1609-composite (yellow), plotted on data for Lynx-Cancer Void galaxies from [Pustilnik et al. \(2011b\)](#), offset vertically by -0.2 dex to allow for the T_e /strong line difference..

5.9. Discussion

KK246 is the most isolated dwarf galaxy in the Local Volume, and J1609-04 is almost as isolated. Thus their star formation tells us about the intrinsic behaviour of a gas-rich dwarf galaxy left to its own devices. It is apparent that these two objects represent quite normal dwarf irregular galaxies. Their metallicities, nitrogen-to-oxygen ratios, mass-to-light ratios and luminosities are typical for their masses. They appear to have evolved in the absence of external disturbance or enrichment in their local environments, so we may conclude that isolated dwarf galaxies do not need to be members of groups or clusters, or to have been influenced tidally to stimulate star formation and evolve normally, if they have a supply of H I. They build metallicities that are intrinsic and typical for their size. This suggests that, as a class, isolated dwarf irregular galaxies may not be good indicators of primordial abundances.

Although it has been suggested that small galaxies may not have sufficient mass to retain their supernova outflows, [Bland-Hawthorn et al. \(2011\)](#) showed that full three-dimensional modelling assuming a clumpy medium indicated that a Dark Matter halo (virial radius) mass of $3 \times 10^6 M_{\odot}$ is sufficient for a galaxy to gravitationally bind its supernova debris, and thus continue star formation while retaining chemical signatures laid down in the earlier epochs. Further evidence for this is that virtually no HIPASS H I object is known without an accompanying galaxy or galaxy-component ([Koribalski et al. 2004](#); [Doyle et al. 2005](#); [Meurer et al. 2006](#); [Karachentsev et al. 2008](#)). This was also demonstrated using disk evolutionary modelling by [Taylor & Webster \(2005\)](#). This implies that anywhere a concentration of neutral hydrogen occurs, a (dwarf) galaxy will evolve. It also indicates that the nebular metallicities of the two galaxies in this study reflect fully the star formation that has occurred in them.

From direct analysis of HST WFC3 photometry (Karachentsev et al. 2006), KK246 shows more than one star forming episodes. The old stellar population implied by H-band luminosity suggests it has been forming stars over a protracted period. H-band imagery suggests that the same is true for J1609-04. It is not clear how frequently star forming episodes occur in galaxies like these, and they may only happen occasionally. From studies of isolated blue compact dwarf (BCD) galaxies, Sánchez Almeida et al. (2008) have concluded that there is a duty cycle of 30:1 (quiescence to star burst). To judge from the BCD population in the SIGRID sample (Nicholls et al. 2011), and the presence of at least two stellar populations in KK246 and J1609-04, this may be an underestimate. A better figure may be 10:1 or less, especially for less intense starburst episodes.

The individual star-forming regions in J1609-04 vary in metallicity between 8.0 and 8.2. The metallicity of the regions do not correlate with their intrinsic luminosities, but this could be explained by the regions being of slightly different ages. The H I region surrounding KK246 implies a plentiful supply of neutral hydrogen available for cold mode accretion. Such accretion has been observed in the Void Galaxy Survey in some galaxies (van de Weygaert et al. 2011), and in Sag DIG in the Local Group (Young & Lo 1997).

From this, one may postulate a narrative for the development of small isolated galaxies. If they form early in the history of the universe, with continuing H I available for cold inflow accretion, they will exhibit periodic star formation and evolve normally. Their stellar populations will span a range of ages. Supernova ejecta and stellar winds from the older stars will enrich the interstellar medium of the galaxy and a substantial fraction of the metallicity will be retained. As a result the nebular metallicities will grow with time and will not be exceptionally low. While Pustilnik & Kniazev (2007) suggest that galaxies form later and evolve more slowly in regions of low density, this appears inconsistent with the old stellar populations in the two objects discussed here.

We also speculate that extremely low metallicity objects such as 1Zw18 (Izotov & Thuan 1999) and SBS 0335-052W (Izotov et al. 2005) are probably exceptional, and the absence of significant older stellar populations indicates that they have most likely formed recently from pristine gas. The details of the older stellar population of 1Zw18 are not completely settled (Garnett et al. 1997; Aloisi et al. 1999; Papaderos et al. 2002), but it has been claimed that there is no stellar population older than ~ 500 Myr (Hunt et al. 2003; Izotov & Thuan 2004a). The question is still in dispute (Annibali et al. 2013; Papaderos & Östlin 2012). The irregular nature and complex kinematics of the H I regions surrounding 1Zw18 (van Zee et al. 1998c) and to a lesser extent, SBS 0335-052W (Ekta et al. 2009), suggests that they are still in the process of forming. They may be the modern analogs of the so-called “Faint Blue Galaxies” at redshifts $1 < z < 2$ (Babul & Ferguson 1996; Ellis 1997). This has also been suggested by Papaderos & Östlin (2012). The “bloated” objects noted in the SIGRID sample (Nicholls et al. 2011) may be similar objects. We have already observed some of these, and we plan to present data on their metallicities in a subsequent paper.

5.10. Conclusions

In this paper we present the first spectroscopic and nebular metallicity analysis of the two isolated dwarf gas-rich irregular galaxies, [KK98]246 and MCG-01-41-006. These objects

were observed at resolutions of 3000 and 7000, with very good signal-to-noise ratios, using the WiFeS IFU spectrograph on the ANU 2.3 m telescope at Siding Spring. To measure the metallicities, we have used the T_e direct method (for the MCG galaxy) and the latest strong line methods from [Dopita et al. \(2013\)](#). We find that despite their location within or at the edge of the Local Void, their metallicities are no lower than other similar less isolated dwarf galaxies, with values of 8.17 ± 0.01 and 8.04 ± 0.05 , respectively (and 7.96 ± 0.06 for J1609-04 (2) and (5) using the T_e method). We suggest that isolated dwarf galaxies like these, with available inflows of H I gas, will evolve normally, without the need for interactions with other galaxies. As a result, we believe that dwarf galaxies with exceptionally low metallicities are not the norm in voids, and that isolated dwarf irregular galaxies do not necessarily provide insights into the primordial IGM

CHAPTER 6

Metal-poor dwarf galaxies in the SIGRID galaxy sample. I. H II region observations and chemical abundances

All you really need to know for the moment is that the universe is a lot more complicated than you might think, even if you start from a position of thinking it's pretty damn complicated in the first place.

Douglas Adams, *Hitchhiker's Guide to the Galaxy*

This chapter was previously published as 'Metal-poor dwarf galaxies in the SIGRID galaxy sample. I. H II region observations and chemical abundances', Nicholls, D. C., Jerjen, H., Dopita, M. A., and Basurrah, H., ApJ, 780, 88. The work presented here is entirely my own, taking into account suggestions from my co-authors. Minor typographical errors have been corrected, and sections, tables and figures have been renumbered to conform with the layout of the thesis.

6.1. Chapter summary

In this chapter I present the results of observations of seventeen H II regions in thirteen galaxies from the SIGRID sample of isolated gas rich irregular dwarf galaxies. The spectra of all but one of the galaxies exhibit the auroral [O III] 4363Å line, from which I calculate the electron temperature, T_e , and gas-phase oxygen abundance. Five of the objects are blue compact dwarf galaxies, of which four have not previously been analysed spectroscopically. I include one unusual galaxy which exhibits no evidence of the [N II] $\lambda\lambda$ 6548,6584Å lines, suggesting a particularly low metallicity ($< Z_{\odot}/30$). I compare the electron temperature based abundances with those derived using eight of the new strong line diagnostics presented by Dopita et al. (2013). Using a method derived from first principles for calculating total oxygen abundance, I show that the discrepancy between the T_e -based and strong line gas-phase abundances have now been reduced to within ~ 0.07 dex. The chemical abundances are consistent with what is expected from the luminosity–metallicity relation. I derive

estimates of the electron densities and find them to be between ~ 5 and $\sim 100 \text{ cm}^{-3}$. I find no evidence for a nitrogen plateau for objects in this sample with metallicities $0.5 > Z_{\odot} > 0.15$.

6.2. Introduction

The metallicity of H II regions in small isolated dwarf galaxies is key to investigating the physical processes that govern star formation in undisturbed stellar systems.¹ The Small Isolated Gas Rich Irregular Dwarf galaxy (SIGRID) sample of small isolated gas rich irregular dwarf galaxies (Nicholls et al. 2011) was selected with the aim of exploring the behaviour of the mass– or luminosity–metallicity relation at the low end of the mass scale. This is based on the observation that nebular metallicity decreases with galaxy stellar mass/luminosity (see, for example, Tremonti et al. 2004; Lee et al. 2006). However, the low end of the mass scale shows significantly more scatter in metallicity than the high end in the Tremonti SDSS data. By selecting isolated dwarf galaxies, it was our intention to see if this scatter persisted, and whether it was an intrinsic property of small galaxies. The SIGRID study is complementary to the “Choirs” study which looks for tidal dwarf emission line galaxies in group environments (Sweet et al. 2014). It is distinct from the Spitzer Local Volume Legacy survey used by Berg et al. (2012) and the SDSS data of Tremonti et al. (2004) in using targets specifically chosen for their isolation. It is most similar in concept to the study by Pustilnik et al. (2011b) of galaxies in the Lynx-Cancer void, but is limited to small very isolated dwarf objects.

Other questions that the SIGRID observations are intended to address are the existence or otherwise of a primary nitrogen “plateau” at metallicities below $Z=8.45$ (van Zee et al. 1998a), and the relationship between oxygen abundances determined using “direct method”, based on the measurement of the electron temperature and the estimation of the ionisation correction factors to account for unseen ionisation stages, and “strong line” technique, based on a calibration of the bright emission lines and emission line ratios.

There has not been good agreement to date between the two methods, attributed to the empirical nature of the strong line methods. They have been calibrated in terms of the direct method, and have not until recently had an analytical basis. The direct method has been used as a standard for temperature and metallicity measurement, against which the strong line methods have been calibrated. Dopita et al. (2013) subsequently presented a set of strong line diagnostic grids derived from the Mappings photoionisation modelling code, based on the latest atomic data (see Nicholls et al. 2013). We use both the new atomic data and the new diagnostic grids in our analysis.

One might expect there to be greater scatter in the mass–metallicity relation at low masses, due to (1) measurement noise in nebular spectra in fainter galaxies, and (2) different star formation histories in the galaxies. Lee et al. (2006) suggest that the apparent scatter diminishes in observations at longer wavelengths ($4.5 \mu\text{m}$), and we present additional optical spectral evidence on this question.

¹In this paper we attempt to be explicit in our terminology, using the term “oxygen abundance”, and referring to “metallicity” only in widely used terms such as “mass–metallicity” and to refer to total chemical abundances. In addition, the abundance of oxygen measured from spectra is the gas-phase abundance, and does not take into account the oxygen in dust grains.

The behaviour of the ratio of nitrogen to oxygen abundances at low metallicities also shows increased scatter at lower metallicity. The current consensus appears to be that there is a low metallicity plateau in $\log(\text{N}/\text{O})$, indicating the existence of primary nitrogen (see, for example, [Vila Costas & Edmunds 1993](#); [van Zee et al. 1998a](#); [Contini et al. 2002](#); [van Zee & Haynes 2006](#); [Pilyugin et al. 2010](#); [Pérez-Montero & Contini 2009](#); [Berg et al. 2012](#); [Andrews & Martini 2013](#)). However, these previous works were not confined to small isolated dwarf galaxies. Results in our earlier paper on two isolated Local Void dwarf galaxies ([Nicholls et al. 2014c](#)), indicated that $\log(\text{N}/\text{O})$ did not plateau at low metallicity, suggesting no evidence for primary nitrogen. In this paper we present additional evidence for this.

The paper is structured as follows: in Section 6.3 we detail the sample selection, the spectroscopic observations, and the data reduction details. $\text{H}\alpha$ images of each observed target, spectra, and de-reddened nebular emission line fluxes are presented in Section 6.4. In Section 6.5 we present the principal results of the analyses: electron temperatures, gas-phase nebular metallicities with the diagnostic grids, the nitrogen to oxygen flux ratios, the $[\text{S II}]$ line ratios and electron densities, and the luminosity–metallicity results. In Section 6.6 we discuss these results, including the anomalies, and in Section 6.7 we present our conclusions. A discussion of methods used to estimate errors in the emission line fluxes is given in the Appendix.

6.3. Observations

6.3.1. Sample selection

The SIGRID sample was selected to identify small isolated gas-rich irregular dwarf galaxies using the criteria described in [Nicholls et al. \(2011\)](#). All objects are members of the Survey for ionisation in Neutral Gas Galaxies (SINGG) catalog ([Meurer et al. 2006](#)), selected from their H I signatures in the H I Parkes All-Sky Survey (HIPASS) ([Meyer et al. 2004](#)) and the presence of $\text{H}\alpha$ emission from star forming regions. From this sample we have, to date, observed 34 objects using Integral Field Unit (IFU) optical spectroscopy, as detailed below. From these observations we report here on 12 galaxies where the $[\text{O III}]$ auroral line is evident, allowing us to calculate the electron temperature T_e , and the gas-phase oxygen abundance; and an additional galaxy, J1118-17, with an unusual spectrum with no observed $[\text{N II}]$ lines. In four objects, two separate H II regions were observed which exhibited the auroral line, resulting in 18 separate H II region observations. Three objects (J1152-02, J1225-06, J1328+02) are not members of the final SIGRID sample, but had been observed during the refining of that sample. They were later excluded due to possible influence by regional galaxy groups and clusters, although they are clearly isolated objects, as evidenced by their isolation Δ index values ([Nicholls et al. 2011](#)). Five objects qualify as Blue Compact Dwarf (BCD) galaxies, using the definition by [Sung et al. \(2002\)](#) and discussed by [Nicholls et al. \(2011\)](#), though they have not previously been identified as such.

6.3.2. Spectroscopic observations

The targets were observed using the WiFeS IFU spectrograph ([Dopita et al. 2007, 2010](#)) on the Australian National University 2.3 m telescope at Siding Spring. The WiFeS instrument

is a double-beam image-slicing IFS, designed specifically to maximise throughput. It covers the spectral range 3500–9000 Å, at resolutions of 3000 (full spectral range) and 7000 (long wavelength limit 7000 Å). It has a science field of view (FOV) of 25×38 arc sec. As most of the SIGRID objects subtend angles less than its FOV, WiFeS is an ideal instrument to measure nebular metallicities in the ionised hydrogen star-forming regions. The instrument generates a data cube that allows exploration of nebular and continuum spectra in different regions of the target objects. Typically, even in poor seeing WiFeS resolves SIGRID object star formation regions easily, making possible exploration of excitation and abundances in different regions of each object. In these observations, resolutions used were $R=3000$ for the blue camera and $R=7000$ for the red, spanning a usable wavelength range of ~ 3600 to 7000 Å. Short period (150 second on object, 75 second on sky) nod-and-shuffle observations were used for all objects, to allow near-complete removal of the sky lines. The exposure times recorded in column 5 of Table 6.1 are the on-object integration times.

Details of the observations are given in Table 6.1. The sample is described in detail in [Nicholls et al. \(2011\)](#): essentially, the objects lie between redshifts of 300 and 1650 km s⁻¹, have neutral hydrogen masses less than and R-band magnitudes fainter than the Small Magellanic Cloud, low rotation velocities, show evidence of current active star formation, and are isolated, away from galaxy clusters and the tidal effects of other galaxies. All objects exhibit low (gas-phase) oxygen abundance ($\log(O/H) \lesssim Z_{0.3\odot}$), as we describe below. The seeing listed in Column 7 shows that in all but one case, (J1403-27), the seeing was average for Siding Spring. Even in that case, the seeing was better than the spaxel sample size, resulting in little if any flux loss.

Several classes of object were identified in [Nicholls et al. \(2011\)](#), including “bloaters”, which are objects considerably more spatially extended than their masses would suggest. One of these is J1118-17. It is very faint, but as we show below, appears to have a very low metallicity. In the light of the results obtained for the relatively faint object, J1118-17 (s1 and s2 targets), it would have been desirable to undertake significantly longer integration times, but observing conditions (weather and moonlight) did not permit this. We intend to undertake further longer integration time observations for this unusual object. The spectrum of J1118-17s1 is very noisy with few usable spectral lines, so we have analysed only s2—the two objects appear similar apart from luminosity. We reported results for J1609-04, a very isolated galaxy at the edge of the Local Void, in a previous paper ([Nicholls et al. 2014c](#)), and the results are included again here for completeness.

6.3.3. Data reduction

The data were reduced using the revised WiFeS Python “Pywifes” pipeline ([Childress et al. 2014](#)). This involves steps generally similar to those described in [Dopita et al. \(2010\)](#) for the older pipeline: bias modelling and subtraction, flat fielding, arc line identification and wavelength calibration, cosmic ray removal, sky-line subtraction using nod-and-shuffle, initial data cube construction and atmospheric dispersion correction, standard flux star calibration, telluric correction, assembly into the final data cubes and, where necessary, combination of multiple cubes into a final object data cube. The standard stars used were taken from [Bessell \(1999\)](#). Spectral sampling was undertaken using a 6 arc sec diameter circular spatial area centred on each H II region, through the full wavelength range of the

Table 6.1 Observations of objects from SIGRID sample

Object (HIPASS ID)	Alternate ID (NED)	RA (J2000)	Decl. (J2000)	Observed (date)	Exp. (min.)	seeing (arc sec)	aur. (#)	D (Mpc)	$\log(m_{HI})$ (m_{H_0})	M_R (mag.)	Delta index	Comments
J0005-28	ESO149-G013	00 05 31.8	-28 05 53	27-Aug-11	60	1.5	1	10.2	8.23	-15.3	-2.1	BCD
J1118-17(s2)	n/a	11 18 03.1	-17 38 31	13-Mar-11	80	1.5	0	13.5	8.56	-13.5	-2.2	v. low N II
J1152-02A,B	UGC 06850	11 52 37.2	-02 28 10	07-Mar-11	60	2.2	2	13.5	8.31	-16.7	-1.7	BCD
J1225-06s2	LEDA 1031551	12 25 40.0	-06 33 07	11-May-10	60	2.8	1	20.2	8.48	-14.2	-1.5	
J1328+02	LEDA 135827	13 28 12.1	+02 16 46	13-May-10	40	1.8	1	15.5	7.93	-15.2	-0.7	
J1403-27	ESO510-IG052	14 03 34.6	-27 16 47	11-May-10	60	3-5	1	17.5	8.72	-16.6	-1.8	BCD
J1609-04[2][5]	MCG-01-41-006	16 09 36.8	-04 37 13	25-Aug-11	60	2-2.4	2	14.8	8.30	-16.1	-2.9	
J2039-63A,B	LEDA 329372	20 38 57.2	-63 46 16	16-Sep-09	60	1.3	2	22.8	8.31	-16.5	-1.4	BCD
J2234-04B	MCG-01-57-015	22 34 54.7	-04 42 04	26-Aug-11	60	1.3	1	20.5	8.50	-16.2	-0.2	
J2242-06	LEDA 102806	22 42 23.5	-06 50 10	09-Jul-10	60	1.8-2	1	14.1	7.95	-15.6	-0.7	
J2254-26	MCG-05-54-004	22 54 45.2	-26 53 25	16-Sep-09	60	1.3	1	12.1	8.46	-16.1	-2.1	BCD
J2311-42A,B	ESO291-G003	23 11 10.9	-42 50 51	27-Aug-11	60	1.8-2	2	19.1	8.19	-16.5	-1.3	
J2349-22	ESO348-G009	23 49 23.5	-22 32 56	06-Oct-10	80	1.8-2	1	7.7	7.99	-14.7	-0.5	

¹ Object data from [Nicholls et al. \(2011\)](#)

² Columns 1 and 2: object ID; Columns 3 and 4: coordinates; Column 5: observation date; Column 6: exposure time on object; Column 7: regions with [O III] auroral line; Column 8: distance (Mpc); Column 9: neutral hydrogen mass; Column 10: R-band-magnitude; Column 11: isolation index; Column 12: comments

data cube, to obtain spectra for each region. Line fluxes were measured from these spectra using IRAF/splot. Particular care was taken to account for any stellar absorption features underlying the Balmer emission lines, although in all cases, this was minor or absent, due to low stellar continuum. In fact, the stellar continuum was extremely faint, with the exception of the object J0005-28 (see Figure 6.8, displayed on a log-intensity scale). Unlike single slit spectra, with IFU data cubes, we are able to select the entire area of the H II region from which to extract the spectrum, and exclude the majority of the galaxy stellar background, resulting in better signal-to-noise. Test sample sizes showed that all the detectable H α and [O III] in each H II region lay within the sample aperture, except where there are closely adjacent H II regions (e.g., J1609-04), where limiting the sample size to 6 arc sec diameter avoids sampling a different region. Ideally, single spaxel-based analysis would be preferable to multi-spaxel sampling, but these objects are so faint that the resultant noise is prohibitive. Flux de-reddening was performed on the raw flux data using two methods. First, for consistency with other work, we used the dust reddening formulae from Cardelli et al. (1989) with $A_V=3.1$, using the resultant Balmer line flux ratios as a check. To confirm these results, we used the dust models from Fischera & Dopita (2005), using a relative extinction curve with $R_V^A = 4.3$, where $R_V^A = A_V/(E_{B-V})$ and A_V is the V-band extinction. This is discussed in more detail in Vogt et al. (2013, Appendix 1). We used an initial Balmer decrement ratio of 2.82 for H α /H β , corresponding to an electron temperature of 12 500K, adjusted the electron temperature using the direct method derived from the [O III] line ratios, then adjusted the apparent Balmer ratios by varying the value of A_V for the best fit to the H γ /H β ratio, using the ratio H δ /H β as a check, fitting to the Storey & Hummer (1995) Case B Balmer ratios. The de-reddened flux values reported in Table 6.2 are those using the Cardelli method. In all cases, the two approaches gave similar results (to within $\sim 3\%$ in the de-reddened Balmer line ratios). In only one case, J2234-04, object A, did the de-reddening fail to provide a plausible result, and this has been excluded from the results reported here. It appears likely that two or more incompletely removed cosmic ray artefacts were the cause of the problem.

6.4. Results

6.4.1. H α images

Images of the objects listed in Table 6.1 are shown in Figure 6.1. These are 38×25 arc sec H α slices from the WiFeS data cubes. Spectra were extracted from these cubes using 6 arc sec diameter samples, centred on each (bright) H II region. Note that the seeing during the observations of object 7, J1403-27, was poor—3 to 5 arc sec—so the dimensions of the image do not indicate the true size of the H II region. The image scaling does not reflect the true brightness, but has been adjusted to illustrate the extent of the fainter parts of the H II regions. The sample size is larger than the worst seeing so avoids any sample size flux losses. In all but the one case the sample size is much larger than the object (see Table 6.1).

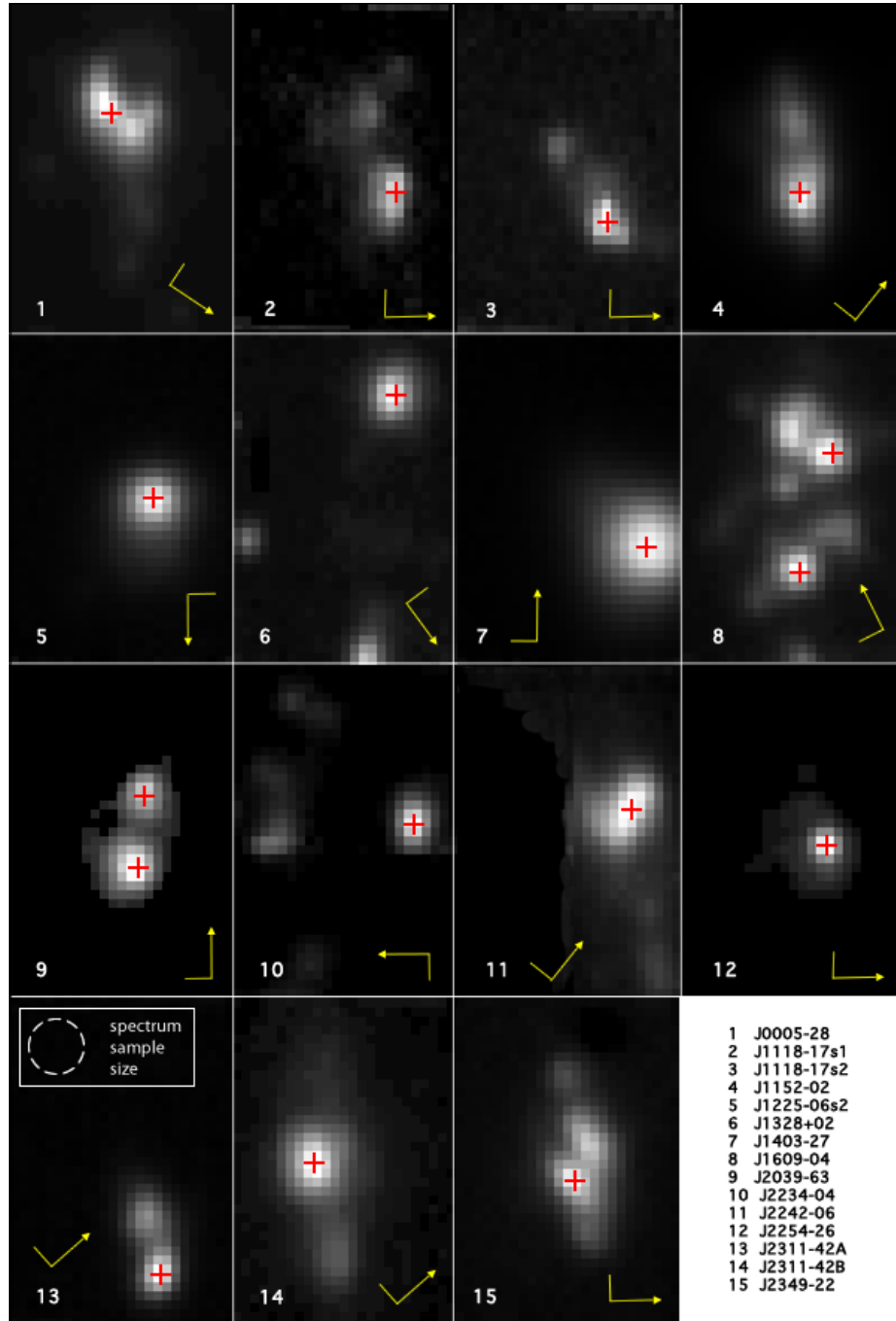


Figure 6.1 $H\alpha$ slices from WiFeS 35×28 arc sec image cubes. The size of the areas sampled to extract spectra is shown in panel 13. North is indicated by the long arrow and East by the bar ($\pm 15^\circ$). The red crosses mark the centre of the sampled areas. Note that the images have been stretched to show the fainter areas.

6.4.2. Spectra

Spectra extracted from the WiFeS data cubes are shown in Figures 6.2–6.7. The current data reduction pipeline creates a “sag” artefact for wavelengths shorter than $\sim 4000 \text{ \AA}$, in the absence of a strong stellar continuum². Stellar continua are weak or non-existent in most objects except for J0005-28, J2242-06, and J2349-42. Defective CCD chip amplification at the time of the observations caused two high noise regions in the spectrum of J2242-06, which have been replaced in Figure 6.3 with straight lines. Incipient noise from these two chip amplifiers is apparent in other spectra, but does not impact on any of the important diagnostic emission lines. De-reddened fluxes, equivalent widths, and logarithmic extinction coefficients ($c(\text{H}\beta)$) for the observed optical nebular lines are shown in Table 6.2. As noted in the appendix, the extinction coefficients were calculated using the Cardelli reddening law with $A_V = 3.1$. Similar results ($\pm 3\%$) were obtained using methods derived from Fischera & Dopita (2005). The equivalent widths are large for some objects, indicating the very low continua, because the host galaxies are very small and faint, and the spectra were measured from an area sampling only the immediate area of the H II region.

Figure 6.5 is a close up of the spectra in Figures 6.2 to 6.4, from 4200 \AA to 4500 \AA , illustrating the $\text{H}\gamma$ and auroral $[\text{O III}] 4363 \text{ \AA}$ lines. The signal to noise is mainly very good, but for three of the 14 objects in Figures 6.2 to 6.4, the detections are real but noisy (see Table 6.2).

6.4.3. Notes on particular objects

The spectrum from J1118-17s2 is shown in Figure 6.6. An enlarged section of the spectrum of J1118-17s2 near $\text{H}\alpha$ is shown in Figure 6.7, illustrating the apparent absence (to within the noise) of $[\text{N II}]$, although both $[\text{S II}]$ lines are apparent. This lack of any evidence for nitrogen suggests a particularly low metallicity, which we have estimated below using strong line diagnostic measurements. This object (and the associated J1118-17s1) warrants further observation to reduce the noise and establish the $[\text{N II}]$ flux. We have not presented the spectrum of J1118-17s1 as the signal-to-noise ratio was very poor and did not permit reliable measurement of any fluxes other than $\text{H}\alpha$, $\text{H}\beta$ and $[\text{O III}] 5007 \text{ \AA}$.

Figure 6.8 shows the emission line rich spectrum of the bright BCD J0005-28 with flux on a logarithmic scale. Twelve Balmer lines can be seen, allowing particularly accurate de-reddening to be calculated. The de-reddening process based on the $\text{H}\alpha$ to $\text{H}\beta$ ratio gave ratios to within 0.3% for $\text{H}\delta$ and 12% for $\text{H}\epsilon$ of the expected values for Case B.

²This is discussed in detail in Childress et al. (2014). It is an artefact of the data reduction pipeline that occurs for objects with very little stellar continuum, observed with the older WiFeS CCD detectors, whereby the spectrum “droops” at either end of the passband. It does not affect the flux measurements for individual emission lines. It is most evident in Figure 6.3, middle left panel.

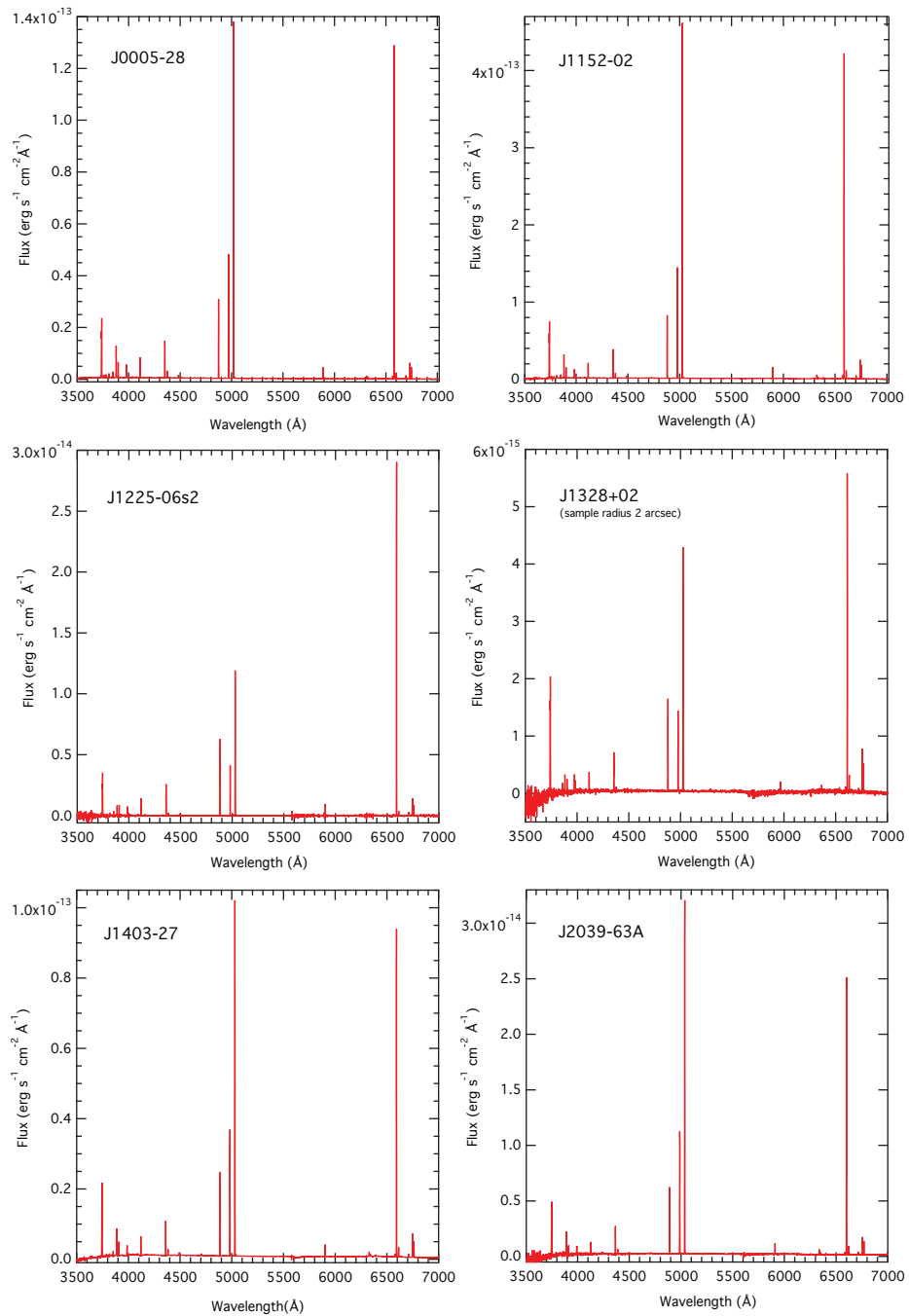


Figure 6.2 Spectra for J0005-28, J1152-02, J1225-06s2, J1328+02, J1403-27, and J2039-63A

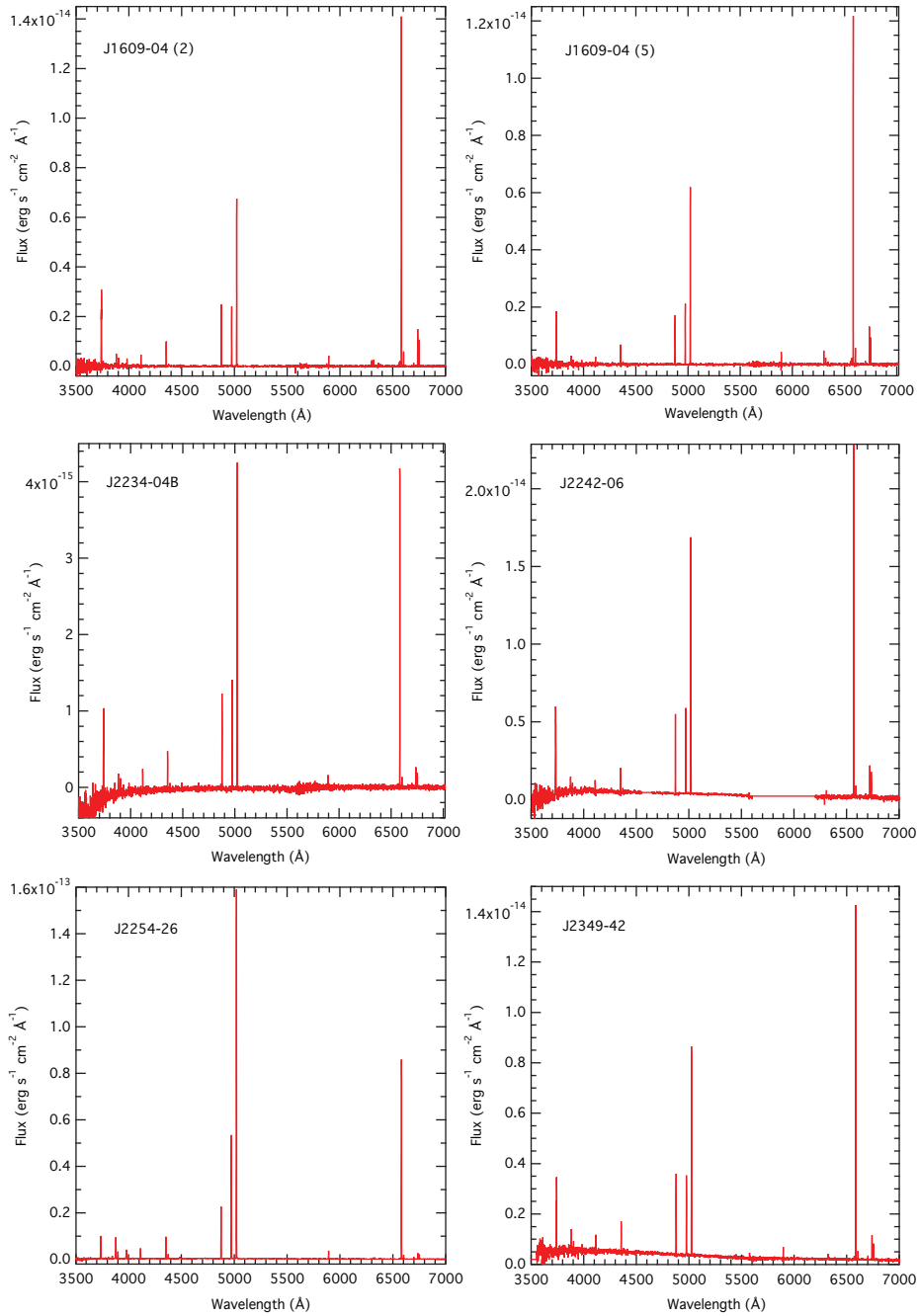


Figure 6.3 Spectra for J1609-04(2), J1609-04(5), J2234-04B, J2242-06, J2254-26, and J2349-42

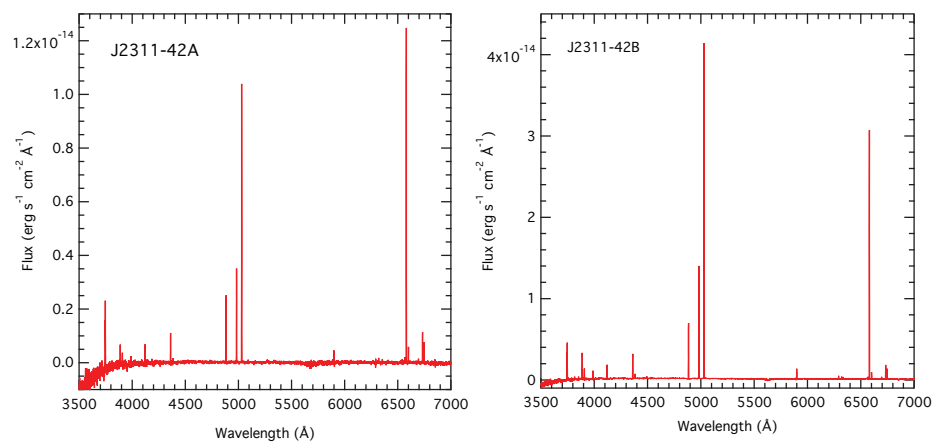


Figure 6.4 Spectra for J2311-42A and J2311-42B

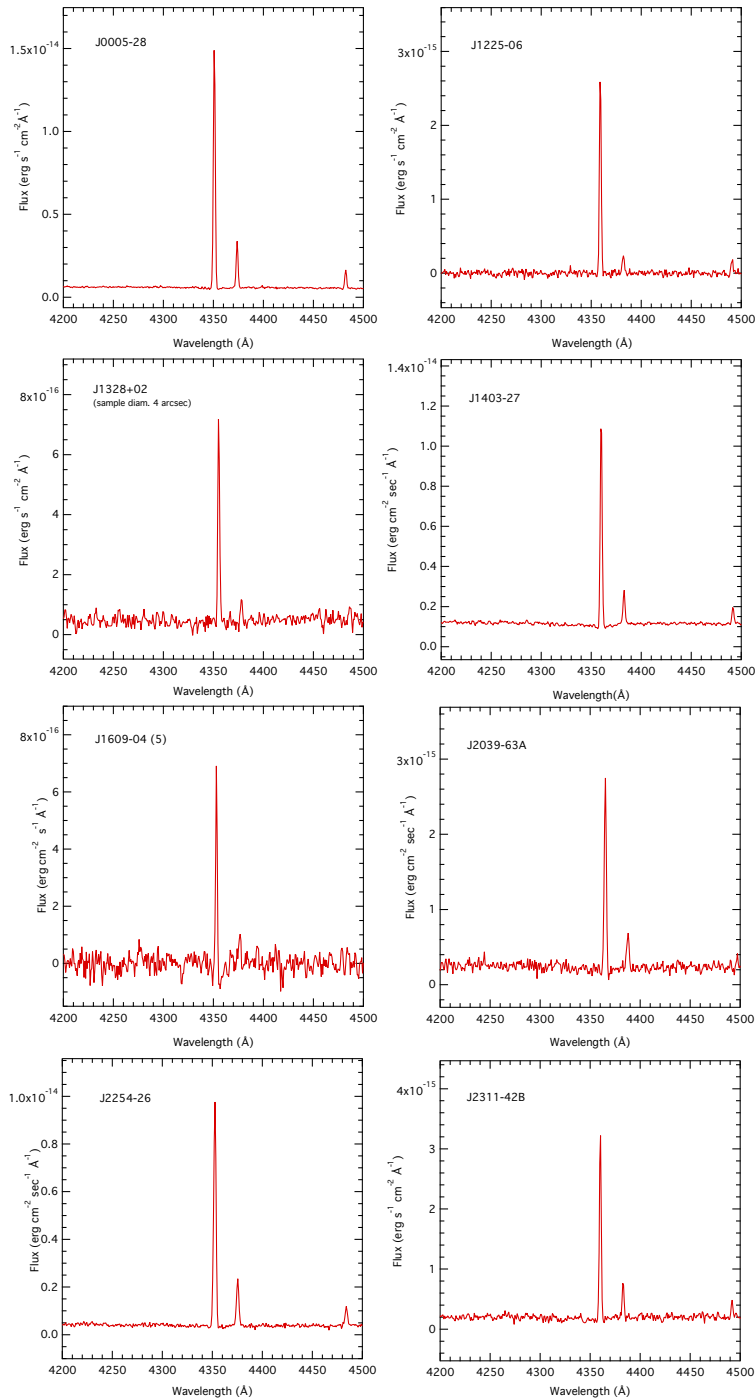


Figure 6.5 Close up of the H γ and [O III] 4363 Å lines for eight of the objects

Table 6.2 Reddening corrected line fluxes normalised to $H\beta=100$, with measured $H\beta$ ($\text{erg s}^{-1} \text{cm}^{-2} \text{\AA}^{-1}$), equivalent widths for $H\alpha$ and $H\beta$, and extinction coefficient, $c(H\beta)$.

Ion	$I(\lambda)/I(H\beta) \times 100$					
	J0005-28	J1118-17s2	J1152-02A	J1152-02B	J1225-06s2	J1328+02
[O II] 3726	90.39 ± 2.26	56.17 ± 30.70	119.11 ± 4.92	139.31 ± 7.76	77.69 ± 3.47	183.97 ± 7.76
[O II] 3729	117.91 ± 2.81	188.64 ± 33.35	171.01 ± 5.95	200.03 ± 8.98	108.84 ± 4.10	240.15 ± 8.88
[Ne III] 3869	39.98 ± 4.53	—	49.23 ± 1.48	46.29 ± 2.13	16.37 ± 1.89	20.30 ± 3.20
H δ 4102	26.35 ± 1.01	28.45 ± 18.13	25.91 ± 0.96	26.31 ± 1.04	26.26 ± 1.82	23.95 ± 2.40
H γ 4340	47.30 ± 1.58	35.79 ± 14.70	41.11 ± 1.40	42.75 ± 1.48	48.01 ± 1.95	46.40 ± 2.79
[O III] 4363	9.11 ± 0.42	—	6.82 ± 0.35	6.37 ± 0.39	4.83 ± 0.76	5.24 ± 1.14
H β 4861	100.00 ± 3.08	100.00 ± 9.85	100.00 ± 3.08	100.00 ± 3.14	100.00 ± 3.63	100.00 ± 3.89
[O III] 4959	150.49 ± 4.60	20.84 ± 6.76	172.31 ± 5.27	146.69 ± 4.57	62.66 ± 2.31	83.86 ± 3.65
[O III] 5007	451.97 ± 13.64	79.06 ± 8.78	517.38 ± 15.60	439.80 ± 13.33	190.32 ± 6.92	256.14 ± 8.82
[O I] 6300	2.69 ± 0.21	—	3.55 ± 0.18	3.73 ± 0.23	1.87 ± 1.12	—
[S III] 6312	1.62 ± 0.15	—	1.73 ± 0.12	1.76 ± 0.17	—	—
[N II] 6548	2.31 ± 0.18	—	2.25 ± 0.14	2.19 ± 0.16	—	3.36 ± 1.49
H α 6563	279.20 ± 8.48	282.90 ± 13.67	282.48 ± 8.94	281.77 ± 8.58	277.53 ± 9.10	279.03 ± 9.88
[N II] 6584	4.76 ± 0.24	1.48 ± 4.81	6.99 ± 0.33	6.54 ± 0.37	4.05 ± 0.81	14.65 ± 1.95
[S II] 6716	11.92 ± 0.44	11.72 ± 4.75	15.64 ± 0.78	17.38 ± 0.69	11.85 ± 1.10	33.53 ± 2.20
[S II] 6731	8.76 ± 0.34	6.98 ± 4.60	11.29 ± 0.52	12.38 ± 0.54	8.27 ± 0.82	21.78 ± 2.02
H β 4861	8.52E-14	1.16E-15	2.90E-13	1.34E-13	2.10E-14	3.56E-15
EW(H α)	685	717	1032	642	2482	234
EW(H β)	187	—	122	77.3	120	118
$c(H\beta)$	0.068	0.169	0.128	0.021	0.186	0.024
Ion	J1403-27	J1609-04(2)	J1609-04(5)	J2039-63A	J2039-63B	J2234-04B
[O II] 3726	122.74 ± 3.47	229.01 ± 10.95	209.89 ± 10.93	133.55 ± 6.62	75.86 ± 6.24	158.79 ± 11.01
[O II] 3729	165.52 ± 4.33	255.80 ± 11.48	230.35 ± 11.33	182.27 ± 7.59	103.61 ± 6.79	151.26 ± 10.86
[Ne III] 3869	38.81 ± 1.62	25.85 ± 4.58	30.13 ± 7.57	50.07 ± 4.25	38.62 ± 39.43	30.33 ± 59.65
H δ 4102	27.67 ± 1.24	27.20 ± 3.38	20.43 ± 3.85	25.63 ± 2.22	24.68 ± 2.84	26.40 ± 4.85
H γ 4340	48.07 ± 1.78	49.41 ± 3.15	48.30 ± 3.65	49.77 ± 2.58	48.82 ± 3.83	42.68 ± 4.19
[O III] 4363	7.66 ± 0.49	2.27 ± 1.03	6.10 ± 2.90	9.72 ± 1.07	8.39 ± 2.22	6.69 ± 2.52
H β 4861	100.00 ± 3.26	100.00 ± 4.42	100.00 ± 4.47	100.00 ± 3.63	100.00 ± 3.80	100.00 ± 5.35
[O III] 4959	142.26 ± 4.45	91.29 ± 3.85	110.15 ± 4.69	172.74 ± 5.67	156.84 ± 5.74	117.99 ± 5.75
[O III] 5007	420.32 ± 12.75	266.71 ± 9.23	322.78 ± 11.06	502.15 ± 15.50	462.63 ± 14.91	347.28 ± 12.84
[O I] 6300	3.66 ± 0.32	5.66 ± 1.05	6.65 ± 1.28	5.32 ± 0.64	2.79 ± 1.37	—
[S III] 6312	1.97 ± 0.25	—	—	1.83 ± 0.53	—	—
[N II] 6548	2.32 ± 0.31	6.18 ± 1.42	4.96 ± 1.23	2.76 ± 0.58	—	—
H α 6563	280.10 ± 8.75	285.58 ± 12.71	279.82 ± 9.38	279.63 ± 8.88	280.15 ± 9.35	256.49 ± 9.73
[N II] 6584	7.69 ± 0.48	11.92 ± 1.10	12.58 ± 1.62	8.65 ± 0.78	5.69 ± 1.37	7.20 ± 1.90
[S II] 6716	19.52 ± 0.89	29.77 ± 1.68	27.18 ± 1.88	19.11 ± 1.10	12.29 ± 1.25	15.52 ± 2.26
[S II] 6731	13.87 ± 0.72	20.96 ± 1.42	18.69 ± 1.62	14.22 ± 0.95	8.19 ± 1.54	11.17 ± 2.31
H β 4861	9.07E-14	1.57E-14	1.72E-14	2.52E-14	7.05E-15	2.39E-15
EW(H α)	286	215	157	301	459	—
EW(H β)	66.2	77.6	48.1	69.5	150	—
$c(H\beta)$	0.216	0.448	0.619	0.219	0.028	0
Ion	J2242-06	J2254-26	J2311-42A	J2311-42B	J2349-22	
[O II] 3726	135.40 ± 7.22	66.71 ± 2.24	137.44 ± 9.49	92.28 ± 4.03	113.10 ± 7.12	
[O II] 3729	184.51 ± 8.20	83.32 ± 2.57	206.55 ± 10.87	106.01 ± 4.30	155.67 ± 7.97	
[Ne III] 3869	29.29 ± 4.04	55.79 ± 2.14	36.57 ± 5.50	51.11 ± 2.98	34.21 ± 5.55	
H δ 4102	27.35 ± 2.80	25.74 ± 1.06	30.15 ± 3.99	27.72 ± 1.92	22.54 ± 4.01	
H γ 4340	44.60 ± 2.67	46.15 ± 1.63	51.15 ± 3.56	47.21 ± 2.26	44.22 ± 3.72	
[O III] 4363	5.12 ± 1.62	10.11 ± 0.55	5.61 ± 2.06	9.45 ± 1.05	4.87 ± 2.61	
H β 4861	100.00 ± 3.79	100.00 ± 3.14	100.00 ± 4.57	100.00 ± 3.76	100.00 ± 4.45	
[O III] 4959	99.12 ± 3.71	224.02 ± 6.80	133.40 ± 5.62	192.18 ± 6.29	95.81 ± 4.44	
[O III] 5007	296.46 ± 9.65	680.52 ± 20.52	397.17 ± 14.26	569.46 ± 17.61	272.65 ± 9.88	
[O I] 6300	3.47 ± 1.52	1.82 ± 0.18	2.37 ± 1.59	2.39 ± 0.54	3.31 ± 0.92	
[S III] 6312	—	1.89 ± 0.16	—	2.45 ± 0.66	1.18 ± 0.86	
[N II] 6548	—	1.74 ± 0.16	5.09 ± 1.93	1.90 ± 0.50	3.05 ± 0.99	
H α 6563	274.34 ± 9.40	281.58 ± 8.61	281.95 ± 10.43	280.83 ± 8.83	280.33 ± 11.13	
[N II] 6584	8.41 ± 0.61	15.32 ± 0.27	11.86 ± 1.74	6.42 ± 0.67	6.32 ± 1.00	
[S II] 6716	23.19 ± 2.10	9.01 ± 0.38	23.58 ± 1.91	14.28 ± 0.88	18.54 ± 1.41	
[S II] 6731	15.49 ± 1.87	6.84 ± 0.32	16.01 ± 1.71	9.80 ± 0.77	12.73 ± 1.23	
H β 4861	1.13E-14	7.17E-14	8.78E-15	2.10E-14	8.85E-15	
EW(H α)	211	811	1982	631	103	
EW(H β)	47.9	177	710	106	30	
$c(H\beta)$	0	0.071	0.180	0.127	0.115	

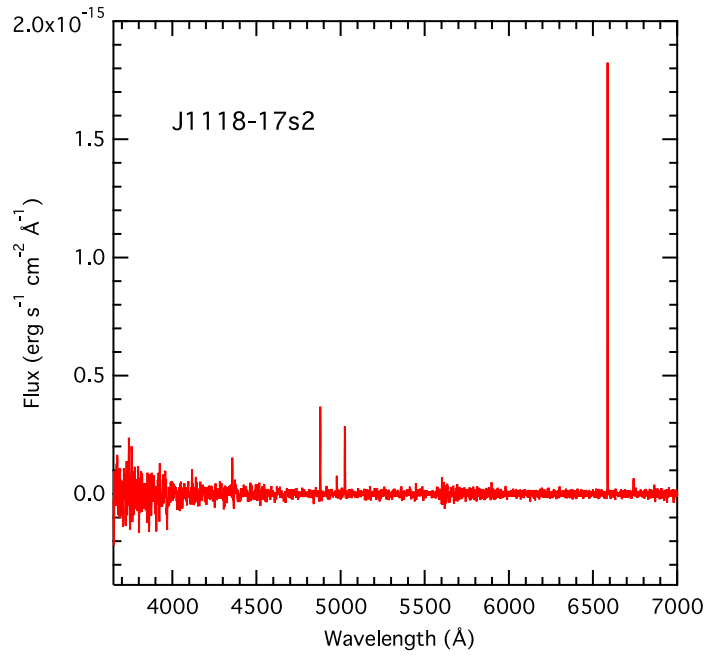


Figure 6.6 Spectrum for J1118-17s2 (pipeline "sag" removed).

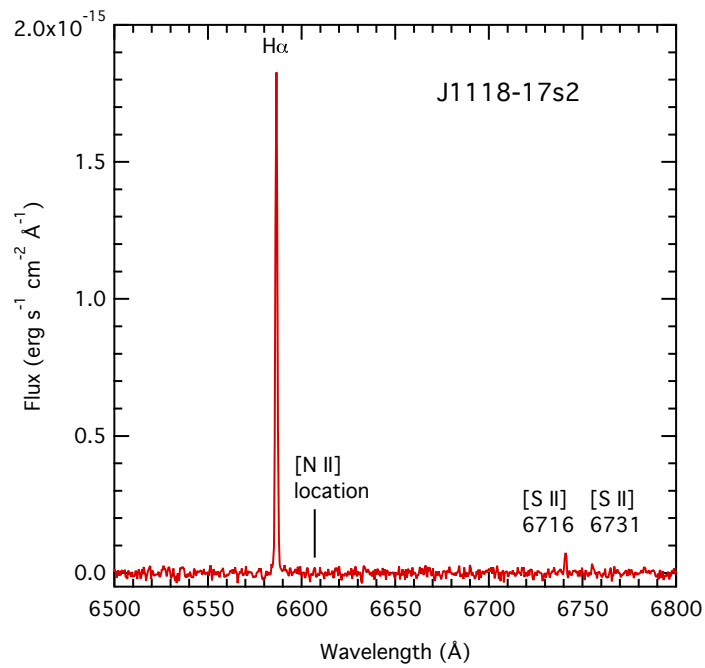


Figure 6.7 Section of spectrum for J1118-17s2, showing apparent absence of any [N II] emission lines.

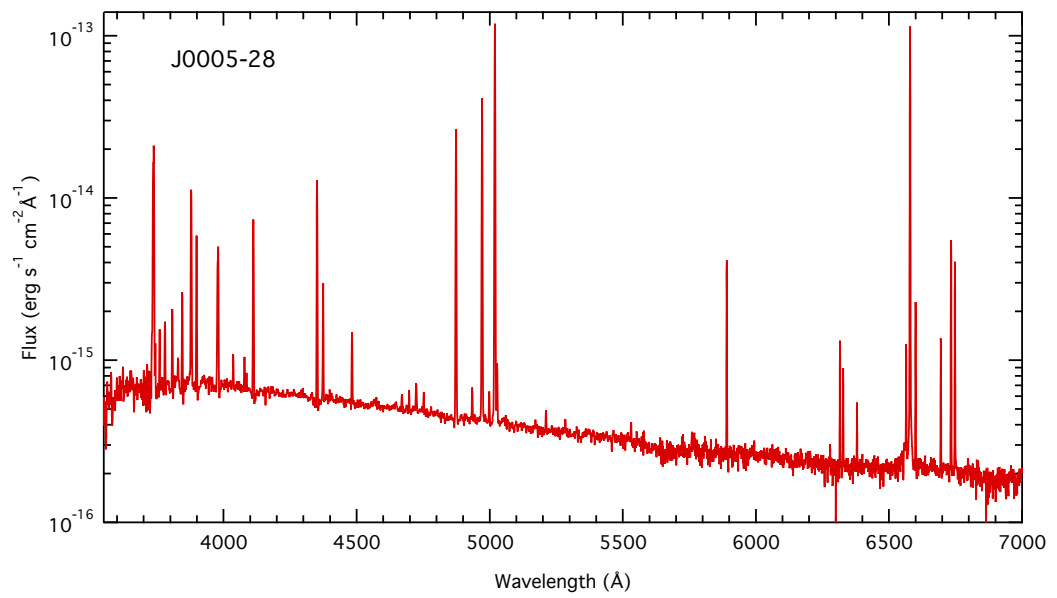


Figure 6.8 Spectrum of J0005-28, log flux axis. Several Balmer lines are apparent, and the [O III] 4363 Å line is strong.

6.5. Nebular metallicities

6.5.1. Electron temperatures and oxygen abundances

The electron temperature, T_e , can be derived from collisionally excited line fluxes, for a variety of ionic species, provided the auroral line is observed (in the case of O III, the 4363 Å line). The method most frequently used makes use of the ratio of fluxes of the bright [O III] lines to the auroral line. This is a well-established technique (see discussions in [Osterbrock & Ferland 2006](#); [Nicholls et al. 2013](#)), but it calculates only the O⁺⁺ abundance, not the total gas-phase abundance of oxygen. In most H II regions, the contributions to total oxygen from O and O⁺⁺⁺ are minor, so in addition to O⁺⁺, we only need to calculate the contribution from O⁺.

If the equivalent auroral lines for [O II], [N II] and [S III] are present in the spectra, the electron temperatures can be calculated using these lines too, and since they peak at different regions in the H II region, the auroral lines collectively sample the complete volume. When these auroral lines are not observed, empirical methods can be used to estimate the O⁺ abundance, for example in [Izotov et al. \(2006, Equations 3 and 4\)](#). However, as those authors note, the methods depend on having reliable atomic data (energy levels, transition probabilities, and collision strengths). Consequently we have approached the problem again from first principles, using the latest atomic data, to derive the total oxygen abundance³.

The rate of collisional excitation for O⁺⁺ from the ³P ground state(s) to the ¹D₂ level is given, for the thermal equilibrium case ([Nicholls et al. 2012](#)), by,

$$r_{12} = n_e n_{O^{++}} \left(\frac{h^2}{(2\pi m_e)^{3/2}} \right) \frac{1}{g_1 \sqrt{k_B T_e}} \Upsilon_{12}(T) \exp\left(-\frac{E_{12}}{k_B T_e}\right), \quad (6.1)$$

where h is the Planck constant, m_e is the electron mass, g_1 is the statistical weight of the ground state (= 9 for O⁺⁺), k_B is the Boltzmann constant, Υ_{12} is the net effective collision strength for collisional excitations from the ground ³P states to the ¹D₂ state and E_{12} is the energy level of the ¹D₂ state. Ignoring the small contribution to the population of the ¹D₂ level from radiative cascade from higher energy levels, the rate of emission of photons from that level is equal to the rate of excitation, i.e., $r_{12} = r_{21}$. The emissivity of [O III] from transitions from the ¹D₂ ($\lambda\lambda$ 5007, 4959 and 4931) level is proportional to $r_{21} \times E_{12}$. Here we have used the total effective collision strengths for the forbidden ¹D₂ to ³P transitions, so we use the flux-weighted photon energy, corresponding to a wavelength of 4997 Å, for E_{12} .

The emissivity of H β is proportional to $n_e \times n_{H^+} \times \alpha_B^{\text{eff}}(\text{H}\beta)$ ([Dopita & Sutherland 2003](#)), where n_e is the electron density, n_{H^+} is the ionised hydrogen density, and $\alpha_B^{\text{eff}}(\text{H}\beta)$ is the effective emissivity for H β , which takes into account photon energies and branching ratios, and for which values have been computed by [Storey & Hummer \(1995\)](#).

Given that the ratio of the flux of O III to that of H β is equal to the ratio of their emissivities multiplied by their photon energies, for a given geometry, one may reorganise the above equations to derive an expression for the ratio of the number density of O⁺⁺ ions to hydrogen

³In this work, we do not have data for the [O II] $\lambda\lambda$ 7320,30 lines, so the Izotov method provides a useful comparison.

ions (i.e., the O^{++} abundance) in terms of the flux ratio of [O III] (1D_2) to $H\beta$,

$$\frac{n_{O^{++}}}{n_{H^+}} = \frac{\text{flux}(O^{++})}{\text{flux}(H\beta)} \cdot g_1 \cdot \sqrt{T_e} \cdot \alpha_B^{\text{eff}}(H\beta) \cdot \exp(E_{12}/(kT_e)) \times 115885.4 / (E_{12} \cdot \Upsilon_{12}) \quad (6.2)$$

where T_e is the electron temperature derived from the [O III] line ratio, for which there is a simple expression from [Nicholls et al. \(2013\)](#),

$$T_e = a (-\log_{10}(\mathcal{R}) - b)^{-c}, \quad (6.3)$$

where, for [O III],

$$\mathcal{R} = \frac{j(\lambda 4363)}{j(\lambda 5007) + j(\lambda 4959)}, \quad (6.4)$$

and $a = 13229$, $b = 0.92350$, and $c = 0.98196$.

In an identical fashion, one may derive an expression for the abundance of O II using the observed fluxes from the [O II] 3726,3729 $\lambda\lambda$ lines,

$$\frac{n_{O^+}}{n_{H^+}} = \frac{\text{flux}(O^+)}{\text{flux}(H\beta)} \cdot g_{1(O^+)} \cdot \sqrt{T_e} \cdot \alpha_B^{\text{eff}}(H\beta) \cdot \exp(E_{12(O^+)}/(kT_e)) \times 115885.4 / (E_{12(O^+)} \cdot \Upsilon_{12(O^+)}), \quad (6.5)$$

where, in this case, T_e is the electron temperature derived from the [O II] ratio (see [Nicholls et al. 2013](#)) using the ratio of the 7320,30 $\lambda\lambda$ lines to the 3726,3729 $\lambda\lambda$ lines. If, as in the case of these observations, the NIR lines are not available, it is possible to derive an expression for the [O II] electron temperature from the Mappings photoionisation models as a polynomial in terms of *total* gas-phase oxygen abundance,

$$T_e([O II]) = T_e([O III]) \times (3.0794 - 0.086924 Z - 0.1053 Z^2 + 0.010225 Z^3) \quad (6.6)$$

where $Z = 12 + \log(O/H)$.

This does not provide the final answer, and it is necessary to iterate to a final value for the abundance of O^+ , starting by using the O^{++} abundance as the total oxygen abundance. The process converges in less than five iterations. [Garnett \(1992\)](#) and [López-Sánchez et al. \(2012\)](#) have used a simpler approach, expressing the low ionisation zone temperature (effectively the [O II] temperature) in terms of the [O III] temperature, which does not require iteration. [Garnett \(1992\)](#) used a linear relation, whereas [López-Sánchez et al. \(2012\)](#) used a more complex fit to photoionisation model data.

Equation 6.7 shows the expression used by [López-Sánchez et al. \(2012\)](#):

$$T_e(OII) = T_e(OIII) + 450 - 70 \times \exp\left[(T_e(OIII)/5000)^{1.22}\right] \quad (6.7)$$

Equation 6.7 gives total oxygen abundance values close to those from iterating Equation 6.6. Values determined for oxygen abundances are not exact, because of the nature of the approximations used, the calculated values for oxygen abundances depend on the photoionisation models used to build the models, and the use of a model derived from a single value of the ionisation parameter, q . Testing the two methods (Equations 6.6 and 6.7) against artificial data indicates that they generate total oxygen abundances within 1% of the input values. The iterative approach (Equation 7.5) is marginally the more consistent of the two over a range of ionisation parameter values.

The above equations may be simplified for computation by using accurate expansions in terms of the [O III] electron temperature to $\alpha_B^{\text{eff}}(\text{H}\beta)$, $\Upsilon(^1D_2)$, and $\Upsilon(^2D_{3/2,5/2}^0)$. The Case B emissivity data for H β as a function of temperature, from [Storey & Hummer \(1995\)](#) may be fit with a simple power law,

$$\alpha_B^{\text{eff}}(\text{H}\beta) = -1.7221\text{e-}26 + 1.4772\text{e-}22 \times T_e^{-0.75538} \quad (6.8)$$

The effective collision strengths for the $\text{O}^{++} \ ^1D_2$ level ([Palay et al. 2012](#)), from which the $\lambda\lambda 4959, 5007$ doublet originates, can be fit with a simple exponential function of temperature,

$$\Upsilon(^1D_2) = 3.0733 - 0.94563 \times \exp((5000 - T_e)/12105), \quad (6.9)$$

and the effective collision strengths for O^+ from [Tayal \(2007\)](#) for the composite upper state, $^2D_{3/2,5/2}^0$, from which the $\lambda\lambda 3726, 9$ doublet originates, can similarly be fit by a linear function of temperature,

$$\Upsilon(^2D_{3/2,5/2}^0) = 1.3394 + 1.3443\text{e-}06 \times T_e. \quad (6.10)$$

Applying these methods to the present observations, we obtain the electron temperatures and total gas-phase oxygen abundances shown in Table 6.4. The values for J1118-16s2 are not listed as the $\lambda 4363$ line was not observed. The uncertainties in T_e were calculated from the flux error values, in Equation 7.3, and propagated through to the abundance values. See the appendix for a discussion of the error estimation.

6.5.2. Strong-line diagnostic grids

There are two principal methods for determining oxygen abundances from H II region optical spectra, the direct or electron temperature (T_e) method and the strong line methods. The T_e method is possible if one of the auroral lines is observed at adequate signal-to-noise ($> 3\sigma$), usually [O III] 4363Å. This is the case in all but one of the galaxies discussed here and is detailed below. The so-called strong line methods use flux ratios of the prominent nebular lines to determine abundances (e.g., [Dopita et al. 2013](#); [Kewley & Dopita 2002](#); [Kewley & Ellison 2008](#)). Conventionally, the strong line methods were empirical, calibrated against results using the direct method. However, recently, [Dopita et al. \(2013\)](#) have extensively revised the strong line techniques, developing diagnostic grids based on the Mappings photoionisation modelling code, using the latest atomic data, and the possibility that the electrons exhibit a non-equilibrium κ energy distribution ([Nicholls et al. 2012, 2013](#)). The grids are new, and the ratios used have been selected to maximise the orthogonality of the parameters, avoiding to a large extent the degeneracy of older diagnostics, and to solve for both metallicity and ionisation parameter. These new diagnostics generate values for both the oxygen abundance and the ionisation parameter, q , and give substantially more consistent abundance values than the older methods. This can be seen by comparing the metallicity results for the different diagnostics from Table 6.3 and the older diagnostic results listed in Table 6.4. In Table 6.3, the diagnostics involving the ratio [N II]/[S II] and [N II]/[O II] are particularly consistent, differing by typically <0.03 dex.

The ionisation parameter q (sometimes expressed as $U = q/c$, where c is the speed of light) is the ratio of the number of ionising source photons passing through a unit volume to the

neutral hydrogen density. The photon flux matches the number of new ions it produces, and as q has the dimensions of velocity, it can be understood as the maximum speed at which the boundary of the ionised region can move outwards (Dopita & Sutherland 2003). q is at its maximum at the inner edge of the ionised region of an H II region, and falls to zero at the outer edge of the ionised nebula, where the ionising flux is fully depleted. A problem with older diagnostics such as R_{23} is that measured metallicities depend on the ionisation parameter. There have been previous attempts to solve for the ionisation parameter (McGaugh 1994; Kewley & Dopita 2002; Pilyugin & Thuan 2005) but these new diagnostics solve for its value independently of the metallicity, and consequently, take into account the ionisation gradients present in H II regions. The diagnostics chosen here are also relatively insensitive to non-equilibrium (κ) electron energy distributions, especially for values of $\kappa > 20$. In addition, κ distributions have a smaller effect on the excitation of lower metallicity H II regions than in higher metallicity objects. For this reason, and in the interests of clarity, we present here only the equilibrium (Maxwell-Boltzmann, or $\kappa = \infty$) results.

Figures 6.9 and 6.10 plot the log flux ratios for the observed objects on the diagnostic grids from Dopita et al. (2013). Not all of the objects can be accommodated within these grids. There are several possible reasons, and these will be discussed in detail in the second paper in this series. One likely cause relates to electron densities. The grids shown here are calculated for an electron density, $n_e \sim 5 \text{ cm}^{-3}$. For the majority of the observed objects, this is accurate, but for some the densities are somewhat higher. Below we analyse the ratios of the two [S II] lines (6716 and 6731 Å) which are a useful diagnostic of electron density (Osterbrock & Ferland 2006), and it is clear that some of the objects exhibit higher densities. Some of the “misfit” points can be accommodated on grids calculated for higher electron densities (see below and Figure 6.12).

6.5.3. Strong Line metallicities

Table 6.3 lists the oxygen abundances and ionisation parameters computed from the new diagnostic grids using the “pyqz” interpolation described in Dopita et al. (2013). While the interpolation scheme does not always work reliably for near-vertical grid lines, leading to null results, it is clear that different diagnostics yield somewhat different results. However, the consistency is far better than earlier methods permitted. We have found that for low metallicity objects ($< 0.5 Z_{\odot}$), diagnostics listed in Table 6.3 involving $\log(N_{\text{II}}/S_{\text{II}})$ give values for the metallicity that differ by typically less than 0.02 dex and diagnostic using the $\log(N_{\text{II}}/O_{\text{II}})$ ratios are similar. It is also evident from Table 6.3 that the direct methods are nearly all lower by ~ 0.13 dex than the best $\log(N_{\text{II}}/S_{\text{II}})$ strong line diagnostic values. This is in agreement with the findings of López-Sánchez et al. (2012) that the direct method abundances are generally lower than strong line estimates. However, with the newer atomic data, the recalculated direct method abundances, and the revised Mappings photoionisation code, these differences are smaller. For comparison we also present the results of older strong line diagnostics, in Table 6.4. Perhaps the most variable result is that for J1118-17s2. This is not surprising, as the [N II] flux is poorly defined. It appears likely that an oxygen abundance figure of ~ 7.2 ($\sim Z_{\odot}/30$) is a reasonable estimate.

It is worth noting that the Mappings photoionisation modelling grids used here take into

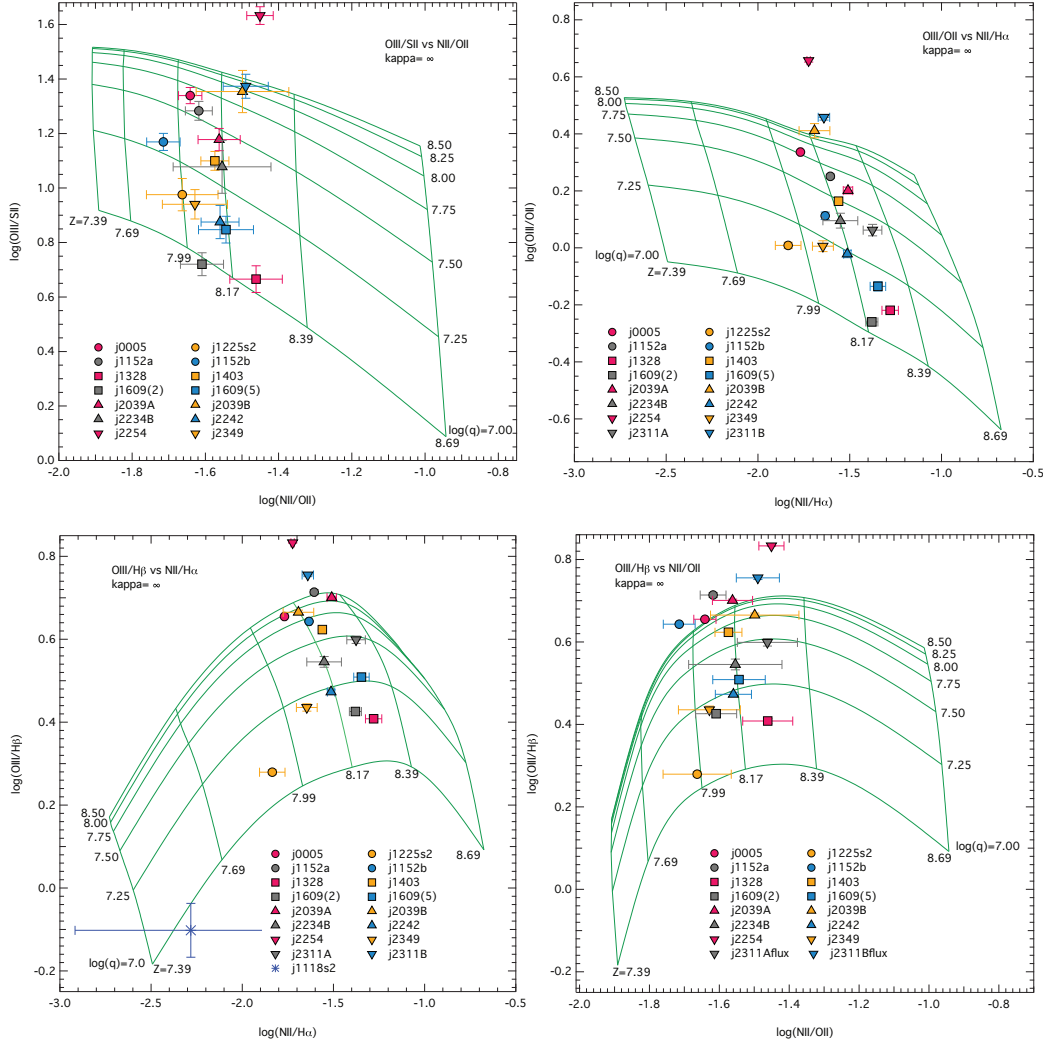


Figure 6.9 Observed flux ratios plotted on the OIII/SII–NII/OII, OIII/OII–NII/H α , OIII/H β –NII/H α and OIII/H β –NII/OII grids

account the total oxygen abundance, i.e., both the gas-phase oxygen and that incorporated in dust grains. When comparing the electron temperature and strong line abundances, it is necessary to increase the electron temperature oxygen abundance values by ~ 0.07 dex, to allow for the oxygen in dust grains that the direct method does not account for. This, of course, assumes a particular level of dust in the interstellar medium (ISM). In the Mappings strong line diagnostic grids, we assume a 1.0 solar dust depletion. Rémy-Ruyer et al. (2014) found that the gas-to-dust ratio varies considerably between objects, depending on their individual star formation histories, particularly at the low end of the galaxy mass scale. This is a further complication for any attempt to estimate the total oxygen abundance in an H II region. López-Sánchez (2010) has shown a correlation between the reddening coefficient $c(H\beta)$ and the gas-to-dust ratio in Wolf-Rayet galaxies, and it is likely that a similar relation holds for smaller dwarf galaxies. (We do not have the necessary FIR data to allow us to calculate the dust mass here). In the meantime, the direct method oxygen abundance measurements provide a lower limit to the total oxygen.

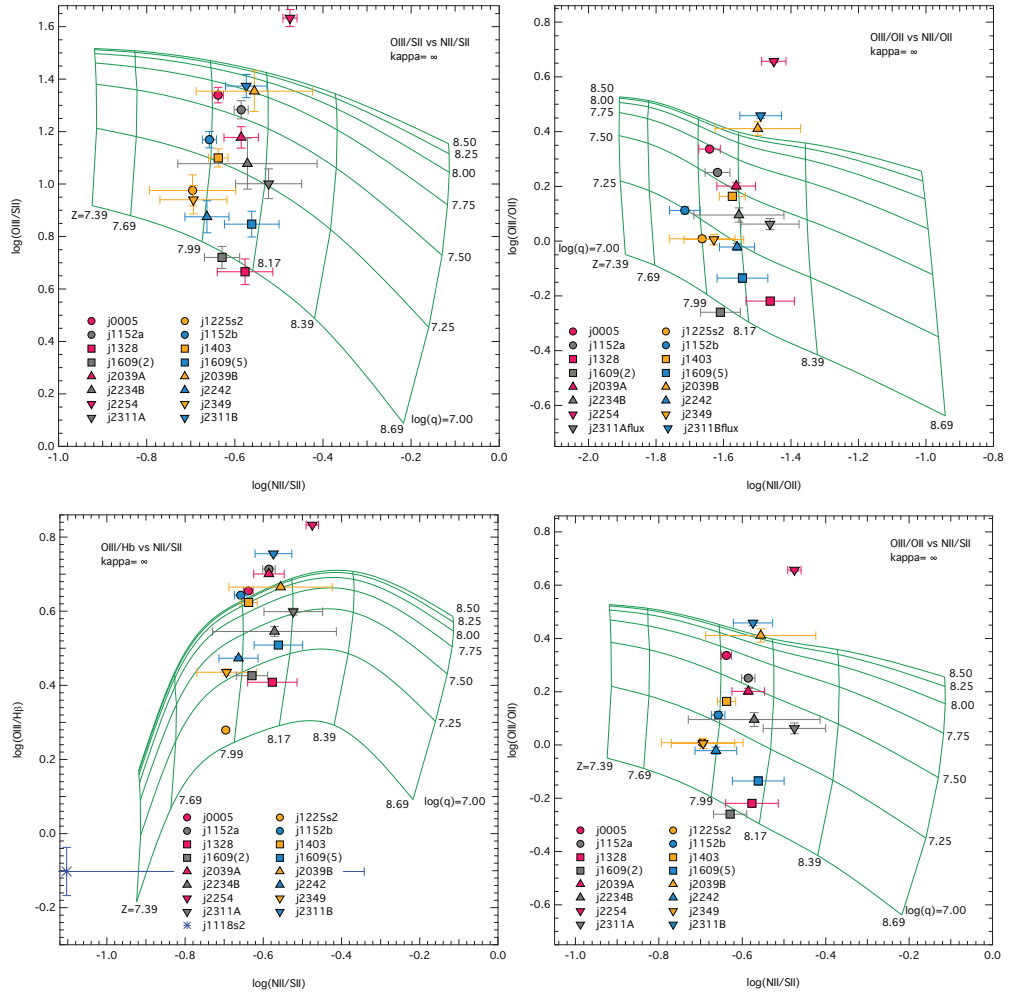


Figure 6.10 Observed flux ratios plotted on the OIII/SII–NII/SII, OIII/OII–NII/OII, OIII/Hb–NII/SII and OIII/OII–NII/SII grids

Table 6.3 Metallicity results from Strong Line grids for $\kappa = \infty$.

Diagnostic:	NII/SII vs OIII/SII	NII/SII vs OIII/Hb	NII/OII vs OIII/OII	NII/OII vs OIII/SII	NII/SII vs OIII/OII	NII/OII vs OIII/Hb	NII/Ha vs OIII/Hb	NII/Ha vs OIII/OII
J0005-28								
z	8.012	–	8.0428	8.0355	8.0114	–	8.1191	8.1011
log(<i>q</i>)	7.6328	–	7.7212	7.6596	7.6845	–	7.9568	7.7802
mean z	8.012±0.000							
mean log(<i>q</i>)	7.659±0.037							
J1118-17s2								
Z	–	–	–	–	–	–	7.5448	7.4741
log(<i>q</i>)	–	–	–	–	–	–	6.9500	6.7092
mean z	7.509±0.050							
mean log(<i>q</i>)	6.830±0.170							
J1152-02A								
z	8.0896	–	8.0762	8.0736	8.0868	–	–	8.198
log(<i>q</i>)	7.5707	–	7.5506	7.5611	7.558	–	–	7.6697
mean z	8.088±0.002							
mean log(<i>q</i>)	7.564±0.009							
J1152-02B								
z	7.9802	–	7.8965	7.9038	7.9819	–	8.1878	8.118
log(<i>q</i>)	7.3404	–	7.2459	7.3072	7.2869	–	7.7019	7.3713
mean z	7.981±0.001							
mean log(<i>q</i>)	7.376±0.166							
J1225-06s2								
z	7.9289	7.9321	7.9924	7.9891	7.9256	7.9736	7.9106	7.9261
log(<i>q</i>)	7.1382	7.0849	7.1958	7.157	7.1611	7.0573	7.0925	7.1651
mean z	7.929±0.003							
mean log(<i>q</i>)	7.128±0.039							
J1328+02								
z	8.1465	8.1159	8.2471	8.2413	8.1337	8.2524	8.3003	8.2909
log(<i>q</i>)	6.9894	7.1697	7.0976	7.0408	7.0481	7.1428	7.0164	7.123
mean z	8.132±0.015							
mean log(<i>q</i>)	7.069±0.092							
J1403-27								
z	8.0137	8.0161	8.1393	8.1363	8.0106	–	8.2286	8.1978
log(<i>q</i>)	7.2684	8.045	7.4556	7.343	7.3739	–	7.5551	7.4934
mean z	8.013±0.003							
mean log(<i>q</i>)	7.562±0.421							
J1609-04(2)								
z	8.0654	8.0303	8.0418	8.0447	8.0681	8.0722	8.243	8.1959
log(<i>q</i>)	6.992	7.2226	6.9825	6.9856	6.9843	7.2026	–	7.0429
mean z	8.055±0.021							
mean log(<i>q</i>)	7.066±0.135							

The diagnostic grids are described in detail in [Dopita et al. \(2013\)](#). The uncertainties quoted are based on the variance of the average values for the first five diagnostics listed here. “–” indicates the diagnostic does not return a value for abundance or ionization parameter.

6.5.4. log(N/O)

In this section we use the approach from our previous paper, [Nicholls et al. \(2014c\)](#). One of the more important parameters in understanding galactic evolution is the nitrogen abundance, and in particular, the ratio of nitrogen to oxygen. The observations reported here include relatively low noise measurements of both [N II] and [O II], allowing us to explore the values of log(N/O) for each H II region. To calculate the value of N/O from

Table 6.3 Metallicity results from Strong Line grids for $\kappa = \infty$ (continued)

Diagnostic:	NII/SII vs OIII/SII	NII/SII vs OIII/Hb	NII/OII vs OIII/OII	NII/OII vs OIII/SII	NII/SII vs OIII/OII	NII/OII vs OIII/Hb	NII/Ha vs OIII/Hb	NII/Ha vs OIII/OII
J1609-04(5)								
z	8.1435	8.1261	8.1628	8.1616	8.1424	8.1753	8.3091	8.2626
log(<i>q</i>)	7.1225	7.3364	7.1189	7.1261	7.129	7.3023	7.1813	7.182
mean z	8.137±0.010							
mean log(<i>q</i>)	7.196±0.122							
J2039-63A								
z	8.0889	–	8.1589	8.1578	8.0853	–	8.35	8.2661
log(<i>q</i>)	7.4083	–	7.5284	7.4515	7.4722	–	8.3704	7.6159
mean z	8.087±0.003							
mean log(<i>q</i>)	7.440±0.045							
J2039-63B								
z	8.1379	8.1515	–	8.2147	–	–	8.1677	–
log(<i>q</i>)	7.7838	8.127	–	7.9763	–	–	7.9284	–
mean z	8.145±0.010							
mean log(<i>q</i>)	7.955±0.243							
J2234-04B								
z	8.1115	8.1104	8.1667	8.1643	8.1079	8.1659	8.1713	8.1742
log(<i>q</i>)	7.3037	7.4352	7.368	7.3359	7.3459	7.3929	7.0618	7.3863
mean z	8.110±0.002							
mean log(<i>q</i>)	7.362±0.067							
J2242-06								
z	7.9952	7.9712	8.1484	8.1391	7.9836	8.15	8.16	8.1612
log(<i>q</i>)	7.0778	7.3706	7.2361	7.1386	7.1563	7.2384	6.7332	7.2408
mean z	7.983±0.012							
mean log(<i>q</i>)	7.202±0.152							
J2254-26								
no results								
J2311-42A								
z	8.1817	8.1705	8.2661	8.2633	8.1760	–	8.3488	8.3167
log(<i>q</i>)	7.2614	7.5276	7.3981	7.3311	7.3515	–	7.5032	7.4314
mean z	8.176±0.006							
mean log(<i>q</i>)	7.380±0.135							
J2311-42B								
z	8.1222	–	–	8.2207	–	–	–	–
log(<i>q</i>)	7.8286	–	–	8.1406	–	–	–	–
mean z	8.122±nan							
mean log(<i>q</i>)	7.829±nan							
J2349-22								
z	7.9360	7.9091	8.0443	8.0398	7.9293	8.0464	8.0732	8.0699
log(<i>q</i>)	7.1122	7.3623	7.2168	7.1481	7.1602	7.2239	6.656	7.2224
mean z	7.925±0.014							
mean log(<i>q</i>)	7.212±0.133							

The diagnostic grids are described in detail in [Dopita et al. \(2013\)](#). The uncertainties quoted are based on the variance of the average values for the first five diagnostics listed here “–” indicates the diagnostic does not return a value for abundance or ionization parameter.

[N II] and [O II] line fluxes, we use empirical formulae from [Izotov et al. \(2006\)](#), Equations (3) and (6). (This approach was used to allow for the temperature dependence of the [N II] and [O II] fluxes). These equations reduce to:

Table 6.4 [O III] electron temperatures and gas-phase oxygen abundances

Object	T_e (K)	Z^1 (this work)	Z (Izotov06)	Z(grid s) 2	δZ^3	M91	Old strong line 4		
							KK04	PP04	PP04
J0005-28	14719 \pm 107	7.847 \pm 0.007	7.858	8.012	0.165	8.104	8.306	7.954	7.951
J1152-02A	12248 \pm 99	8.151 \pm 0.007	8.178	8.088	-0.063	8.297	8.466	7.988	8.034
J1152-02B	12722 \pm 161	8.094 \pm 0.009	8.108	7.981	-0.113	8.288	8.455	8.001	8.021
J1225-06s2	16560 \pm 1067	7.499 \pm 0.062	7.462	7.929	0.430	7.750	7.999	8.053	7.910
J1328+02	14846 \pm 1287	7.867 \pm 0.085	7.835	8.132	0.265	8.234	8.397	8.190	8.165
J1403-27	14021 \pm 208	7.939 \pm 0.015	7.942	8.013	0.074	8.199	8.381	8.031	8.054
J1609-04b2	10431 \pm 1372	8.345 \pm 0.147	8.393	8.055	-0.290	8.323	8.471	8.152	8.127
J1609-04b5	14234 \pm 2850	7.959 \pm 0.191	7.944	8.137	0.178	8.313	8.468	8.136	8.140
J2039-63A	14383 \pm 528	7.966 \pm 0.035	7.976	8.087	0.121	8.321	8.485	8.023	8.076
J2039-63B	13982 \pm 1446	7.894 \pm 0.102	7.911	8.145	0.251	8.066	8.276	7.976	7.992
J2234-04B	14029 \pm 2107	7.897 \pm 0.140	7.890	8.110	0.213	8.118	8.312	8.059	8.058
J2242-06	13626 \pm 1665	7.921 \pm 0.126	7.906	7.983	0.062	8.109	8.300	8.094	8.074
J2254-26	12870 \pm 129	8.090 \pm 0.010	8.129	—	—	8.250	8.433	7.912	7.976
J2311-42A	12582 \pm 1629	8.091 \pm 0.132	8.100	8.176	0.085	8.254	8.425	8.098	8.129
J2311-42B	13451 \pm 464	8.011 \pm 0.034	8.038	8.122	0.111	8.217	8.403	7.963	8.018
J2349-22	13835 \pm 3015	7.858 \pm 0.213	7.839	7.925	0.067	8.015	8.222	8.064	8.015

¹ Z(this work) derived from Equations 7.2, 7.5, and 6.6² The Z(grid s) values are the average of the new grids involving the $\log(N_{\text{H}}/S_{\text{H}})$ and $\log(N_{\text{H}}/O_{\text{H}})$ ratios.³ δZ is the difference between Z(grid s) and Z(this work).⁴ Older strong line methods (columns 7-10) described in Kewley & Ellison (2008)

$$\log\left(\frac{N}{O}\right) = \log\left(\frac{NII\ 6584 + 6548}{OII\ 3726 + 3729}\right) + 0.273 - 0.726/T_{e4} + 0.007 * T_{e4} - 0.02 * \log(T_{e4}), \quad (6.11)$$

where T_{e4} is the [O III] electron temperature in units of 10,000 K. This equation differs only by a small constant offset (0.033) from that quoted by [Pagel et al. \(1992, Equation \(9\)\)](#), most probably due to the latter using older atomic data.. We assume the same electron temperature for OII and NII (reasonable, as they both arise primarily from the outer parts of the H II region), and further, that $N^+/O^+ = N/O$, following [Pilyugin et al. \(2010\)](#) and others. The errors from these assumptions are likely to be of the same order as the measurement uncertainties. The results are shown in [Table 6.6](#).

Using the abundance values listed in [Table 6.6](#), we can plot $\log(N/O)$ versus oxygen abundance. [Figure 6.11](#) shows the data from this work (yellow triangles), data from other SIGRID objects from [Nicholls et al. \(2014c\)](#) (brown triangles) and data from [van Zee et al. \(1998b\)](#) (black circles). The SIGRID data are consistent with the van Zee results, without any obvious evidence of a floor. However, [Berg et al. \(2012\)](#) state that the nitrogen floor does not become apparent until the oxygen abundance falls below $Z=7.7$, so the SIGRID data do not resolve the question of whether the floor exists. While the data for J1118-17s2 are not plotted because the value of the [N II] flux is not well defined, the best estimate values for this object ($\log(N/O) \lesssim 2.481$ and $Z \lesssim 7.2$) extend the trend considerably further in the same direction, off the graph, below and to the left. If correct, this suggests a very low level for any primary nitrogen, but further observations are necessary to confirm this. The red curve is the fit to the van Zee data used in the Mappings model grids, from [Dopita et al. \(2013, Figure 3\)](#), making allowance for the oxygen depletion into dust grains.

There is an increased scatter in the distribution with decreasing oxygen abundance (Z). Two possibilities may contribute to this. First, as there are populations of older stars in these galaxies (for example, KK246, [Nicholls et al. 2014c](#)), so intermediate mass AGB stars will contribute nitrogen to the interstellar medium (ISM) through hot-bottom burning processes. Second, the amounts contributed by such processes will depend on the (unknown) star formation histories of different galaxies. As the abundances derived using the strong line diagnostics depend at least in part on the $\log(N\ II/S\ II)$ ratio, the results are sensitive to deviations in the nitrogen fit from the theoretical fit used in the Mappings models, which was derived from the [van Zee et al. \(1998a\)](#) data (see [Dopita et al. 2013](#)), so any error here affects the model outcomes.

[Figure 6.11](#) shows that, at lower metallicities, the data exhibit increasing scatter and may even have started to fork into two branches. The upper region of the scatter may indicate nitrogen enrichment by Wolf-Rayet WN stars, as suggested by [López-Sánchez & Esteban \(2010\)](#). Smaller galaxies may divide into two classes, those with (or that have had) WN stars, and those without, depending on the stochastic nature of individual star formation events. [Edmunds & Pagel \(1978\)](#) have suggested the [N/O] ratio of H II regions in a galaxy arise from nitrogen that is significantly primary in origin, and are a measure of the early star formation history. While this may be correct for larger galaxies, at least in the case of the very isolated dwarf galaxy KK246, it is not the case, as the $\log(N/O)$ ratio is low but there is evidence of older stellar populations ([Nicholls et al. 2014c](#)). The presence or absence of WN stars in a dwarf galaxy's H II regions is a plausible explanation for this scatter or

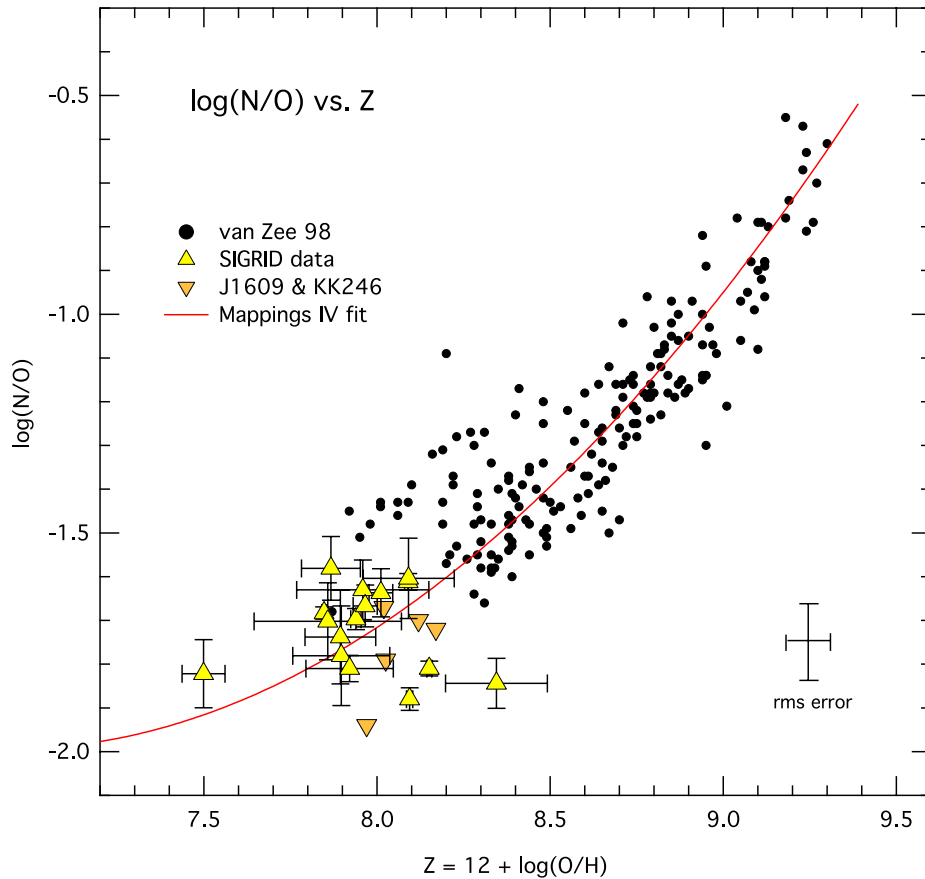


Figure 6.11 Log(N/O) versus oxygen abundance, Z

bifurcation. This would be consistent with the observations of the Blue Compact Dwarf galaxy, HS0837+4717 (Pustilnik et al. 2004; Pérez-Montero et al. 2011). The object appears to harbour over 100 Wolf-Rayet stars and has both a very low oxygen abundance and a high nitrogen abundance.

6.5.5. S II line ratios

The flux ratios of the two [S II] lines at 6716 and 6731 Å are good indicators of electron density (section 5.6, Osterbrock & Ferland 2006). Table 6.5 shows the variation of this ratio calculated for electron densities n_e of ~ 5 and ~ 50 cm $^{-3}$, for an ionisation parameter $\log(q) = 7.5$, typical for H II regions. The trends in the [S II 6716]/[S II 6731] line ratio are due to two factors: (1) the relatively small dependence of the line ratio on $n_e \sqrt{T_e}$ resulting from the collisional excitation rates of the S II line upper states, and (2) the use of the isobaric setting in the Mappings photoionisation modelling code, such that the density structure of the S II region is a function of the (varying) temperature within it, which depends on metallicity.

Table 6.6 shows the measured [S II] line ratios and electron densities, calculated using PyNeb (Luridiana et al. 2012), for all objects except J1118-17s2, for which we have no electron temperature. Comparing the observed S II line flux ratios to Table 6.5, it is reasonable to conclude that the Mappings values show J0005-28, J1152-02A&B, J1403-27, J2039-63A, J2234-04B, J2254-26 have electron densities greater than the low density limit ($n_e \lesssim 5$ cm $^{-3}$), while the remainder are low electron density objects. This is confirmed quantitatively using

Table 6.5 Calculated [S II] line ratios vs gas-phase oxygen abundance ($Z = 12 + \log(\text{O}/\text{H})$) for $n_e = 10$ and 100 cm^{-3} and ionization parameter $\log(q) = 7.5$

Z	7.39	7.69	7.99	8.17	8.39	8.69
$n_e=10$	1.439	1.439	1.439	1.440	1.441	1.445
$n_e=100$	1.394	1.393	1.391	1.389	1.384	1.373

Calculated using Mappings IV photoionization code (Dopita et al. 2013)

PyNeb to estimate the actual electron densities.

Figure 6.12 shows the diagnostic grids for $\text{O III}/\text{H}\beta$ versus $\text{N II}/\text{S II}$ at the two electron densities—the blue (upper) grid is for $n_e \sim 50 \text{ cm}^{-3}$, the green (lower) is for $\sim 5 \text{ cm}^{-3}$. It is clear that all but J2254-26 can be accommodated even on the higher electron density grid. The abundances for each object are very similar on both grids, but the estimated ionisation parameter $\log(q)$ changes. Similar results apply for the other diagnostic grids. It is interesting to note that J2254-26 has the highest calculated electron density of the observed objects.

Table 6.6 $\log(\text{N}/\text{O})$, $\log(\text{N II}/\text{O II})$, [S II] line ratios and electron densities

Object	$\log(\text{N}/\text{O})^1$	$\log(\text{NII}/\text{OII})$	S II line ratio ²	$n_e(\text{cm}^{-3})^3$
J0005-28	-1.683±0.014	-1.641±0.010	1.360±0.022	57.5±18.7
J1152-02A	-1.810±0.017	-1.618±0.015	1.385±0.051	40.5±36.9
J1152-02B	-1.880±0.026	-1.715±0.024	1.404±0.034	24.0±23.0
J1225-06s2	-1.822±0.078	-1.663±0.077	1.432±0.204	—
J1328+02	-1.581±0.073	-1.462±0.051	1.540±0.162	—
J1403-27	-1.697±0.024	-1.574±0.017	1.408±0.054	20.5±100%
J1609-04b2	-1.844±0.057	-1.609±0.037	1.420±0.095	17.6±100%
J1609-04b5	-1.630±0.068	-1.544±0.054	1.455±0.148	—
J2039-63A	-1.667±0.048	-1.562±0.036	1.344±0.090	73.2±100%
J2039-63B	-1.738±0.107	-1.499±0.107	1.501±0.411	—
J2234-04B	-1.781±0.114	-1.556±0.114	1.389±0.492	35.5±100%
J2242-06	-1.810±0.030	-1.56±0.03	1.497±0.249	—
J2254-26	-1.612±0.019	-1.451±0.015	1.317±0.039	96.8±34.0
J2311-42A	-1.604±0.092	-1.463±0.066	1.473±0.204	—
J2311-42B	-1.637±0.055	-1.49±0.041	1.456±0.122	—
J2349-22	-1.702±0.088	-1.628±0.068	1.457±0.176	—

¹ $\log(\text{N}/\text{O})$ calculated from $\text{N II}/\text{O II}$ flux ratios using Equation 6.11 and electron temperatures from Table 6.4

² n_e uncertainties calculated using the line ratio uncertainties, except where these are large, where they exceed the value of n_e , and are quoted as 100%.

³ '—' indicates electron densities $\lesssim 5 \text{ cm}^{-3}$.

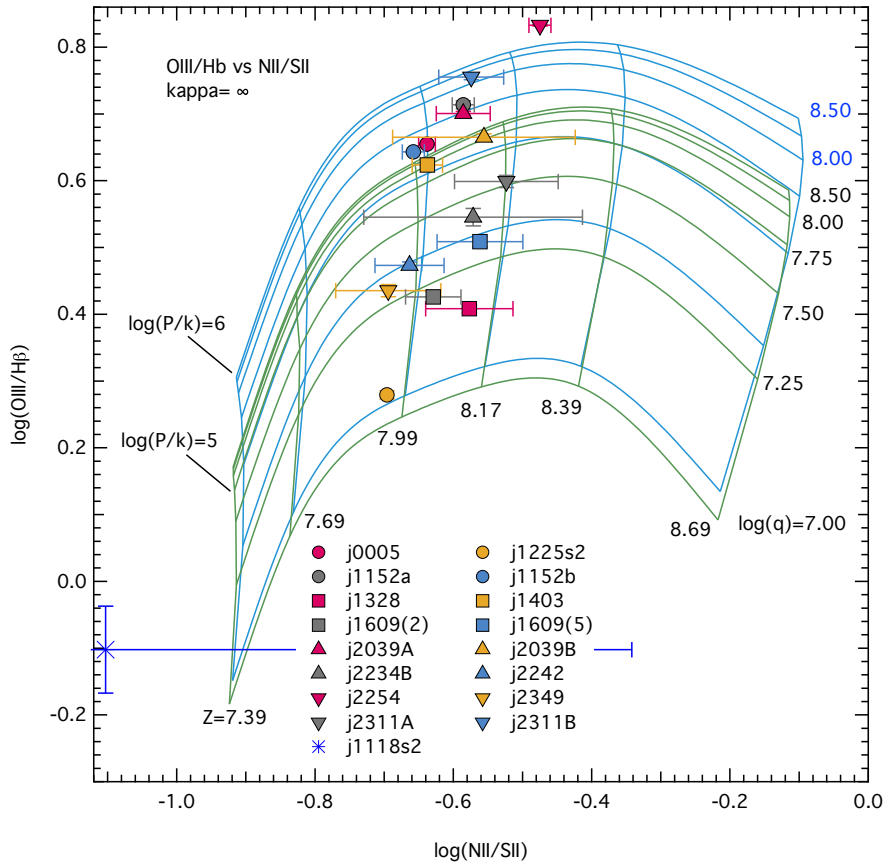


Figure 6.12 Comparison of diagnostic grids for the ratios $\log(\text{OIII}/\text{H}\beta)$ versus $\log(\text{NII}/\text{OII})$ for electron densities $n_e \sim 5$ and $\sim 50 \text{ cm}^{-3}$ (isobaric case, $\log(P/k) = 5$ and 6 , respectively, where P is the pressure and k is the Boltzmann constant.)

6.5.6. T_e : Oxygen gas-phase abundance

Figure 6.13 shows electron temperature, plotted versus gas-phase oxygen abundance, Z , from Table 6.4. $Z (=12+\log(\text{O}/\text{H}))$ is derived using the formulae in Equations (7.2) and (7.5). The quadratic fit to the data with 66% confidence errors is:

$$T_e = -(0.3239 \pm 0.1540)(Z - 7.50)^2 - (0.4370 \pm 0.1410)(Z - 7.50) + (1.6493 \pm 0.0340) \times 10^4 \quad (6.12)$$

While Figure 6.13 may be used to calculate the total gas-phase oxygen abundance from the $[\text{O III}]$ electron temperature, it applies only to the data presented here, and we will provide a substantially more accurate fit to the model-derived curve in paper 2 (Chapter 7).

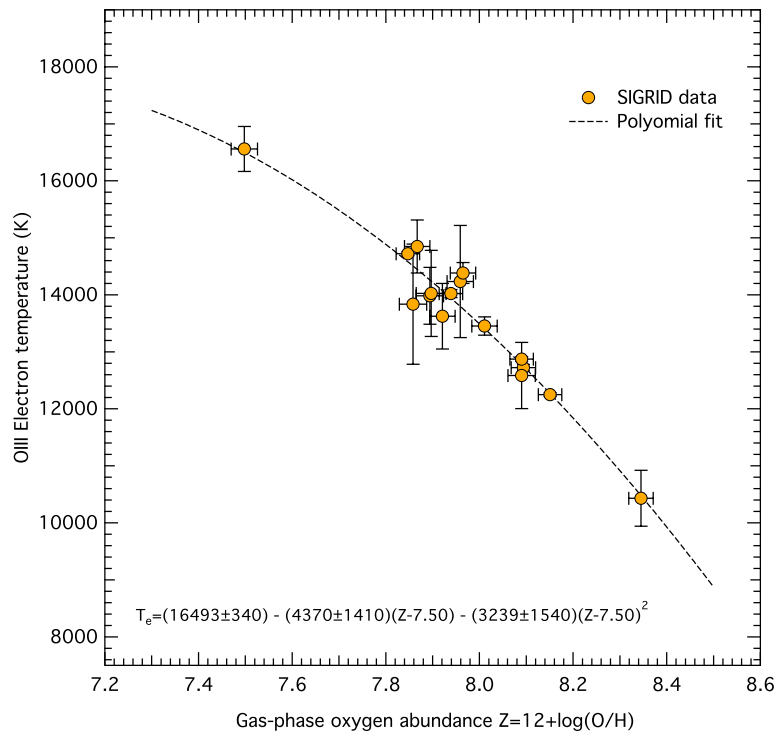


Figure 6.13 T_e versus gas-phase oxygen abundance from Equations 7.2 and 7.5

6.6. Discussion

6.6.1. Mass–Metallicity

Mass (or luminosity) versus metallicity behaviour is one of the important evolutionary diagnostics for galaxies. It has been extensively mapped for larger galaxies (e.g., Tremonti et al. 2004), but it is less well known for dwarf galaxies. It has been studied by several authors (Lee et al. 2006; Pustilnik et al. 2011b; Berg et al. 2012; Andrews & Martini 2013). Exploring it was one of the initial motivations for the SIGRID sample (Nicholls et al. 2011). Figure 6.14 shows the gas-phase oxygen abundance versus neutral hydrogen mass (left panel, data from Meurer et al. (2006) and Table 6.1) and gas-phase oxygen abundance versus absolute B-band magnitude (right panel).

There is no clear trend in the first graph, suggesting the neutral hydrogen mass is not strongly correlated with metallicity, at least in this sample. In the right panel, we compare the SIGRID data against data from the Pustilnik et al. (2011b) survey of galaxies in the Lynx-Cancer void. The SIGRID data are consistent with the Pustilnik et al. data, and both samples are selected for isolation. The four blue points in the right panel are objects from Pustilnik et al., but which meet the more stringent selection criteria for the SIGRID sample, for luminosity, galaxy type and isolation (distance from nearest neighbour). The trend line is from Lee et al. (2003) for field dI galaxies, but which were not otherwise selected for isolation. Both the Pustilnik and SIGRID data tend to fall below the line, indicating that more isolated objects have slightly lower metallicities than similar objects in more congested regions, as suggested by Pustilnik et al. (2011b).

There is insufficient data in our observations to confirm the increasing spread of metallicity

values at low mass, as implied by Tremonti et al. (2004, Figure 6). However, the $\log(N/O)$ data (Figure 6.11) are consistent with such a spread.

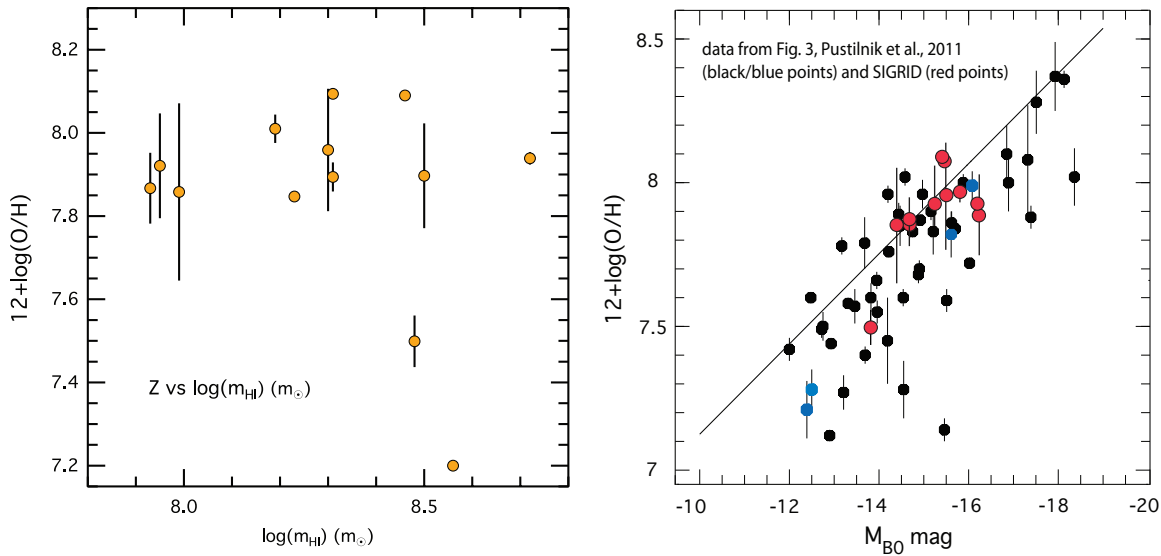


Figure 6.14 Left Panel: Oxygen abundance versus neutral hydrogen mass (from Table 6.1). Right Panel: Oxygen abundance versus absolute B-band magnitude, comparing data from Figure 3 from Pustilnik et al. (2011b) with SIGRID data. Eleven SIGRID objects have measured B-band magnitudes. The four blue points are those from the Pustilnik sample which meet the luminosity, galaxy type, and isolation selection criteria for SIGRID. The straight line fit is for field dI galaxies from Lee et al. (2003). The B-band magnitudes for the SIGRID sample have been taken from the NASA Extragalactic Database (NED).

6.6.2. Comparison of metallicity methods

In this work, we have calculated the gas-phase oxygen abundance using the electron temperature direct method routine developed here, and the diagnostic grids. Table 6.4 compares the electron temperature abundances using the methods described here with those using the iterative method from Izotov et al. (2006), with the same input temperatures; and the most reliable values from the diagnostic grids, those using the $\log(N_{II}/S_{II})$ and $\log(N_{II}/O_{II})$ diagnostics. The values derived using the two T_e methods are similar, suggesting that the method developed here is reliable. See also a discussion of this in the forthcoming paper 2 (Chapter 7).

It is interesting to note that the diagnostic grid abundances, with two notable exceptions, are consistently a little higher than the direct method values, consistent with the findings of López-Sánchez et al. (2012). The average value of the difference δZ is 0.104 ± 0.171 . The complete explanation of this difference is unclear, but in part it can be explained by the nature of the diagnostic grids derived from the Mappings photoionisation modelling code. In the grids, we have assumed a dust depletion of 1.0 solar (Dopita et al. 2013), to account for the elements locked up in dust grains. This leads to an overestimate of 0.07 dex in the abundance values derived from the diagnostic grids, compared to the gas-phase-only oxygen abundances from the direct method, explaining about half of the discrepancy.

It is useful to examine two of the “outliers” in Table 6.4, where the diagnostic grid oxygen abundances differ substantially from the electron temperature oxygen abundances. J1225-06s2 has a very low oxygen abundance, ~ 7.45 , from the direct method, and ~ 7.9 from

the grids. This could be explained if there is more N II than implied by the Mappings models parameters, although this is not obvious from Table 6.6. There may also be increased nitrogen due to enrichment by WN stars, as in the case of HS 0837+4717 (Pustilnik et al. 2004; Pérez-Montero et al. 2011). The oxygen abundance discrepancy for J1609-04(2) is very likely a result of uncertainty in the flux of the [O III] 4363 Å auroral line, which is weak in this object.

The diagnostic grids themselves (Table 6.3) are somewhat discrepant in the values yielded for oxygen abundances. In particular, two trends are clear. First, diagnostics involving $\log(N_{\text{II}}/S_{\text{II}})$ are particularly consistent, and the closest to the oxygen abundances derived using the direct method. Diagnostics involving [O II] fluxes are nearly as consistent. This concordance and consistency lead us to believe that these diagnostics are the most reliable, and we have used the means of the $\log(N_{\text{II}}/S_{\text{II}})$ and $\log(N_{\text{II}}/O_{\text{II}})$ diagnostics in Table 6.4. Second, diagnostics involving $\log(N_{\text{II}}/H\alpha)$ give somewhat higher oxygen abundances than both the other diagnostics and the direct method values. The source of these discrepancies is unclear, but may be related to the abundance fit for nitrogen used in Mappings. They do not materially affect the results reported here, provided we rely on the $\log(N_{\text{II}}/S_{\text{II}})$ and $\log(N_{\text{II}}/O_{\text{II}})$ diagnostics and direct method oxygen abundances.

6.6.3. Further analysis and investigations

In the second paper examining these observations (next Chapter), we will explore the effect of three-dimensional diagnostic charts. These use three independent diagnostic ratios plotted and explored in three dimensions, whose purpose is to investigate whether the observations lie on a diagnostic plane, along the lines of Vogt et al. (2014). We will examine the effects of using diagnostic grids calculated using higher electron densities. We will investigate the effects of optically thin H II regions, and show that they can have considerable effects on the diagnostics, and that there is evidence of optical thinness in some of the observed objects. We will re-examine the electron temperature versus oxygen abundance plots, for both these observations and for 124 SDSS objects from Izotov et al. (2006). Using the Mappings photoionisation modelling code, we will demonstrate that with reasonable assumptions about the star clusters exciting H II regions, there is an effective upper limit to the temperature that can be reached, even in optically thin regions. The implications appear to be that some of the high temperatures reported in low metallicity H II regions may be somewhat in error. We will demonstrate the effect of taking into account the additional contribution to total oxygen abundance of the oxygen in dust grains. We will also suggest that the apparent spread in metallicities at the low end of the mass-metallicity relation are due to stochastic effects in stellar mass distributions in the small star clusters exciting H II regions in small irregular galaxies.

6.7. Conclusions

In this paper we have presented the results of observations of seventeen H II regions in thirteen small isolated dwarf irregular galaxies, most from the SIGRID sample, all but one exhibiting the [O III] auroral line. All have measured oxygen abundances <8.2 ($<0.3 Z_{\odot}$),

one has an apparent abundance of 7.44 and another very low metallicity object with $Z \sim 7.2$. We have derived a method for calculating total gas-phase oxygen abundances using only the optical spectra between 3700 and 7000 Å. This method gives very similar results to previous empirical fit methods. From an analysis of abundances and ionisation parameters using the diagnostic grids developed by [Dopita et al. \(2013\)](#), we find the direct method oxygen abundances are consistently within 0.07 dex of the strong line diagnostic results, making allowance for the oxygen locked up in dust grains. From the line ratio of the two red [S II] lines we find that the electron densities occurring in the objects observed are between ~ 5 and 100 cm^{-3} . The nitrogen abundance, as expressed in $\log(\text{N}/\text{O})$, continues the trend evident in [van Zee et al. \(1998b\)](#), but from this sample we find no clear evidence for a nitrogen floor. There is increased scatter at lower oxygen abundances, and some evidence for a bifurcation in the trend, possibly due to the presence of WN stars in some of the H II regions. The slope of the luminosity–metallicity relation for these observations is very close to that for void galaxies in [Pustilnik et al. \(2011b\)](#). The spectra from an apparently very low metallicity galaxy, J1118-17s2, show no nitrogen lines: we intend to undertake follow up observations on this galaxy to estimate the metallicity more accurately.

6.8. Appendix: Emission line flux error estimation

This appendix describes the methods used to estimate emission line flux uncertainties for spectra extracted from WiFeS data cubes of objects in the SIGRID sample. The data reduction process is described in detail in [Childress et al. \(2014\)](#), and in this paper in Section 6.3.3. Briefly, the steps where noise is involved or systematic errors are incurred are bias subtraction, flat fielding, cosmic ray removal, sky-line subtraction using nod-and-shuffle, and standard flux star calibration. The principle sources of uncertainty are the CCD detector and amplifier readout noise, and the amplification of this noise through the data reduction chain; the effects of cosmic rays and sky lines, and their removal (partial or complete); the calibration of the emission line fluxes using standard star flux data; the de-reddening process; and the measurement of the line fluxes from the flux-calibrated spectra.

As the IFU data frame is convolved into a data cube in the pipeline, the process of error calculation is more complex than for single slit or echelle spectroscopy. For the spectral noise uncertainties, there are two approaches we could take. One is to estimate the errors accumulating from each step, such as described for echelle spectroscopy by [Skillman et al. \(1994\)](#). The other approach, used here, is to measure the statistical noise from spectra extracted from the reduced data cube, and to estimate the systematic errors arising from the de-reddening and flux calibration, which are independent of the statistical noise. Unlike single slit spectra, with IFU data cubes, we are able to select the entire area of the H II region from which to extract the spectrum, and exclude the majority of the galaxy stellar background, resulting in better signal-to-noise. Note that the statistical noise varies with the size of the sampled spaxel area, due to averaging. For the objects in this study, sampling using a 6 arc sec diameter circular spatial area maximises the amount of flux from the H II region and minimises both the statistical noise, through averaging, and the stellar continuum from the area outside the H II region.

In every case, the galaxies were so faint that the stellar extent was at best barely detectable. However, images from the DSS survey and from the SINGG data (as illustrated in [Nicholls et al. 2011](#)) suggest the individual galaxies are less than or approximately equal to the FOV of the WiFeS spectrograph, 25×38 arc sec. The benefit of the IFU is that the sample was centered on the H II region, and excluded virtually all areas of the galaxies without H II emission.

Line fluxes and noise were measured from the extracted spectra using IRAF/splot. The standard splot 'k-k' method was used to fit a gaussian to each emission line, to measure the equivalent width (where possible), the gaussian full width at half maximum, and the integrated flux. Noise was measured on both sides of the emission line using the splot 'm-m' method. These results were checked using the deblend 'd-d' method, but using a single line, which automatically generates values of the same parameters. Particular care was taken to account for any stellar absorption features underlying the Balmer emission lines, although in all cases, this was minor or absent, due to low stellar continuum. In fact, the stellar continuum was extremely faint, with the exception of the object J0005-28 (see Figure 6.8, displayed on a log-intensity scale). Test sample sizes showed that all the detectable H α and [O III] in each H II region lay within the sample aperture. The observed fluxes mostly peak at or less than a radius of 2.5 arc sec, except where there are closely

adjacent H II regions (e.g., J1609-04). For these, limiting the sample size to 6 arc sec diameter avoided sampling a different H II region. Ideally, single spaxel-based analysis would be preferable to multi-spaxel sampling, but these objects are so faint that the resultant noise is prohibitive.

Detector noise is added to the data frame during bias subtraction and flat fielding, as the bias and flat field frames used also incur readout noise. The sky subtraction process using the nod and shuffle process or the sky frame method adds additional noise during the subtraction process. Nod-and-shuffle sky subtraction was used for all H II region observations, with sub-exposure times chosen to be shorter than the shortest observed fluctuation in the OH airglow lines (Frey et al. 2000). The removal of the critical OH lines is effectively complete in all observations. The [O I] airglow lines are at wavelengths that did not interfere with any of the observed H II region spectral lines.

Cosmic ray removal is reasonably efficient, using the Laplacian kernel technique described by van Dokkum (2001). The process is not perfect, but virtually all the remaining cosmic ray artefacts are removed using the imcombine process. In isolated cases, separate cosmic rays occur on all object data frames at the same location, and this can lead to erroneous results, but this can be detected by the labour intensive process of inspecting all the lines on all the IFU slitlets (25) on all the data frames (usually 3). Figure 6.15 shows part of a raw WiFeS blue data frame including segments of 7 slitlets (of a total 25), centred on the H γ and [O III] λ 4363 auroral line, for the galaxy J0005-28. The auroral line is very prominent in this frame, to the left of the H γ line.

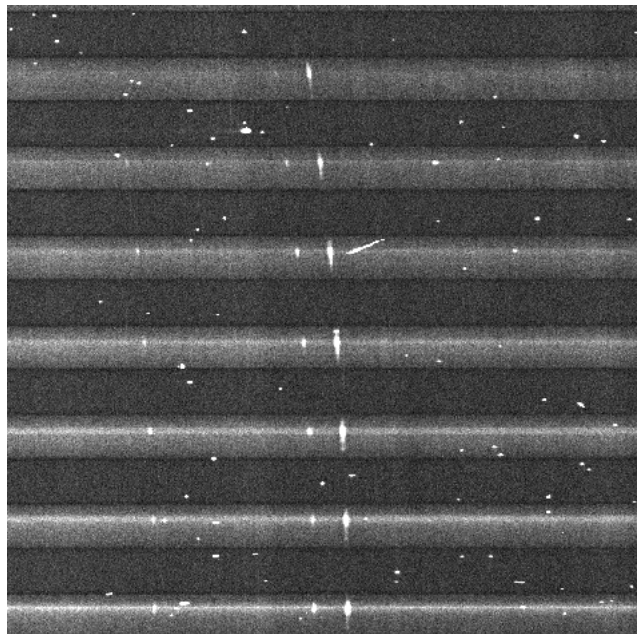


Figure 6.15 Section of a single WiFeS IFU raw data frame for J0005-28 with cosmic ray artefacts, centred on the H γ line, showing sections of 7 slitlets. Each frame was inspected to check for cosmic ray contamination of key lines. Note that, due to the optical paths in the WiFeS IFU blue camera, the right side of the image corresponds to shorter wavelengths.

In addition to the intrinsic statistical noise amplified through the data reduction pipeline, when measuring the emission line fluxes, it is necessary to take into account any broad absorption lines in the stellar continuum, on which the nebular spectra are superimposed.

There are three approaches here. The first is to correct for an assumed 2 \AA EW absorption in each line, as described in [Skillman et al. \(1994\)](#). The second is to use an automated method such as the LZIFU IDL program developed by several workers at the University of Hawaii, which fits model stellar continua to observed spectra and then calculates the emission line fluxes (a paper on this application is planned). The third approach, which we use here, works better when the stellar continuum is weak, as with the objects reported here. It involves manual fitting of gaussian profiles to the emission lines using standard IRAF/splot methods. The technique described by [Berg et al. \(2013\)](#) is very similar in detail to the method used here.

The errors arising from the de-reddening process are due to uncertainties in the nature and amount of dust between the nebular emission and the observer. In the case of the SIGRID objects considered here, all are further than 10° from the galactic equator, to avoid significant reddening by Milky Way dust. We calculated the de-reddening using two independent methods and used the differences between the results as an estimate of the de-reddening errors. We used the dust reddening formulae from [Cardelli et al. \(1989\)](#) with $A_V = 3.1$, adjusting the de-reddening to set the resultant Balmer $H\alpha/H\beta$ flux ratios to the [Storey & Hummer \(1995\)](#) Case B Balmer ratios for the calculated [O III] electron temperature. We used the ratios of $H\gamma$ and $H\delta$ to $H\beta$ as confirmation. To confirm these results, we employed the dust models from [Fischera & Dopita \(2005\)](#), using a relative extinction curve with $R_V^A = 4.3$, where $R_V^A = A_V/(E_{B-V})$ and A_V is the V-band extinction. This is discussed in more detail in [Vogt et al. \(2013, Appendix 1\)](#). We used an initial Balmer decrement ratio of 2.82 for $H\alpha/H\beta$, corresponding to an electron temperature of 12 500K, adjusted the electron temperature using the direct method derived from the [O III] line ratios, then adjusted the apparent Balmer ratios by varying the value of A_V for the best fit to the $H\gamma/H\beta$ ratio, using the ratio $H\delta/H\beta$ as a check, again fitting to the Storey and Hummer Case B Balmer ratios.

The de-reddened flux values reported in Table 6.2 are those using the Cardelli method. In all cases, the two approaches gave similar results: The average difference between the two methods for the important diagnostic lines varies between 0.1% and 0.7%. As a consequence, we have adopted a figure of 1% for the de-reddening error. In only one case, J2234-04, object A, did the de-reddening fail to provide a plausible result, and this has been excluded from the results reported here. It appears likely that two or more incompletely removed sets of cosmic ray artefacts were the cause of the problem, in this particular case.

Flux calibration errors depend on how well one can fit flux-calibrated vales to the standard stars. The standard stars used were taken from [Bessell \(1999\)](#), using Bessell's recalibration of Hamuy's Southern Spectrophotometric Standards ([Hamuy et al. 1992](#)). Calibrating to these standards is likely to be more accurate than the older Oke standards ([Oke 1990](#)), but we have retained an estimated 2% error for calibrating the flux values, as per [Berg et al. \(2013\)](#).

We have recently corrected a problem with the measured [O II] line fluxes. The source of the problem is a sharp absorption edge at 3850\AA , due to the adhesive used in the beam splitter, and the lack of any significant output below about 3900\AA from the lamps used for flat exposures to identify and correct this problem. The lamps are now being replaced, and future measurements using WiFeS will no longer require this compensation. The problem was understood in the testing phase of the construction of WiFeS, and was identified in the observations from poor matches to the diagnostic grids that involve [O II] in the ratios. To

compensate requires boosting the [O II] flux by a factor of $\times 1.5$. It affects only the [O II] $\lambda\lambda$ 3726,9 lines. It does not make a substantial difference to the calculated oxygen abundances or other results.

CHAPTER 7

Metal-poor dwarf galaxies in the SIGRID galaxy sample. II. The electron temperature–abundance calibration and the parameters that affect it

There are two possible outcomes: if the result confirms the hypothesis, then you've made a measurement. If the result is contrary to the hypothesis, then you've made a discovery.

Enrico Fermi

This chapter is the paper accepted for publication in The Astrophysical Journal (July 2014) under the title 'Metal-poor dwarf galaxies in the SIGRID galaxy sample. II. The electron temperature–abundance calibration and the parameters that affect it.', Nicholls, D. C., Dopita, M. A., Sutherland, R. S., Jerjen, H., and Kewley, L. J.. The work is entirely my own, though incorporating comments and suggestions from my co-authors. Minor typographical errors have been corrected, and sections, tables and figures have been renumbered to conform with the layout of the thesis.

7.1. Chapter summary

In this paper, we use the Mappings photoionisation code to explore the physical parameters that impact on the measurement of electron temperature and abundance in H II regions. In the previous paper (Chapter 6) we presented observations and measurements of physical properties from the spectra of 17 H II regions in 14 isolated dwarf irregular galaxies from the SIGRID sample. Here, we analyze these observations further, together with three additional published data sets. We explore the effects of optical thickness, electron density, ionisation parameter, ionisation source, and non-equilibrium effects on the relation between electron temperature and metallicity. We present a standard model that fits the observed data remarkably well at metallicities between one tenth and 1 solar. We investigate the effects of optically thin H II regions, and show that they can have a considerable effect on

the measured electron temperature, and that there is evidence that some of the observed objects are optically thin. We look at the role of the ionisation parameter and find that lower ionisation parameter values give better fits at higher oxygen abundance. We show that higher pressures combined with low optical depth, and also κ electron energy distributions at low κ values, can generate the apparent high electron temperatures in low-metallicity H II regions, and that the former provides the better fit to observations. We examine the effects of these parameters on the strong line diagnostic methods. We extend this to three-dimensional diagnostic grids to confirm how well the observations are described by the grids.

7.2. Introduction

The term “electron temperature” in an H II region usually refers to the apparent [O III] electron temperature, T_e , derived from the [O III] optical spectra of the nebula, using a simple method based on the relative collisional excitation rates of the 1D_2 and 1S_0 levels of O^{++} (see, e.g., [Osterbrock & Ferland 2006](#); [Nicholls et al. 2012](#)). This (with similar measurements for O^+) is used as the basis for calculating the total oxygen abundance, when the electron temperatures are available.

Spectra arising from collisional excitation in a particular region in the nebula will exhibit the characteristics of the local electron temperature (or electron energy distribution) and radiative environment of that region, but observed electron temperatures are only mean electron temperatures, as they are calculated from emission lines averaged over a range of zones in the nebula, and with a range of physical temperatures. The abundance of oxygen is then determined from the integrated fluxes of [O III] and [O II], using the derived [O III] and [O II] electron temperatures (see, e.g., [Izotov et al. 2006](#)). The apparent abundance is therefore only approximately related to the true oxygen abundance. The matter is complicated further if there are non-equilibrium electron energy distributions, as suggested by [Nicholls et al. \(2012, 2013\)](#) and [Dopita et al. \(2013\)](#).

Due to the highly non-uniform physical structures in real H II regions, no general photoionisation model is yet capable of precisely reproducing the observed spectral emissions. The simplest approximation to an H II region is the uniform “single slab” model. This is a poor approximation to the behaviour of a real H II region, as it assumes all the ionic species are uniformly distributed and at the same physical temperature, and need to be corrected to reflect the true distribution of ions and temperatures. For example, the [O II] emission arises predominantly from the cooler (usually outer) regions of the nebula, whereas the [O III] emission is more uniformly distributed. Assuming that the two ions are emitting at the same temperature will overestimate the [O II] flux (per atom) and thus underestimate the [O II] abundance in a real nebula. Empirical- or theory-based correction factors are often applied ([Garnett 1992](#); [López-Sánchez et al. 2012](#)). Other ionisation states, for example, O^{+++} and O , occur in the highest and lowest excitation (usually innermost and outmost) regions of the nebula, respectively. Unobserved species such as O^{+++} which affect the populations of observed species are accounted for the so-called “ionisation correction factors”, discussed by many authors (see, for example, [Peimbert & Costero 1969](#); [Stasińska 1978](#); [Aller 1984](#); [Diaz et al. 1987](#); [Izotov et al. 1994](#); [Esteban & Peimbert 1995](#); [Vilchez & Esteban 1996](#); [Esteban](#)

et al. 2004; Stasińska 2005; Bresolin et al. 2005; Izotov et al. 2006; López-Sánchez & Esteban 2009).

Taking into account this three-dimensional structure, a more realistic model is the three dimensional “Strömgren sphere”, with a stellar or star cluster excitation source at the centre, a stellar-wind-evacuated central region, and radial zones of ionised gas at different physical temperatures. These give rise to differing amounts of spectral emission from different ionic species, the observed results of which are the integrated spectral emissions from all the radial zones for each ionic species. The models can then be compared with the spectra observed in real H II regions. Current photoionisation models such as Mappings IV (Dopita et al. 2013) are based on this physical structure.

A still better approximation to real nebulae is to assume a spatially inhomogeneous turbulent structure for the nebula (Sutherland et al., in progress, and earlier work, Bland-Hawthorn et al. 2011), but modelling this is significantly more computationally demanding. Indeed, one look at the complexities of the Orion, M17, and 30-Doradus nebulae shows such variation in form as to defy accurate modelling. While extra-galactic H II regions appear unresolved in more distant galaxies, they are very likely structurally as complex as the nearby nebulae, and at best, even inhomogeneous and fractal models are only approximations to reality. Nonetheless, spherical models are very useful in exploring the effects of different physical parameters on the observed spectra.

In this work, we use the Strömgren Sphere model, using the Mappings IV photoionisation code (see appendix for the details of changes in the current version of the code since that described in Dopita et al. 2013)¹. To obtain information on the oxygen abundance of an observed but spatially unresolved H II region, we need to identify the key physical parameters affecting the apparent electron temperature, and use these in the models to compare with observations. From these we derive a relation between the intrinsic nebular oxygen abundance and the apparent (i.e., volume and luminosity averaged) [O III] mean electron temperature. The models are then used to generate relationships between electron temperature, T_e , and oxygen abundance, $12+\log(\text{O}/\text{H})$, for the model H II region, to which the observed apparent electron temperature of a real object may be compared.

The electron temperatures that our models generate within an H II region vary between $\sim 30,000$ K and ~ 100 K, with 10,000 K being typical. The inner zones (at higher temperatures) have smaller volumes, per unit thickness, than the outer zones. Measurements of the [O III] and [O II] apparent electron temperatures from spectra reflect the average conditions in core and outer regions of the nebula, respectively. The [O III] temperature provides an average over the bulk of the internal regions of an H II region, and is the most useful (and most widely used) single measurement of the conditions in the nebula. However, it is important to recognise that this single value does not characterise the entire H II region.

This work continues on from our previous paper (Nicholls et al. 2014a, hereafter “paper 1”). The paper is structured as follows. In Section 7.3, we discuss the measurement of electron temperatures and the calculation of oxygen abundances, relating the outputs from the Mappings photoionisation model code to data from the SIGRID sample (Nicholls et al.

¹Mappings is a comprehensive modelling code capable of studying a wide range of possible astrophysical nebular structures and physical phenomena, rather than a tailor-made model for specific objects. As such it may be compared with other similar complex modelling codes, as described by Péquignot et al. (2001).

2011) and [paper 1](#) (Chapter 6), Sloan Digital Sky Survey (SDSS) data from [Izotov et al. \(2006\)](#) (Data Release 3 from [York et al. 2000](#)), low-metallicity emission line galaxy data from [Izotov et al. \(2012\)](#), and data for Wolf–Rayet galaxies from [López-Sánchez & Esteban \(2009, 2010\)](#). These observations span a range of nebular metallicities between one-fiftieth and 1 solar. We examine the calculation of the electron temperature and the chemical abundances. In Section 7.4, we consider the electron temperature–chemical abundance relation. In Section 7.5, we examine the effect of optical depth at the Lyman edge of hydrogen at 912Å. In Section 7.6, we consider the effect of the FUV spectral energy distribution of the central star cluster. In Section 7.7, we investigate the effects of pressure in H II regions. In Section 7.8, we explore the role of the ionisation parameter. In Section 7.9, we look at the effects dust. In Section 7.10, we explore the consequences of κ non-equilibrium electron energy distributions. In Section 7.11, we summarise the effects of these parameters. In Section 7.12, we look at the use of diagnostic line ratio grids from [Dopita et al. \(2013\)](#), and in Section 7.13, we extend this to examine the extra information yielded by using three-dimensional grids. In Section 7.14, we discuss our findings, and in Section 7.15, we present our conclusions.

7.3. Electron temperature and oxygen abundance

7.3.1. Calculating electron temperatures

Determining the electron temperature from [O III] spectra from an H II region has been discussed frequently in the literature. The simplest technique is to use a graph of the 4363Å and 5007+4959Å [O III] lines, as shown in [Osterbrock & Ferland \(2006, Figure 5.1\)](#). Other techniques have been proposed, such as the iterative method in [Izotov et al. \(2006\)](#), which has its origin in work by [Seaton \(1975\)](#). Here we have used the formulae derived from our Mappings photoionisation models, presented in [Nicholls et al. \(2013\)](#), using the O⁺⁺ collision strength data from [Palay et al. \(2012\)](#) (see Equation (7.2) below). All methods are based on the change of the relative populations of the ¹D₂ and ¹S₀ energy levels of O⁺⁺ with temperature. When using the same O⁺⁺ collision strength data, the methods give very similar results. The choice of collision strength data is important, as different data can lead to electron temperatures differing by as much as 5% at an electron temperature of 15,000 K (see Figure 2 in [Nicholls et al. 2013](#)). The Palay data tend to give lower [O III] electron temperatures than older data sets. The recent collision strength calculations by [Storey et al. \(2013\)](#) tend to give higher electron temperatures, similar to those from [Lennon & Burke \(1994\)](#). We have not been able to use these recent data in the Mappings photoionisation models as calculations for the upper level data needed by Mappings do not converge (P. Storey, private. communication, 2014). For a detailed discussion of the effects of different collision strength data, see [Nicholls et al. \(2013\)](#).

7.3.2. Limitations in electron temperature calculations

There is an important limitation in the methods used to measure the [O III] electron temperature, for very low-metallicity H II regions. For the observational data considered in this paper, we have used the equations presented in [Nicholls et al. \(2013\)](#). These are derived from the Mappings models in [Dopita et al. \(2013\)](#), and apply for metallicities between one-twentieth

and 1 solar. Alternative methods used by [Izotov et al. \(2006, 2012, and references therein\)](#) have a longer history, and are based on the original work of [Seaton \(1975\)](#), for which fit parameters were only calculated for electron temperatures between 5,000 K and 20,000 K. The range restrictions in these methods limit the temperature ranges that can be calculated reliably. Although both methods can generate values for the electron temperature $> 20,000$ K, such values are the result of extrapolation outside the range of application, and are therefore not reliably based in physics. At higher temperatures the physics coming into play involves processes that do not affect the results at lower temperatures. Models that do not allow for the increasing importance of the higher temperature processes will necessarily be unreliable. Any significant, unaccounted for, change in behaviour outside the specified ranges will lead to erroneous calculated temperatures. Consequently, extrapolation is problematic, and values of $T_e \gtrsim 20,000$ K cannot be considered reliable, if calculated using the methods discussed here.

7.3.3. Oxygen abundance

Oxygen abundance is used as a proxy for total metallicity as it is the dominant heavy element species observable in the optical spectrum, its spectral lines are present throughout H II regions, and it is produced in stellar nuclear reactions that give rise to the other major heavy element components (e.g., C and N). It is present in H II regions in five forms: O^{+++} , O^{++} , O^+ , O^0 and in dust. O^{+++} is present only in the highest ionisation zones closest to the stellar excitation source in H II regions, and does not contribute significantly to total oxygen. O^{++} is the dominant form of oxygen in many low-metallicity H II regions where it occupies much of the body of the H II region. O^+ is excited in the outer zones, or regions where the higher energy photons have been depleted, and O^0 is present only at the low-ionisation outer edges. However, some H II regions have dominant O^+ excitation (see, for example, [Esteban et al. 2009; Izotov et al. 2012](#)). In the models presented here, we consider only a simple spherically symmetric model with a central strongly ionising star cluster.

Figure 7.1 illustrates these points, showing the ionic fractions for the gaseous oxygen species calculated using the Mappings IV photoionisation code, as a function of radius for a spherical H II region, from the minimum radius, R_{min} , at which the Strömgen sphere is gas-filled, to the maximum, R_{max} , defined as the radius at which the atomic hydrogen is 99% neutral. The parameters for this calculation are $\log(q)=7.5$, $12+\log(O/H)_{total}=0.1solar$, optically thick, equilibrium electron energies, isobaric with $\log(P/k) = 5$, and using the Starburst99 excitation model as described in Section 7.4 below. It is clear that O^{++} is the dominant ionic fraction over most of the volume of the nebula, O^+ contributes mainly in the outer regions, and O^0 only at the outer edge or lowest excitation regions.

The ionisation parameter and the metallicity and oxygen abundance were defined in [paper 1](#) (Chapter 6), but it is useful to repeat these definitions here. The ionisation parameter q (sometimes expressed as $\mathcal{U} = q/c$, where c is the speed of light) is the ratio of the number of ionising source photons passing through a unit volume to the neutral hydrogen density. The photon flux matches the number of new ions it produces, and as q has the dimensions of velocity, it can be understood as the maximum speed at which the boundary of the ionised region can move outwards ([Dopita & Sutherland 2003](#)). q is at its maximum at the inner edge of the ionised region of an H II region, and falls to zero at the outer edge of the ionised

nebula, where (if) the ionising flux is fully depleted. A value of $\log(q) = 8.5$ (corresponding to $\log(\mathcal{U}) = -1.98$) is at the high end of values likely to be found in an H II region (see, for example, [Yeh & Matzner 2012](#)). A more typical value for H II regions is $\log(q) = 7.5$, and we use these values as reference levels in this paper. In these models, the density is set by the pressure and temperature, through the parameter $\log(P/k)$, discussed in detail in Section 7.7 below. As a standard, we use $\log(P/k) = 5.0$. The local value of the electron density set in this way depends on both the $\log(P/k)$ value and the local electron temperature: the actual electron density is $n_e \sim 5 \text{ cm}^{-3}$.

The metallicity is usually expressed in terms of the total oxygen abundance, as oxygen is the most prominent heavy element measurable in the optical spectrum, and is the most abundant species in H II regions after hydrogen and helium. It is defined in terms of numerical values as $12 + \log(\text{O}/\text{H})$. An alternative method is to define metallicity in terms of solar abundances. Here (and in the Mappings models) we use the solar data from [Grevesse et al. \(2010\)](#). Metallicity is also sometimes described using the parameter Z , but this is also used as an abundance by mass, so we have not used it in this paper. A further point to note is that the oxygen abundance measured from optical spectra is the gas-phase abundance, and does not account for oxygen locked up in dust. In our models, we have assumed solar depletion levels in dust, resulting in a difference of 0.07 dex between total oxygen abundance and gas-phase abundance. See the detailed discussion in Section 7.9 below.

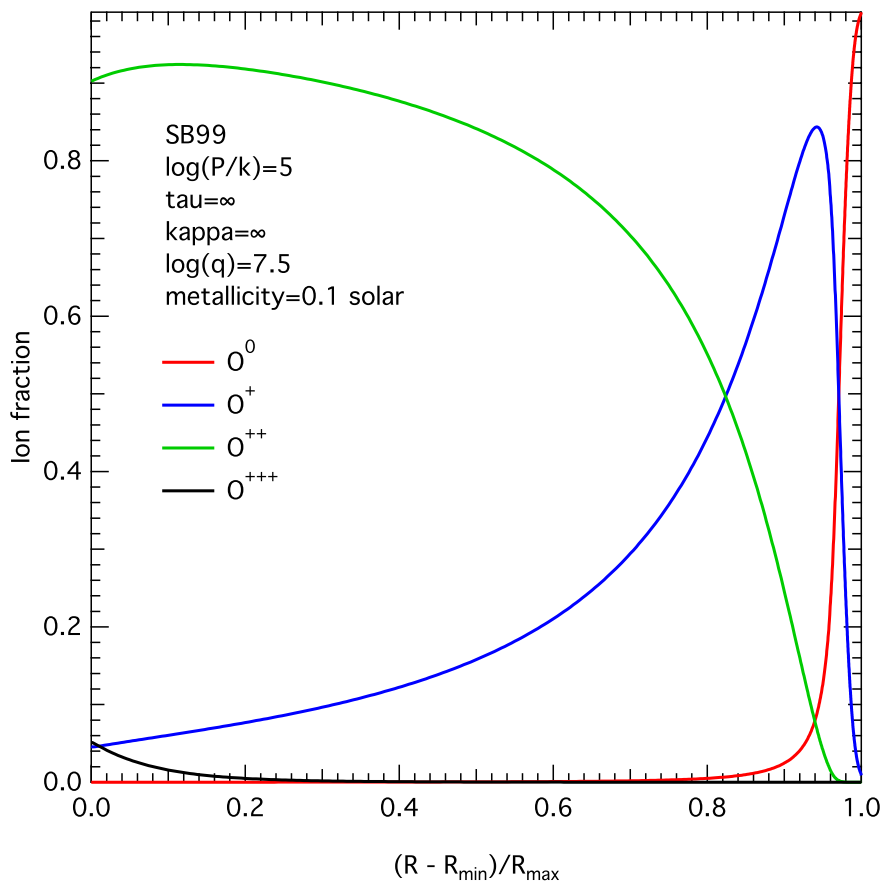


Figure 7.1 Ionic fractions for oxygen species versus radius from Mappings IV

7.3.4. Calculating the oxygen abundance

It is conventional to measure the apparent electron temperatures for O III from the 4363, 4958, and 5007Å lines, and for O II using the 3726/9 and 7320Å region lines. In the observations reported in [paper 1](#) (Chapter 6), however, we did not measure the NIR [O II] lines, nor the upper state [N II] lines which provide an alternative measure, so we have calculated $T_e(\text{O II})$ iteratively instead. A similar approach was taken by [Izotov et al. \(2006\)](#) for some of their data, and by [López-Sánchez et al. \(2012\)](#).

As we showed in [paper 1](#) (Chapter 6), the number density of O^{++} ions to hydrogen ions (i.e., the O^{++} abundance) can be expressed in terms of the flux ratio of O III(1D_2) to H_β ²,

$$\frac{n_{\text{O}^{++}}}{n_{\text{H}^+}} = \frac{\text{flux}(\text{OIII})}{\text{flux}(\text{H}_\beta)} \cdot g_1 \cdot \sqrt{T_e} \cdot \alpha_B^{\text{eff}}(\text{H}_\beta) \cdot \exp(E_{12}/(kT_e)) \times 115885.4/(E_{12} \cdot \Upsilon_{12}) \quad (7.1)$$

where T_e is the apparent electron temperature derived from the O III line ratio, for which there is a simple expression from [Nicholls et al. \(2013\)](#),

$$T_e = a (-\log_{10}(\mathcal{R}) - b)^{-c}, \quad (7.2)$$

where the flux ratio for [O III] is,

$$\mathcal{R} = \frac{j(\lambda 4363)}{j(\lambda 5007) + j(\lambda 4959)}, \quad (7.3)$$

and $a=13205$, $b=0.92506$, and $c=0.98062$. These parameters have been revised slightly from the earlier version, based on the latest outputs from the Mappings IV photoionisation code (version 4.12), but the electron temperatures are close to the earlier values. A similar equation accommodates the effects of the electron density (Equation (35), [Nicholls et al. 2013](#)).

Similarly, from [paper 1](#) (Chapter 6), the abundance of O^+ can be expressed in terms of the observed fluxes from the [O II] $\lambda 3726$ and $\lambda 3729$ lines,

$$\frac{n_{\text{O}^+}}{n_{\text{H}^+}} = \frac{\text{flux}(\text{OII})}{\text{flux}(\text{H}_\beta)} \cdot g_{1(\text{OII})} \cdot \sqrt{T_e} \cdot \alpha_B^{\text{eff}}(\text{H}_\beta) \cdot \exp(E_{12(\text{OII})}/(kT_e)) \times 115885.4/(E_{12(\text{OII})} \cdot \Upsilon_{12(\text{OII})}), \quad (7.4)$$

where, in this case, T_e is the apparent electron temperature derived from the [O II] ratio (see [Nicholls et al. 2013](#)) using the ratio of the 7320-30 Å lines to the 3726/9 Å lines. When the NIR lines are not available, it is possible to derive an expression for the [O II] electron temperature from the Mappings photoionisation models as a polynomial in terms of *total* oxygen gas-phase abundance,

$$T_e(\text{OII}) = T_e(\text{OIII}) \times (3.0794 - 0.086924 \zeta - 0.1053 \zeta^2 + 0.010225 \zeta^3) \quad (7.5)$$

where $\zeta = 12 + \log(\text{O}/\text{H})$.³ This equation is used iteratively, as discussed in [paper 1](#) (Chapter 6), starting by using the O^{++} abundance as the total oxygen abundance. This process converges

² T_e is the electron temperature, g_1 is the statistical weight of the transition ground state, k is the Boltzmann constant, Υ_{12} is the net effective collision strength for collisional excitations from the ground states to the upper state, E_{12} is the energy level of the upper state, and $\alpha_B^{\text{eff}}(\text{H}_\beta)$ is the effective emissivity for H_β .

³ Here we use ζ for the oxygen numerical abundance measured from spectra, to distinguish it from Z , the oxygen abundance by mass.

rapidly in five iterations or less. Garnett (1992) and López-Sánchez et al. (2012) have used a simpler approach, expressing the low ionisation zone temperature (effectively the [O II] temperature) in terms of the [O III] temperature, which does not require iteration.

Equation (7.6) shows the expression used by López-Sánchez et al. (2012):

$$T_e(\text{OII}) = T_e(\text{OIII}) + 450 - 70 \times \exp \left[(T_e(\text{OIII})/5000)^{1.22} \right] \quad (7.6)$$

Equation (7.6) gives total oxygen abundance values close to those from iterating Equation (7.5). Values determined for oxygen abundances are not exact, because of the nature of the approximations used, the calculated values for oxygen abundances depend on the photoionisation models used to build the models, and the use of a model derived from a single value of the ionisation parameter, q . We tested the two methods (Equations 7.5 and 7.6) against artificial data from Mappings, and find that they generate total oxygen abundances within 1% of the input values. The iterative approach (Equation (7.5)) is marginally the more consistent of the two over a range of ionisation parameter values. Using the polynomial and exponential fits to the parameters in these equations from paper 1 (Chapter 6) (Equations 6-9), we can calculate the total gas-phase oxygen abundance from the observed NUV [O II] and optical [O III] lines.

7.3.5. Limitations due to estimates of the [O II] temperatures and abundances

There are at least four sources of uncertainty in determining [O II] electron temperatures, and in general these are significantly less accurately measured than the [O III] electron temperatures. First, directly estimating the electron temperature requires measurements of the 3726,9Å and 7320,30Å lines in the ultraviolet and infrared, which are not always available in any given set of observations—the SDSS, for example, does not measure the UV lines unless they are redshifted into the spectroscopic passband. Second, both sets of lines are usually subject to signal-to-noise problems. Third, both Equations 7.5 and 7.6 depend on the model parameters used. The models themselves depend on the computed collision strengths. In the case of O II, there are several collision strength data sets (McLaughlin & Bell 1998; Pradhan et al. 2006; Tayal 2007; Kisielius et al. 2009) which are not in full agreement, resulting in slightly different calculated electron temperatures. These propagate into the estimation of O II abundance values, and thus into the total oxygen abundance. Finally, the electron temperature formula determined from single slab models varies with the ionisation parameter, $\log(q)$, which differs for each observed object. The observational problems for [O II] temperatures were also discussed by Kennicutt et al. (2003).

In this work, we have used the following sources: in Mappings IV we use the Tayal 2007 collision strengths; the generic [O II] electron temperature formula derived from single slab Mappings IV models used in Dopita et al. (2013); and the iterative method to calculate total oxygen abundance (Equation (7.5)). Uncertainties arising from the flux measurements remain the largest source of error.

7.3.6. Results from published data

Table 7.1 shows the data from paper 1 (Chapter 6) for 16 objects from the SIGRID sample for which oxygen abundances are available from both the direct T_e method (Equations 7.1, 7.4

above) and the strong line methods using the diagnostic grids from [Dopita et al. \(2013\)](#). We have used the diagnostic grids for $\log(N_{\text{II}}/S_{\text{II}})$ versus $\log(O_{\text{III}}/S_{\text{II}})$ and $\log(N_{\text{II}}/S_{\text{II}})$ versus $\log(O_{\text{III}}/H_{\beta})$ as they provide the most consistent results, as noted in [paper 1](#) (Chapter 6). Column 5 in Table 7.1 shows the difference between the direct and strong line methods. In general, the strong line methods give higher oxygen abundances, with a mean excess of 0.149 dex. This is consistent with the findings of [López-Sánchez et al. \(2012\)](#). The primary source of this difference is that the diagnostic grids we use here include the total oxygen content, that is, the gas-phase oxygen plus the oxygen incorporated in dust grains, whereas the direct method yields only the gas-phase oxygen. This contributes a difference of 0.07 dex, or half the observed amount. As we will show below, there are other sources contributing to the observed differences.

Table 7.1 Apparent electron temperatures, derived gas-phase oxygen abundances, strong line abundances and abundance differences for SIGRID objects, from [Nicholls et al. \(2014a\)](#) (Chapter 6)

Object	T_e (K) ¹	Direct	Strong Line ²	Delta ³
J0005-28	14719	7.847	8.012	0.165
J1152-02A	12248	8.151	8.088	-0.063
J1152-02B	12722	8.094	7.981	-0.113
J1225-06s2	16560	7.499	7.929	0.430
J1328+02	14846	7.867	8.132	0.265
J1403-27	14021	7.939	8.013	0.074
J1609-04(2)	10431	8.345	8.055	-0.290
J1609-04(5)	14234	7.959	8.137	0.178
J2039-63A	14383	7.966	8.087	0.121
J2039-63B	13982	7.894	8.145	0.251
J2234-04B	14029	7.897	8.110	0.213
J2242-06	13626	7.921	7.983	0.062
J2254-26	12870	8.090	—	—
J2311-42A	12582	8.091	8.176	0.085
J2311-42B	13451	8.011	8.122	0.111
J2349-22	13835	7.858	7.925	0.067

¹ T_e and $12+\log(O/H)$ values from [paper 1](#), Table 3

² Strong line values are the average of the new grids involving the $\log(N_{\text{II}}/S_{\text{II}})$ and $\log(N_{\text{II}}/O_{\text{II}})$ ratios, where available, from [paper 1](#), Table 4

³ Delta is the difference between columns 3 and 4.

7.4. The [O III] electron temperature–abundance relation

Figure 7.2 is a plot of the theoretical [O III] electron temperature versus oxygen abundance for Mappings isobaric model curves for $\log(q)=8.50$, $\kappa = \infty$, for optically thick nebulae, and an electron density of $\sim 7.5 \text{ cm}^{-3}$ ($\log(P/k)=5$). The figure shows the observational points derived from the SIGRID survey (yellow circles), selected SDSS DR3 data from ([Izotov et al. 2006](#), ; black circles), ([Izotov et al. 2012](#), ; small beige circles), and [López-Sánchez & Esteban \(2009\)](#), ; blue circles). Mean error bars for each sample are shown. Detailed error bars have been omitted for clarity, but are shown in [paper 1](#) (Chapter 6) and [Izotov et al. \(2006\)](#). The

effects of hydrogen optical depth, excitation sources, pressure, ionisation parameter, dust, and κ non-equilibrium electron distributions are discussed in detail in Sections 7.5 through 7.10 (below). While the uncertainties in the plotted values are larger than the detailed trends in the data, nonetheless, the data points provide a useful basis for examining the impact of different physical parameters on the behaviour of an H II region.

The 125 objects selected from the SDSS DR3 data in Izotov et al. (2006) exclude those with large uncertainties and those without flux data for the [O II] 3726 and 3729 Å lines, and oxygen abundances in the range for which the model curves apply: $7.32 < 12 + \log(\text{O}/\text{H}) < 8.69$. The data selected from Izotov et al. (2012) are those with error bars less than 15% of the measurements, and oxygen abundances in the range for which the model curves apply. The total gas-phase metallicities were calculated from the published data using the formulae in Equations 7.1 and 7.4. We found that the spread of values using these equations is less than the spread using the original formulae in Izotov et al. (2006), suggesting the new method may give more reliable results, or that using the observed [O II] 7320/30 Å fluxes is prone to higher uncertainty, as suggested by Kennicutt et al. (2003). Note that the horizontal axis is the gas-phase rather than the total (gas+dust) abundance, which differ by 0.07 dex.

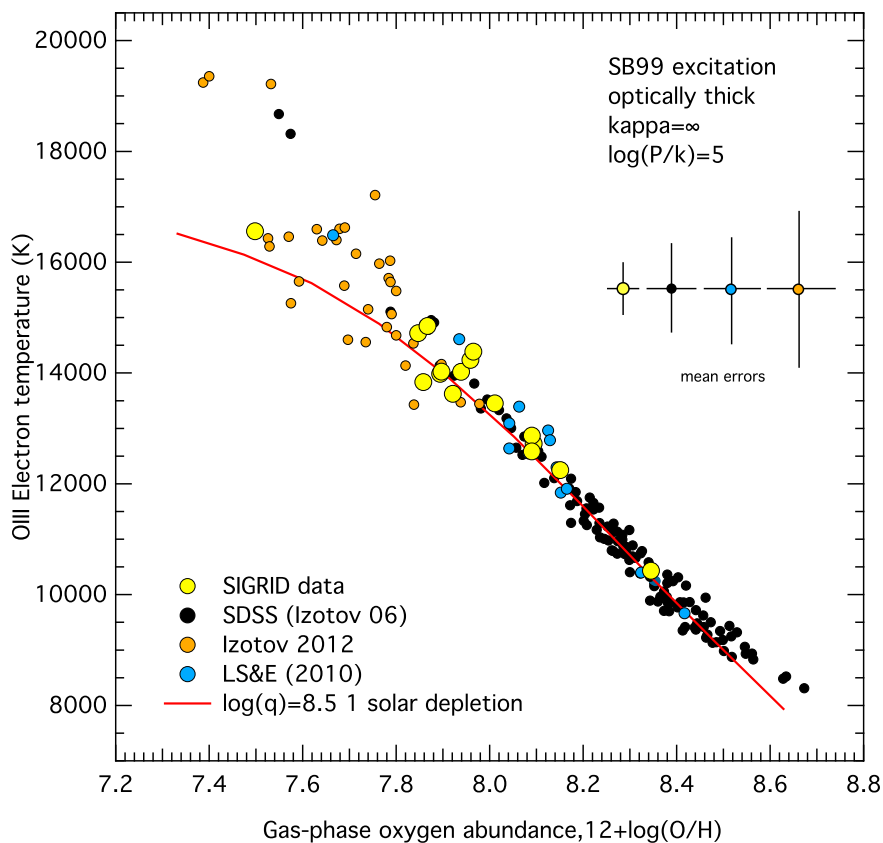


Figure 7.2 Observed apparent electron temperature versus gas-phase oxygen abundances from the SIGRID data (paper 1 (Chapter 6)), Izotov et al. (2006, 2012) and López-Sánchez & Esteban (2009), and Mappings photoionisation model curve (red) for $\log(q)=8.50$ (see the text).

The data from Izotov et al. (2006, 2012) were chosen because they are consistent sets of data from single observational sources. The sparse low metallicity coverage of the SDSS data is augmented using data from Izotov et al. (2012). The two sets cover the range from one-fiftieth solar to 1 solar. This spans the range covered by the models used, one-twentieth

solar to 1 solar. (The [Izotov et al. \(2006\)](#) data extends above 1 solar metallicity, but we have truncated the selection for comparing with the models.) Additional data from [López-Sánchez & Esteban \(2009, 2010\)](#) were also investigated. The results are nearly identical. Using their published line fluxes, there were 13 objects for which data was available to use the same methods to calculate T_e and $12+\log(\text{O}/\text{H})$ that we use here for the SIGRID and Izotov data. The results of these calculations exactly overlie the other data. The mean error bars shown were calculated from the flux errors in the original observations, propagated through the temperature and abundance calculations, and are somewhat larger than those reported in the source papers.

Figure 7.2 shows a remarkable fit of the Mappings model to the observed data (notwithstanding the size of the uncertainties), although the data points with lower oxygen abundances (< 8.0) tend to lie increasingly above the model curve with lower abundance. An analytical fit to the model curve is given in Equation (7.7), which applies for oxygen abundances in the range $7.4 < 12 + \log(\text{O}/\text{H}) < 8.7$. This equation provides a quick means of estimating abundance once the [O III] electron temperature has been measured.

$$\zeta = 1.0324 + 30.364 \times t_4 - 43.019 \times t_4^2 + 25.694 \times t_4^3 - 5.6791 \times t_4^4 \quad (7.7)$$

where $\zeta = 12 + \log(\text{O}/\text{H})$, $t_4 = T_e/10000$, with an average fit error in ζ of 0.004 dex. Note that this fit should not be used for extrapolation outside the model limits.

Figure 7.2 shows two SDSS data points at low abundance and high temperature from the [Izotov et al. \(2006\)](#) data. Both points refer to a single object (observed twice in SDSS), HS0837+4717. This is an extraordinary object, with very high nitrogen abundance, and the presence of over 100 WN stars in the central cluster ([Pustilnik et al. 2004](#); [Pérez-Montero et al. 2011](#)). The more recent IFU spectral analysis by Pérez-Montero gives a significantly lower apparent electron temperature than the SDSS observations, although it is still high (see Figure 7.4).

Figure 7.2 is key to exploring the factors influencing the behaviour of electron temperature with oxygen abundance, using the data from [Izotov et al. \(2006, 2012\)](#), [López-Sánchez & Esteban \(2009\)](#), and the SIGRID data from [paper 1](#) (Chapter 6) as guides to the actual behaviour of H II regions. In the figure, it is clear that the model suggests the electron temperature falls below a linear trend as the oxygen abundance decreases. This can be understood by considering the physical processes occurring in spherically symmetric “Strömgren sphere” H II regions. In the (innermost) region of highest excitation, the temperature is highest, but the volume is relatively small compared to cooler regions further from the excitation source. The observed fluxes are the volume-weighted averages. The larger volumes of cooler lower ionisation (outer) regions dilute the effect of the hotter inner regions. The net result is that for any particular excitation source there is a limit to the observed apparent electron temperature that can be reached in a spherical model, no matter how low the oxygen abundance, and this is lower than the temperature of the innermost ionised region. As a result, the apparent electron temperature would be expected to fall below a simple linear trend as oxygen abundance decreases, which is what our models show. The only variables are the slope of the trend at higher metallicities, and the maximum apparent electron temperature that can be reached. These geometric arguments apply to any H II region, although the detailed averaging processes in complex nebulae can only be approximated using simple

spherical models. This model also ignores other physical parameters that can increase the apparent electron temperature. It should be noted that in real H II regions or in models fitting such real regions, the “central” regions may well not be the hottest (See, for example [Stasińska 1978](#); [Stasińska et al. 2013](#); [Esteban et al. 2009](#)). However, for the purposes of this study which explores the effects of individual physical parameters, we use models that are by definition hottest at the centre.

This investigation was stimulated by the apparent inability of simple models to match the observed T_e –abundance data. The problem has been known for over a decade in the context of low-metallicity blue compact dwarf galaxies. It was explored by [Stasińska & Schaerer \(1999\)](#) in the context of the complex nebosity in I Zw 18. However, the mismatch is not confined to that object, but is generic to most low-metallicity H II regions. More recently, [Péquignot \(2008\)](#) modeled the complex structures in I Zw 18 and concluded that simpler models did not adequately account for small-scale gas density fluctuations, which can be important when the collisional excitation of hydrogen contributes significantly to the cooling of the gas. In this work, we have taken a different approach, in part because the structures in the H II regions we consider are not resolved. The Mappings code takes detailed account of all the excitation, ionisation, heating, and cooling mechanisms and the effects of dust, present in H II regions, and their complex interactions, rather than attempting to tailor a fit to individual objects. In this paper we use Mappings with a Strömgren Sphere model to explore separately the effects of several individual parameters. These include the optical depth of hydrogen in the nebula, the pressure/density, the ionisation parameter, the nature of the ionising radiation from the central star cluster, the effect of dust, and non-equilibrium κ electron energy distributions. All of these affect the shape of the model curves for apparent electron temperature versus oxygen abundance. We explore these effects and how well they fit the observations in the following sections.

7.5. The effect of optical depth at the Lyman limit

The first important parameter is the optical thickness (at the Lyman limit in hydrogen at 912Å) in the H II regions. In optically thin nebulae we find higher values for T_e at low metallicities than predicted for optically thick regions. We also identify parameters that might indicate optically thin H II regions. The question has been addressed by [Köppen \(1979\)](#) in the context of clumpy nebulae with optically thin condensations, and more recently by [Pellegrini et al. \(2012\)](#), who measured the optical depth of H II regions in the Magellanic Clouds.

With the present data, individual H II regions are not resolved as well as the nearby regions in the Magellanic Clouds, so a more general approach is necessary. Figure 7.3 shows three narrow-band images of the Rosette nebula (NGC 2237). The central star cluster and stellar wind evacuated central region are clearly visible in the [O III] and H α images. There is some suggestion that the area in the top left quadrant is optically thin, which lacks strong [S II] flux. An observer looking at this object from a distance sees some of the optical spectral lines arising from regions within the ionised region (optically thin), and some from regions where all the ionising photons from the central star cluster have been absorbed (optically thick). In our model nebulae, the brightness of the inner regions is significantly less than

from the outer regions, so that the net effect is to average over a range of optical depths, but skewed in favor of the brighter, optically thick regions.



Figure 7.3 5

007Å, H α , [S II] 6716/31 Å narrow band images.]Rosette Nebula (NGC 2237) H II region, in [O III] 5007Å, H α , [S II] 6716/31 Å narrow band images. The [O III] is predominantly in the inner zone and the [S II] in the outer zone. The central star cluster and stellar-wind-evacuated core are apparent in the [O III] and H α frames. There is also evidence of an optically thin region in the upper left quadrant, where the [S II] is not prominent. Image reproduced with permission from Steven Coates

(<http://coatesastrophotography.com>)

To illustrate the effect of an optically thin nebula, we use the Mappings code to generate the relation between observed apparent electron temperature and oxygen abundance, taking an extreme case where the optical depth, $\tau=1$. Figure 7.4 shows the same data as in Figure 7.2, with the addition of the $\tau=1$ model curve (dashed black), and the data from Pérez-Montero et al. (2011) for the extreme object (HS0837+4717). It is clear that this optically thin model ($\tau=1$ and $\log(P/k)=5$) is capable of explaining some (but not all) of the observed higher values of T_e in the observations.

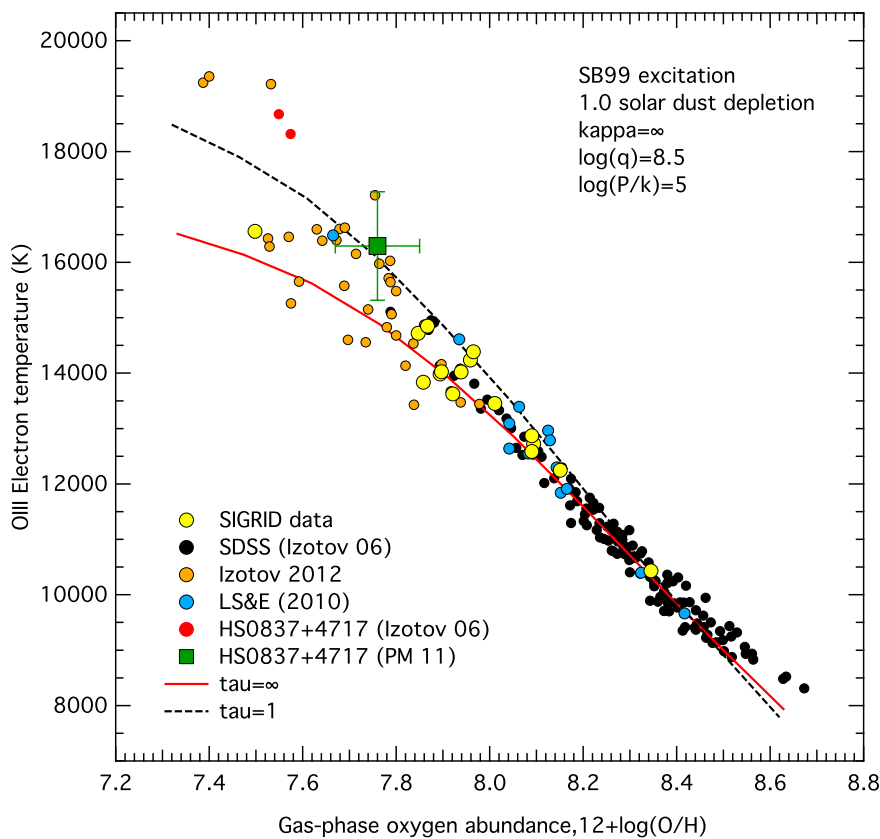


Figure 7.4 Observed apparent electron temperature versus oxygen abundance, with Mappings model curves for the optically thick and $\tau=1$ cases (see text). The red SDSS data points for the blue compact dwarf HS0837+4717 correspond to the more precisely measured data from Pérez-Montero et al. (2011, green square).

7.5.1. Nebular structure

Figure 7.5 shows the normalised fluxes of different ions as a function of radius, calculated using the Mappings IV.1.2 photoionisation code, with similar settings to Figure 7.1. The 4363Å line arising from the higher energy 1S_0 O III level is enhanced compared to the 5007Å line in the inner regions of the nebula where the electron temperature is higher, as shown by the T_e curve (black line). Similar diagrams have been published by other authors, for example, Figure 1 in Pellegrini et al. (2012)

It is worth noting that the curve in Figure 7.4 for low optical depth (dashed black) falls below the optically thick curve (red) with increasing metallicity. The physical origin of this cross-over is the nature of the thermal balance inside an H II region at different metallicities. At low metallicity, as shown by the black curve in Figure 7.5, the temperature decreases monotonically with increasing radius. Hydrogen and helium play the main role in absorbing high-energy photons from the central star cluster. They are more efficient at absorbing the softer photons, so the spectral energy distribution hardens with increasing radius, and some of the hard photons may leak out of the nebula. At higher metallicities, the heavier elements start to play an important role in the heating and cooling in the outer regions of the nebula. Due to their numerous energy levels, they are able to absorb the higher energy photons in the harder spectral energy distribution more efficiently than hydrogen and helium. This causes additional heating in the outer regions of the nebula, leading to a rise in temperature,

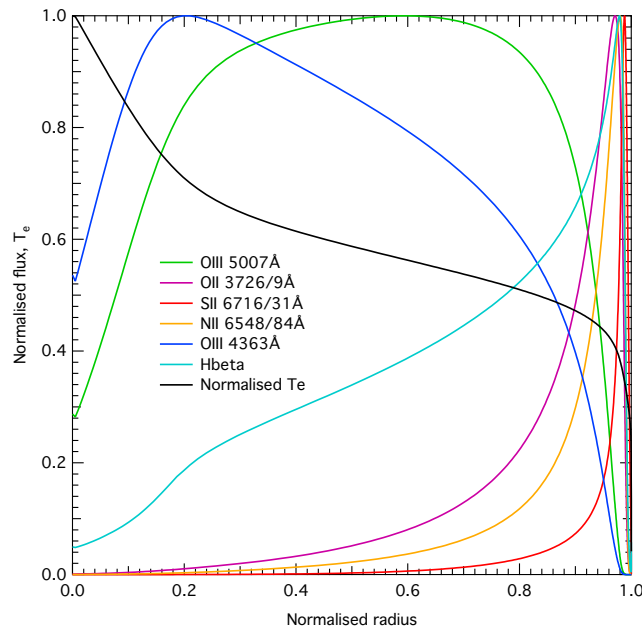


Figure 7.5 normalised fluxes and T_e , versus radius, low metallicity (0.1 solar)

as the heating and cooling processes balance and establish an equilibrium. Consequently, as the metallicity increases, the temperature curve shown in Figure 7.5 starts to flatten out, and can actually increase in the outer regions of the nebula at higher metallicities. For optically thin nebulae, the outer regions of the nebula are truncated, so the hotter outer zones are removed, and the apparent net temperature falls, leading to a greater decrease of apparent temperature at higher metallicity with decreasing optical depth, compared to the behaviour at lower metallicity. Consequently, the low optical depth curve falls away faster with increasing metallicity than the optically thick curve, as shown in Figure 7.4.

7.5.2. Optical depth diagnostics

Figure 7.5 shows how the majority of the [N II], [S II] and—to a slightly lesser extent—[O II] emissions are confined to the outer regions of the nebula. If the nebula is optically thin, the outer regions are truncated, and the total emissions from these outer species are substantially reduced, whereas the [O III] lines and $H\beta$ are emitted throughout the body of the nebula and are only gradually reduced by truncating the outer layers. This behaviour—the lack of bright [N II] and [S II] edges to H II regions—was used by Pellegrini et al. (2012) in analyzing the optical thickness of H II regions in the Magellanic Clouds. This suggests that spectral line ratios might be useful diagnostics of low optical depth in nebulae where the edges of H II regions are not well resolved. Candidate line ratios would be [O II]/[O III], [N II]/[O III] and [S II]/[O III].

Of these three opacity diagnostic options, the [S II]/[O III] ratio appears to be the most useful for several reasons. The [S II] lines are well resolved from the strong $H\alpha$ Balmer line. They are not subject to the nitrogen enrichment processes that cause an increasing spread in [N II] fluxes at low oxygen abundance. The [S II] lines are almost invariably present in the spectra of H II regions at good signal-to-noise ratios, and the [S II] emission region is more strongly concentrated at the lower excitation outer edges of an H II region than the [O II]. To

illustrate this diagnostic, Figure 7.6 shows $\log([\text{SII}]/[\text{OIII}]_{4959})$ versus oxygen abundance, for Mappings models of several values of optical depth and $\log(q)$, and the observed values of the SDSS objects from Izotov et al. (2006), the emission line galaxies from Izotov et al. (2012) and the SIGRID objects from paper 1 (Chapter 6)⁴.

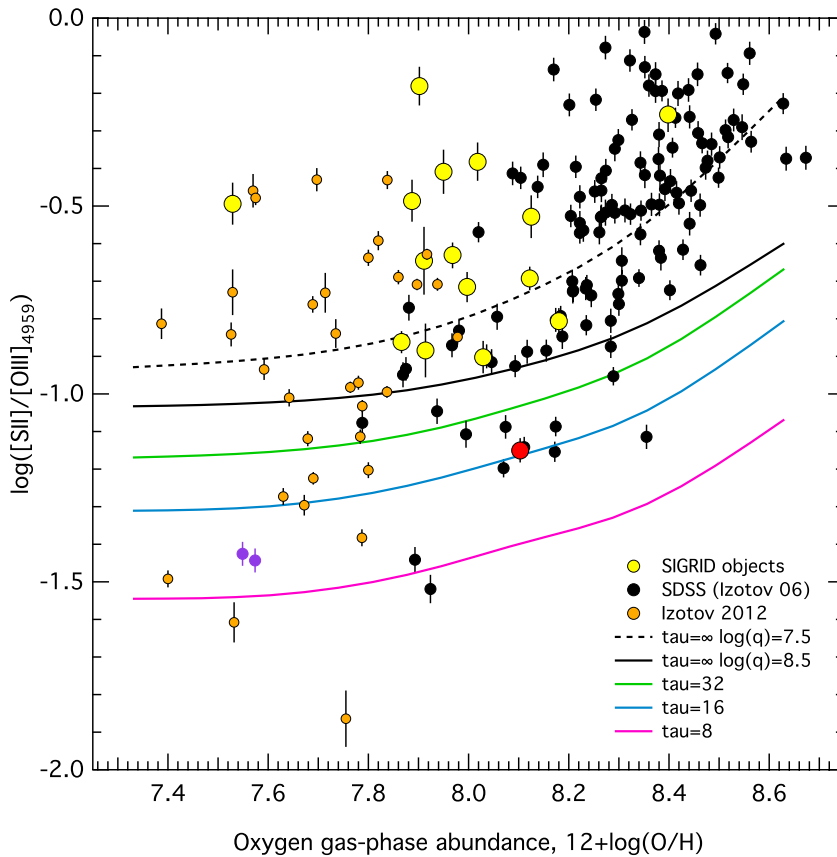


Figure 7.6 $\log([\text{SII}]/[\text{OIII}]_{4959})$ diagnostic for optical depth, comparing observations with model curves. Objects below the black solid line ($\log(q)=8.5$) are optically thin candidates, and those below the dashed black line ($\log(q)=7.5$) are probable candidates. The purple circles are the two SDSS observations of HS0837+4717 and the large red circle is the SIGRID object J2254–26.

It is evident that the majority of the observations fall above the optically thick line for $\log(q)=8.5$, and roughly half fall above the same curve for $\log(q)=7.5$, illustrating the interaction of the line ratio interpretations with the ionisation parameter. The error bars are all smaller than the separation of the model curves. Thus, it is not possible to distinguish between the effect of the ionisation parameter, $\log(q)$, and the optical thickness for borderline objects. However, it is also clear that more extreme objects can be identified, such as J2254–26 from the SIGRID list (red circle) and the SDSS double points for HS0837+4717 (purple circles) (Pellegrini et al. (2012) did not obtain fluxes for the S II lines due to its redshift). The scarcity of objects with optical depth $\tau < 8$ may be due to the flux weighting of the contributions from parts of the nebular with different optical depths, which is dominated by the brighter, more optically thick regions.

As a comparison, Figure 7.7 shows the same curves for $\log([\text{OII}]_{3727}/[\text{OIII}]_{4959})$. The theoretical curves for higher values of τ become degenerate, and while they show the same general

⁴We use the $[\text{O III}]_{4959}$ line in these calculations as the brighter $[\text{O III}]_{5007}$ line fluxes are not reported in Izotov et al. (2006).

trend, the diagram is not in complete agreement with the $\log([\text{SII}]/[\text{OIII}_{4959}])$ and implies lesser optical depth. Given the weighting from the brighter, thicker regions of the model nebula, it is likely that the $\log([\text{OII}]/[\text{OIII}])$ diagnostic underestimates the optical depth. The twin SDSS points for HS0837+4717 (purple circles), the datum for this object from Pellegrini et al. (2012), and SIGRID object J2254-26 (red circle) again stand out as optically thin. It is also worth noting that the model curves are derived from a simple Strömngren Sphere model, whereas the observed data arise from more complex structures.

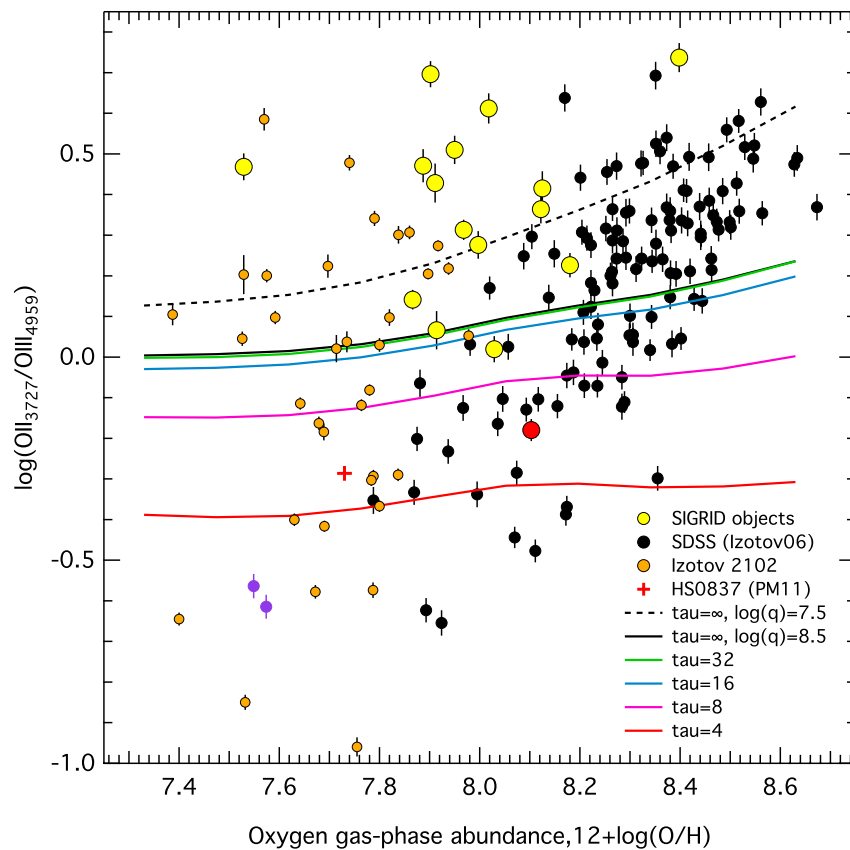


Figure 7.7 /

$[\text{OIII}]$) diagnostic for optical depth, comparing observations with model curves from Mappings.] $\log([\text{OII}]/[\text{OIII}])$ diagnostic for optical depth, comparing observations with model curves from Mappings. Objects below the black solid line are optically thin candidates. The red circle is SIGRID object J2254–26 and the purple circles are the SDSS observations for HS0837+4717.

7.5.3. Combining spectra from different optical depths

In real H II regions, the emitted spectra are likely to arise from regions with different optical depths. For distant objects where the individual regions are not resolved, the spectra are hybrid, combining spectra from a range of optical depths. Figure 7.8 shows the behaviour of the $[\text{O III}]$ apparent electron temperatures from these hybrid sources. The solid curves correspond to mixtures of spectra from optically thick regions with those from optically thin regions where $\tau=1$, in ratios between 1:8 and 8:1. The components of the composite spectra are weighted according to the H_{β} luminosity of each spectrum. In this diagram, the electron

temperatures computed from the combined spectra are normalised to the temperature curve for optically thick regions. All models are for $\kappa = \infty$ and $\log(\eta)=8.5$. Single optically thin regions with $\tau=1, 2,$ and 4 are shown (dashed lines) for comparison. The hybrid spectra give temperature/abundance curves that do not exactly match any single value of τ , but below an oxygen abundance of ~ 8.0 , the curve for $\tau=2$ corresponds quite closely to a mixture of 3.5:1 (thin to thick), and the curve for $\tau=4$ to a mixture of 1.5:1 (thin to thick). The cross-over point of the hybrid curves corresponds to that in Figure 7.4 and is the result of the changing fluxes with increasing metallicity as generated by the models, and the normalisation of the averaged T_e to the optically thick model.

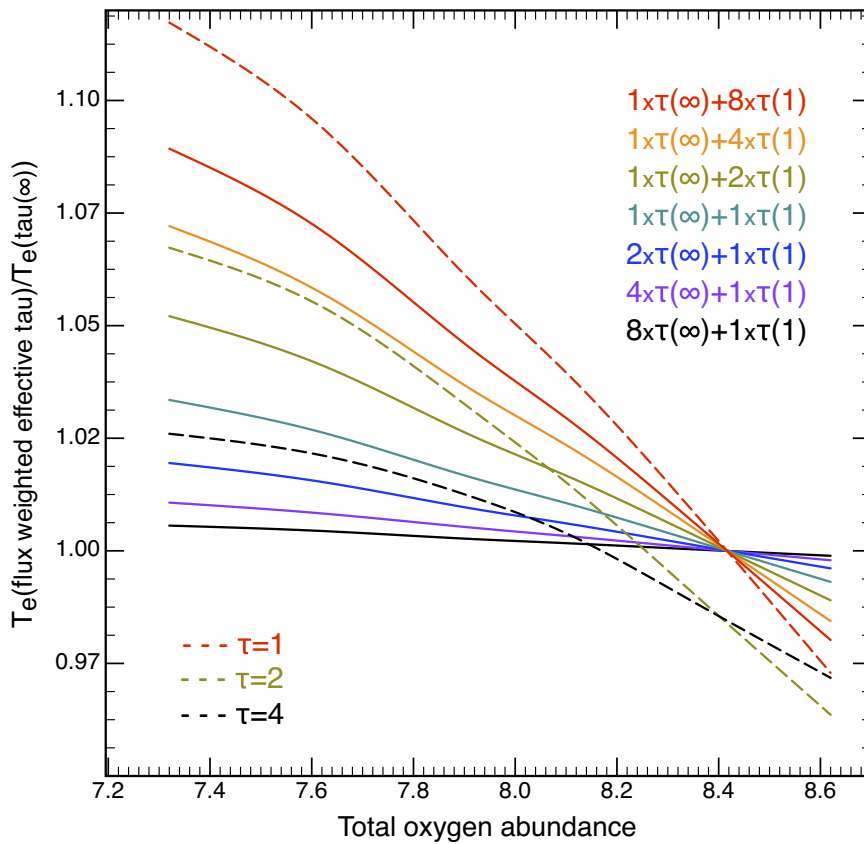


Figure 7.8 Effect of combining spectra from different optical depths. The cross-over point of the hybrid curves corresponds to that in Figure 7.4 and is the result of the changing fluxes with increasing metallicity as generated by the models, and the normalised T_e . See Section 7.5.1 for a detailed discussion.

7.6. Effect of the UV Spectral Energy Distribution

The Mappings models used here are calculated for an oxygen abundance range from 0.05 to 1.0 solar, based on the Starburst99 code from [Leitherer et al. \(1999\)](#), with a Salpeter initial mass function, $dN/dm \propto m^{-2.35}$, a lower mass cut-off at $0.1 M_{\odot}$ and an upper mass cut-off at $120 M_{\odot}$, with continuous star formation (described in [Dopita et al. 2000, 2013](#)). We use a stellar population of $10^6 M_{\odot}$ to avoid stochastic effects on the shape of the EUV continuum. The Starburst99 code does not provide good coverage for very low metallicities

and hot star clusters, so we have used a blackbodies at 50,000 K, 75,000 K and 100,000 K as high-temperature sources⁵. Figure 7.9 shows the Mappings model results for these sources, compared to the Starburst99 model source. It is evident that while high temperature excitation sources can generate higher apparent electron temperatures at low oxygen abundances, the overall fit to the observed data for blackbodies is not as good as the Starburst 99 model. However, for any particular object, such as HS0837+4717, a higher excitation source may well contribute to a higher apparent electron temperature. We have also explored the effect of single hot star models derived using the WMBasic code (Pauldrach et al. 2001, and related papers), with results very similar to the blackbody models.

A problem we face in exploring the effects of the central ionisation source is the lack of spectral energy distribution models at low metallicities. There are two important deficiencies. The first is the lack of evolutionary tracks for a range of massive low-metallicity stars. As a result, our models are limited to oxygen abundances at and above 0.05 solar. The second matter that needs attention, once we have adequate low-metallicity stellar models, is to build small-number statistical models for small star clusters likely to be found in small H II regions. The spread of nebular abundances at low metallicities (Figure 6, Tremonti et al. 2004) for a given stellar mass, and a similar spread in log(N/O) values (paper 1) for a given oxygen abundance, which exceed the uncertainties in many cases, suggest that stochastic effects are important in modelling stellar masses in small H II regions in small galaxies.

Even with appropriate low-metallicity stellar models, however, the energy distribution from the cluster exciting the H II region may not completely account for the excess [O III] 4363Å fluxes observed in low-metallicity nebulae. For example, Stasińska & Schaerer (1999) found that, even taking into account extreme ionising radiation sources, photoionisation models could not account for the 4363Å flux in I Zw 18. Our models are consistent with this conclusion.

⁵For this work, we used version 6 of Starburst99. Version, 7, just released, does include important new atmospheres (Leitherer et al. 2014; Leitherer 2014), but not yet at the metallicities we need to take this work to lower abundances.

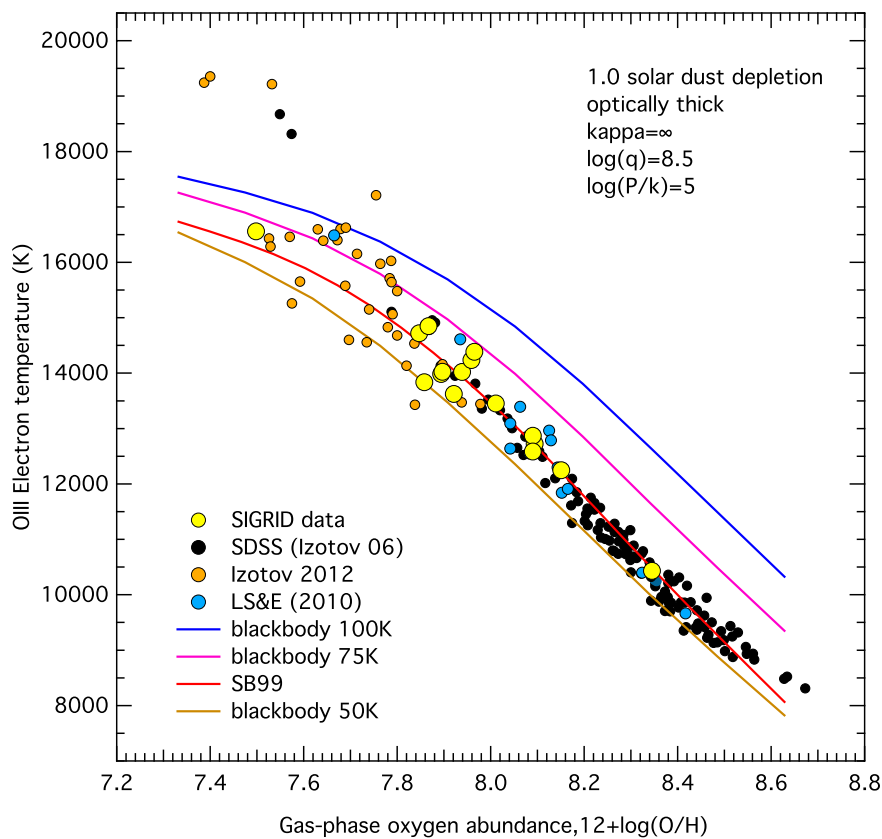


Figure 7.9 Mappings models using different excitation sources.

7.7. Pressure effects

The electron density, n_e , in an H II region can have important effects on the emitted spectrum. The parameter varies throughout the nebula, but it is useful to explore how setting a global value for the $n_e \times T_e$ affects the electron temperature measurements. In our Mappings simulations, we use an isobaric model (constant pressure) using the parameter P/k (where P is the pressure and k is the Boltzmann constant). $P/k = n_{tot} \times T_e$, where n_{tot} is the total particle number density, and $n_{tot} \approx n_e \times 2.07$ at low metallicities. Thus, for isobaric models, the product of the total number density and the electron temperature is constant. While the electron densities *per se* are not constant in these models, the $\log(P/k)$ values, together with the electron temperatures, set the electron densities, e.g., if the electron temperature is 10,000 K and $\log(P/k) = 6$, the electron density is $\sim 48.4 \text{ cm}^{-3}$.

Fixed pressure models are more physically realistic than fixed density (isochoric) models, in part because they allow the density to increase near the ionisation front. At typical temperatures and densities, the sound crossing time for an H II region is of the same order as the lifetime of the region, so, in general, pressures will equilibrate. In the Mappings code, for constant-pressure models, the density is a dependent parameter, set by P and T_e . The density structure emerges from the models, and the densities vary with the model. For low metallicity (one-twentieth solar) and $\log(P/k) = 5$, model hydrogen (ionised and neutral) number densities vary typically from 1.5 to 20 cm^{-3} at inner and outer zones. For higher metallicities (1 solar), hydrogen number densities vary from 5 to 290 cm^{-3} at inner and outer

zones. For $\log(P/k) = 6$, the comparable figures are 15 to 150 cm^{-3} and 40 to 1700 cm^{-3} .

Requiring the pressure to be fixed affects the ionisation parameter, $\log(q)$, and at higher densities, $\log(q)$ can increase significantly in the inner parts of the H II region, to $\log(q) > 9.3$ for an initial model setting (at the inner boundary of the H II region) of $\log(q) = 8.5$, and consequent significantly higher electron temperatures. Figure 7.10 shows the model results for pressures of $\log(P/k) = 5$ and 6, corresponding approximately to electron densities of 5 cm^{-3} and 50 cm^{-3} . These models use the same excitation sources as the other models in this work, and therefore the same number and energy distribution of ionising photons, except where stated, as in Section 7.6. The higher electron density SIGRID objects ($5 \text{ cm}^{-3} < \rho_e < 100 \text{ cm}^{-3}$), determined from the ratio of the 6716 and 6731 Å S II lines (paper 1) are shown in blue. They lie above the $\log(P/k) = 5$ model curve. It is clear that higher electron densities can explain some apparent electron temperatures above the standard ($\log(P/k) = 5$) curve, though not to the extent of the optically thin models. In particular, the measured electron density for the low abundance SIGRID object, J1225–06s2 is $< 10 \text{ cm}^{-3}$, so its position on the graph is most likely explained by it being optically thin.

The results for the object HS0837+4717 and several of the emission line galaxy data lie significantly above the model curves, which suggests that other factors such as optical thinness also contribute to generating higher apparent electron temperatures. This is shown in Figure 7.11, where the magenta curve takes into account both higher densities, corresponding to $\log(P/k) = 6$, and optical thickness $\tau = 1$. This is an extreme case, and indicates a likely upper limit for the apparent electron temperatures in the spherically symmetric model H II regions, assuming equilibrium electron energies. We will show later that higher electron densities affect the strong line diagnostic grids, and improve the fit to observed data.

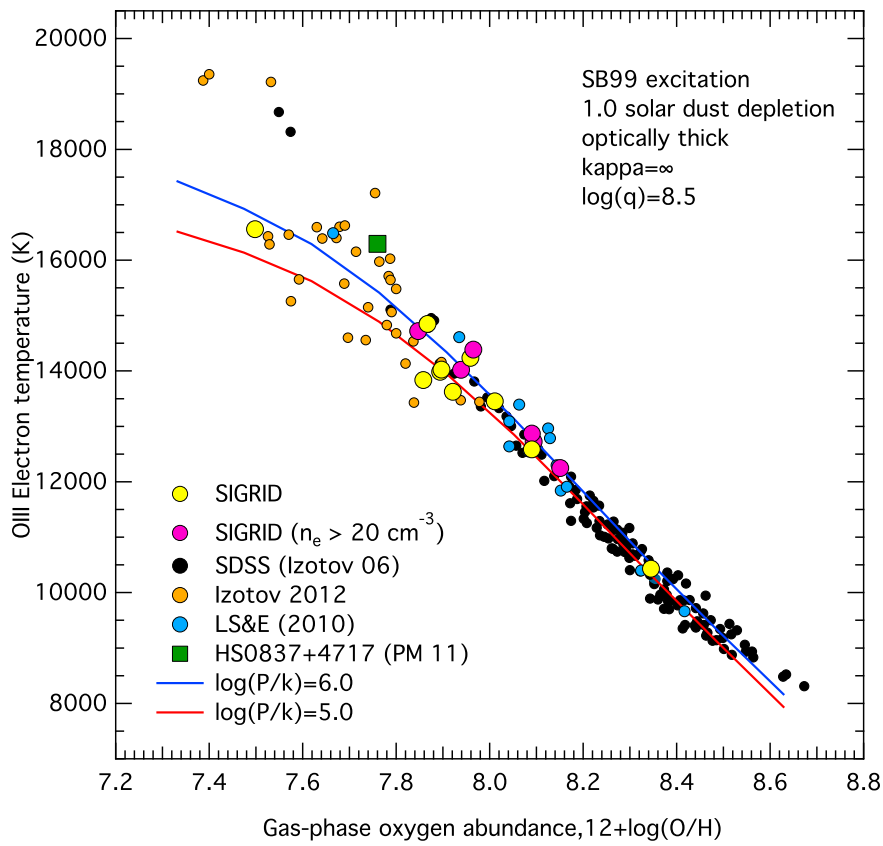


Figure 7.10 Mappings models using different electron densities. The SIGRID objects with measured electron densities $n_e > 20 \text{ cm}^{-3}$ are marked in magenta.

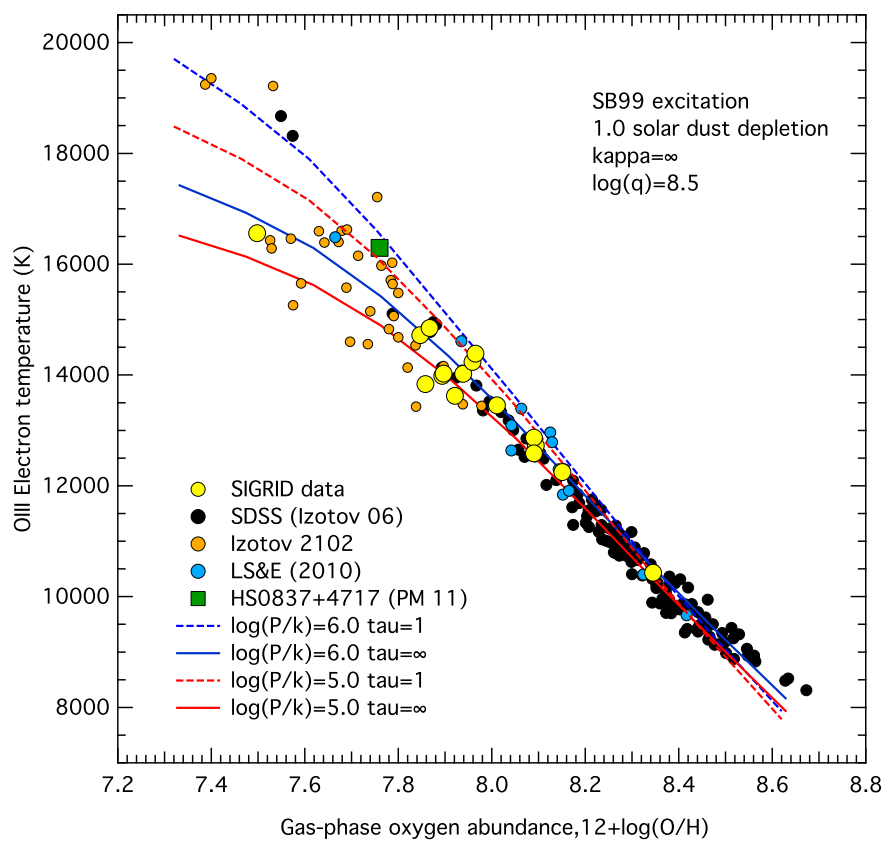


Figure 7.11 As for Figure 7.10, but showing optical thicknesses $\tau = \infty$ and 1. The optically thin higher pressure model can account for the observational data.

7.8. Effect of the ionisation parameter, q

The ionisation parameter q is the ratio of the number of ionising source photons passing through a unit volume to the neutral hydrogen density, as discussed in Section 7.3.3, above. The maximum value of q depends on the nature of the central star cluster and the size of the evacuated region, and thus on the strength of the stellar winds from the central cluster. The behaviour of the ionisation parameter, q , was analyzed in detail by [Dopita et al. \(2006\)](#). They found that q decreases as an ionising central star cluster ages: after 2 Myr, q decreases rapidly due to the decrease in ionising flux as massive stars evolve into red supergiants, and the increase in the mechanical energy due to the stellar winds of Wolf-Rayet stars. At ~ 3.5 Myr, supernova explosions contribute further to the internal pressure of the bubble. The ionisation parameter depends strongly on the chemical abundance, for two reasons. First, at higher abundance, the stellar winds have a higher opacity and absorb a greater fraction of the ionising photons, thus reducing q . Second, stellar atmospheric scattering of photospheric photons is more efficient at higher abundance, leading to more efficient conversion of luminous energy to mechanical energy at the source of the stellar winds, and leading to a reduction in q . [Dopita et al. \(2006\)](#) found that these factors lead to a dependence of q on oxygen abundance of $q \propto Z^{-0.8}$. This dependence of q on oxygen abundance is illustrated in Figure 7.12: the model curves at lower $\log(q)$ track the behaviour of the SDSS objects better as oxygen abundance increases. This trend was earlier noted for SDSS galaxies by [Dopita et al. \(2006\)](#) and for H II regions in general by [Dopita et al. \(2000\)](#).

A more realistic description (and the subject of future work) would be to plot a single curve where the $\log(q)$ value varies continuously with oxygen abundance. This would more accurately fit the observed data for $12+\log(\text{O}/\text{H}) \gtrsim 8.3$.

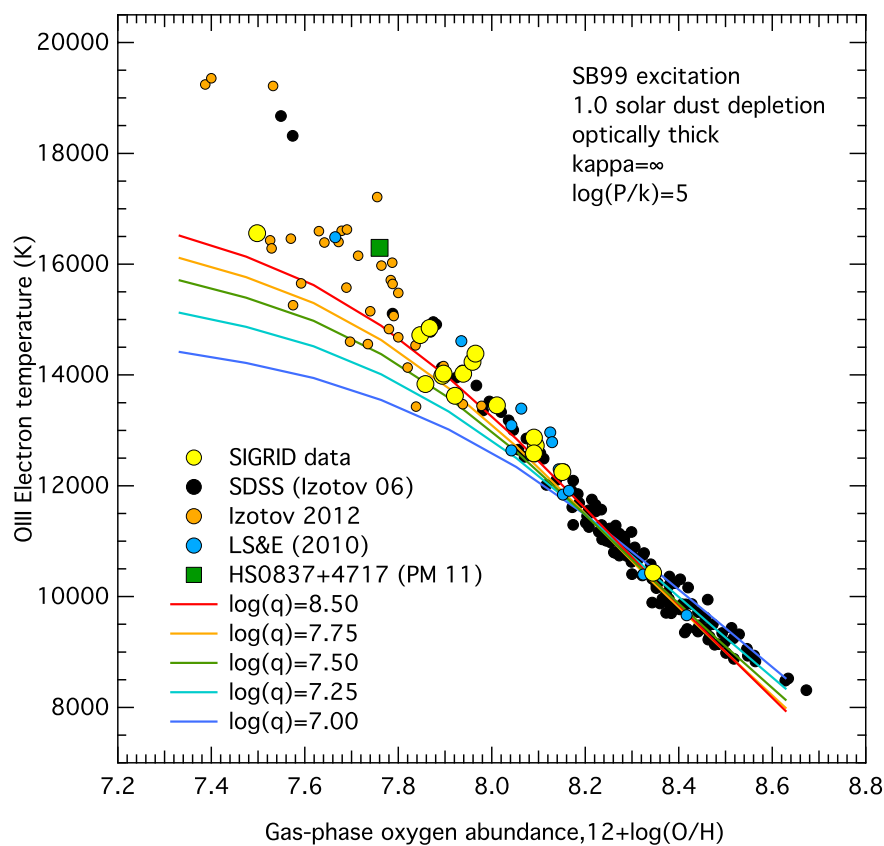


Figure 7.12 Mappings IV model curves for the [O III] electron temperature as a function of oxygen abundance, for a range of values of the ionisation parameter $\log(q)$. Lower values of $\log(q)$ track the observations better at higher oxygen abundances.

7.9. The effect of dust

As stars in galaxies evolve, older (asymptotic giant branch) stars, Wolf–Rayet stars, and supernova ejecta enrich the interstellar gas, and dust forms, locking up oxygen in silicates and carbonaceous grains. This dust is an important component of the molecular clouds where star clusters form that ionise new H II regions. Dust is important in the thermal balance of present day H II regions (see, e.g., [Dopita & Sutherland 2003](#)). [Dopcke et al. \(2011\)](#) find that dust cooling affects the fragmentation of very low-metallicity gas clouds and plays an important role in shaping the stellar initial mass function even at very low metallicities.

The amount of oxygen present in dust is not readily measurable from the optical spectra, but we estimate it here at $\sim 15\%$ of the total. This corresponds to a contribution from dust to the total oxygen abundance of 0.07 dex. In this work, we calculate the fraction of other elements in dust grains with respect to oxygen using the abundance ratios from the solar data from [Grevesse et al. \(2010\)](#). This is discussed in detail in [Dopita et al. \(2013\)](#).

The nature of the dust in H II regions is poorly understood. [van Hoof et al. \(2004\)](#) studied the effects of dust grain size on the observed features of H II regions, using models based on the CLOUDY spectral synthesis code. They found that grain size can have a significant effect on the emitted spectrum. Unlike the CLOUDY code, Mappings fully resolves the

grain charge for all the grain sizes.⁶ Further, [Groves et al. \(2004\)](#) noted that several of the observable properties of dust can be equally well reproduced by different theoretical grain size distributions and compositions. Thus, the observable properties of dust are not especially sensitive to dust grain sizes, but the question obviously requires more work. As a consequence, Mappings uses the simplest grain composition and grain size distribution model that is consistent with the known properties of the dust in the solar neighbourhood, adopting the dust grain size power law model from [Mathis et al. \(1977\)](#). In Mappings, the atomic depletion in dust is consistent with amount of dust formed.

Further, the amount of dust in a galaxy is quite variable. [Rémy-Ruyer et al. \(2014\)](#) found that there is a large scatter in the gas-to-dust ratio in star-forming galaxies over a 2-dex range of metallicities. From FIR Herschel measurements, [Fisher et al. \(2014\)](#) suggest that dust may be rarer in low-metallicity galaxies than previously thought, due to the lack of heavier elements in low-metallicity environments and dust destruction occurring in active star forming regions. The latter is suggested by the presence of [Fe III] lines in the spectra of several of the observational data discussed here. In either case, the oxygen abundance measured from optical spectra is the gas-phase oxygen abundance and provides a lower limit for total oxygen. As our models use the total oxygen abundance, the model curves plotted in this paper have had the computed dust-phase oxygen subtracted to permit comparison with the spectral data (a reduction of 0.07 dex in abundance). Dust is also not uniformly distributed in real nebulae, but in the models we present here, we assume that it is sufficiently uniform to allow us to account for the dust physics with a uniform model.

Figure 7.13 shows the plot from Figure 7.2, with additional curves for dust-free models. Dust depletion appears to cause a small reduction in [O III] electron temperature between one-twentieth and one-fifth solar metallicity, but the net effect is not large.

⁶The energy of photoelectrons emitted by dust grains depends on the charge of the grain. In addition to the work function absorbing the photoionising energy, the grain charge creates a potential barrier that affects the energy available to the ejected electron, which is then available to heat the surrounding medium. The stronger the initial positive charge of the grain, the less the available heating from the ejected electron. The grain potential is a function of grain size, as their absorption spectrum changes with grain size (e.g. [Draine & Lee 1984](#)) so to compute the photoelectric heating due to dust, a spectrum of grain sizes needs to be calculated and integrated to give the heating. A single average grain size does not replicate this.

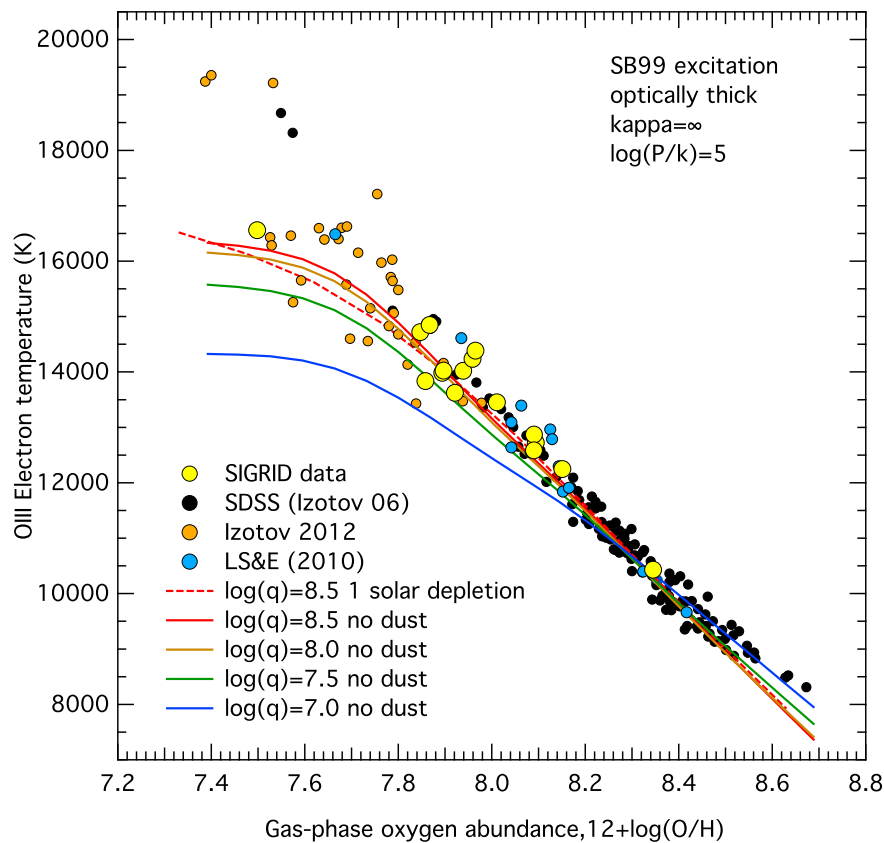


Figure 7.13 Observed [O III] electron temperature versus gas-phase oxygen abundances, and Mappings photoionisation model curves with 1 solar depletion dust, and no dust, for a range of $\log(q)$.

7.10. Effect of non-equilibrium κ electron energy distributions

The effects of non-equilibrium electron energy distributions in H II regions were explored by Nicholls et al. (2012, 2013). The current version of the Mappings photoionisation code can calculate the effect of κ electron energies (Dopita et al. 2013). κ -distributions have a high-energy power law tail and can readily affect the apparent electron temperature. They can be generated by Alfvén waves, magnetic re-connection, shocks, super-thermal atom or ion heating (as in a stellar wind H II region interaction zone), or by fast primary electrons produced by photoionisation with X-ray or EUV photons. These are all sources of long-range injection of high-energy electrons, distinct from the normal UV photoionisation effects from central star clusters.

Figure 7.14 shows the result of Mappings models for κ values of 4, 6, 10, 20, 50 and infinity (equilibrium), with model curves plotted for total oxygen abundances between one-twentieth and 1 solar⁷. At values of $\kappa > 10$ (i.e., close to Maxwell-Boltzmann equilibrium), the effects are more obvious for higher metallicities, but for lower, more extreme departures from equilibrium, these electron energy distributions appear capable of describing the excess flux of [O III] 4363Å observed in objects with low oxygen abundance. As before, we limit the plotted observations to those with apparent electron temperatures < 20,000 K, and

⁷The temperatures and oxygen abundances plotted are the values that one obtains by assuming emission line fluxes from a Maxwell-Boltzmann equilibrium energy distribution (Nicholls et al. 2012)

oxygen abundance $>$ one-twentieth solar, consistent with the limits to the model ranges. It is evident that appropriate values of κ can describe the apparent electron temperature behaviour, and at face value, κ electron energies are an alternative explanation to optically thin nebulae at higher pressures.

However, two important questions arise in interpreting Figure 7.14. First, can such extreme departures from thermal equilibrium occur in H II regions? At present the only direct measurements we have as guides are from solar system plasmas. κ energy distributions appear almost universally in solar system plasmas, from the solar wind, through planetary magnetospheres, to the heliosheath. In particular, proton energy distributions where $1.6 \lesssim \kappa < 2.5$ are observed directly in the heliosheath (Livadiotis & McComas 2011, 2012; Livadiotis et al. 2011). Using entropy considerations based on Tsallis q -nonextensive statistics (Tsallis 2009), these authors argue that stable states can exist that are significantly out of equilibrium. If the entropy-based arguments hold, it is possible that stable extreme κ electron energy distributions occur in H II regions.

The second question, if κ electron energy distributions are present, is, why does the effect of more extreme distributions start to appear at oxygen abundances below 0.15 solar ($12 + \log(\text{O}/\text{H}) \sim 7.8$)? Figure 7.14 suggests that the departure from the equilibrium model (bottom, red) curve commences (for some but not all objects) at this oxygen abundance. If this departure is caused, or contributed to in significant part, by extreme κ distributions, there are evidently physical phenomena affecting the generation of κ distributions that come into play at lower metallicities that are less important at higher metallicities. One may speculate on two possible causes. The first is some form of “quenching” of kappa distributions at higher metallicities. This may not be correct if the conclusions of Dopita et al. (2013) are correct, where they find that values of $\kappa \sim 20$ explain the behaviour of electron temperature for observed data at higher metallicities, > 1 solar. This would imply the presence of κ electrons at higher metallicities. Values of $\kappa \sim 50$ may also explain the trend in electron temperatures for $12 + \log(\text{O}/\text{H}) \gtrsim 8.4$.

A second possibility is if there are excitation mechanisms present in the stellar winds around low-metallicity H II region star clusters that are less prevalent in stellar winds at higher metallicities. With our current limited knowledge of the physics of low-metallicity O- and B-star winds, we can say no more than that this explanation is plausible.

Finally, if κ distributions are present in parts of H II regions, the effect on the spectrum of averaging over the whole H II region, such as we have with the observed data here, may dilute the observed non-equilibrium effects. The spatial variation in κ distributions, if present, is likely to be more obvious in nearby H II regions, where individual structures in the nebulae can be distinguished.

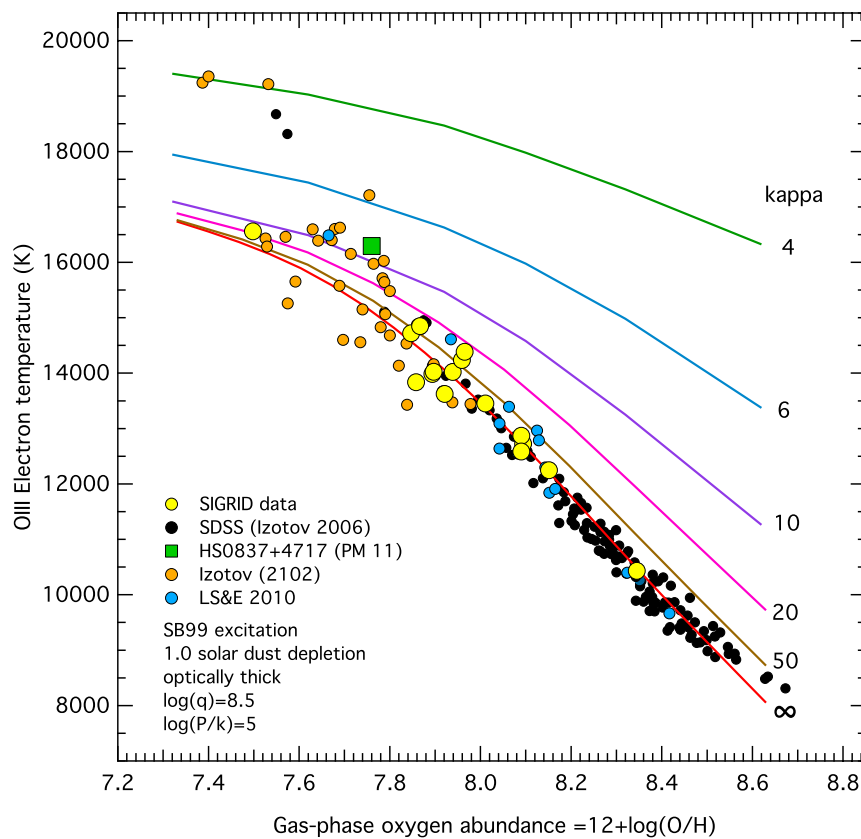


Figure 7.14 Mappings models using different κ electron energy distributions.

7.11. Summary of factors affecting the measurement of apparent electron temperature

Using the Mappings photoionisation code and a three-dimensional Strömgen Sphere model, we find that the ‘standard’ equilibrium model ($\log(q) = 8.5$, $\tau = \infty$, $\kappa = \infty$, Figure 7.2 and Equation (7.7)) does a good job of fitting the majority of the observational data points for oxygen abundances $>$ one-fifth solar. There are a number of parameters that can be used to explain divergences in temperature from the equilibrium model for lower metallicities. Higher temperature objects that lie above the ‘standard’ curve can be explained by electron density variations, higher energy excitation sources, dust, optically thin nebulae, and non-equilibrium κ electron energy distributions. Low optical depth appears to make an important contribution, and its contribution can be confirmed using diagnostics such as the $[\text{SII}]/[\text{OIII}]$ line ratio (Figure 7.6). Electron densities and high-energy excitation sources also contribute to higher electron temperatures. Dust does not appear to make a major contribution, if it is uniformly distributed. There is a considerable degree of degeneracy between these factors, but the equilibrium model ‘standard’ curve provides a reliable first order basis for determining total oxygen gas-phase abundance for a given measured O III apparent electron temperature, above one-fifteenth solar abundance. The error bars on the data are in some places larger than the trends the data exhibit, but the trends nonetheless illustrate the effects of the physical parameters we have discussed. For oxygen abundances below one-fifteenth solar in the spherical H II region model, high apparent

electron temperatures can be explained by non-equilibrium electron energy distributions, or a combination of higher pressure and low optical depth. The former requires the additional explanation of why its effects are only apparent for oxygen abundances below 0.15 solar.

Finally, the photoionisation model assumptions are important. Mappings is a comprehensive modelling system, which uses the current best available atomic data. The code has been revised in a few key areas since the earlier paper (Dopita et al. 2013) to give more consistent results (see the Appendix), but the numerical results are not substantially changed, with the exception of somewhat higher [O III] apparent electron temperatures at low oxygen abundance ($+\sim 500\text{K}$)⁸. The formulae used here and in paper 1 (Chapter 6) are those derived from the earlier paper. Errors arising from collision strength uncertainties may amount to a difference in gas-phase oxygen abundance of $\sim \pm 0.03$, leading to uncertainties in the model curves that are within the published uncertainties in the data. The most significant unknown is how well a symmetric Strömgren Sphere model is able to replicate the behaviour of real H II regions. We plan to explore this further.

7.12. Diagnostic grids

7.12.1. Two-dimensional grids for different densities and Lyman limit optical depths

The convention in strong line methods is to plot observed data values on a two-dimensional grid of line ratios that will allow measurement of metallicities (e.g., Kewley & Dopita 2002; Kewley & Ellison 2008). Dopita et al. (2013) presented new diagnostic strong line grids computed using the Mappings code, for a range of values of oxygen abundance, $12+\log(\text{O}/\text{H})$, the ionisation parameter, $\log(q)$, and the non-equilibrium energy distribution parameter, κ , for optically thick nebulae at low density. As shown in paper 1 (Chapter 6), some of the SIGRID data points did not fit on these standard diagnostic grids, meaning it was not possible to use the grids to measure abundances and ionisation parameters. This led us to ask if some variation in the grids would permit the measurement of $12+\log(\text{O}/\text{H})$ and $\log(q)$ for objects that did not fit on the standard grids. Fortunately, it is a simple matter to compute grids with different physical parameters. Here we present grids for higher pressure ($\log(P/k)=6$) than the earlier published grids, and a range of values of the optical depth, τ and the non-equilibrium energy parameter, κ .

Figure 7.15 compares two diagnostic grids, $\log([\text{O III}]/\text{H}\beta)$ versus $\log([\text{N II}]/\text{H}\alpha)$ (upper row), and $\log([\text{O III}]/\text{H}\beta)$ versus $\log(\text{N II}/\text{S II})$ (lower row) for the standard lower pressure (and thus density) case ($\log(P/k)=5$, left column), and at higher pressure ($\log(P/k)=6$, right column). All but one SIGRID object can be accommodated on the grids for $\log(P/k)=6$. This is consistent with Figure 7.10, where the higher density objects tend to lie above the standard T_e versus $12+\log(\text{O}/\text{H})$ curve. The grids give similar values for oxygen abundance for either value of $\log(P/k)$ for each observation, but the higher $\log(P/k)$ set give slightly lower values for $\log(q)$. This can be understood from Figures 7.10 and 7.12—the boost in $\log(P/k)$ is compensated for by a drop in $\log(q)$, which brings down the $\log(q)$ values for outliers onto the diagnostic grid.

⁸We plan to make Mappings IV available as a web page application for real-time use in the near future.

Figure 7.15 also shows two additional data sets. The red points, from Izotov et al. (2006), show scatter, probably caused by measurement uncertainties. The abundance values between the two sets of grids (upper and lower rows) are also somewhat discrepant. This is most likely due to uncertainties in the measurements, the de-reddening, and in the collision strength data used to create the grids. However, the abundances are in general much more consistent than the older strong line methods. Of the two diagnostics, the lower row is least susceptible to de-reddening errors and is the more reliable, as well as avoiding the degeneracy apparent in the upper row for higher ionisation parameters and abundances.

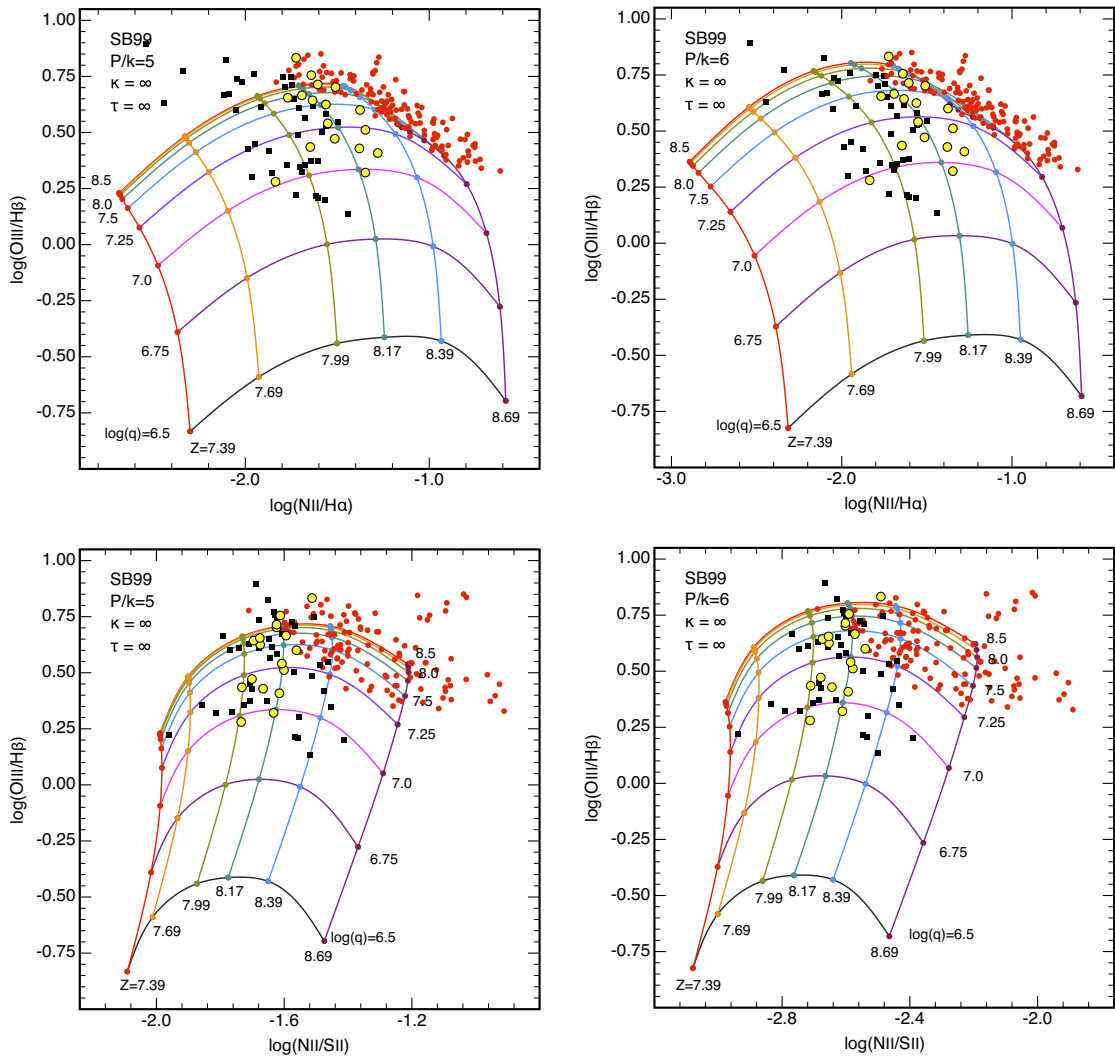


Figure 7.15 Observational data (SIGRID, yellow; Izotov et al. (2006), red; and Izotov et al. (2012), black) plotted on diagnostic grids for $\log(\text{OIII}/\text{H}\beta)$ versus $\log(\text{NII}/\text{H}\alpha)$, upper row, and $\log(\text{OIII}/\text{H}\beta)$ versus $\log(\text{NII}/\text{SII})$, lower row, for low density, $\log(P/k)=5$ (left column) and higher density, $\log(P/k)=6$ (right column). The error bars for the SIGRID objects are given in Figures 10 and 12 of [paper 1](#) (Chapter 6). The errors involving $[\text{NII}]$ fluxes are significantly greater than those for $[\text{OIII}]$. They have been omitted here to aid clarity.

Figure 7.16 shows the grids for $\log(P/k) = 6$ (as in Figure 7.15, upper right panel) with additional curves for a range of optical depths (left panel), and a range of values of κ (right panel). It suggests that lower optical depths offer some explanation for the off-grid data points, whereas grids involving lower κ values do not significantly improve the fit of the

observations onto the grids. In both cases, the τ - and κ -extended grids roll away from the data points, in the case of κ , very rapidly, so that this diagnostic plot is degenerate for κ . So κ does not provide information that will allow us to evaluate $12+\log(\text{O}/\text{H})$ or $\log(q)$ for points initially off the grid. Both panels suggest three-dimensional shapes for the grids, and that plotting three diagnostic ratios on three orthogonal axes may provide new information. We explore this below.

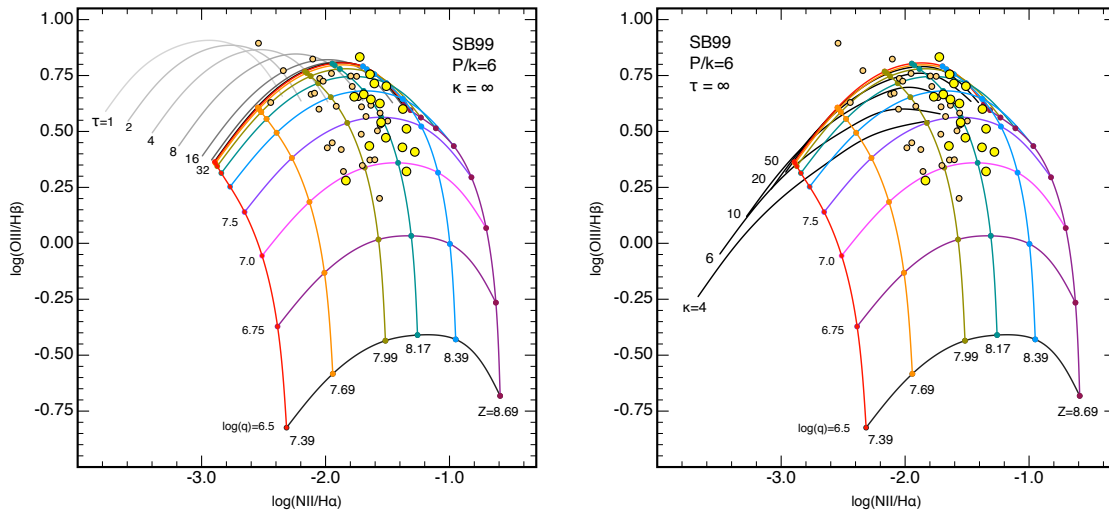


Figure 7.16 SIGRID data plotted on diagnostic grids for $\log(\text{O III}/\text{H}\beta)$ versus $\log(\text{N II}/\text{H}\alpha)$, overlaid with plots for a range of values of optical thickness, $\tau=1, 2, 4, 8, 16, 32$ at $\log(q)=8.5$ (left pane), and for $\kappa=4, 6, 10, 20, 50$ at $\log(q)=8.5$. The latter curves fold behind the basic plot.

7.13. Investigating three-dimensional diagnostic graphs

The three-dimensional nature of the diagnostics is suggested in the two-dimensional grids, particularly in Figure 7.16. This invites us to plot three-dimensional figures to explore the possibility further. Plotting and manipulation of three-dimensional graphs is not simple. Vogt et al. (in press) have used Python routines to generate two-dimensional projections of three-dimensional graphs for high metallicity objects from the SDSS data, allowing them to separate H II regions from AGNs and LINERs. For this work we have used the GRAF application written for OS X by one of the present authors (R.S.S.), which provides a particularly flexible tool for investigating the three-dimensionality of the diagnostics, although we have not yet used it to generate 3-D PDF files.⁹

Figure 7.17 shows the outcome of this three-dimensional manipulation. We have combined three diagnostic ratios for $\log(\text{N II}/\text{H}\alpha)$, $\log(\text{O III}/\text{H}\beta)$ and $\log(\text{N II}/\text{S II})$ on the x, y and z axes respectively, and have rotated these about the y -axis to compare the location of the observational data with respect to the diagnostic curves.

The main grid in both panels is for a range of oxygen abundance between one-twentieth solar and 1 solar, and a range of ionisation parameters between 6.5 and 8.5 (log), for $\log(P/k)$

⁹Three-dimensional projected diagrams displayed here were prepared using GRAF 4.7.3 (OS X) software authored by R.S.S., available as (unsupported) beta software at <http://miocene.anu.edu.au/graf/>

$= 6$, $\kappa = \infty$ and $\tau = \infty$. The additional free-standing arcs are the grid lines for the same abundance range and P/k , for $\log(q) = 8.5$, for $\kappa = \infty$ and $\tau = 8, 16, 32$ and 64 (left panel); and for $\tau = \infty$ and $\kappa = 6, 10, 20$ and 50 (right panel). We have only plotted the highest value of $\log(q)$ for the non-equilibrium and optically thin cases, to make the plots easier to read.

The data from SIGRID observations and from [Izotov et al. \(2012\)](#) are plotted over these curves. It is evident that the observational data are described better by the left panel (optically thin and equilibrium energies) than by the right (optically thick and κ electron energies). This illustrates how three-dimensional diagnostics may be used to discriminate between two otherwise alternative two-dimensional descriptions.

While these results are preliminary in nature, they demonstrate the utility of three-dimensional manipulation of three sets of diagnostic ratios in augmenting the standard two-dimensional grids, to show which parameters can be used to fit the observations better to the grids. Although we have not been able to demonstrate this in the present paper, manually rotating the diagrams shows that the location of several of the observed data points are better described by optically thin diagnostic grids than by the non-equilibrium grids.

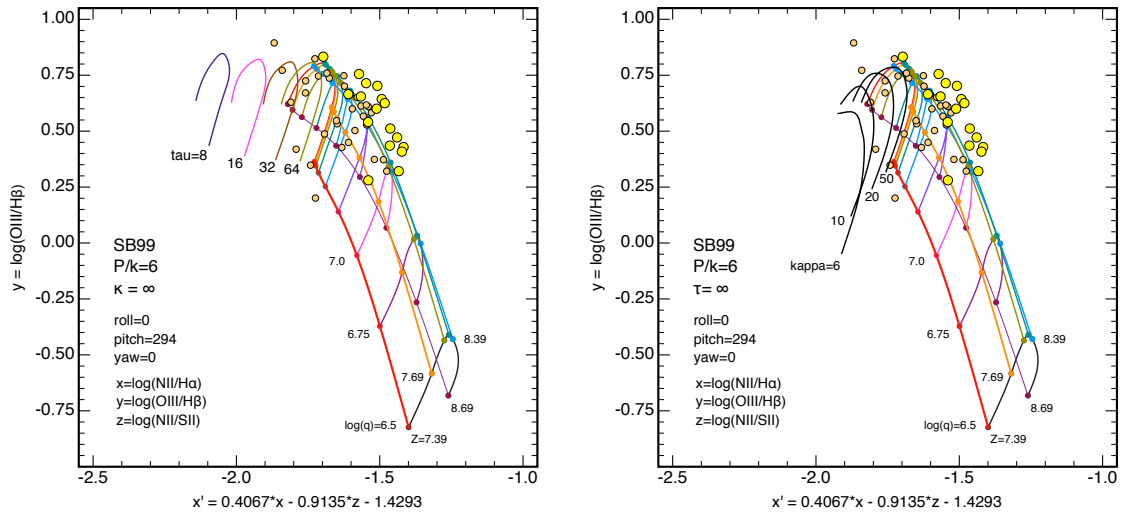


Figure 7.17 Left Panel: Three-dimensional projection of $\log(N_{\text{II}}/H\alpha)$ and $\log(N_{\text{II}}/S_{\text{II}})$ versus $\log(O_{\text{III}}/H\beta)$ diagnostic grids (Figures 7.15, 7.16, with $\log(P/k) = 6$), rotated about the y -axis as indicated, showing the optically thick equilibrium diagnostic grids with the $\log(q) = 8.50$ grid lines for four values of the H I optical depth, τ . Right Panel: Similar grids, but with the $\log(q) = 8.5$ grid lines for four values of the non-equilibrium parameter κ . Both figures show the data for the SIGRID objects (larger circles) and from [Izotov et al. \(2012\)](#) (smaller circles).

7.14. Discussion

Measured $[O_{\text{III}}]$ electron temperatures reported in the literature using simple analysis techniques only provide general guides to the physical conditions in an H II region. No H II region is thermally uniform, so temperatures measured from the emitted spectra can only be a volume- and intensity-weighted average of the internal conditions. In addition to this averaging process, other parameters impact on the measured spectra. These include the electron and hydrogen densities, the nature of the central ionising radiation source, whether

or not the electron energies are in equilibrium, and possibly most important, whether the nebula is optically thin.

Increasing attention has been paid in recent years to the possibility of optically thin nebulae (Pellegrini et al. 2012, and references therein). Zastrow et al. (2013), for example, find that H II regions in their galaxy sample show evidence of optically thin pathways, provided the systems are old enough ($\gtrsim 3$ Myr) for mechanical feedback to have cleared optical thin paths, but young enough ($\lesssim 5$ Myr) that the ionising central star cluster is still present. It appears likely that H II regions may be optically thin much earlier than this. In the case of the central UC1 cluster in M17, Hanson et al. (1997) studied nine O-stars still on the zero-age main sequence, suggesting an age for the cluster and the H II region of 1 Myr or less. Using *JHK* band photometry, Jiang et al. (2002) deduced an age for the central cluster of < 3 Myr. In the same cluster, discrete X-ray sources are present corresponding to individual stars, as well as an extended diffuse X-ray field (Townsend et al. 2003). This ionising radiation is evidently escaping from the H II region, indicating the region is optically thin. This was also reported for the ultra-low abundance object, I Zw 18, by Péquignot (2008). Given that the H II regions are inhomogeneous, it is plausible that parts of them may be optically thin as soon as they are visible. So it is to be expected that some of the observations considered here exhibit characteristics readily explained by low values of the optical depth, τ . As we note, the radiation emitted from our optically thick model nebulae is brighter than from otherwise similar optically thin nebulae. For a distant H II region, given the likelihood that some of a nebula will be optically thick and other parts optically thin, these regions will not be resolved, and the resultant spectrum is a weighted mean of the two. The summed or ‘hybrid’ result is skewed in favor of the brighter, optically thick contribution. Thus, any suggestion of optical thinness in the integrated spectra indicates a substantial fraction of the nebula is optically thin. The effect on apparent electron temperatures of these hybrid spectra are shown in Figure 7.8.

The next most important parameter affecting how well the model T_e versus $12 + \log(\text{O}/\text{H})$ curves fit the observations is $\log(P/k)$. The SIGRID observations for objects whose electron densities, determined from the S II line ratios, are $> 20 \text{ cm}^{-3}$ lie consistently above the standard model ($\log(q) = 8.5$, $\tau = \infty$, $\kappa = \infty$, $\log(P/k) = 5$), and their positions on the plot are therefore readily explained by higher pressure and consequent higher electron densities (Figure 7.10).

The nature of the UV spectral energy distribution of the ionising star cluster is also of critical importance to the resulting nebular spectra, but it is one where the modelling process is probably least well developed. The photoionisation models depend on there being reliable stellar spectral energy distribution models, and at low metallicities extensive stellar models are lacking. We use the Starburst99 models that give reasonable high energy photon fluxes, but we are limited to a minimum oxygen abundance of 0.05 solar. This is an area where further work is important, to understand the behaviour of low-metallicity H II regions affected by strong starburst events. The data considered here are consistent with the findings of Dopita et al. (2006) that the ionisation parameter decreases with increasing metallicity. Finally, our models suggest that κ non-equilibrium electron energy distributions can generate high apparent electron temperatures, but if this is correct, it is not clear why their effect only becomes apparent at low metallicity. The three-dimensional diagnostic grid

plots suggest that κ is a less satisfactory explanation for these high electron temperatures than a combination of low optical depth and higher pressure.

7.15. Conclusions

In this paper, we have explored the various parameters affecting the measurement of apparent electron temperatures in H II regions. We have used the data for the SIGRID observations from [paper 1](#) (Chapter 6), the SDSS data from [Izotov et al. \(2006\)](#), low-metallicity emission line galaxy data from [Izotov et al. \(2012\)](#) and for Wolf-Rayet galaxies from [López-Sánchez & Esteban \(2009, 2010\)](#) to demonstrate these effects. The standard equilibrium, optically thick model with $\log(q) = 8.5$ fits the observations remarkably well. The deviations from the fit are slight for metallicities above one-fifth solar, and can be explained by other physical parameters coming into play. For the low-metallicity objects considered here, the important parameters are the ionisation parameter, $\log(q)$, the optical thickness, τ , κ electron energies, and the pressure/density, specified by $\log(P/k)$. The nature of the central ionisation star cluster source is also important, but the models available for spectral energy distributions at low-metallicity limit our exploration here. This is an important area for further investigation.

We have developed diagnostic plots to identify objects that are not optically thick, and it is clear that some of the observations can be readily explained by this effect. Other objects show clear evidence of the effects of higher electron densities. Together, these two factors offer a plausible explanation of the observed data. While non-equilibrium κ electron energy distributions may affect the observations, they require very low values of κ in some cases, and an explanation for their disappearance at higher abundances.

We have used modelling of three-dimensional grids to augment the standard two-dimensional diagnostics, and suggest that this is an area with considerable potential, given the right manipulative tools. We conclude that the highest measured electron temperatures that fall within the bounds of the fitting approximations can be satisfactorily explained by a combination of pressure ($\log(P/k) \gtrsim 6$) and optically thin nebulae ($8 < \tau < \infty$).

7.16. Appendix: Revisions to the Mappings photoionisation modelling code

The current version of the Mappings photoionisation modelling code is IV.1.4. As the work described in this paper depends heavily on the Mappings code, it is useful to summarise the major changes since the previous version (IV.0) ([Dopita et al. 2013](#)). A new integration scheme has been implemented, along with improved equilibrium calculations, to achieve a more precise balance of heating and cooling. The new code model performs better in H II regions and planetary nebula models when compared to the Lexington benchmarks ([Péquignot et al. 2001](#)), with more consistent ionisation state and temperature averages, compared to previous Mappings versions. Photoelectric cross sections for C, N, O, He I and He II have been revised to take into account the latest experimental and model atomic data. Hydrogen and helium charge exchange reactions for both recombination and ionisation

204 The electron temperature–abundance calibration and parameters affecting it

have been updated, as are the ways in which these are handled. The hydrogenic free-bound recombination calculations have been revised, with new coefficients, to ensure detailed balance and energy conservation.

CHAPTER 8

Conclusions

Although the Universe is under no obligation to make sense, students in pursuit of the Ph.D. are.

Robert P. Kirshner, 1991

In this work I set out to measure and analyse the spectra of a sample of isolated dwarf irregular galaxies, to see if they showed evidence of low metallicity primordial gas. While their nebular metallicities are somewhat lower than those reported for similar galaxies in more crowded environments, the majority of the evidence assembled so far suggests that these galaxies evolve normally, with numbers of star formation episodes.

One galaxy, however, the very faint object, J1118-17s2, shows no evidence of the red [N II] lines to the limit of the observed noise. This suggests a very low metallicity, without providing the information necessary to measure it exactly. The observations of other SIGRID objects suggest that they are similar to those reported in other studies of field and void dwarf irregular galaxies.

In the analysis of the spectra undertaken here, I have used new approaches to determining the total oxygen abundances, both for the direct method and the diagnostic grids. The latter now appear to generate such consistent results—in contrast to the older strong line methods—that they provide a new reference standard to compare with direct method and recombination line results.

While exploring problems with my data analysis, I unexpectedly found that non-equilibrium κ energy distributions offered a new and plausible explanation for the abundance discrepancy between recombination line measurements and collisionally excited line measurements. However, I also found that this does not appear to play a major role in low metallicity objects such as those reported here.

8.0.1. Future work

There is much more observational work to be done measuring the spectra of the remaining SIGRID objects, especially the faint extended or “bloater” objects (of which J1118-17(s1+s2)

is the only measured example). While I have, perforce, concentrated in this work on the observations for which the signal to noise values are highest, it appears likely that valuable results will accrue from observing the fainter objects. Observations of such faint objects will push the instrumentation to its detecting limit, but the work may yield important results, if J1118-17 is typical. The new CCD detectors and flat-field lamps installed for the WiFeS spectrograph should improve both the signal to noise and the flux calibration processes, leading to more reliable abundances and temperatures, and a better response for these objects. It is also important to explore the nitrogen to oxygen ratio, to see whether there is evidence at the lowest oxygen abundances for a plateau arising from primary nitrogen. The present work has not provided sufficient information to resolve this question.

It might be thought that observing the SIGRID objects using the 8/10-metre class telescopes in Hawai'i or Chile would offer superior results. But it is important to note that the WiFeS instrument on the ANU 2.3 metre telescope is exceptional, being optically very fast with high throughput, and having a field of view that is well suited to objects of the angular dimensions of the SIGRID sample. It is tempting to consider this prospect, given the extraordinary climatic events (Appendix A) that impinged on the observations reported here. However, it is unlikely that the larger telescopes would offer improved, or even equivalent, signal to noise. There may be small objects in the sample, for example the H II region in KK246, which would suit the available IFU instrumentation in locations with substantially better seeing and weather prospects, and this is worth investigating.

The SIGRID objects have plentiful quantities of neutral hydrogen, by definition, as they were selected from the HIPASS catalog. One object, the very isolated dwarf KK246, is known to be surrounded by a large envelope of neutral hydrogen, many times larger than the visible galaxy (Kreckel et al. 2011). Other similar observations of isolated dwarf galaxies show similar envelopes (Kreckel et al. 2012), and it is probable that this is true for the other SIGRID objects. It is important to map the neutral hydrogen surrounding these objects at high resolution at 21cm to confirm this possibility, because it will add to our understanding of the structure and evolution of small isolated galaxies.

A separate question is whether the κ electron energy distribution is present in H II regions. The hypothesis runs counter to the current accepted view of H II regions. If non-equilibrium energy distributions occur in gaseous nebulae as they do in solar system plasmas, the idea has the potential to revolutionise the study of both H II regions and planetary nebulae. Thus it is very important to follow up with observations of objects where such distributions can be confirmed—for example, planetary nebulae such as NGC 7009 (Dinerstein et al. 2000). Given that the physical conditions in nearby H II regions such as the Orion nebula are very diverse, it is important to search small regions of these objects for features diagnostic of the existence (or otherwise) of κ distributions. One technique, suggested in Chapter 4, is to compare the electron temperatures for [O III] and [S III], which, if available with sufficient signal to noise, should permit a simultaneous measurement of both the effective electron temperature and κ . There is sufficient uncertainty in the astrophysical community over the κ distribution that it is important to resolve the issue.

Bibliography

- Abazajian, K., et al. 2003, *AJ*, 126, 2081 ([ADS entry](#))
- Aggarwal, K. M. 1993, *ApJS*, 85, 197 ([ADS entry](#))
- Aggarwal, K. M., & Keenan, F. P. 1999, *ApJS*, 123, 311 ([ADS entry](#))
- Aldrovandi, S. M. V., & Gruenwald, R. B. 1985, *A&A*, 147, 331 ([ADS entry](#))
- Allen, M. G., Groves, B. A., Dopita, M. A., Sutherland, R. S., & Kewley, L. J. 2008, *ApJS*, 178, 20 ([ADS entry](#))
- Aller, L. H., ed. 1984, *Astrophysics and Space Science Library*, Vol. 112, *Physics of Thermal Gaseous Nebulae* (Dordrecht: D. Reidel Publishing Co.) ([ADS entry](#))
- Aloisi, A., Tosi, M., & Greggio, L. 1999, *AJ*, 118, 302 ([ADS entry](#))
- Andrews, B. H., & Martini, P. 2013, *ApJ*, 765, 140 ([ADS entry](#))
- Annibali, F., et al. 2013, *AJ*, 146, 144 ([ADS entry](#))
- Arthur, S. J., Henney, W. J., Mellema, G., de Colle, F., & Vázquez-Semadeni, E. 2011, *MNRAS*, 414, 1747 ([ADS entry](#))
- Babul, A., & Ferguson, H. C. 1996, *ApJ*, 458, 100 ([ADS entry](#))
- Baker, J. G., Menzel, D. H., & Aller, L. H. 1938, *ApJ*, 88, 422 ([ADS entry](#))
- Begum, A., Chengalur, J. N., & Karachentsev, I. D. 2005, *A&A*, 433, L1 ([ADS entry](#))
- Bell, E. F., & de Jong, R. S. 2001, *ApJ*, 550, 212 ([ADS entry](#))
- Berg, D. A., Skillman, E. D., Garnett, D. R., Croxall, K. V., Marble, A. R., Smith, J. D., Gordon, K., & Kennicutt, Jr., R. C. 2013, *ApJ*, 775, 128 ([ADS entry](#))
- Berg, D. A., et al. 2012, *ApJ*, 754, 98 ([ADS entry](#))
- Bessell, M. S. 1999, *PASP*, 111, 1426 ([ADS entry](#))

- Binette, L., Matadamas, R., Hägele, G. F., Nicholls, D. C., Magris C., G., Peña-Guerrero, M. Á., Morisset, C., & Rodríguez-González, A. 2012, *A&A*, 547, A29 ([ADS entry](#))
- Bland-Hawthorn, J., Sutherland, R., & Karlsson, T. 2011, in *EAS Publications Series*, Vol. 48, *EAS Publications Series*, ed. M. Koleva, P. Prugniel, & I. Vauglin (Les Ulis, France: EDP Sciences), 397–404 ([ADS entry](#))
- Bohm, D., & Aller, L. H. 1947, *ApJ*, 105, 131 ([ADS entry](#))
- Bowen, I. S. 1928, *ApJ*, 67, 1 ([ADS entry](#))
- Bregman, J. N. 2007, *ARA&A*, 45, 221 ([ADS entry](#))
- Bresolin, F., Schaerer, D., González Delgado, R. M., & Stasińska, G. 2005, *A&A*, 441, 981 ([ADS entry](#))
- Burbidge, E. M., Burbidge, G. R., Fowler, W. A., & Hoyle, F. 1957, *Reviews of Modern Physics*, 29, 547 ([ADS entry](#))
- Butkevich, A. G., Berdyugin, A. V., & Teerikorpi, P. 2005, *MNRAS*, 362, 321 ([ADS entry](#))
- Cardelli, J. A., Clayton, G. C., & Mathis, J. S. 1989, *ApJ*, 345, 245 ([ADS entry](#))
- Cellone, S. A., & Buzzoni, A. 2007, in *Groups of Galaxies in the Nearby Universe*, ed. I. Saviane, V. D. Ivanov, & J. Borissova, 91–95 ([ADS entry](#))
- Childress, M. J., Vogt, F. P. A., Nielsen, J., & Sharp, R. G. 2014, *Ap&SS*, 349, 617 ([ADS entry](#))
- Collier, M. R. 1993, *Geophys. Res. Lett.*, 20, 1531 ([ADS entry](#))
- Contini, T., Treyer, M. A., Sullivan, M., & Ellis, R. S. 2002, *MNRAS*, 330, 75 ([ADS entry](#))
- Dalcanton, J. J., et al. 2009, *ApJS*, 183, 67 ([ADS entry](#))
- De Lucia, G., Kauffmann, G., Springel, V., White, S. D. M., Lanzoni, B., Stoehr, F., Tormen, G., & Yoshida, N. 2004, *MNRAS*, 348, 333 ([ADS entry](#))
- Diaz, A. I., Terlevich, E., Pagel, B. E. J., Vilchez, J. M., & Edmunds, M. G. 1987, *MNRAS*, 226, 19 ([ADS entry](#))
- Dinerstein, H. L., Lafon, C. E., & Garnett, D. R. 2000, in *Astronomical Society of the Pacific Conference Series*, Vol. 199, *Asymmetrical Planetary Nebulae II: From Origins to Microstructures*, ed. J. H. Kastner, N. Soker, & S. Rappaport, 301 ([ADS entry](#))
- Disney, M. J., Romano, J. D., Garcia-Appadoo, D. A., West, A. A., Dalcanton, J. J., & Cortese, L. 2008, *Nature*, 455, 1082 ([ADS entry](#))
- Dopcke, G., Glover, S. C. O., Clark, P. C., & Klessen, R. S. 2011, *ApJ*, 729, L3+ ([ADS entry](#))
- Dopita, M. A., Hart, J., McGregor, P., Oates, P., Bloxham, G., & Jones, D. 2007, *Ap&SS*, 310, 255 ([ADS entry](#))
- Dopita, M. A., Kewley, L. J., Heisler, C. A., & Sutherland, R. S. 2000, *ApJ*, 542, 224 ([ADS entry](#))
- Dopita, M. A., & Sutherland, R. S. 2000, *ApJ*, 539, 742 ([ADS entry](#))

- . 2003, *Astrophysics of the Diffuse Universe* (New York: Springer) ([ADS entry](#))
- Dopita, M. A., Sutherland, R. S., Nicholls, D. C., Kewley, L. J., & Vogt, F. P. A. 2013, *ApJS*, 208, 10 ([ADS entry](#))
- Dopita, M. A., et al. 2006, *ApJ*, 647, 244 ([ADS entry](#))
- . 2010, *Ap&SS*, 327, 245 ([Link](#))
- Doyle, M. T., et al. 2005, *MNRAS*, 361, 34 ([ADS entry](#))
- Draine, B. T., & Lee, H. M. 1984, *ApJ*, 285, 89 ([ADS entry](#))
- Edmunds, M. G., & Pagel, B. E. J. 1978, *MNRAS*, 185, 77P ([ADS entry](#))
- Ekta, B., Pustilnik, S. A., & Chengalur, J. N. 2009, *MNRAS*, 397, 963 ([ADS entry](#))
- Ellis, R. S. 1997, *ARA&A*, 35, 389 ([ADS entry](#))
- Esteban, C. 2002, in *Revista Mexicana de Astronomia y Astrofisica Conference Series*, Vol. 12, *Revista Mexicana de Astronomia y Astrofisica Conference Series*, ed. W. J. Henney, J. Franco, & M. Martos, 56–61 ([ADS entry](#))
- Esteban, C., Bresolin, F., Peimbert, M., García-Rojas, J., Peimbert, A., & Mesa-Delgado, A. 2009, *ApJ*, 700, 654 ([ADS entry](#))
- Esteban, C., & Peimbert, M. 1995, *A&A*, 300, 78 ([ADS entry](#))
- Esteban, C., Peimbert, M., García-Rojas, J., Ruiz, M. T., Peimbert, A., & Rodríguez, M. 2004, *MNRAS*, 355, 229 ([ADS entry](#))
- Fang, X., & Liu, X.-W. 2011, *MNRAS*, 415, 181 ([ADS entry](#))
- Fischera, J., & Dopita, M. 2005, *ApJ*, 619, 340 ([ADS entry](#))
- Fisher, D. B., et al. 2014, *Nature*, 505, 186 ([ADS entry](#))
- Frey, H. U., Mende, S. B., Arens, J. F., McCullough, P. R., & Swenson, G. R. 2000, *Geophys. Res. Lett.*, 27, 41 ([ADS entry](#))
- Gaensler, B. M., et al. 2011, *Nature*, 478, 214 ([ADS entry](#))
- García-Rojas, J., & Esteban, C. 2007, *ApJ*, 670, 457 ([ADS entry](#))
- García-Rojas, J., Esteban, C., Peimbert, A., Peimbert, M., Rodríguez, M., & Ruiz, M. T. 2005, *MNRAS*, 362, 301 ([ADS entry](#))
- García-Rojas, J., Esteban, C., Peimbert, M., Costado, M. T., Rodríguez, M., Peimbert, A., & Ruiz, M. T. 2006, *MNRAS*, 368, 253 ([ADS entry](#))
- García-Rojas, J., Esteban, C., Peimbert, M., Rodríguez, M., Ruiz, M. T., & Peimbert, A. 2004, *ApJS*, 153, 501 ([ADS entry](#))
- Garnett, D. R. 1992, *AJ*, 103, 1330 ([ADS entry](#))

- Garnett, D. R., Skillman, E. D., Dufour, R. J., & Shields, G. A. 1997, *ApJ*, 481, 174 ([ADS entry](#))
- Gil de Paz, A., Madore, B. F., & Pevunova, O. 2003, *ApJS*, 147, 29 ([ADS entry](#))
- Graham, N. E., & White, W. B. 1988, *Science*, 240, 1293 ([ADS entry](#))
- Grcevich, J., & Putman, M. E. 2009, *ApJ*, 696, 385 ([ADS entry](#))
- Grebel, E. K. 1997, in *Reviews in Modern Astronomy*, Vol. 10, *Reviews in Modern Astronomy*, ed. R. E. Schielicke, 29–60 ([ADS entry](#))
- Grevesse, N., Asplund, M., Sauval, A. J., & Scott, P. 2010, *Ap&SS*, 328, 179 ([ADS entry](#))
- Groves, B. A., Dopita, M. A., & Sutherland, R. S. 2004, *ApJS*, 153, 9 ([ADS entry](#))
- Guseva, N. G., Papaderos, P., Meyer, H. T., Izotov, Y. I., & Fricke, K. J. 2009, *A&A*, 505, 63 ([ADS entry](#))
- Hamuy, M., Walker, A. R., Suntzeff, N. B., Gigoux, P., Heathcote, S. R., & Phillips, M. M. 1992, *PASP*, 104, 533 ([ADS entry](#))
- Hanson, M. M., Howarth, I. D., & Conti, P. S. 1997, *ApJ*, 489, 698 ([ADS entry](#))
- Harvey-Smith, L., Madsen, G. J., & Gaensler, B. M. 2011, *ApJ*, 736, 83 ([ADS entry](#))
- Hebb, M. H., & Menzel, D. H. 1940, *ApJ*, 92, 408 ([ADS entry](#))
- Henry, R. B. C., & Worthey, G. 1999, *PASP*, 111, 919 ([ADS entry](#))
- Hudson, C. E., Ramsbottom, C. A., & Scott, M. P. 2012, *ApJ*, 750, 65 ([ADS entry](#))
- Huggins, W., & Miller, W. A. 1864, *Royal Society of London Philosophical Transactions Series I*, 154, 437 ([ADS entry](#))
- Hummer, D. G., Berrington, K. A., Eissner, W., Pradhan, A. K., Saraph, H. E., & Tully, J. A. 1993, *A&A*, 279, 298 ([ADS entry](#))
- Hunt, L. K., Thuan, T. X., & Izotov, Y. I. 2003, *ApJ*, 588, 281 ([ADS entry](#))
- Hunter, D. A., & Elmegreen, B. G. 2004, *AJ*, 128, 2170 ([ADS entry](#))
- Iovino, A. 2002, *AJ*, 124, 2471 ([ADS entry](#))
- Izotov, Y. I., Guseva, N. G., Fricke, K. J., & Papaderos, P. 2009, *A&A*, 503, 61 ([ADS entry](#))
- Izotov, Y. I., Stasińska, G., Guseva, N. G., & Thuan, T. X. 2004, *A&A*, 415, 87 ([ADS entry](#))
- Izotov, Y. I., Stasińska, G., Meynet, G., Guseva, N. G., & Thuan, T. X. 2006, *A&A*, 448, 955 ([ADS entry](#))
- Izotov, Y. I., & Thuan, T. X. 1999, *ApJ*, 511, 639 ([ADS entry](#))
- . 2004a, *ApJ*, 616, 768 ([ADS entry](#))
- . 2004b, *ApJ*, 602, 200 ([ADS entry](#))

- Izotov, Y. I., Thuan, T. X., & Guseva, N. G. 2005, *ApJ*, 632, 210 ([ADS entry](#))
- . 2012, *A&A*, 546, A122 ([ADS entry](#))
- Izotov, Y. I., Thuan, T. X., & Lipovetsky, V. A. 1994, *ApJ*, 435, 647 ([ADS entry](#))
- Izotov, Y. I., Thuan, T. X., & Stasińska, G. 2007, *ApJ*, 662, 15 ([ADS entry](#))
- Jerjen, H., Binggeli, B., & Barazza, F. D. 2004, *AJ*, 127, 771 ([ADS entry](#))
- Jerjen, H., & Dressler, A. 1997, *A&AS*, 124, 1 ([ADS entry](#))
- Jiang, Z., et al. 2002, *ApJ*, 577, 245 ([ADS entry](#))
- Karachentsev, I. D., Karachentseva, V. E., Huchtmeier, W. K., & Makarov, D. I. 2004, *AJ*, 127, 2031 ([ADS entry](#))
- Karachentsev, I. D., & Makarov, D. I. 1999, in *IAU Symposium*, Vol. 186, *Galaxy Interactions at Low and High Redshift*, ed. J. E. Barnes & D. B. Sanders, 109–116 ([ADS entry](#))
- Karachentsev, I. D., Makarov, D. I., & Kaisina, E. I. 2013, *AJ*, 145, 101 ([ADS entry](#))
- Karachentsev, I. D., Makarov, D. I., Karachentseva, V. E., & Melnik, O. V. 2008, *Astronomy Letters*, 34, 832 ([ADS entry](#))
- Karachentsev, I. D., Makarov, D. I., Karachentseva, V. E., & Melnyk, O. V. 2011, *Astrophysical Bulletin*, 66, 1 ([ADS entry](#))
- Karachentsev, I. D., & Nasonova, O. G. 2010, *MNRAS*, 405, 1075 ([ADS entry](#))
- Karachentsev, I. D., & Nasonova (Kashibadze), O. G. 2010, *Astrophysics*, 53, 32 ([ADS entry](#))
- Karachentsev, I. D., et al. 2006, *AJ*, 131, 1361 ([ADS entry](#))
- Kennicutt, Jr., R. C., Bresolin, F., & Garnett, D. R. 2003, *ApJ*, 591, 801 ([ADS entry](#))
- Kennicutt, Jr., R. C., Lee, J. C., Funes, José G., S. J., Sakai, S., & Akiyama, S. 2008, *ApJS*, 178, 247 ([ADS entry](#))
- Kewley, L. J., & Dopita, M. A. 2002, *ApJS*, 142, 35 ([ADS entry](#))
- Kewley, L. J., & Ellison, S. L. 2008, *ApJ*, 681, 1183 ([ADS entry](#))
- Kingdon, J. B., & Ferland, G. J. 1995, *ApJ*, 450, 691 ([ADS entry](#))
- Kirby, E. M., Jerjen, H., Ryder, S. D., & Driver, S. P. 2008, *AJ*, 136, 1866 ([ADS entry](#))
- Kisielius, R., Storey, P. J., Ferland, G. J., & Keenan, F. P. 2009, *MNRAS*, 397, 903 ([ADS entry](#))
- Kobayashi, C., Springel, V., & White, S. D. M. 2007, *MNRAS*, 376, 1465 ([ADS entry](#))
- Köppen, J. 1979, *A&AS*, 35, 111 ([ADS entry](#))
- Koribalski, B. S., et al. 2004, *AJ*, 128, 16 ([ADS entry](#))
- Kreckel, K., Peebles, P. J. E., van Gorkom, J. H., van de Weygaert, R., & van der Hulst, J. M. 2011, *AJ*, 141, 204 ([ADS entry](#))

- Kreckel, K., Platen, E., Aragón-Calvo, M. A., van Gorkom, J. H., van de Weygaert, R., van der Hulst, J. M., & Beygu, B. 2012, *AJ*, 144, 16 ([ADS entry](#))
- Kunth, D., & Östlin, G. 2000, *A&A Rev.*, 10, 1 ([ADS entry](#))
- Lauberts, A. 1982, *ESO/Uppsala survey of the ESO(B) atlas* (Garching: ESO) ([ADS entry](#))
- Lebouteiller, V., Heap, S., Hubeny, I., & Kunth, D. 2013, *A&A*, 553, A16 ([ADS entry](#))
- Lee, H., McCall, M. L., Kingsburgh, R. L., Ross, R., & Stevenson, C. C. 2003, *AJ*, 125, 146 ([ADS entry](#))
- Lee, H., Skillman, E. D., Cannon, J. M., Jackson, D. C., Gehrz, R. D., Polonski, E. F., & Woodward, C. E. 2006, *ApJ*, 647, 970 ([ADS entry](#))
- Lee, J. C., Kennicutt, R. C., José G. Funes, S. J., Sakai, S., & Akiyama, S. 2009, *ApJ*, 692, 1305 ([ADS entry](#))
- Leitherer, C. 2014, *ArXiv e-prints* ([ADS entry](#))
- Leitherer, C., Ekström, S., Meynet, G., Schaerer, D., Agienko, K. B., & Levesque, E. M. 2014, *ApJS*, 212, 14 ([ADS entry](#))
- Leitherer, C., et al. 1999, *ApJS*, 123, 3 ([ADS entry](#))
- Lennon, D. J., & Burke, V. M. 1994, *A&AS*, 103, 273 ([ADS entry](#))
- Leubner, M. P. 2002, *Ap&SS*, 282, 573 ([ADS entry](#))
- Liu, X.-W., Storey, P. J., Barlow, M. J., Danziger, I. J., Cohen, M., & Bryce, M. 2000, *MNRAS*, 312, 585 ([ADS entry](#))
- Liu, Y., Liu, X.-W., Luo, S.-G., & Barlow, M. J. 2004, *MNRAS*, 353, 1231 ([ADS entry](#))
- Livadiotis, G., & McComas, D. J. 2009, *Journal of Geophysical Research (Space Physics)*, 114, 11105 ([ADS entry](#))
- . 2010, *ApJ*, 714, 971 ([ADS entry](#))
- . 2011, *ApJ*, 741, 88 ([ADS entry](#))
- . 2012, *ApJ*, 749, 11 ([ADS entry](#))
- Livadiotis, G., McComas, D. J., Dayeh, M. A., Funsten, H. O., & Schwadron, N. A. 2011, *ApJ*, 734, 1 ([ADS entry](#))
- Loewenstein, M. 2001, *ApJ*, 557, 573 ([ADS entry](#))
- Loose, H.-H., & Thuan, T. X. 1986, in *Star-forming Dwarf Galaxies and Related Objects*, 73–88 ([ADS entry](#))
- López-Sánchez, Á. R. 2010, *A&A*, 521, A63 ([ADS entry](#))
- López-Sánchez, Á. R., Dopita, M. A., Kewley, L. J., Zahid, H. J., Nicholls, D. C., & Scharwächter, J. 2012, *MNRAS*, 426, 2630 ([ADS entry](#))

- López-Sánchez, Á. R., & Esteban, C. 2009, *A&A*, 508, 615 ([ADS entry](#))
- . 2010, *A&A*, 517, A85 ([ADS entry](#))
- López-Sánchez, Á. R., Esteban, C., García-Rojas, J., Peimbert, M., & Rodríguez, M. 2007, *ApJ*, 656, 168 ([ADS entry](#))
- Luridiana, V., Morisset, C., & Shaw, R. A. 2012, in *IAU Symposium*, Vol. 283, *IAU Symposium*, 422–423 ([ADS entry](#))
- Madau, P., Pozzetti, L., & Dickinson, M. 1998, *ApJ*, 498, 106 ([ADS entry](#))
- Makarov, D., Makarova, L., Sharina, M., Uklein, R., Tikhonov, A., Guhathakurta, P., Kirby, E., & Terekhova, N. 2012, *MNRAS*, 425, 709 ([ADS entry](#))
- Malmquist, K. G. 1921, *Arkiv Mat. Astron. Fys.*, 16, 1
- Markarian, B. E. 1967, *Astrofizika*, 3, 55 ([ADS entry](#))
- Mateo, M. L. 1998, *ARA&A*, 36, 435 ([ADS entry](#))
- Mathis, J. S., Rumpl, W., & Nordsieck, K. H. 1977, *ApJ*, 217, 425 ([ADS entry](#))
- McGaugh, S. S. 1994, *ApJ*, 426, 135 ([ADS entry](#))
- McLaughlin, B. M., & Bell, K. L. 1998, *Journal of Physics B Atomic Molecular Physics*, 31, 4317 ([ADS entry](#))
- McQuinn, K. B. W., Skillman, E. D., Cannon, J. M., Dalcanton, J. J., Dolphin, A., Stark, D., & Weisz, D. 2009, *ApJ*, 695, 561 ([ADS entry](#))
- McQuinn, K. B. W., et al. 2010, *ApJ*, 721, 297 ([ADS entry](#))
- Meurer, G. R., Carignan, C., Beaulieu, S. F., & Freeman, K. C. 1996, *AJ*, 111, 1551 ([ADS entry](#))
- Meurer, G. R., et al. 2006, *ApJS*, 165, 307 ([ADS entry](#))
- Meyer, M. J., et al. 2004, *MNRAS*, 350, 1195 ([ADS entry](#))
- Mould, J. R., et al. 2000, *ApJ*, 529, 786 ([ADS entry](#))
- Nasonova, O. G., & Karachentsev, I. D. 2011, *Astrophysics*, 54, 1 ([ADS entry](#))
- Nicholls, D. C., Dopita, M. A., Jerjen, H., & Meurer, G. R. 2011, *AJ*, 142, 83 ([ADS entry](#))
- Nicholls, D. C., Dopita, M. A., & Sutherland, R. S. 2012, *ApJ*, 752, 148 ([ADS entry](#))
- Nicholls, D. C., Dopita, M. A., Sutherland, R. S., Jerjen, H., Kewley, L. J., & Basurah, H. 2014a, *ApJ*, 786, 155 ([ADS entry](#))
- . 2014b, *ArXiv e-prints* ([ADS entry](#))
- Nicholls, D. C., Dopita, M. A., Sutherland, R. S., Kewley, L. J., & Palay, E. 2013, *ApJS*, 207, 21 ([ADS entry](#))

- Nicholls, D. C., Evans, W. F. J., & Llewellyn, E. J. 1972, *Journal of Quantitative Spectroscopy and Radiative Transfer*, 12, 549 ([ADS entry](#))
- Nicholls, D. C., Jerjen, H., Dopita, M. A., & Basurah, H. 2014c, *ApJ*, 780, 88 ([ADS entry](#))
- Oke, J. B. 1990, *AJ*, 99, 1621 ([ADS entry](#))
- Osterbrock, D. E., & Ferland, G. J. 2006, *Astrophysics of gaseous nebulae and active galactic nuclei*, 2nd edn. (University Science Books) ([ADS entry](#))
- Owocki, S. P., & Scudder, J. D. 1983, *ApJ*, 270, 758 ([ADS entry](#))
- Pagel, B. E. J., Simonson, E. A., Terlevich, R. J., & Edmunds, M. G. 1992, *MNRAS*, 255, 325 ([ADS entry](#))
- Palay, E., Nahar, S. N., Pradhan, A. K., & Eissner, W. 2012, *MNRAS*, 423, L35 ([ADS entry](#))
- Papaderos, P., Izotov, Y. I., Thuan, T. X., Noeske, K. G., Fricke, K. J., Guseva, N. G., & Green, R. F. 2002, *A&A*, 393, 461 ([ADS entry](#))
- Papaderos, P., & Östlin, G. 2012, *A&A*, 537, A126 ([ADS entry](#))
- Pauldrach, A. W. A., Hoffmann, T. L., & Lennon, M. 2001, *A&A*, 375, 161 ([ADS entry](#))
- Peña-Guerrero, M. A., Peimbert, A., Peimbert, M., & Ruiz, M. T. 2012, *ApJ*, 746, 115 ([ADS entry](#))
- Peimbert, A. 2003, *ApJ*, 584, 735 ([ADS entry](#))
- Peimbert, M. 1967, *ApJ*, 150, 825 ([ADS entry](#))
- Peimbert, M., & Costero, R. 1969, *Boletín de los Observatorios Tonantzintla y Tacubaya*, 5, 3 ([ADS entry](#))
- Peimbert, M., Storey, P. J., & Torres-Peimbert, S. 1993, *ApJ*, 414, 626 ([ADS entry](#))
- Pellegrini, E. W., Oey, M. S., Winkler, P. F., Points, S. D., Smith, R. C., Jaskot, A. E., & Zastrow, J. 2012, *ApJ*, 755, 40 ([ADS entry](#))
- Péquignot, D. 2008, *A&A*, 478, 371 ([ADS entry](#))
- Péquignot, D., et al. 2001, in *Astronomical Society of the Pacific Conference Series*, Vol. 247, *Spectroscopic Challenges of Photoionized Plasmas*, ed. G. Ferland & D. W. Savin, 533 ([ADS entry](#))
- Pérez-Montero, E., & Contini, T. 2009, *MNRAS*, 398, 949 ([ADS entry](#))
- Pérez-Montero, E., et al. 2011, *A&A*, 532, A141 ([ADS entry](#))
- Petrini, D., & da Silva, E. P. 1997, *A&A*, 317, 262 ([ADS entry](#))
- Pierrard, V., & Lazar, M. 2010, *Sol. Phys.*, 267, 153 ([ADS entry](#))
- Pilyugin, L. S., & Thuan, T. X. 2005, *ApJ*, 631, 231 ([ADS entry](#))

- Pilyugin, L. S., Vílchez, J. M., & Thuan, T. X. 2010, *ApJ*, 720, 1738 ([ADS entry](#))
- Pradhan, A. K., Montenegro, M., Nahar, S. N., & Eissner, W. 2006, *MNRAS*, 366, L6 ([ADS entry](#))
- Pustilnik, S., Kniazev, A., Pramskij, A., Izotov, Y., Foltz, C., Brosch, N., Martin, J.-M., & Ugryumov, A. 2004, *A&A*, 419, 469 ([ADS entry](#))
- Pustilnik, S. A., & Kniazev, A. Y. 2007, in *IAU Symposium*, Vol. 235, *Galaxy Evolution across the Hubble Time*, ed. F. Combes & J. Palous, 238–238 ([ADS entry](#))
- Pustilnik, S. A., Martin, J.-M., Tepliakova, A. L., & Kniazev, A. Y. 2011a, *MNRAS*, 417, 1335 ([ADS entry](#))
- Pustilnik, S. A., Tepliakova, A. L., & Kniazev, A. Y. 2011b, *Astrophysical Bulletin*, 66, 255 ([ADS entry](#))
- Rémy-Ruyer, A., et al. 2014, *A&A*, 563, A31 ([ADS entry](#))
- Rich, J. A., Dopita, M. A., Kewley, L. J., & Rupke, D. S. N. 2010, *ApJ*, 721, 505 ([ADS entry](#))
- Ricotti, M., & Gnedin, N. Y. 2005, *ApJ*, 629, 259 ([ADS entry](#))
- Ricotti, M., Gnedin, N. Y., & Shull, J. M. 2008, *ApJ*, 685, 21 ([ADS entry](#))
- Rizzi, L., Tully, R. B., Makarov, D., Makarova, L., Dolphin, A. E., Sakai, S., & Shaya, E. J. 2007, *ApJ*, 661, 815 ([ADS entry](#))
- Rodríguez, L. F., Gómez, Y., & Tafoya, D. 2012, *MNRAS*, 420, 279 ([ADS entry](#))
- Saji, N. H., Goswami, B. N., Vinayachandran, P. N., & Yamagata, T. 1999, *Nature*, 401, 360 ([ADS entry](#))
- Sánchez Almeida, J., Muñoz-Tuñón, C., Amorín, R., Aguerri, J. A., Sánchez-Janssen, R., & Tenorio-Tagle, G. 2008, *ApJ*, 685, 194 ([ADS entry](#))
- Sargent, W. L. W., & Searle, L. 1970, *ApJ*, 162, L155+ ([ADS entry](#))
- Saviane, I., Momany, Y., da Costa, G. S., Rich, R. M., & Hibbard, J. E. 2008, *ApJ*, 678, 179 ([ADS entry](#))
- Schlafly, E. F., & Finkbeiner, D. P. 2011, *ApJ*, 737, 103 ([ADS entry](#))
- Schlegel, D. J., Finkbeiner, D. P., & Davis, M. 1998, *ApJ*, 500, 525 ([ADS entry](#))
- Searle, L. 1971, *ApJ*, 168, 327 ([ADS entry](#))
- Seaton, M. J. 1975, *MNRAS*, 170, 475 ([ADS entry](#))
- Shaw, R. A., & Dufour, R. J. 1995, *PASP*, 107, 896 ([ADS entry](#))
- Shizgal, B. D. 2007, *Ap&SS*, 312, 227 ([ADS entry](#))
- Shull, J. M., & van Steenberg, M. E. 1985, *ApJ*, 298, 268 ([ADS entry](#))

- Skillman, E. D., Televich, R. J., Kennicutt, Jr., R. C., Garnett, D. R., & Terlevich, E. 1994, *ApJ*, 431, 172 ([ADS entry](#))
- Spitzer, L. 1962, *Physics of Fully Ionized Gases*, 2nd edn. (New York: Interscience Publishers) ([ADS entry](#))
- Stasińska, G. 1978, *A&A*, 66, 257 ([ADS entry](#))
- Stasińska, G. 2002, in *Revista Mexicana de Astronomia y Astrofisica Conference Series*, Vol. 12, *Revista Mexicana de Astronomia y Astrofisica Conference Series*, ed. W. J. Henney, J. Franco, & M. Martos, 62–69 ([ADS entry](#))
- Stasińska, G. 2004, in *Cosmochemistry. The melting pot of the elements*, ed. C. Esteban, R. García López, A. Herrero & F. Sánchez, 115–170 ([ADS entry](#))
- . 2005, *A&A*, 434, 507 ([ADS entry](#))
- Stasińska, G., Morisset, C., Simón-Díaz, S., Bresolin, F., Schaerer, D., & Brandl, B. 2013, *A&A*, 551, A82 ([ADS entry](#))
- Stasińska, G., & Schaerer, D. 1999, *A&A*, 351, 72 ([ADS entry](#))
- Stein, P., Jerjen, H., & Federspiel, M. 1997, *A&A*, 327, 952 ([ADS entry](#))
- Storey, P. J., & Hummer, D. G. 1995, *MNRAS*, 272, 41 ([ADS entry](#))
- Storey, P. J., Sochi, T., & Badnell, N. R. 2013, *ArXiv e-prints* ([ADS entry](#))
- Strigari, L. E., Bullock, J. S., Kaplinghat, M., Simon, J. D., Geha, M., Willman, B., & Walker, M. G. 2008, *Nature*, 454, 1096 ([ADS entry](#))
- Sung, E., Chun, M., Freeman, K. C., & Chaboyer, B. 2002, in *Astronomical Society of the Pacific Conference Series*, Vol. 273, *The Dynamics, Structure & History of Galaxies: A Workshop in Honour of Professor Ken Freeman*, ed. G. S. Da Costa & H. Jerjen, 341–347 ([ADS entry](#))
- Sweet, S. M., Drinkwater, M. J., Meurer, G., Bekki, K., Dopita, M. A., Kilborn, V., & Nicholls, D. C. 2014, *ApJ*, 782, 35 ([ADS entry](#))
- Tayal, S. S. 2007, *ApJS*, 171, 331 ([ADS entry](#))
- Taylor, E. N., & Webster, R. L. 2005, *ApJ*, 634, 1067 ([ADS entry](#))
- Thuan, T. X., Lecavelier des Etangs, A., & Izotov, Y. I. 2005, *ApJ*, 621, 269 ([ADS entry](#))
- Tikhonov, A. V., & Karachentsev, I. D. 2006, *ApJ*, 653, 969 ([ADS entry](#))
- Timmes, F. X. 1991, in *Supernovae*, ed. S. E. Woosley, 619 ([ADS entry](#))
- Tolstoy, E., Hill, V., & Tosi, M. 2009, *ARA&A*, 47, 371 ([ADS entry](#))
- Tonry, J. L., Blakeslee, J. P., Ajhar, E. A., & Dressler, A. 2000, *ApJ*, 530, 625 ([ADS entry](#))
- Torres-Peimbert, S., & Peimbert, M. 1977, *Rev Mex Astron y Astrofis*, 2, 181 ([ADS entry](#))

- Townsley, L. K., Feigelson, E. D., Montmerle, T., Broos, P. S., Chu, Y.-H., & Garmire, G. P. 2003, *ApJ*, 593, 874 ([ADS entry](#))
- Tremonti, C. A., et al. 2004, *ApJ*, 613, 898 ([ADS entry](#))
- Treumann, R. A. 1999, *Phys. Scr*, 59, 19 ([ADS entry](#))
- . 2001, *Ap&SS*, 277, 81 ([ADS entry](#))
- Tsallis, C. 2009, *Introduction to Nonextensive Statistical Mechanics* (New York: Springer) ([ADS entry](#))
- Tsallis, C., Levy, S. V. F., Souza, A. M. C., & Maynard, R. 1995, *Physical Review Letters*, 75, 3589 ([ADS entry](#))
- Tsamis, Y. G., Barlow, M. J., Liu, X.-W., Danziger, I. J., & Storey, P. J. 2003, *MNRAS*, 345, 186 ([ADS entry](#))
- Tully, R. B., Rizzi, L., Shaya, E. J., Courtois, H. M., Makarov, D. I., & Jacobs, B. A. 2009, *AJ*, 138, 323 ([ADS entry](#))
- Tully, R. B., & Shaya, E. J. 1984, *ApJ*, 281, 31 ([ADS entry](#))
- Tully, R. B., Shaya, E. J., Karachentsev, I. D., Courtois, H. M., Kocevski, D. D., Rizzi, L., & Peel, A. 2008, *ApJ*, 676, 184 ([ADS entry](#))
- van de Weygaert, R., et al. 2011, *The Void Galaxy Survey* eds. Ferreras, I. & Pasquali, A. (Berlin: Springer), 17 ([ADS entry](#))
- van Dokkum, P. G. 2001, *PASP*, 113, 1420 ([ADS entry](#))
- van Hoof, P. A. M., Weingartner, J. C., Martin, P. G., Volk, K., & Ferland, G. J. 2004, *MNRAS*, 350, 1330 ([ADS entry](#))
- van Zee, L., & Haynes, M. P. 2006, *ApJ*, 636, 214 ([ADS entry](#))
- van Zee, L., Salzer, J. J., & Haynes, M. P. 1998a, *ApJ*, 497, L1 ([ADS entry](#))
- van Zee, L., Salzer, J. J., Haynes, M. P., O'Donoghue, A. A., & Balonek, T. J. 1998b, *AJ*, 116, 2805 ([ADS entry](#))
- van Zee, L., Westpfahl, D., Haynes, M. P., & Salzer, J. J. 1998c, *AJ*, 115, 1000 ([ADS entry](#))
- Vasyliunas, V. M. 1968, *J. Geophys. Res.*, 73, 2839 ([ADS entry](#))
- Vila Costas, M. B., & Edmunds, M. G. 1993, *MNRAS*, 265, 199 ([ADS entry](#))
- Vilchez, J. M., & Esteban, C. 1996, *MNRAS*, 280, 720 ([ADS entry](#))
- Vogt, F. P. A., Dopita, M. A., & Kewley, L. J. 2013, *ApJ*, 768, 151 ([ADS entry](#))
- Vogt, F. P. A., Dopita, M. A., Kewley, L. J., Sutherland, R. S., Scharwaechter, J., Basurah, H. M., Ali, A., & Amer, M. A. 2014, *ArXiv e-prints* ([ADS entry](#))
- Wang, W., & Liu, X.-W. 2007, *MNRAS*, 381, 669 ([ADS entry](#))

- Warren, B. E., Jerjen, H., & Koribalski, B. S. 2004, *AJ*, 128, 1152 ([ADS entry](#))
- . 2007, *AJ*, 134, 1849 ([ADS entry](#))
- Weisz, D. R., et al. 2011, *ApJ*, 739, 5 ([ADS entry](#))
- Werk, J. K., et al. 2010, *AJ*, 139, 279 ([ADS entry](#))
- Wesson, R., Liu, X.-W., & Barlow, M. J. 2005, *MNRAS*, 362, 424 ([ADS entry](#))
- Wyse, A. B. 1942, *ApJ*, 95, 356 ([ADS entry](#))
- Yeh, S. C. C., & Matzner, C. D. 2012, *ApJ*, 757, 108 ([ADS entry](#))
- York, D. G., et al. 2000, *AJ*, 120, 1579 ([ADS entry](#))
- Young, L. M., & Lo, K. Y. 1997, *ApJ*, 490, 710 ([ADS entry](#))
- Zastrow, J., Oey, M. S., Veilleux, S., & McDonald, M. 2013, *ApJ*, 779, 76 ([ADS entry](#))
- Zhang, Y., Liu, X.-W., Wesson, R., Storey, P. J., Liu, Y., & Danziger, I. J. 2004, *MNRAS*, 351, 935 ([ADS entry](#))
- Zwaan, M. A., et al. 2004, *MNRAS*, 350, 1210 ([ADS entry](#))

APPENDIX A

Weather problems encountered during the observational sessions

I commenced observing near the beginning of what became a strong “La Niña” event, a climate phenomenon described by the Southern Oscillation Index (SOI) ([Graham & White 1988](#)) (see also the [Australian Bureau of Meteorology report](#) on this record breaking event). This overlapped with with a number of negative excursions of the Indian Ocean Dipole (IOD) ([Saji et al. 1999](#)). Both these indices are correlated with increased cloudiness and rainfall in inland Australia. Both affect the weather at Siding Spring Observatory, although it appears the SOI index is the more important. This climatic trend resulted in an exceptionally low clear sky ratio, ~22% clear nights during my observing runs, compared to the average 66% ratio for this site. On the clear nights, the seeing and transparency varied from poor-average to excellent. As a consequence, I was able to observe only ~40% of the objects in the SIGRID galaxy sample.

Figure [A.1](#) shows a plot of the Niño3.4 index and the IOD index for the period 2008-2013. For both these indices, a negative excursion indicates a greater likelihood of rainfall. The vertical bars show the dates of my observing sessions. Chapter 5, Table 1 lists the observation dates of the objects discussed. Three of the observations in that table were obtained by Mike Dopita, to whom I owe a debt of gratitude for augmenting my meagre results.

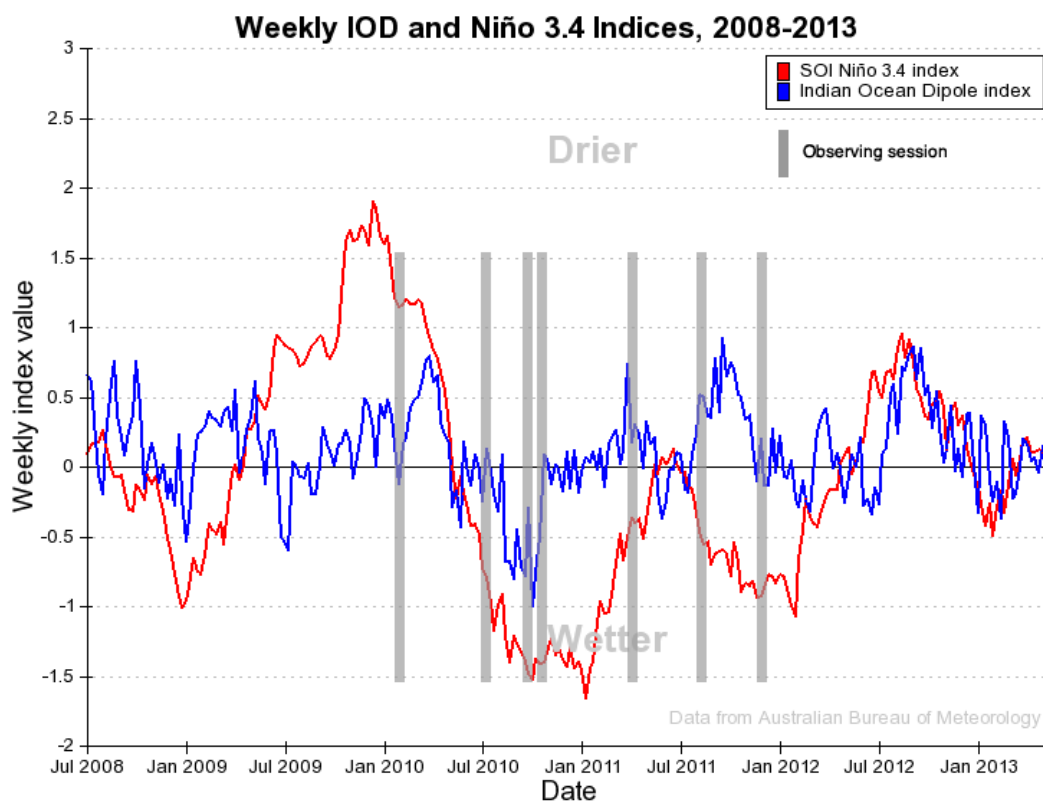


Figure A.1 Niño3.4 and IOD climate indices for the period 2008-2013, with observing session dates marked as vertical bars.